

STATUS OF THESIS

Title of thesis

NON-INVASIVE IMAGE ENHANCEMENT OF COLOUR
RETINAL FUNDUS IMAGES FOR A COMPUTERISED
DIABETIC RETINOPATHY MONITORING AND GRADING
SYSTEM

I, HANUNG ADI NUGROHO

hereby allow my thesis to be placed at the Information Resource Centre (IRC) of
Universiti Teknologi PETRONAS (UTP) with the following conditions:

1. The thesis becomes the property of UTP
2. The IRC of UTP may make copies of the thesis for academic purposes only.
3. This thesis is classified as

Confidential

Non-confidential

If this thesis is confidential, please state the reason:

The contents of the thesis will remain confidential for _____ years.

Remarks on disclosure:



Signature of Author

Permanent address:
Jalan Hibrida UH II/175 Miliran
Jogjakarta 55165
DIY, Indonesia

Date : 18/9/2012

Endorsed by



Signature of Supervisor

PROF IR DR AHMAD FADZIL MOHAMAD HANI
Name of Supervisor
Prof. Ir. Dr. Ahmad Fadzil
Mohamad Hani

Date : 18.9.2012

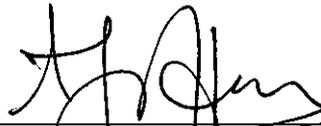
UNIVERSITI TEKNOLOGI PETRONAS
NON-INVASIVE IMAGE ENHANCEMENT OF COLOUR RETINAL FUNDUS
IMAGES FOR A COMPUTERISED DIABETIC RETINOPATHY
MONITORING AND GRADING SYSTEM

by

HANUNG ADI NUGROHO

The undersigned certify that they have read, and recommend to the Postgraduate Studies Programme for acceptance this thesis for the fulfilment of the requirements for the degree stated.

Signature:



Main Supervisor:

PROF IR DR AHMAD FADZIL MOHAMAD HANI
Prof. Ir. Dr. Ahmad Fadzil Mohamad Hani

Signature:



ASSOC. PROF. DR. NOR HISHAM BIN HAMID
Head of Department
Electrical & Electronic Engineering Department
UNIVERSITI TEKNOLOGI PETRONAS
Bandar Seri Iskandar, 31700, Tronoh,
Perak Darul Ridzuan, Malaysia.

Head of Department:

Assoc. Prof. Dr. Nor Hisham Hamid

Date:

19/2/2012

NON-INVASIVE IMAGE ENHANCEMENT OF COLOUR RETINAL FUNDUS
IMAGES FOR A COMPUTERISED DIABETIC RETINOPATHY
MONITORING AND GRADING SYSTEM

by

HANUNG ADI NUGROHO

A Thesis

Submitted to the Postgraduate Studies Programme
as a Requirement for the Degree of

DOCTOR OF PHILOSOPHY

ELECTRICAL AND ELECTRONIC ENGINEERING DEPARTMENT

UNIVERSITI TEKNOLOGI PETRONAS

BANDAR SERI ISKANDAR,

PERAK

SEPTEMBER 2012

DECLARATION OF THESIS

Title of thesis

NON-INVASIVE IMAGE ENHANCEMENT OF COLOUR
RETINAL FUNDUS IMAGES FOR A COMPUTERISED
DIABETIC RETINOPATHY MONITORING AND GRADING
SYSTEM

I, HANUNG ADI NUGROHO

hereby declare that the thesis is based on my original work except for quotations and citations which have been duly acknowledged. I also declare that it has not been previously or concurrently submitted for any other degree at UTP or other institutions.

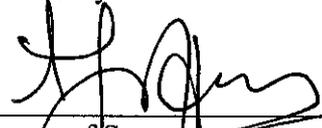


Signature of Author

Permanent address:
Jalan Hibrida UH II/175 Miliran
Jogjakarta 55165
DIY, Indonesia

Date: 18/9/2012.

Witnessed by



Signature of Supervisor
PROF IR DR AHMAD FADZIL MOHAMAD HANI
Prof. Ir. Dr. Ahmad Fadzil
Mohamad Hani

Date: 18.9.2012

DEDICATION

to

my great parents, Bapak Mulyadi dan Ibu Sri Mulyani

my lovely wife, Ririn Mardiasuty

my adorable daughters, Hanim, Maryam and Hasna

ACKNOWLEDGEMENT

First and foremost, I would like to thank Allah, the one and only almighty God, the source and hope for everything in my life.

I would particularly like to thank my supervisor, Prof. Ir. Dr. Ahmad Fadzil M Hani, for his guidance, support and encouragement during my study. I have gained a great deal by learning from his greater experience.

I would also like to express sincere gratitude to Dr Nor Fariza Ngah, Dr Tara Mary George, Dr Elias Hussein, Dr Mariam Ismail, Dr Goh Pik Pin, Nurse Nomarisa and other staffs at Department of Ophthalmology, Hospital Selayang for their knowledge, guidance and help during my data collection and system evaluation.

I would also like to thank those with whom I have worked and discussed during the course of my study. Special thanks to Hermawan Nugroho and Lila Iznita Izhar for generously sharing their time throughout this research. To my dearest friends in Intelligent Signal and Imaging Lab, Esa Prakasa, Hurriyatul Fitriyah, Arwan Ahmad Khoiruddin, Leena Ahmad, Evan Chong and Dileep Kumar and the others who have passed through this lab, thanks for your friendship.

The financial support from the Universiti Teknologi PETRONAS and the research grant from MOSTI Technofund are gratefully acknowledged.

Last but not least, I would like to thank my family members, my great parents, Father Mulyadi and Mother Sri Mulyani, my lovely wife Ririn Mardiasuty, my adorable daughters Rijja Hanim Muthmainnah, Maryam Radhwa Al Hanifah and Hasna Al Mumtazah, my parents in law, all my sisters and brothers for their prayers, their love, their understanding, their patience and their endless encouragement.

ABSTRACT

Diabetic Retinopathy (DR) is a sight threatening complication due to diabetes mellitus affecting the retina. The pathologies of DR can be monitored by analysing colour fundus images. However, the low and varied contrast between retinal vessels and the background in colour fundus images remains an impediment to visual analysis in particular in analysing tiny retinal vessels and capillary networks. To circumvent this problem, fundus fluorescein angiography (FFA) that improves the image contrast is used. Unfortunately, it is an invasive procedure (injection of contrast dyes) that leads to other physiological problems and in the worst case may cause death.

The objective of this research is to develop a non-invasive digital image enhancement scheme that can overcome the problem of the varied and low contrast colour fundus images in order that the contrast produced is comparable to the invasive fluorescein method, and without introducing noise or artefacts. The developed image enhancement algorithm (called RETICA) is incorporated into a newly developed computerised DR system (called RETINO) that is capable to monitor and grade DR severity using colour fundus images. RETINO grades DR severity into five stages, namely No DR, Mild Non Proliferative DR (NPDR), Moderate NPDR, Severe NPDR and Proliferative DR (PDR) by enhancing the quality of digital colour fundus image using RETICA in the macular region and analysing the enlargement of the foveal avascular zone (FAZ), a region devoid of retinal vessels in the macular region. The importance of this research is to improve image quality in order to increase the accuracy, sensitivity and specificity of DR diagnosis, and to enable DR grading through either direct observation or computer assisted diagnosis system.

In this work, RETICA uses two processes to enhance the varied and low contrast colour retinal fundus images. RETICA first normalises varied contrast using an improved iterative Retinex, a method to separate the illumination from the reflectance part of the image. The improved iterative Retinex – one of the contributions of this research work to body of knowledge – uses kurtosis to determine the optimum

number of iteration and overcomes the problem of standard iterative Retinex in which the number of iteration is fixed and pre-determined. Normalisation of varied contrast is followed by separating the retinal pigments makeup, namely macular pigment, haemoglobin and melanin, using Independent Component Analysis (ICA). Independent component image due to haemoglobin exhibits higher contrast of retinal vessels. The use of ICA to enhance the contrast of retinal vessels by revealing the underlying sources in colour retinal fundus images is another contribution of this work since most of the image enhancement methods use pixel manipulation. Three fundus image models, i.e. varied contrast image model, low contrast image model, and varied plus low contrast image models are developed to validate and evaluate the performance of RETICA. Two DR analysis algorithms – semi-automated and fully-automated – are developed to implement RETICA as a part of RETINO for grading DR severity based on the FAZ analysis.

Results show that RETICA successfully normalises the varied contrast and enhances the low contrast of retinal vessels achieving a contrast improvement factor (*CIF*) of 5.389 comparable to that of the invasive FFA with *CIF* of 5.796. Findings from two clinical studies conducted at Hospital Selayang show a strong correlation between FAZ enlargement measured by both DR analysis algorithms using colour fundus images and corresponding DR severity level graded by ophthalmologists with correlation factor up to 0.877 for the semi-automated DR algorithm and 0.805 for the fully automated DR algorithm both at a very high significance (*P*) of less than 0.01. This indicates the usability of the FAZ analysis of colour fundus images in grading DR severity. Based on performance tests of RETINO, the semi-automated DR analysis algorithm achieves high values in sensitivity (> 0.84), specificity (> 0.97) and accuracy (0.95) for all DR severity stages. The fully automated DR analysis algorithm also achieves high sensitivity (≥ 0.85), specificity (≥ 0.91) and accuracy (≥ 0.91) for No DR and Mild DR. For the other DR stages (Moderate and Severe/ PDR), the results were not conclusive due to insufficient data.

In summary, three major contributions have been achieved from this research. First is the development of the non-invasive image enhancement technique (RETICA), particularly to enhance the contrast of retinal blood vessels in the colour retinal fundus image. RETICA is beneficial not only for diagnosis of retina-related

diseases through direct observation, but also for segmentation of retinal vasculature using computer-based system. Second is the development of RETINO, which incorporates RETICA, based on both semi and fully automated DR analysis algorithms for early DR detection, DR mass screening, monitoring and grading of DR severity. Third contribution is the implementation of the developed technique on digital colour retinal fundus images and not fundus fluorescein angiograms for FAZ determination and measurement since no measurement of FAZ was studied based on digital colour fundus image so far. The method also allows DR screening by non-eye trained healthcare providers. The developed DR grading algorithms based on FAZ analysis is also a new non-invasive protocol for grading of DR severity, which at present uses pathology-based direct ophthalmology for daily practice.

ABSTRAK

Diabetik Retinopati (DR) merupakan komplikasi mata yang berpunca daripada diabetis mellitus. Ianya menular di retina dan boleh mengancam penglihatan. Patologi-patologi DR boleh dipantau melalui analisis imej fundus warna. Walau bagaimanapun, kontras yang rendah dan berubah diantara pembuluh darah retina dan latar belakang dalam imej fundus warna sentiasa menjadi penghalang kepada analisis visual khususnya dalam menganalisis pembuluh darah kecil retina dan rangkaian kapilari. Untuk mengatasi masalah ini, fundus fluorescein angiografi (FFA) yang meningkatkan kontras imej fundus digunakan. Malangnya, ia adalah prosedur invasif (suntikan pewarna kontras) yang boleh mendatangkan masalah fisiologi yang lain dan dalam keadaan yang paling buruk boleh menyebabkan kematian.

Objektif kajian ini adalah untuk membangunkan satu skim peningkatan imej digital bukan invasif yang boleh mengatasi masalah yang berkait rapat dengan imej fundus warna yang mempunyai kontras yang rendah dan berubah supaya kontras yang dihasilkan setanding dengan kaedah fluorescein yang invasif, dan tanpa menjanakan gangguan atau artifak. Algoritma peningkatan imej maju ini (dikenali sebagai RETICA) digunakan di dalam sistem DR berkomputer (dikenali sebagai RETINO) yang baru dibangunkan, dan mampu untuk memantau dan menggred DR dengan hanya menggunakan imej fundus warna. RETINO juga mempunyai keupayaan untuk menggred tahap keparahan DR menjadi lima peringkat, iaitu No DR, Mild NPDR, Moderate NPDR, Severe NPDR dan PDR dengan meningkatkan kualiti imej digital fundus warna menggunakan RETICA pada kawasan makular dan menganalisis pembesaran zon avascular foveal (FAZ), sebuah kawasan yang tidak mempunyai pembuluh darah retina di dalam makular. Kepentingan kajian ini adalah untuk menambah baik kualiti imej untuk meningkatkan kejituan, kepekaan dan spesifisiti bagi diagnosis DR, dan untuk membolehkan penggredan DR sama ada melalui pemerhatian secara langsung atau melalui sistem diagnosis komputer bantuan.

Di dalam kerja ini, RETICA menggunakan dua proses untuk meningkatkan imej retina fundus warna yang mempunyai kontras yang rendah dan berubah. Pertama

RETICA menormalkan kontras yang berubah dengan menggunakan Retinex lelaran yang ditingkatkan, iaitu satu kaedah untuk memisahkan pencahayaan dari sebahagian pantulan dari imej. Retinex lelaran yang ditingkatkan – salah satu sumbangan utama kajian ini – menggunakan kurtosis untuk menentukan jumlah optimum lelaran dan menyelesaikan masalah Retinex lelaran yang standard dimana jumlah lelaran adalah tetap dan sudah ditentukan di awal. Menormalkan kontras yang berubah diikuti dengan memisahkan komposisi binaan pigmen retina, iaitu pigmen makula, haemoglobin dan melanin, dengan menggunakan Analisis Komponen Bebas (ICA). Imej komponen bebas yang dihasilkan daripada hemoglobin mempamerkan kontras pembuluh darah retina yang lebih tinggi. Penggunaan ICA untuk meningkatkan kontras pembuluh darah retina dengan mendedahkan sumber-sumber asas dalam imej fundus retina warna merupakan satu lagi sumbangan kerja ini kerana kebanyakan kaedah peningkatan imej menggunakan manipulasi piksel. Tiga model imej fundus telah dibangunkan dan digunakan untuk mengesahkan dan menilai prestasi RETICA, iaitu model imej dengan kontras yang berubah, model imej dengan kontras yang rendah dan model imej dengan kontras yang rendah dan berubah. Dua algoritma analisis DR - semi-automatik dan automatik sepenuhnya - telah dibangunkan untuk melaksanakan RETICA sebagai sebahagian RETINO dalam penggredan tahap keparahan DR berdasarkan analisis FAZ.

Hasil kajian menunjukkan bahawa RETICA berjaya menormalkan kontras yang berubah dan meningkatkan kontras pembuluh darah retina yang rendah dengan mencapai faktor peningkatan kontras (*CIF*) sebanyak 5.389 setanding kepada FFA invasif yang mencapai *CIF* sebanyak 5.796. Hasil daripada dua kajian klinikal yang dijalankan di Hospital Selayang menunjukkan korelasi yang kuat antara pembesaran FAZ yang diukur oleh kedua-dua algoritma analisis DR menggunakan imej fundus warna dengan tahap keparahan DR yang digredkan oleh pakar oftalmologi. Faktor korelasi menunjukkan sehingga kepada 0,877 bagi algoritma DR semi-automatik dan 0,805 untuk algoritma DR automatik sepenuhnya dan kedua-dua di kepentingan yang amat tinggi (*P*) kurang daripada 0.01. Ini menunjukkan kesesuaian dan kebolegunaan FAZ yang diperolehi dengan algoritma DR untuk imej fundus warna yang dibangunkan untuk menggred keparahan DR itu. Berdasarkan ujian prestasi pada RETINO, algoritma analisis DR separa automatik ini mencapai nilai yang tinggi

dalam kepekaan (> 0.84), spesifisiti/pengkhususan (> 0.97) dan kejitian (0.95) untuk semua peringkat DR. Algoritma analisis DR automatik sepenuhnya secara statistik mencapai kepekaan (≥ 0.85), spesifisiti/pengkhususan (≥ 0.91) dan kejitian (≥ 0.91) yang tinggi bagi No DR and Mild DR. Bagi peringkat DR yang lain (Moderate and Severe/ PDR), keputusan tidak dapat memberikan kesimpulan berikutan ketidakcukupan data.

Secara umumnya, tiga sumbangan besar telah dicapai dari kajian ini. Pertama ialah pembangunan teknik peningkatan imej bukan invasif (RETICA), terutamanya untuk meningkatkan kontras saluran darah retina dalam retina fundus imej warna. RETICA adalah bermanfaat bukan sahaja untuk diagnosis penyakit berkaitan retina melalui pemerhatian secara langsung, tetapi juga untuk segmentasi vaskulatur retina menggunakan sistem berasaskan komputer. Sumbangan kedua ialah pembangunan RETINO, yang menggabungkan RETICA, berdasarkan kedua-dua analisis algoritma separuh dan automatik sepenuhnya DR bagi pengesanan peringkat awal DR, saringan massa pesakit DR, pemantauan dan penggredan keterukan DR. Sumbangan ketiga ialah pelaksanaan teknik maju pada digital retina fundus imej warna dan bukan pada fundus fluorescein angiogram bagi menentukan dan pengukuran FAZ kerana belum ada kajian tentang pengukuran FAZ berdasarkan digital imej fundus warna setakat ini. Kaedah ini juga membolehkan pemeriksaan DR oleh penyedia penjagaan kesihatan mata yang tidak terlatih. Pembangunan RETICA dan aplikasi pada imej-imej digital fundus warna bagi penentuan pembesaran FAZ dalam pemantauan dan penggredan tahap keparahan DR, terutama pada peringkat awal, telah menjadi sumbangan utama kajian ini. Algoritma penggredan DR yang dibangunkan berdasarkan analisis FAZ juga merupakan protokol baru yang bukan invasif bagi penggredan keparahan DR, yang pada masa ini menggunakan secara langsung berasaskan patologi oftalmologi untuk amalan harian.

In compliance with the terms of the Copyright Act 1987 and the IP Policy of the university, the copyright of this thesis has been reassigned by the author to the legal entity of the university,

Institute of Technology PETRONAS Sdn Bhd.

Due acknowledgement shall always be made of the use of any material contained in, or derived from, this thesis.

© Hanung Adi Nugroho, 2012

Institute of Technology PETRONAS Sdn Bhd

All rights reserved

TABLE OF CONTENTS

STATUS OF THESIS.....	i
APPROVAL PAGE.....	ii
TITLE PAGE.....	iii
DECLARATION OF THESIS	iv
DEDICATION.....	v
ACKNOWLEDGEMENT	vi
ABSTRACT.....	vii
ABSTRAK.....	x
COPYRIGHT PAGE	xiii
TABLE OF CONTENTS.....	xiv
LIST OF TABLES.....	xviii
LIST OF FIGURES	xx
CHAPTER 1 INTRODUCTION	1
1.1 Background of Study	1
1.1.1 Varied and Low Contrast of Retinal Images	4
1.1.2 Retinal Image Enhancement.....	8
1.2 Problem Statement.....	11
1.3 Research Objective and Scope of Work	12
1.4 Contribution of Thesis	14
1.5 An Overview of Thesis Structure	15
CHAPTER 2 LITERATURE REVIEW	16
2.1 Image Contrast.....	16
2.2 Retinal Image Enhancement.....	18
2.2.1 Enhancement Techniques for Varied Contrast Images	19
2.2.2 Enhancement Techniques for Low Contrast Image	23
2.3 Comparative Study on Retinal Image Enhancement	27
2.4 Retinex Theory and Its Application in Image Processing	29
2.4.1 Retinex Algorithms.....	30

2.4.1.1 Non-Iterative Local Retinex Methods	32
2.4.1.2 Non-Iterative Global Retinex Methods	33
2.4.1.3 Iterative Retinex Methods	35
2.4.2 Applications of Retinex in Image Processing.....	36
2.5 Independent Component Analysis.....	37
2.5.1 Linear ICA Model	38
2.5.2 Limitations and Ambiguities in ICA	39
2.5.3 Statistical Independence and Non-Gaussianity	40
2.5.4 Measuring Non-Gaussianity	41
2.5.5 Pre-processing Data for ICA	44
2.5.5.1 Centring	44
2.5.5.2 Whitening	44
2.5.6 ICA Algorithms	45
2.5.6.1 Maximisation of Non-Gaussianity	46
2.5.6.2 Maximum Likelihood Estimation	50
2.5.6.3 Minimisation of Mutual Information	51
2.5.7 Applications of ICA in Image Processing	52
2.6 Summary.....	53
CHAPTER 3 MODELING OF VARIED AND LOW CONTRAST COLOUR RETINAL FUNDUS IMAGES	56
3.1 Introduction.....	56
3.2 Structure of the Eye and the Retina	58
3.3 Light Interaction	62
3.4 Retinal Fundus Image Models	68
3.4.1 Varied Contrast Image Model	77
3.4.2 Low Contrast Image Model.....	83
3.4.3 Varied and Low Contrast Image Model	86
3.5 Retinal Fundus Spectral Absorbance.....	89
3.6 Summary.....	91
CHAPTER 4 DEVELOPMENT OF NON-INVASIVE IMAGE ENHANCEMENT METHOD (RETICA)	94
4.1 Introduction.....	94

4.2 Contrast Normalisation.....	96
4.3 Contrast Enhancement.....	99
4.4 Validation of RETICA.....	104
4.5 Algorithms for Comparative Study	107
4.6 Results and Analysis.....	110
4.6.1 Contrast Normalisation.....	111
4.6.2 Contrast Enhancement.....	123
4.6.3 RETICA for Image Enhancement	127
4.6.4 Comparative Study	131
4.7 Summary.....	140
CHAPTER 5 RETICA FOR A COMPUTERISED DIABETIC RETIONOPATHY MONITORING AND GRADING SYSTEM (RETINO).....	143
5.1 Introduction.....	143
5.2 Semi-Automated RETINO DR Grading System.....	148
5.2.1 Enhancement of Retinal Blood Vessels.....	150
5.2.2 Segmentation of Retinal Blood Vessels	152
5.2.3 Determination of Foveal Avascular Zone	152
5.2.4 Gaussian Bayes Classifier for Grading of DR.....	153
5.2.5 V-Fold Cross Validation for Performance Evaluation	156
5.3 Fully Automated RETINO DR Grading Algorithm	157
5.3.1 Enhancement of Retinal Blood Vessels.....	159
5.3.2 Segmentation of Retinal Blood Vessels	159
5.3.3 Determination and Analysis of Foveal Avascular Zone.....	162
5.4 Accuracy Analysis on Determination of FAZ.....	167
5.5 Study Protocol	171
5.6 Results and Analysis.....	174
5.6.1 Analysis of FAZ	174
5.6.2 Statistics of Diabetic Patients	177
5.6.3 DR Grading Using Gaussian Bayes Classifier	179
5.6.4 Accuracy Analysis of FAZ.....	192
5.7 Summary.....	200
CHAPTER 6 CONCLUSION.....	205

6.1 Discussion.....	205
6.2 Contribution and Future Works.....	209
REFERENCES	211
LIST OF PUBLICATIONS.....	242
APPENDIX A: APPROVAL OF INTERVENTIONAL CLINICAL STUDY (MOH/CRC/CTA004/100209-RVD130309)	245
APPENDIX B: APPROVAL OF OBSERVATIONAL CLINICAL STUDY (NMRR-08-842-1997).....	246
APPENDIX C: RETICA ALGORITHM (MATLAB CODE).....	247
APPENDIX D: RETINO ALGORITHM (MATLAB CODE)	251
APPENDIX E: CERTIFICATE OF AWARD (ITEX 2009)	261
APPENDIX F: CERTIFICATE OF AWARD (iENA 2009)	262
APPENDIX G: A KERNEL USED IN THE SEGMENTATION OF RETINAL BLOOD VESSELS (SECTION 5.3.2).....	263
LIST OF PUBLICATIONS	
APPENDICES	
A APPROVAL OF INTERVENTIONAL CLINICAL STUDY (MOH/CRC/CTA004/100209-RVD130309)	
B APPROVAL OF OBSERVATIONAL CLINICAL STUDY (NMRR-08-842- 1997)	
C RETICA ALGORITHM (MATLAB CODE)	
D RETINO ALGORITHM (MATLAB CODE)	
E CERTIFICATE OF AWARD (ITEX 2009)	
F CERTIFICATE OF AWARD (iENA 2009)	
G A KERNEL USED IN THE SEGMENTATION OF RETINAL BLOOD VESSELS (SECTION 5.3.2)	

LIST OF TABLES

Table 2-1 Advantages and disadvantages of different enhancement techniques for varied contrast images	23
Table 2-2 Advantages and disadvantages of different enhancement techniques for low contrast images	27
Table 2-3 Advantages and disadvantages of several Retinex algorithms.....	36
Table 3-1 Comparison between minimum sample size and sample size obtained of the component in each colour channel	70
Table 3-2 Statistical data of macular pigment, haemoglobin and melanin intensities in RGB channels	76
Table 3-3 Constants k and α obtained for macular pigment, haemoglobin and melanin in RGB channels.....	78
Table 4-1 Kurtosis and related optimum number of iteration for Retinex algorithm for melanin, macular pigment and haemoglobin in each colour channel.....	121
Table 4-2 Statistics of green band of low-contrast image model and ICA component images.....	126
Table 4-3 Kurtosis and related optimum number of iteration of RETICA for melanin, macular pigment and haemoglobin in each colour channel of the varied and low-contrast image model.....	129
Table 4-4 Statistics of green band of varied and low-contrast image model and ICA images.....	131
Table 4-5 Statistics of Red, Green and Blue channels of the varied and low-contrast fundus image model.....	132
Table 4-6 Comparative results of several image enhancement algorithms on the varied and low-contrast fundus image model.....	137
Table 5-1 International Clinical DR Disease Severity Scale [205]	144
Table 5-2 Contrast and Contrast Improvement Factor (<i>CIF</i>) obtained from applying different window size for CLAHE	151
Table 5-3 Correlation coefficients (CC) measured (1) between radius and area of FAZ obtained by applying a specific number of radial segments and (2) between FAZ radius obtained by applying a specific number of radial segments and FAZ radius obtained manually (reference)	163
Table 5-4 FAZ determination (radius) based on ground truth and DR system measurements	170

Table 5-5 Colour fundus image and FFA image distribution.....	177
Table 5-6 Statistics of FAZ areas for semi-automated DR algorithm	178
Table 5-7 Statistics of FAZ radii for fully automated DR algorithm	179
Table 5-8 Measure of goodness of fit for Gaussian distribution on FINDeRS	180
Table 5-9 DR Gaussian Bayes classifier based on FAZ area with progression stages for different LPPRs.....	182
Table 5-10 Optimal Gaussian Bayes classifiers for all DR stages.....	183
Table 5-11 DR Gaussian Bayes classifier with progression range	183
Table 5-12 Correlation between FAZ area and (1) DR severity 1 (no DR, mild NPDR, moderate NPDR, severe NPDR and PDR), (2) DR severity 2 (mild NPDR, moderate NPDR, severe NPDR and PDR)	184
Table 5-13 Measure of agreement using Kappa coefficient between ophthalmologist and DR algorithms in grading of (1) DR severity 1 (no DR and DR – all stages), (2) DR severity 2 (no DR and mild) and DR severity 3 (no DR, mild and moderate) and DR severity 4 (no DR, mild, moderate and severe/ PDR).....	186
Table 5-14 Performance analysis of the semi-automated and fully automated DR algorithms in classifying DR severity levels	188
Table 5-15 Quartile and Boxplot Range of DR Stages.....	193
Table 5-16 Statistics of FAZ radii for accuracy analysis of DR grading system	193
Table 5-17 Correlation between radius of FAZ obtained by DR system and ground truth.....	194
Table 5-18 Statistics of error of FAZ radii and areas for the accuracy analysis of the fully automated DR algorithm.....	195
Table 5-19 Comparison of performance among several computerised DR grading systems.....	198

LIST OF FIGURES

Figure 1.1 Examples of ionising radiation imaging modalities	1
Figure 1.2 Examples of non-ionising radiation imaging modalities.....	2
Figure 1.3 Examples of varied and low contrast images obtained from different medical imaging modalities.....	3
Figure 1.4 A diagrammatic cross-section of the eye.....	5
Figure 1.5 A model of ocular fundus showing pathways of remitted light	6
Figure 1.6 Uneven contrast occurs between images (a and b) and within an image (c)	7
Figure 1.7 Image formation model	11
Figure 2.1 Diagram of general Retinex algorithms	32
Figure 2.2 Diagram of ICA problem.....	39
Figure 2.3 Estimating the ICs using whitening and separating processes	45
Figure 2.4 Flowchart of ICA by maximisation of non-Gaussianity	47
Figure 3.1 Varied contrast occurs in the colour fundus image	56
Figure 3.2 Varied contrast between two colour retinal fundus images of the same eye acquired using the same fundus camera	57
Figure 3.3 Low contrast of retinal vessels and capillaries in the macular region.....	57
Figure 3.4 Schematic diagram of structure of the eye	58
Figure 3.5 Diagrammatic cross-section of the eye.....	59
Figure 3.6 Optical density (spectral absorbance) of macular pigment, retinal blood (haemoglobin) and melanin based on data obtained from [186].....	61
Figure 3.7 diagram of principle of fundus camera reproduced from [188]	63
Figure 3.8 Fundus illumination and imaging paths using a fundus camera from (a) side view and (b) front view.....	64
Figure 3.9 Schematic presentations of the van Norren and Tiemeijer model.....	66
Figure 3.10 A model of ocular fundus showing light propagation.....	67
Figure 3.11 Retinal pigments are mixed in the colour retinal fundus image.....	68
Figure 3.12 Nonmydriatic fundus camera Kowa 7 used to capture colour retinal fundus images.....	69

Figure 3.13 (a) An example of retinal colour fundus image with (b) a sample of inferior temporal retinal blood vessels and (c) pixel's intensities of the corresponding areas	71
Figure 3.14 (a) Processing time of two images with different resolution at several numbers of iteration, (b) ratio between processing time of the two image models	72
Figure 3.15 (a) An example of retinal colour fundus image with (b) its cropped macular region and (c), (d) and (e) show pixel's intensities of the corresponding areas	74
Figure 3.16 A colour retinal fundus image with enlarged macular region	76
Figure 3.17 Image intensity variation $i(x)$ as a function of pixel's position x for (a) Macular pigment, (b) Haemoglobin and (c) Melanin on each red, green and blue channel.....	79
Figure 3.18 Variation of image intensities in fundus image models for (a) Macular pigment, (b) Melanin and (c) Haemoglobin with the referred vertical pixel position	80
Figure 3.19 Varied contrast fundus image model.....	81
Figure 3.20 (a) Varied contrast fundus image model and its related intensity variation of melanin in (b) red, (c) green and (d) blue channels	82
Figure 3.21 Varied contrast fundus image model and its related intensity variation of haemoglobin in (b) red, (c) green and (d) blue channels.....	83
Figure 3.22 Varied contrast fundus image model and its related intensity variation of macular pigment in (b) red, (c) green and (d) blue channels.....	83
Figure 3.23 Probability distribution function of the normalised pixel intensities of Macular Pigment of (a) Red channel, (b) Green channel, (c) Green channel, Haemoglobin of (d) Red channel, (e) Green channel, (f) Green channel and Melanin of (g) Red channel, (h) Green channel, (i) Green channel	84
Figure 3.24 Development of low-contrast retinal fundus image model	85
Figure 3.25 Colour distribution of (a) Macular pigment, (b) Haemoglobin and (c) Melanin generated in an image model of 320 x 320 pixels.....	85
Figure 3.26 Low contrast fundus image model	86
Figure 3.27 Varied and low contrast fundus image model is obtained from multiplication between low contrast and varied contrast image models in (a) Red channel, (b) Green channel and (c) Blue channel. (d) Colour fundus image models for low-contrast, varied contrast, and varied and low-contrast.....	88
Figure 3.28 Varied and low-contrast fundus image model.....	89
Figure 3.29 Model of spectral absorbance of the ocular fundus.....	90

Figure 4.1 Proposed method (RETICA) for contrast normalisation and contrast enhancement of retinal blood vessels on colour fundus image	95
Figure 4.2 Flowchart for contrast normalisation based on Retinex algorithm	97
Figure 4.3 Model of spectral absorbance of the ocular fundus.....	100
Figure 4.4 A flowchart of contrast enhancement of retinal vessels based on ICA...	102
Figure 4.5 Reference masks for (a) Melanin, (b) Macular pigment, (c) Haemoglobin (retinal blood vessels) on melanin and (d) Haemoglobin (retinal blood vessels) on macular pigment	106
Figure 4.6 Varied contrast fundus image and its (b) Red, (c) Green and (d) Blue channel images	111
Figure 4.7 Comparison of melanin's intensity variation on an image profile between red channel image model and its Retinex output images with several iterations	113
Figure 4.8 Comparison of melanin's intensity variation on an image profile between green channel image model and its Retinex output images with several iterations	113
Figure 4.9 Comparison of melanin's intensity variation on an image profile between blue channel image model and its Retinex output images with several iterations	114
Figure 4.10 Comparison of macular pigment's intensity variation on an image profile between red channel image model and its Retinex output images with several iterations	116
Figure 4.11 Comparison of macular pigment's intensity variation on an image profile between green channel image model and its Retinex output images with several iterations	116
Figure 4.12 Comparison of macular pigment's intensity variation on an image profile between blue channel image model and its Retinex output images with several iterations	117
Figure 4.13 Comparison of haemoglobin's intensity variation on an image profile between red channel image model and its Retinex output images with several iterations	119
Figure 4.14 Comparison of haemoglobin's intensity changes on an image profile between green channel image model and its Retinex output images with several iterations	119
Figure 4.15 Comparison of haemoglobin's intensity changes on an image profile between blue channel image model and its Retinex output images with several iterations	120

Figure 4.16	Retinal fundus image model in (a) Red, (b) Green and (c) Blue channel images and their corresponding Retinex outputs in (d) Red, (e) Green and (f) Blue channel images	122
Figure 4.17	(a) Low-contrast fundus image model and its (b) Red, (c) Green and (d) Blue channel images	124
Figure 4.18	(a) Green band image with (b) its corresponding histogram, (c) ICA 1 st component image with (d) its corresponding histogram, (e) ICA 2 nd component image with (f) its corresponding histogram, (g) ICA 3 rd component image with (h) its corresponding histogram.....	125
Figure 4.19	Varied and low-contrast fundus image model and its (b) Red, (c) Green and (d) Blue channel images	128
Figure 4.20	Varied and low-contrast fundus image model in (a) Red, (b) Green and (c) Blue channel images and their corresponding contrast normalisation outputs in (d) Red, (e) Green and (f) Blue channel images and contrast enhancement outputs showing (g) 1 st IC image, (h) 2 nd IC image and (i) 3 rd IC image.....	130
Figure 4.21	(a) Green band image with (e) its corresponding histogram, (b) green band image after HE with (f) its corresponding histogram, (c) green band image after CS with (g) its corresponding histogram, (d) green band image after AHE with (h) its corresponding histogram, (i) green band image after ACE with (m) its corresponding histogram, (j) green band image after CLAHE with (n) its corresponding histogram, (k) green band image after HF with (o) its corresponding histogram and (l) haemoglobin-related component image with (p) its corresponding histogram.....	134
Figure 4.22	Contrast improvement factor (<i>CIF</i>) and ratio (R_{sdc}) between standard deviation and average contrast of the varied and low fundus image model after performing seven different algorithms	138
Figure 5.1	DR statistics of registered diabetic patients in Malaysia [203]	143
Figure 5.2	Extensive micro-aneurysms in both (a) colour fundus and (b) FFA images [179].....	145
Figure 5.3	FFA shows the perifoveal capillary network in FAZ.....	146
Figure 5.4	Computerised DR Monitoring and Grading System (RETINO).....	147
Figure 5.5	Flowchart of the semi-automated DR algorithm.....	149
Figure 5.6	FAZ determination by connecting vessel end-points inside the circle (with the radius, which is the mean distance of all end-points from the centre point) from eight radial segments	153
Figure 5.7	Flowchart of the fully automated DR algorithm	158
Figure 5.8	A schematic diagram of FAZ obtained by the ground truth and the DR system	168

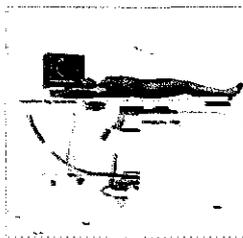
Figure 5.9 A flowchart of accuracy analysis on determination of FAZ	169
Figure 5.10 Flowchart of the interventional clinical study protocol.....	172
Figure 5.11 Flowchart of the observational clinical study protocol	173
Figure 5.12 Fundus image analysis of FAZ using semi-automated DR algorithm, (a) Digital retinal fundus image showing macular region, (b) Extracted retinal vessels with end points in macular region using CLAHE-based method, (c) Vessel end points in macular region are overlaid with the RETICA-enhanced image, (d) More accurate estimation of vessel end points shown by FAZ area.	175
Figure 5.13 Fundus image analysis of FAZ using fully automated DR algorithm, (a) Digital retinal fundus image showing macular region, (b) RETICA-enhanced image on macular region overlaid with the colour fundus image, (c) Segmented retinal vessels and detected vessel end-points on macular region, (d) The determined FAZ area and radius	176
Figure 5.14 Probability mass function of FAZ area for each DR severity level and its estimated Gaussian distribution.....	180
Figure 5.15 LPPRs for DR grading.....	181
Figure 5.16 Two samples of colour fundus images (a) severe misclassified as moderate NPDR (b) PDR correctly classified as PDR.....	192
Figure 5.17 FAZ radii DR system against ground truth	194
Figure 5.18 (a) FAZ radii obtained by the fully automated DR algorithm against ground truth (b) FAZ areas obtained by the fully automated DR algorithm against ground truth	197

CHAPTER 1

INTRODUCTION

1.1 Background of Study

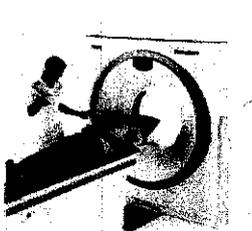
Medical images obtained from medical imaging modalities contain information to diagnose pathologies, grade severity of diseases, monitor disease treatment and guide therapeutic procedures. Medical imaging modalities are favourable to probe the anatomical structure, function, and pathology of human body. Based on the source of energy, medical imaging modality is divided into two, ionising radiation (invasive) and non-ionising radiation (non-invasive) imaging modalities [1]. The ionising radiation imaging modalities use radiation that can damage living tissue by disrupting and destroying individual cells at molecular level. Figure 1.1 shows some examples of this kind of imaging modalities including fluoroscopy, mammography, Computed Tomography (CT), and Positron Emission Tomography (PET).



a. Fluoroscopy



b. Mammography



c. Computed tomography

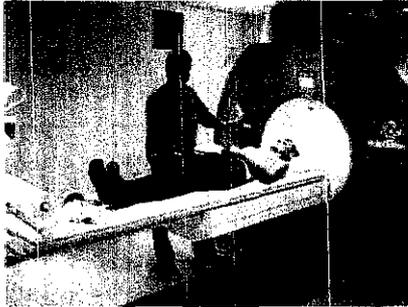


d. Positron Emission Tomography

Figure 1.1 Examples of ionising radiation imaging modalities

The non-ionising radiation imaging modalities use radiation such as radio frequency (RF) waves, extremely low frequency (ELF) fields, infrared (IR), visible

light, and ultra violet (UV) that each has sufficient energy to move or cause atoms to vibrate around in a molecule, yet not enough to remove electrons. Figure 1.2 below shows imaging modalities that use non-ionising radiation such as magnetic resonance imaging (MRI), ultrasound, optical 3D scanner and fundus camera.



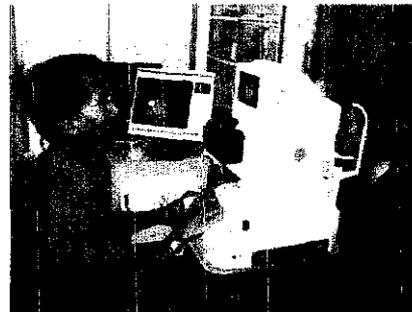
a. Magnetic resonance imaging



b. Ultrasound



c. Optical 3D scanner

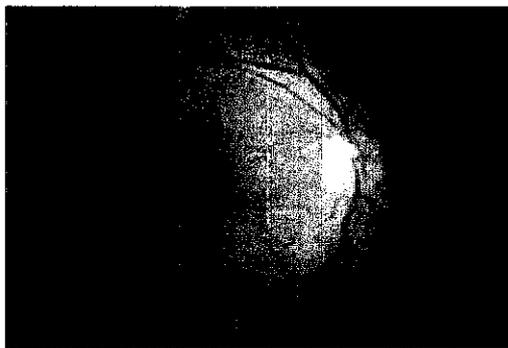


d. Fundus camera

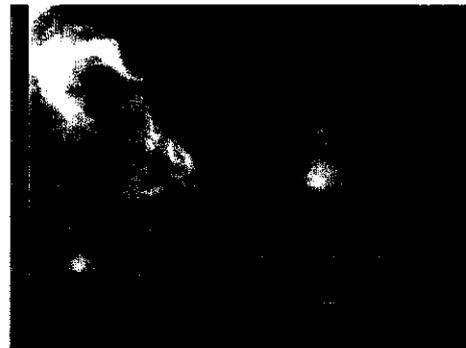
Figure 1.2 Examples of non-ionising radiation imaging modalities

One of the most common problems for all these imaging modalities is varied contrast and low contrast of the produced images. Contrast in an image refers to a measure of the magnitude of intensity differences between different regions or two adjacent pixels. Varied contrast is usually perceived as spurious smooth variation of image intensity and commonly referred to as uneven or non-uniform illumination, illumination variation, intensity inhomogeneity or non-uniformity, intensity variation, shading or bias artefact [2-3]. Low contrast on the other hand appears when different objects in an image show similar intensity characteristics. Some of these problems are due to technical limitations of the medical imaging devices and acquisition techniques while others correspond to the frequently unavoidable imaged-objects. Some of these contributing factors include complexity of imaging situations, disease opacity, poor focus, variability of data among patients, inadequate illumination and imperfect image acquisition process resulting in noise and artefacts [4].

The problems of varied and low contrast emerge in many medical images produced by medical imaging modalities. The problems for instance could be seen in retinal images obtained by fundus camera [5], fluoroscopic images obtained by fluoroscopy [6], magnetic resonance (MR) images obtained by Magnetic Resonance Imaging - MRI [7], mammography images obtained by digital X-ray mammography [8], CT images obtained by CT angiography [9] and ultrasound images [10]. Figure 1.3 below shows some examples of medical images obtained by different medical imaging modalities.



a. Colour retinal fundus image



b. Mammography image [11]



c. MR image



d. Ultrasound image [12]

Figure 1.3 Examples of varied and low contrast images obtained from different medical imaging modalities

Colour retinal fundus images, as shown in figure above suffer from the problems of varied contrast due to their spherical surface, making the reflection in the centre of the retina to be brighter than that in the edge of the retina. Both in mammography and in ultrasound images, the objects of interest, such as malignant tissues usually appear in low contrast. In magnetic resonance images, proper adjustment of T_1 and T_2 parameters, which is essential to obtain good quality images, is relatively to be difficult.

In medical treatment, an accurate detection of pathologies in the early stages of the diseases importantly is to reduce the risks of severe cases or even of deaths that the patient has to deal with. In medical cases where images are required to monitor and grade the disease's severity level based on the pathological changes of the biological organs, accurate diagnosis may become difficult if the contrast between normal objects and abnormal ones (pathologies) is subtle. Noise and artefacts that make direct analysis of these images more difficult often confound these low contrast medical images.

Varied contrast in medical images similarly causes problems in a computer-aided diagnosis system especially for automated image analysis methods, such as segmentation [13-14], registration [15], feature extraction [16] and classification [17]. These problems not merely degrade image quality but also significantly hamper automated analysis [18].

1.1.1 Varied and Low Contrast of Retinal Images

This research investigates the problems in varied contrast and low contrast of colour retinal fundus images. In ophthalmology, analysis of colour retinal fundus images is able to determine several diseases related to the retina such as Diabetic Retinopathy (DR) - a sight threatening complication due to diabetes mellitus affecting the retina. International Diabetes Federation (IDF) (2009) estimated that approximately 285 million people around the world suffer from diabetes and predicted an increase of the number to be 438 million within 20 years at the rate of 7 million people developing diabetes per year [3]. In Malaysia, National Eye Database in 2007 additionally reported that among 10,856 cases with diabetes, 36.8% has some form of DR, of which 7.1% comprises proliferative diabetic retinopathy (PDR) [4].

A digital fundus camera acquires retinal fundus images by capturing the illumination reflected from the retinal surface. During the acquisition process, the light illuminates on different parts of the retina and the amount of this illuminating light varies depending on the direction of the illuminating flash and varies from image to image.

Ocular fundus represents a structure of the back of the eyes and consists of multiple layers of tissue. Generally, the structure of the eye can be classified into two main groups, namely ocular media and ocular fundus [19]. Ocular media, which is located between the ocular fundus and the observer, consists of cornea, lens and vitreous; the ocular fundus meanwhile consists of the retina, the retinal pigment epithelium, the choroid and the sclera. Furthermore, the fundus layers beneath the retina consist of two pigments, namely melanin and haemoglobin, which dominate the overall appearance of the fundus. From a diagrammatic cross-section of the eye as shown in Figure 1.4, the ocular fundus part is of important since this part mainly affects the appearance of the colour retinal fundus image.

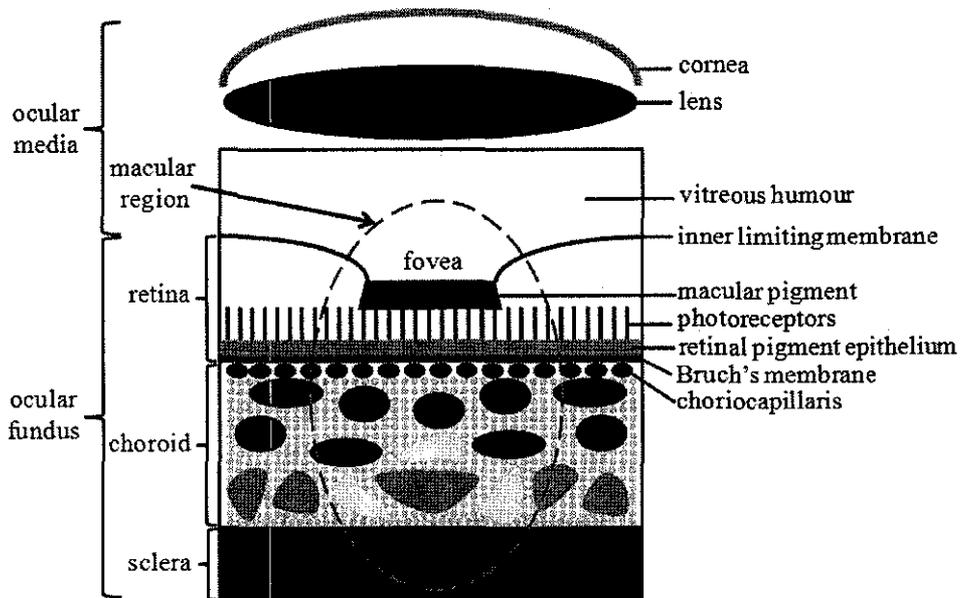


Figure 1.4 A diagrammatic cross-section of the eye

The photoreceptor layer, which is also called as visual pigment, is composed of light-sensitive cells called rods and cones, characterized by different sensitivity to light. The cones are smaller and very highly concentrated in the fovea, the part of the retina on the visual axis and responsible for central vision. In addition, the layers of other cells and blood vessels covering the peripheral retina thin out and disappear over the fovea, allowing uninterrupted exposure of the image. There are no rods in the fovea. However, rods dominate peripheral (non-central) vision. Under the photoreceptors is a dark layer known as retinal pigment epithelium (RPE). The RPE contains melanin granules that absorb excess light and transport oxygen, nutrients and

cellular wastes between the photoreceptors and the choroid. The choroid is a layer of blood vessels that supplies oxygen and nutrients to the outer layers of the retina. The innermost choroid, called the choriocapillaris, is a dense net of flattened capillaries that forms a blood-filled shell lying parallel to the basal side of the RPE. Bruch's membrane separates the blood vessels of the choroid from the retinal pigment epithelium layer. The rest of the choroid is filled with larger blood vessels and melanin-containing melanocytes. The melanin content of the retinal pigment epithelium varies among individuals. However, only the melanin content of the choroid depends on skin pigmentation. The final layer of significance is the sclera, the fibrous, thick, white outer covering of the eye. Therefore, a reflectance of the fundus can be understood as a ratio of a total amount of reflected light to the total incident light propagating through several fundus layers. Figure 1.5 depicts a model of ocular fundus showing possible pathways of the remitted light.

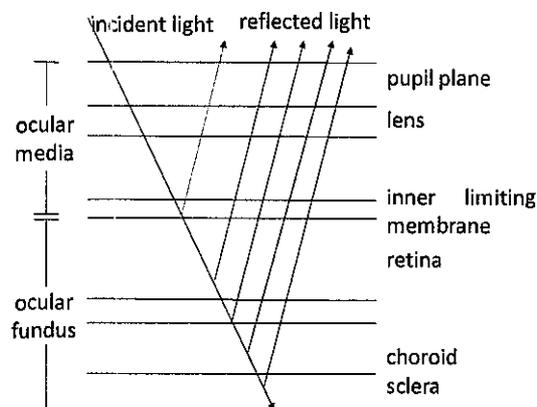


Figure 1.5 A model of ocular fundus showing pathways of remitted light

The slight changes of the biological structure and pigment construction lead to variation in colour of the retinal fundus. It is therefore necessary to understand the retinal fundus colour based on the structure and pigment construction to model fundus spectral absorbance image.

Despite the controlled acquisition process, retinal fundus images still suffer from varied contrast. Several factors causing varied contrast are, for example, the curved surface of the retina, the presence of pathologies, and pupil dilation that is highly variable among people. Some retinal pathologies, such as exudates and small blood

leaks appear as bright spots due to the protein contents in these spots, which are more reflective than the retinal surface [20].

The varied contrast prevents an absolute interpretation of the intensities in the image. For instance, the optic disc typically is the brightest object in the retinal image. The varied contrast often causes the area directly under the flash to appear the brightest. The curved retinal surface and the configuration of the light source and camera lead to the fact that the peripheral part of the retina appears darker than the central region. Examples of the variations of contrast that occur among colour retinal fundus images and within a colour retinal fundus image can be seen in Figure 1.6.

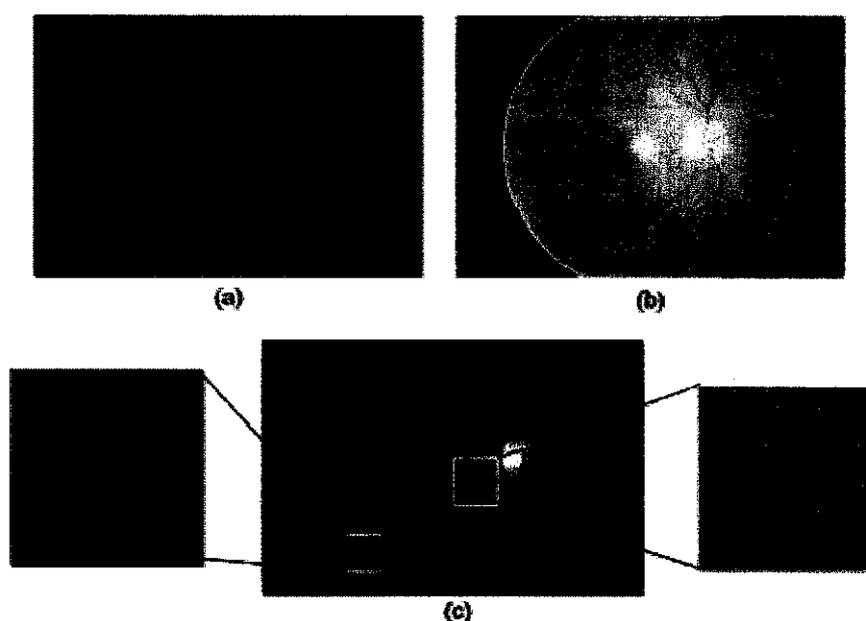


Figure 1.6 Uneven contrast occurs between images (a and b) and within an image (c)

Instead of varied contrast, the contrast between retinal vessels and background is very low. This problem occurs particularly in retinal capillaries that are mostly located in the centre of the retina known as macular region. The retinal capillaries and retinal vessels surrounding the macular region are of very low contrast since they are located in the choroidal layer underneath the macular pigment and the retinal pigment epithelium, which contains melanin. Due to the low contrast between retinal blood vessels and the background in retinal fundus images, it is difficult to determine retinal vasculature that can be used to determine macular area, foveal avascular zone (FAZ) and existence of pathology. In general, the problem of varied and low contrast

in colour retinal fundus images reduces image quality and leads to innaccuracy of segmentation of retinal blood vessels and pathology detection; thus, these eventually reduce the accuracy, sensitivity and specificity of diagnosis of the retinal-related diseases. A report, moreover, explains that the problems of image quality also affect human grading in approximately 10% to 15% of collected digital retinal images [4, 21].

1.1.2 Retinal Image Enhancement

Retinal image enhancement is an important pre-processing step to improve retinal image quality for visual perception and to facilitate diagnosis of retinal-related diseases. In general, retinal image enhancement includes in image enhancement process that is important to transform an image into a more suitable format for computer-aided image processing [22]. The quality of the enhanced image depends on five factors, i.e. spatial resolution, contrast resolution, temporal resolution, illumination and noise [1]. Spatial resolution corresponds to image sharpness (edges) and features' fine detail, while contrast resolution – an ability to distinguish the intensity in an image represented into a gray scale quantisation – corresponds to discrimination of detail within and between objects. Noise consists of undesired objects that deteriorate the visibility of particular objects in an image. A good quality medical image is significantly important for both diagnosis process and subsequent computer-based automated image analysis.

Technically, based on its invasiveness, there are two categorisation of image enhancement, i.e. invasive and non-invasive enhancement. Invasive enhancement concerns with exposing or injecting some contrasting agents into the human body. In radiography, for instance, the increase of the radiation dose to the patient results in better x-ray images. X-ray contrast media (e.g. barium, iodine) [23] are often used in any X-ray related to medical imaging modalities (e.g. angiography, CT, fluoroscopy and mammography) by injecting them into an artery or vein. Having absorbed X-radiation, X-ray contrast media thereby are able to increase the contrast between the organ of interest and the surrounding tissue. Injection of X-ray contrast media,

however, may also result in death associated with nephropathy and allergic reactions as reported in [24]. In ophthalmology, fluorescein angiography could result better contrast of retinal vasculatures; yet, due to its invasiveness by injecting contrasting agent (sodium fluorescein) into the blood vessels, this method may also lead to physiological problems such as nausea, vomiting and dizziness [25]. The worst case of adverse reactions following fluorescein injection, what is more, could be fatal anaphylactic shock, which eventually leads to death [26]. It has been reported by Yannuzzi *et al.* that the frequency rate for death cases due to fluorescein injection is 1:222,000 [27]. Hence, even though fluorescein angiography can produce better contrast of retinal fundus images, it is not recommended for medical routine use [28]. In some cases related to the use of non-ionising imaging modalities for acquisition of medical images, injection of contrasting agent into the human body is not necessary to achieve better contrast of acquired images. Instead, patients must undergo an acquisition process with increasing power levels or a longer time exposure to obtain better contrast of images. For instance, the large power level of ultrasound may result in better ultrasound images. In the case of MRI, the longer the time of image acquisition is, the better the magnetic resonance images are. Even contrasting agent, for example micro-bubble contrast agents [29] and gadolinium [30], is sometimes used in ultrasound and MRI respectively to enhance a specific tissue of interest. Nevertheless, the use of such contrast agent may result in adverse effects such as headache, nausea, vomiting, dizziness in case of ultrasound [31] and may result in nephrogenic systemic fibrosis in MRI [32].

Implementation of these procedures in fact is a compromise between technical evaluation and artistic appraisal. At this point, it must take account of the comfort and safety of the patients before acquiring medical images. Excessive radiation dose to obtain perfect images, finally, is not acceptable. A good concern for a suitable compromise between the power levels or the injection of contrasting agent and patient safety comes to be significant to achieve better image quality. Another way to improve quality is by using non-invasive enhancement techniques.

Non-invasive image enhancement techniques, also known as digital image enhancement techniques, fundamentally, refer to mathematical techniques to improve

the quality of a given image enabling the enhanced image to show better visual perception and contrast of certain features than the original one for a specific problem-oriented application. Through digital image processing techniques, the implementation of non-invasive image enhancement is on manipulation of image intensities to improve image quality without any intervention into human body. Most of the enhancement techniques focus on noise removal (smoothing), contrast enhancement (feature enhancement), contrast normalisation (illumination normalisation) and image sharpening to improve the visual perception of the image [33]. The other enhancement techniques are to be a pre-processing step to provide better input for subsequent automated image processing algorithm in a computerised system such as edge detection and object segmentation [34].

In retinal images, it is important to enhance the low contrast tiny objects of interest selectively. Yet, to distinguish low contrast tiny objects and to increase their contrast without any distortions are becoming complicated. The major problem is how to discern the low contrast tiny objects of interest and noise since most of the image enhancement techniques tend to filter out the low contrast tiny object as noise. Moreover, retinal images suffer not only from low contrast, but also from varied contrast resulting in poor quality images. For that reason, the main challenge in developing a non-invasive retinal image enhancement technique is to determine significant image features and distinguish them from other objects, such as noise or artefacts to make the enhancement process applied on image features only to obtain the best possible enhanced images. A detail review on non-invasive image enhancement on retinal images is presented in a separated chapter.

Some studies have been conducted to compare the performance of several retinal image enhancement techniques. Yousiff *et al.* [35] conducted a comparative study for performance evaluation of nine different techniques for contrast enhancement and illumination equalisation of retinal fundus image on two publicly available databases of total 60 images [36-37]. The eight different techniques are green band image [38], histogram equalisation [39], adaptive histogram equalisation [40], adaptive local contrast enhancement [41], background subtraction of retinal blood vessels [42], division by an over-smoothed version [43], desired average intensity [44] and

estimation of background luminosity and contrast variability [5]. The performance of each technique is evaluated by using a matched-filter vasculature segmentation algorithm [45]. The results show that adaptive histogram equalisation [40] is the most effective method among the others for having the largest area of 0.874 under the receiving operating characteristics (ROC). It is then followed by the adaptive local contrast enhancement [41] with 0.833 and the histogram equalisation [39] with 0.787 at the second and the third, respectively [35] for improving the retinal vessels segmentation algorithm [41]. Youssif *et al.* [35] also applied hybrid method by combining Sinthanayothin's method on adaptive local contrast enhancement [41] with a method developed by Yang *et al.* on division by an over-smoothed image for contrast normalisation [43]. It is interesting to note that applying contrast enhancement techniques on varied contrast corrected image further can enhance the image and in turn can achieve better result in the segmentation process than just performing ordinary contrast enhancement techniques on the input image.

1.2 Problem Statement

In an image formation model as shown in Figure 1.7 image intensity I corresponding to a particular wavelength (λ) is a product of the illumination L and the reflectance R [46]. Varied contrast is defined as a smooth variation of image intensity that needs to be normalised as part of image enhancement. The varied contrast in the image occurs because of uneven illumination and or subtle difference in the reflectance. The later is commonly due to presence of objects in the image that have similar characteristics or presence of tiny objects, which also leads to the problem of low contrast.

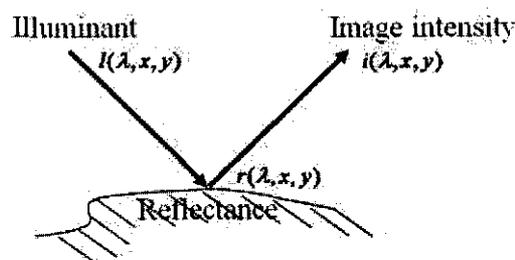


Figure 1.7 Image formation model

A general evaluation on the above review concludes three problems in medical

images. First, it is found that varied contrast is a problem in medical images due to geometrical surface of the objects and configuration of the acquisition system. In retinal fundus image, the varied contrast occurs due to the spherical surface of the retina and the configuration of the light source and camera.

Second, low contrast tiny objects of interest present in medical images are related to biological structure of the objects and the amount of light being absorbed or reflected by these particular objects. These low contrast tiny objects need to be extracted and selectively enhanced to facilitate diagnosis on direct observation or automated image analysis. These problems are significantly important when the diagnosis process involves the observation of these particular low contrast tiny objects to diagnose or to grade the severity level of a disease.

Third, the best method to enhance the low contrast is based on invasive method. In retinal image, fundus fluorescein angiography (FFA) is used to enhance the retinal blood vessels and pathologies. This invasive method, however, is not preferable due to its side effects that may lead to physiological problems and the worst case may cause death.

1.3 Research Objective and Scope of Work

The objective of this research is to develop a non-invasive digital imaging enhancement scheme that can enhance varied and low contrast colour retinal fundus images to be similar to, or better than the contrast produced by invasive method (FFA) without introducing noise or artefacts. The importance of this research is to improve image quality for direct observation and for computer-based automated image analysis. The use of the enhanced images will increase the accuracy, sensitivity and specificity of the diagnosis through either direct observation or computer assisted diagnosis system. The researcher applies Computerised Diabetic Retinopathy System – a particular medical application – to improve the quality of digital colour fundus image for grading of DR severity levels.

This research is to address two main hypotheses. First, in an image formation model, image intensity is a product of the illumination and the reflectance. The varied

contrast due to illumination can be normalised by separating the illumination from the reflectance. The illumination varies slowly, leading its frequency spectrum assumedly to be distributed at low frequencies. If the varied contrast can be determined in a local neighbourhood, the contrast can then be normalised by specialised methods such as Retinex.

The second hypothesis is that the objects are related to the reflectance. By determining the actual sources from the observed (low contrast) RGB image using methods such as Independent Component Analysis (ICA), the objects or areas due to the source of interest, can then be enhanced separately without introducing unwanted artefacts. If the varied contrast can be normalised (contrast normalisation) and low contrast objects can be enhanced (contrast enhancement), the accuracy, sensitivity and specificity of the diagnosis through either direct observation or computer assisted diagnosis system will increase. In this thesis, these two problems, i.e. varied contrast normalisation and low contrast enhancement, are formulated and solved separately.

In this thesis, the problem of low varied and contrast of colour retinal fundus images is investigated. A non-invasive image enhancement scheme based on Retinex and ICA is proposed to overcome the problem of varied and low contrast with application to medical images particularly to colour retinal fundus images.

The researcher attempts to develop a varied and low contrast image model to evaluate the performance of the proposed image enhancement method by collecting data for modelling and evaluation from two clinical studies conducted at Selayang Hospital, Malaysia from July 2008 to March 2010. This database named Fundus Image for Non-invasive Diabetic Retinopathy System (FINDeRS) consists of 315 colour fundus images to be tested. The researcher also adopts several parameters to measure the performance of the proposed method and to compare with other enhancement methods. The proposed method in return is also implemented as part of a computerised Diabetic Retinopathy system to improve on the quality of digital colour fundus image for grading of DR severity levels.

The problem in determination of FAZ in digital colour retinal fundus images has become an initial motivation for this thesis. The FAZ is formed by connecting the

end-points of fine retinal vessels in the macular region. These fine retinal vessels, however, are of low contrast and present in varied contrast of colour fundus images. Even though the proposed method is mainly developed based on colour fundus images, it can also be implemented to other medical images, which have similar characteristics, i.e. problem of varied and low contrast objects.

1.4 Contribution of Thesis

Three major contributions are achieved from this research. The first contribution is the development of the non-invasive image enhancement technique (RETICA) – an hybrid method combining Retinex for contrast normalisation and ICA for contrast enhancement – to solve the problem of both varied and low contrast colour retinal fundus images obtained from non-invasive medical equipment in order to increase the visible details and contrast of tiny biological tissues or objects of interest, i.e. retinal blood vessels. This improvement in turn will avoid the need of applying contrasting agent on patients that can cause physiological problems to them. Having enhanced the contrast of retinal blood vessels in the colour retinal fundus image, RETICA is beneficial not only for diagnosis of retina-related diseases through direct observation, but also for segmentation of retinal vasculature using computer-based system. It moreover can be implemented as pre-processing step for medical image analysis to diagnose retina-related diseases.

The second one is the development of DR system for monitoring and grading of DR severity based on semi-automated and fully-automated algorithms of FAZ analysis on colour retinal fundus image in which ophthalmologists today utilise FFA to obtain fundus angiograms that have high contrast of retinal blood vessels against the background to examine FAZ in diagnosing retina-related diseases. The developed DR system (RETINO) incorporates RETICA to enhance the contrast of the very fine vessels in the macular region from varied and low colour retinal fundus images for an accurate determination of FAZ.

The third contribution is the implementation of the developed technique on digital colour retinal fundus images and not fundus fluorescein angiograms for FAZ

determination and measurement since no measurement of FAZ was studied based on digital colour fundus image so far. The method also allows DR screening by non-eye trained healthcare providers. The developed DR grading algorithms based on FAZ analysis is also a new non-invasive protocol for grading of DR severity, which at present uses pathology-based direct ophthalmology for daily practice. The development of DR grading system will be advantageous to assist ophthalmologists for DR mass screening and monitoring and grading of DR severity.

1.5 An Overview of Thesis Structure

The overall structure of the thesis consists of six chapters, including this introductory chapter. The first chapter presents a brief introduction to medical imaging modalities that resulted in varied and low contrast medical images and the motivation of this study. To set the research objective, the researcher presents and formulates the problem of varied and low contrast images. The second chapter begins with a critical review on the existing image enhancement techniques in addressing the problem of varied and low contrast images. A review on Retinex and ICA and their applications in image processing is also presented in this chapter. Modelling of varied and low contrast images based on probability distributions of image objects to evaluating the performance of the proposed method is in the third chapter, followed by the fourth chapter to discuss about the development of the proposed method and the methodology used in this study. Further, the fourth chapter also includes validation study on the proposed method and presents a comparison between the proposed method and other image enhancement methods on the image model. The fifth chapter in turn describes the implementation of the developed method as part of the computerised system for monitoring and grading of DR using digital colour fundus images. The final chapter of this thesis concludes the entire thesis including a brief summary on the implementation of the findings and potential future research topics in this research area.

CHAPTER 2 LITERATURE REVIEW

2.1 Image Contrast

Created by the difference in reflected luminance from two different adjacent pixels, the image contrast is found to be in line with the characteristics of human visual perception and some crucial physical laws [47-48]. Two of various definitions of image contrast found in the literature have been widely used to measure image contrast in simple patterns. First, contrast is defined as a relation between the luminous intensity values in an image or in specific region of an image in which Michelson defines it as

$$C = \frac{I_{\max} - I_{\min}}{I_{\max} + I_{\min}} \quad (2-1)$$

with I_{\min} and I_{\max} indicating the largest and smallest luminous intensity values, respectively [49]. The second definition of contrast is based on Weber's law [50] and can be formulated as

$$C = \frac{I_f - I_b}{I_b} \quad (2-2)$$

with I_f and I_b indicating the luminance of the specific objects and the background. If Michelson contrast is similarly expressed to that of Weber, the definition of contrast will be

$$C = \frac{\Delta L}{L + \Delta L} \quad (2-3)$$

where $\Delta L = (L_{\max} - L_{\min})/2$ and $L = L_{\min}$. Similarly, Westheimer [51] defines the contrast as

$$C = \frac{2\Delta L}{2L + \Delta L} \quad (2-4)$$

These image contrasts in general denote a dimensionless ratio between absolute luminance difference and average background luminance. Hence, it can be inferred that small luminance difference is insignificant if the average background luminance is high, while the same small luminance difference affects if the average background luminance is low.

Conversely, human visual system perceives contrast as a difference in brightness and colour between two or more objects within the same field of view. It is more sensitive towards any significant changes or a great deal of details and less sensitive to smooth regions. In other words, human subjective perception is more sensitive to contrast than to absolute luminance. Hence, a human can perceive the world in the same way regardless of the significant variations in illumination.

For an objective contrast measurement, most definitions of the aforementioned contrast are purposively to constitute a specific contrast value of the whole image area by measuring a single point of reflectance on a homogeneous intensity background. A problem, however, may arise if one or more points of uttermost darkness or brightness exist in the image. For instance, the image Michelson contrast significantly increases when a single point of extremely bright or extremely dark is added to the low contrast image. On the contrary, the perceived contrast may be decreased as it may greatly vary across the image. It then may become more difficult to have fair comparison of image contrasts from two or more images with the presence of the extremely bright or dark point.

Another definition of image contrast is based on root mean square (RMS) contrast, defined as a standard deviation of the pixel intensities [52-53] and can be used to compare the contrast of two different images. Images have the same contrast if their RMS contrast is equal. The RMS of a two dimensional image is formulated as

$$RMS = \sqrt{\frac{1}{XY} \sum_{i=0}^{Y-1} \sum_{j=0}^{X-1} (I_{ij} - \bar{I})^2} \quad (2-5)$$

with I_{ij} is the i^{th} and j^{th} normalised luminous intensity element of the two dimensional image of size X by Y and \bar{I} is the mean normalised luminous pixel intensities of the image in the range $[0,1]$. Both spatial distribution and spatial frequency content of contrast in the image do not affect the RMS contrast [54]. Rubin and Siegel, related to this, showed that RMS measured from various human face images are equal for those that have equal contrast [53].

2.2 Retinal Image Enhancement

Image enhancement is one of the important tasks in the image processing to ameliorating the quality of the acquired image data for direct human observation both as a subjective phenomenon and for subsequent computer-aided image processing class. It deals with several operations such as contrast normalisation, contrast enhancement, edge enhancement and noise filtering. Contrast normalisation is necessary for images with variation of brightness or contrast whose objects of interest are sometimes found it difficult to recognise. In this case, contrast enhancement is significantly important to make the objects more obvious and distinguishable from the background or other objects. Further, edge enhancement is required to sharpen objects' edges in the image so that the objects are easier to recognise. Noise filtering additionally is needed for images suffering from presence of noise.

Retinal image enhancement is a pre-processing step to improve retinal image quality for visual perception and to facilitate diagnosis of retinal-related diseases such as diabetic retinopathy. There are two categorisation of retinal image enhancement, i.e. invasive and non-invasive enhancement. For invasive enhancement, a contrasting agent (sodium fluorescein) is injected into the human blood vessels to produce better contrast of retinal vasculatures. However, due to its invasiveness, this method may lead to physiological problems such as nausea, vomiting and dizziness [25]. The worst case of adverse reactions following fluorescein injection, what is more, could be fatal anaphylactic shock, which eventually leads to death [26]. It has been reported by Yannuzzi *et al.* that the frequency rate for death cases due to fluorescein injection is 1:222,000 [27]. Hence, even though fluorescein angiography can produce better contrast of retinal fundus images, it is not recommended for medical routine use [28].

For non-invasive enhancement, image intensities are manipulated to improve image quality without any intervention into human body through digital image processing techniques. Image enhancement techniques focus on noise removal (smoothing), contrast enhancement (feature enhancement), contrast normalisation (illumination normalisation) and image sharpening to improve the visual perception of the image for the use of human viewers [33]. The other enhancement techniques are to be a pre-processing step to provide better input for subsequent automated image processing algorithm in a computerised system such as edge detection and object segmentation [34]. In retinal image enhancement, the techniques developed are focused on (1) contrast normalisation as proposed by Wang *et al.* [55], Foracchia *et al.* [5], Tusheng and Yibin [42], Walter and Klein [56], Fleming *et al.* [18] and (2) contrast enhancement (feature enhancement) as developed by Saleh *et al.* [57], Sinthanayothin *et al.* [58], Shimahara *et al.* [59], Noronha *et al.* [60], Wu *et al.* [40] and Soares *et al.* [61].

Dealing with this problem, we extend the discussion on general image enhancement techniques in two areas, i.e. image enhancement techniques to deal with the problem of varied contrast and image enhancement techniques to deal with the problem of low contrast. It is important to discuss on several enhancement techniques applicable not only for specific colour retinal fundus images, but also for other medical images to find possibilities in developing a new and better non-invasive digital imaging enhancement scheme that can enhance varied and low contrast colour retinal fundus images to be similar to, or better than the contrast produced by invasive method (FFA) without introducing noise or artefacts. The following sub-chapters discuss on various image enhancement techniques for varied contrast images and low contrast images.

2.2.1 Enhancement Techniques for Varied Contrast Images

In medical images, current image enhancement techniques to address the problem of varied contrast can be categorised into two, namely prospective and retrospective contrast normalisation methods [62-63]. Prospective contrast normalisation methods,

known as calibration methods, require an acquisition protocol tuned to varied contrast correction, whereas retrospective ones rely on the information in an acquired image and make certain assumptions about the imaged setting purposively being applicable to any image.

Varied contrast in prospective contrast normalisation methods reputedly is a systematic error occurred during the acquisition process resulting in varied contrast images. This systematic error can be compensated using a special imaging sequence device or using an additional phantom image with some identified physical properties resulting in a smoothed acquired image [64]. These correction methods however are not frequently applicable in real situation for requiring an extra measurement and scanning time, and probably causing discomfort for the patients. Moreover, an increase in the background noise may arise as well [65]. In general, prospective approaches can only deal with varied contrast due to machine imperfections; however, the varied contrast problem may also originate from patient-induced data.

Most techniques on contrast normalisation intensively been developed in retrospective methods can be classified into filtering [66-68], surface fitting [69-70], segmentation based [71-72], statistical model [73-75] and other methods [13, 76-77]. Filtering methods using high-pass or low-pass filter is to separate high frequency signal from low frequency artefacts of the image containing anatomical structures as in homomorphic filtering [67].

Homomorphic filtering, a technique based on an illumination and reflectance image model, is performed on a log transform of the image intensity to separating illumination as low-frequency component and reflectance as high-frequency component from an image and to making illumination more uniform. However, this method works well only if varied contrast occurs over the whole image. Homomorphic filtering creates artefacts at the edge between object of interest and background in the image known as edge effects when the image contains an object of interest corrupted by a bias and a uniform background with no bias [68]. Moreover, several manually determined parameters make the implementation of homomorphic filtering even more difficult [78].

Even though filtering methods in general have advantages due to their relatively simple implementation and rapid operation, they are merely suitable for small imaged anatomical structures enabling no information in low frequencies to be erroneously taken out by low-pass filter. Moreover, users also have to select some specified parameters, for instance filter size, causing an additional ambiguity and restricting the possibility of its usage.

Surface fitting methods in turn are to estimate parametric surface taken from dominant or large homogenous regions and to fit it to a set of image features that suffer from varied contrast. The estimated surface is typically polynomial or spline based [79-80]. The weakness of these methods is that the estimation of a varied contrast area is merely from intensities of one dominant region and subsequently extrapolated over the whole image. Another weakness is that these methods may integrate some adverse information during the extrapolation. Surface fitting methods generally will perform well if homogenous areas of the image are distinctive and sufficiently large. Likar *et al.* applied an information minimisation by parametric fourth order polynomial model (M4) and used entropy as a global intensity uniformity for optimisation of complex image formation models to retrospectively correct the uneven illumination in MR images [81]. Method developed by Likar *et al.* [81] beneficially does not require initialisation, assumption of distributions of individual objects and pre-segmentation of defined region. Yet, the difficulty in optimisation may occur due to the application of polynomial correction model with a higher order.

Segmentation-based methods furthermore are to combine and produce better contrast normalisation and segmentation concurrently. However, the number and selection of the explicitly modelled object classes are becoming the problems in this method. Guillemaud and Brady [72] proposed a method based on minimum entropy that automatically determines the number of object classes as an improvement for Well *et al.* technique [82] which needs to select and determine the spatial distribution of the object classes in an image manually. Nevertheless, it is found difficult to determine object classes when the image is unevenly illuminated. This is a non-trivial problem in that contrast normalisation itself is also the main objective. Moreover, the segmentation-based methods' assumption that the distribution of image intensity is

given by a mixture of Gaussian (normal) distribution of individual objects is often invalid; not mentioning another problem when dealing with pathological image data.

Statistical model for contrast normalisation, known as nonparametric non-uniformity normalisation (N3), proposed by Sled *et al.* [73] has been widely used for correcting uneven illumination, particularly in MR data. The excellences of this method are its insensitiveness to pathological data and fully automatic process requiring no model of object classes. The method derives a non-parametric model of object classes from the data itself and employs an iterative optimisation approach to determine both smooth multiplicative illumination component and the true object classes' distribution. The two parameters necessarily to be determined are the parameter to control the smoothness of the estimated non-uniformity and the other parameter to control the trade off between accuracy and convergence rate. In fact it has been reported in [83] that M4 developed by Likar *et al.* [81] performed faster than N3 developed by Sled *et al.* [73]. Tustison *et al.* [74] on the other hand recently has modified this high popular N3 method by replacing the B-spline smoothing strategy and modifying of iterative optimisation used in the original N3 to improve convergence performance.

Lastly, other methods, though not classified into any of the aforementioned categories in contrast normalisation, also exist such as registration against template [76], shape recovery [84], background estimation and subtraction [5, 42]. In registration-based method proposed in [76], two images, i.e. an image undergoing the proposed method and a reference image, are to be registered and to normalise varied contrast by smoothing and dividing themselves. However, the need for an application-specific reference image has become a main disadvantage of this method. In shape recovery based method, Lai and Fang [84] modelled smooth illumination-field function and automatically determined orientation constraints using a finite-element method. The major disadvantage of this method on the contrary is on the use of a linear system with large matrix to solve orientation constraints affecting the computation time. Additionally, the selection of data constraints by sparse sampling may result in imperfect data selection and lead to error in the contrast normalisation. In background estimation and subtraction, foreground-background model has been

initially proposed by [42] and extended by [5]. The local intensity variations field is to estimate model of background image to normalising the luminosity and contrast variability; while Mahalanobis distance is for the background pixel classification. These techniques conversely may face the problem when dealing with the presence of large bright objects, for instance zone with large exudates or laser treatments and large dark areas, for instance large haemorrhages and macula in retinal images in that these areas considerably are not in the luminosity and contrast variability estimation process. The aforementioned main enhancement techniques for varied contrast images are summarized in Table 2-1.

Table 2-1 Advantages and disadvantages of different enhancement techniques for varied contrast images

Enhancement Techniques	Advantages	Disadvantages
Filtering [66-68]	Simple implementation, rapid operation and well-performed if varied contrast occurs over the whole image.	Creation of edge effects (artefacts), manual pre-determined parameters.
Surface fitting [69-70]	Well-performed if homogenous areas of the image are distinctive and sufficiently large.	Estimation of a varied contrast area using intensities of one dominant region may cause some adverse information during the extrapolation.
Segmentation based [71-72]	Produces better contrast normalisation through selection of the explicitly modelled object classes.	Assumption that the distribution of image intensity is given by a mixture of Gaussian (normal) distribution for selection of the explicitly modelled object classes is often invalid for pathological image data.
Statistical model [73-75]	Its insensitiveness to pathological data and fully automatic process require no model of object classes.	Computation time and convergence performance due to its iterative optimisation.

2.2.2 Enhancement Techniques for Low Contrast Image

When the distribution of intensity values containing information is excessively concentrated on a specific range, an image may appear in low contrast. It can be optimised by spreading out the distribution of the significant intensities. The process of a contrast enhancement in turn aims to increase image intensity differences to make

the image or specific objects appeared in the image more obvious. Of numerous enhancement techniques being proposed to overcome the problem of low contrast images, contrast enhancement techniques is mainly categorised into two, namely spatial domain and frequency domain [34, 46]. The spatial domain involves a process of the contrast enhancement by modifying luminous intensity histogram of the input image and the latter technique performs the enhancement process in the frequency domain of the image.

Based on the process of expanding the range of significant intensities, spatial domain can generally be categorised into two, i.e. linear and non-linear techniques. Linear contrast enhancement refers to a process that linearly expands the range of original image intensities into a newly specified intensity distribution to utilise a full range of available brightness value. In image processing, distribution of image intensity values is referred as histogram of the image. Examples of linear contrast enhancement techniques are min-max, percentage and piecewise linear contrast stretching techniques [33]. In linear contrast stretching, original minimum and maximum intensity values of an image are allocated to a new set of intensity values to increasing the dynamic range of histogram of the processed image. The difference between min-max and percentage linear contrast stretching technique is that the first uses particular minimum and maximum values and the latter represents the specific minimum and maximum values into a certain percentage of pixel intensities from the mean of the histogram. When the histogram of an image is bi or remodel, contrast enhancement can be performed in selected areas by stretching certain values of the histogram. A piecewise linear contrast stretching in the image consists of a number of linear enhancement steps that can be described as

$$f(x, y) = \begin{cases} ax, & 0 \leq x \leq x_1 \\ b(x - x_1) + y_{x_1}, & x_1 < x < x_2 \\ c(x - x_2) + y_{x_2}, & x_2 \leq x \leq M \end{cases} \quad (2-6)$$

with a, b and c are gained constants in the respective regions and M is as the maximum luminous intensity value. One major drawback of linear contrast stretching is that each value in the input image can possibly have several values in the output

image - causing certain objects in the original image to lose their correct corresponding brightness value in the processed image.

Non-linear contrast enhancement meanwhile refers to a process to modify the image intensity distribution using a non-linear technique. One of the most commonly used methods is histogram equalisation [33, 85] whose basic idea is to map luminous pixel intensity values in the image to a more uniform distribution. In the histogram equalisation, the mean of luminous intensities of the processed image lies in the middle of gray level intensity of the input image in spite of its mean. Histogram equalisation method can be categorised into two, namely global and local methods [86]. Global histogram equalisation modifies a single histogram obtained from the entire image to enhance the image contrast. Its main disadvantage is its dependence on the global statistics of the image. Histogram equalisation is effective to enhance low contrast image if the image contains one or two distinctive objects and no significant contrast change between these objects and the background. Conversely, rarely does this condition occur in real one. Moreover, applying this technique on the presence of a high peak in the histogram can result in over-enhanced image leading to an unwanted loss of objects' visibility [87].

Local histogram equalisation methods in turn have been proposed to overcome the problems of global histogram equalisation. In these methods, the input image is partitioned into sub-images. Adaptive histogram equalisation (AHE) has been proposed by independently applying histogram equalisation on each sub-image [88-90]. These sub-images are subsequently combined using interpolation method to get the final image [88]. Even though AHE is able to improve image's local contrast and produce more detail image, this method often overemphasizes noise and introduces significant artefacts in the process, for instance at the edges of relatively homogeneous regions [88, 91]. A generalisation of AHE, known as contrast limited adaptive histogram equalisation (CLAHE), has then been developed to overcome the problem of noise amplification [92-93]. CLAHE is an improvement of AHE by modifying an enhancement calculation based on user-specified maximum, i.e. contrast-limit level. This maximum contrast enhancement factor is set up to prevent an over enhancement of noise and reduce halo effects of the AHE. In CLAHE,

contrast-limit level of the histogram and size of the local region of the image (tile) are two important parameters [90]. CLAHE has been widely implemented for image enhancement in medical applications, for instance in enhancement of mammograms [93], retinal images [94], CT images [85] and X-ray images [95]. However, one major drawback in CLAHE is that it easily introduces artificial boundaries between two regions where the contrast between these regions is huge [96-97]. The size of the image tile and the contrast-limit parameter are also image and user dependant that can be disadvantageous to CLAHE.

Other non-linear enhancement techniques based on spatial filtering, such as multichannel filtering [98], blurred masking [99], adaptive contrast enhancement [100] and enhancement using first derivative and local statistics [101] use local information of the image to enhance image details. Again, these techniques also have major drawbacks due to ringing artefacts and noise over enhancement caused by amplification of noise and high contrast edges. Another drawback further may arise if the some local regions are so prominent that the entire image may lose its uniform pattern. A general characteristic of the aforementioned techniques is that they operate based on single-scale spatial domain leading them merely be able to perform a contrast enhancement of a certain size of specific local processing regions.

The other contrast enhancement techniques are based on frequency domain transform. Many studies of frequency domain transform with application to medical image enhancement mainly concentrate on the wavelet transform. Wavelet, as a mathematical tool that is able to simultaneously provide both the time and frequency information of a signal in different scale, has been widely used for a medical images enhancement such as CT images [102], MR images [103], X-ray images [104], retinal fundus images [61], mammograms [105] and ultrasound images [106].

A wavelet-based multi scale analysis provides several sub-band images from the original image and the advantage of analysing each band independently. Each sub-band image contains information based on various scales resulting in the representation of low or high frequency elements on separate images. Noise or similar type of components of the image can be depicted in high resolution (small

scale) and large objects or subtle objects with defined extent can be depicted in medium and low-resolution levels. This categorisation is advantageous to selectively enhance or degrade image features of importance in different resolution level [107].

Table 2-2 Advantages and disadvantages of different enhancement techniques for low contrast images

Enhancement Techniques	Advantages	Disadvantages
Linear contrast stretching techniques [33]	Simple implementation and well-performed of contrast enhancement by stretching certain values of the histogram if the histogram of an image is bimodal.	Losing correct brightness value in the processed image due to possibility of having several values in the output image.
Global histogram equalisation [33, 85]	Effective to enhance low contrast image if the image contains one or two distinctive objects.	Over-enhanced image leading to an unwanted loss of objects' visibility if applying this technique on the presence of a high peak in the histogram.
Local histogram equalisation each sub-image [88-90]	Improve image's local contrast and produce more detail image.	Overemphasizes noise and introduces significant artefacts.
Spatial filtering [98-101]	The use of local information of the image enables to enhance image details.	Ringling artefacts and noise over enhancement caused by amplification of noise and high contrast edges.
Wavelet-based multi scale [108]	Selectively enhance or degrade image features of importance in different resolution level.	The results of wavelet transform is no longer shift invariant.

2.3 Comparative Study on Retinal Image Enhancement

Some studies have been conducted to compare the performance of several medical image enhancement techniques. Yousiff *et al.* [35] conducted a comparative study for performance evaluation of nine different techniques for contrast enhancement and illumination equalisation of retinal fundus image on two publicly available databases of total 60 images [36-37]. The eight different techniques are green band image [38], histogram equalisation [39], adaptive histogram equalisation [40], adaptive local contrast enhancement [41], background subtraction of retinal blood vessels [42], division by an over-smoothed version [43], desired average intensity [44] and estimation of background luminosity and contrast variability [5]. The performance of each technique is evaluated by using a matched-filter vasculature segmentation

algorithm [45]. The results show that adaptive histogram equalisation [40] is the most effective method among the others for having the largest area of 0.874 under the receiving operating characteristics (ROC). It is then followed by the adaptive local contrast enhancement [41] with 0.833 and the histogram equalisation [39] with 0.787 at the second and the third, respectively [35] for improving the retinal vessels segmentation algorithm [41]. Youssif *et al.* [35] also applied hybrid method by combining Sinthanayothin's method on adaptive local contrast enhancement [41] with a method developed by Yang *et al.* on division by an over-smoothed image for contrast normalisation [43]. It is interesting to note that applying contrast enhancement techniques on varied contrast corrected image further can enhance the image and in turn can achieve better result in the segmentation process than just performing ordinary contrast enhancement techniques on the input image.

Salvatelli *et al.* [109] test the performance of homomorphic filtering [46] and morphological filtering [22] for contrast normalisation. They also compare the performance of two contrast enhancement techniques, namely morphological filtering [22] and local contrast enhancement [41]. Each combination of these four image pre-processing techniques is then tested using unsupervised segmentation of the abnormal blood vessels on diabetic retinopathy images. For the result, homomorphic filtering for contrast normalisation and morphological filtering for contrast enhancement are becoming the best combination [109]. Besides, it is believed that both processes of contrast normalisation and contrast enhancement must be simultaneously conducted for better image quality that leads to better segmentation results. Yet, another comparative studies conducted by Rahman *et al.* [110] and Bichao *et al.* [111] interestingly show that Retinex, a method to obtain colour constancy, can produce better image quality in terms of the tonal rendition and dynamic range compression of the processed image than that of histogram-based image processing techniques such as histogram equalisation, manual histogram adjustment and other commonly used techniques, e.g. homomorphic filtering.

Tomazevic *et al.* [62] in evaluating contrast normalisation has compared several retrospective contrast normalisation methods, such as linear and homomorphic filtering [46], morphological filtering [112], fitting a shading model [34] and entropy

minimisation [113]. The method based on entropy minimisation (EMI) for the result achieves the best corrections of the tested methods [62] for producing no spurious intensity variations to the output image and being insensitive to noise. Interestingly, most of the EMI-based methods have been implemented using independent component analysis (ICA), which is a blind statistical method for separating the mixed signals and determining the underlying factors or components from mixtures of a set of random signals, measurements or variables [114-116]. In the next subsection, the Retinex theory and the ICA and their applications in image processing will be reviewed and investigated to solve the problem of varied and low contrast image.

2.4 Retinex Theory and Its Application in Image Processing

Edwin H Land was first to formulate Retinex theory to describe human visual system in perceiving the colour or lightness of the scene [117]. Land found that human visual system preserves information from the object's characteristics, reflectance for example and discards uncertain factors such as varying illumination. It then indicates that even when retinal sensory signals coming from different colour patches under different illuminations are identical, human visual system are able to name the reflectance colour. However, during that time, Land did not understand if the human vision was only formed either in the retina or in the cortex. The term Retinex itself means an amalgamation of retina and cortex, assuming that both retinal eye and brain cortex play a significant role in the vision process.

Retinex theory has four basic principles. First, colour is obtained from three kinds of lightness, namely physical reflectance, perceived reflectance and sensation of lightness that are independently computed for each colour channel. The objective of Retinex is to measure the sensation of lightness to obtain the estimated physical reflectance that is averaged over a particular channel or to obtain perceived reflectance in the event of human visual system. Second, the intensity ratios measured from the surroundings assumedly refer to illumination invariant. Third, combined information from local ratios is used to determine the lightness in a given channel that is measured over large regions. The last, the highest lightness obtained from a specific location in each channel is assumed to have maximum reflectance for

that particular channel.

In the Retinex theory, an image is decomposed into two parts, i.e. illumination and reflectance. Intensity image I at certain point (x, y) corresponding to a particular wavelength (λ) is equal to the product of illumination L and reflectance R .

$$I(\lambda, x, y) = L(\lambda, x, y) \cdot R(\lambda, x, y) \quad (2-7)$$

The basis of the Retinex theory considers the slow variation of intensity resulting in the distribution of frequency spectrum at low frequencies. The illumination part of the image is estimated and the output image considered as the reflectance part is obtained by subtracting this estimation from the original image. The reflectance part, which is invariant to illumination condition, is used to obtain reliable object recognition. Land and McCann further developed a computational proposed extension of the Retinex theory called as the 'Reset Retinex' to show that the reflectance value of a particular pixel can be determined by taking the ratio of the pixel intensity with other pixels in the image [118]. Numerous algorithms have been developed and some of them will be explained in the next subsections.

2.4.1 Retinex Algorithms

The main idea of Retinex algorithms assumes that a perceived reflectance depends on a relative measure of lightness, known as sensation of lightness correlating to the reflectance of the objects. The implementation of Retinex theory in general can be categorised into two, i.e. non-iterative and iterative methods based on a process of estimating the illumination part. The non-iterative methods are categorised into two, namely global and local Retinex methods. In the non-iterative global Retinex methods, one-dimensional geometrical structure, i.e. paths is used to scan the image content. First, illumination part of the image is estimated using information obtained from pixel intensity along multiple random paths within the image. The obtained illumination part is subsequently to estimate the reflectance part of the image. The difference among global Retinex methods is the type of path used. There are several global Retinex methods depending on the used paths, such as piecewise linear paths

[119], Brownian paths [120] and double spirals [121]. In most of natural images, Retinex algorithms with many piecewise linear paths - sometimes known as random walks algorithms- are required to produce better-enhanced images but this will affect the computational time. Brownian paths and double spirals are used to reduce the computational time required by the piecewise linear paths while preserving the basic underlying principles. Global Retinex methods using global information obtained from the separation process of illumination and reflectance are capable to maintain the original tone of the image. Even so, these methods tend to produce poor detail recovering in the dark regions in particular [122].

In the non-iterative local Retinex methods, the neighbouring pixel intensities are to estimate the illumination part of the image followed by the estimation of the reflectance part of the image. The main difference among local Retinex methods is the way to estimate the illumination information, for instance single scale Retinex (SSR) using Gaussian estimation [123] and multi-scale Retinex (MSR) using Gaussian estimation [124]. Using local information obtained from the separation process of illumination and reflectance, local Retinex methods are able to recover better fine details in the image compared to that of global Retinex methods. Since only local information is used, the original tone of the image on the contrary is often not well maintained.

The iterative Retinex methods essentially are a multilevel one-dimensional Retinex implementation and have been developed by Frankle and McCann [125-126] and further refined by Funt *et al.* [127]. These methods elaborate the information from the surrounding areas of pixel of interests similarly to that of the global Retinex ones in obtaining the reflectance part of the image.

The different Retinex algorithms usually have the same system diagram as shown in Figure 2.1 and the difference among them concentrates on the actual estimation of the illumination part of the image.

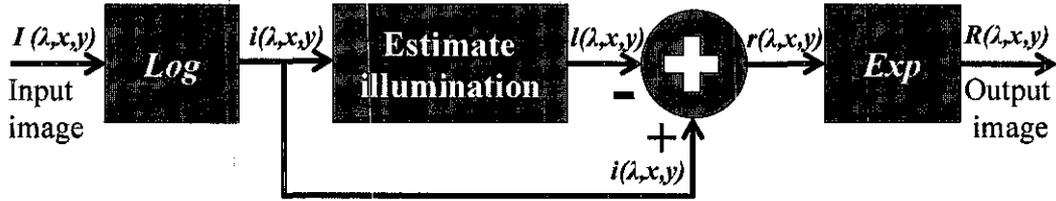


Figure 2.1 Diagram of general Retinex algorithms

The initial step is to convert the intensities of the input image of a specific wavelength (λ) using logarithmic function with $i(\lambda, x, y) = \log I(\lambda, x, y)$, $l(\lambda, x, y) = \log L(\lambda, x, y)$ and $r(\lambda, x, y) = \log R(\lambda, x, y)$. The reflectance R of the image is estimated in its logarithmic form r as the difference between logarithms of I and L and formulated as

$$\log R(\lambda, x, y) = \log (I(\lambda, x, y)) - \log (L(\lambda, x, y)) \quad (2-8)$$

The use of logarithmic conversion offers advantages both physiologically in which referring to the sensitivity of human visual system and numerically in which preferring additions to multiplications. In practice, many different algorithms based on Retinex theory have been developed and some of them are reviewed below.

2.4.1.1 Non-Iterative Local Retinex Methods

The reflectance R of a specific wavelength (λ) at a particular pixel (x, y) in which $\lambda \in R, G, B$ represents three colour channels in digital colour image is first estimated as the normalised sum of ratios between the intensity $I(\lambda, x, y)$ and the highest intensity travelled by each of the M random paths $\{p_i : i = 1, 2, 3, \dots, M\}$ along the image where each random path ends at (x, y) . The estimated reflectance achieved by the non-iterative local Retinex methods is formulated as

$$R(\lambda, x, y) = \frac{1}{M} \sum_{i=1}^M \frac{I(\lambda, x, y)}{I(h_i)} \quad (2-9)$$

with h_i as the point with the highest intensity along path p_i .

2.4.1.2 Non-Iterative Global Retinex Methods

The idea of global Retinex method is to use the information of the surrounding areas of pixel of interests to estimate the illumination and subsequently to update the intensity of the pixel of interests. Land proposed centre-surround Retinex algorithm [128] is as an improvement of his initial random paths Retinex algorithm [118]. Land's method computes the lightness of the generic image pixels from a particular wavelength (λ) as the logarithm of the ratio between intensity $I(x, y)$ and the average value of the neighbouring locations, sampled with a density that decays as the inverse square of the distance from the centre. The lightness produced by the centre-surround Retinex algorithm showing the estimated reflectance is formulated as

$$\log R(\lambda, x, y) = \log \left(\frac{I(\lambda, x, y)}{\langle \{I(\lambda, x_s, y_s), (x_s, y_s) \in Surround\} \rangle_w} \right) \quad (2-10)$$

with $\langle \bullet \rangle_w$ representing the weighted average operator. Different from (2-9) in which the ratio is calculated based on the pixel with highest intensity; (2-10) calculates the ratio based on a weighted average intensity value of the surroundings. Jobson *et al.* [123] continued Land's work with the use of the weighted average of the surround as an estimated illumination part of the image that can be obtained by convolving the image function $I(\lambda, x, y)$ with a normalised kernel function F . This algorithm, known as SSR, is defined as

$$\log R(\lambda, x, y) = \log \left(\frac{I(\lambda, x, y)}{F(\lambda, x, y) * I(\lambda, x, y)} \right) \quad (2-11)$$

$$\log R(\lambda, x, y) = \log I(\lambda, x, y) - \log [F(\lambda, x, y) * I(\lambda, x, y)], \quad \lambda \in \{R, G, B\} \quad (2-12)$$

The Retinex output $R(\lambda, x, y)$ represents the estimated reflectance part of the image, $F(\lambda, x, y)$ represents the normalised surround function where $\iint F(\lambda, x, y) dx dy = 1$ and "*" denotes the convolution operation. Jobson *et al.* [123] estimated the illumination part by means of a Gaussian form subsequently subtracted from the

original image to obtain the estimated reflectance that is invariant to illumination. Even though various surround functions, such as inverse square spatial surround [128] and exponential absolute value [129] can be used, Gaussian surround function offers good dynamic range compression and advantages of being more distinctively regional [130]. For a particular wavelength λ , the Gaussian function is defined as

$$F(\lambda, x, y, \sigma) = Ce^{-((x^2+y^2)/\sigma^2)} \quad (2-13)$$

with C that is selected so that $\iint F(\lambda, x, y, \sigma) dx dy = 1$ and σ is the scale that controls the Gaussian surround function and needs to be determined in advance. The scale determines the type of information needed by the Retinex. The smaller scales provide more dynamic range compression and the larger scales provide more tonal rendition. Hence, a trade-off in determining the scale of the surround function is necessary to achieve optimal dynamic range compression and tonal rendition.

In practice, it is difficult to determine such a single scale to achieve both aforementioned objectives. Therefore, superposition of weighted several different scales of SSR, also known as MSR, is an obvious choice to balance these two effects. The MSR estimates the reflectance part from the ratio of the image intensities to their averaged local intensities to achieve both tonal rendition and dynamic range compression simultaneously. First, the image is decomposed into a set of images to obtain the image averages at different spatial resolutions by employing Gaussian filters of different sizes. Next, a set of images used to measure the reflectance are produced by dividing the original image by that of the decomposed image. Then, a logarithmic function is applied to each of the images to reduce the image dynamic range. The displayed image is eventually reconstructed by jointly adding the compressed images according to each of the weighting factors. The MSR is formulated as

$$\log R(\lambda, x, y) = \sum_{n=1}^N \omega_n \{ \log I_i(\lambda, x, y) - \log [F_n(\lambda, x, y) * I_i(\lambda, x, y)] \} \quad (2-14)$$

$$\log R(\lambda, x, y) = \sum_{n=1}^N \omega_n \log \left(\frac{I(\lambda, x, y)}{F(\lambda, x, y) * I(\lambda, x, y)} \right) \quad (2-15)$$

in which N is the number of scales, ω_n is the weighting factors for the n^{th} scale and $\sum_{n=1}^N \omega_n = 1$. Jobson *et al.* [124] showed that the weighting factor $\omega_n = 1/3$ with $N=3$ is sufficient for most of the MSR applications.

2.4.1.3 Iterative Retinex Methods

McCann *et al.* improved the random walks Retinex algorithm [118] by developing a multilevel one-dimensional Retinex implementation [125-126]. These iterative Retinex methods [125-126] calculates the long-distance interactions and then gradually moves to short-distance interactions among pixels. In each step, the spacing between the pixels being compared decreases. The direction among pixels also alters at each step in clockwise order. At each step, the pixels comparison is implemented to estimate the reflectance part using the ratio – product – reset – average operation, which is iteratively computed in a certain number of times. This number of iteration turns out to be an important image-dependent parameter of the algorithm. After estimating the reflectance part of the image at the longest-distance, the resulting values are used as initial estimation of reflectance for the next level of interaction. Subsequent comparisons between pixels are continually performed to refine the estimated reflectance until the spacing decreases to one pixel and the final product is obtained.

Ratio and product are the processes of accumulating and comparing resulting in the revision of a newer product in each pixels comparing process. Reset operation is to normalise the newer product exceeding the sustainable maximum. Averaging aims to estimate and update one pixel's luminance. The ratio-product-reset-average operation is performed by calculating the ratio between images I (in a specific channel) and its spatially shifted version and offset by some displacement distances formulated as

$$\log O_{x,y}^* = \frac{Reset \left[(\log I_{x,y} - \log I_{xs,ys}) + \log O_{xs,ys} \right] + \log O_{x,y}}{2} \quad (2-16)$$

where $(\log I_{x,y} - \log I_{xs,ys})$ is the ratio and $\left[(\log I_{x,y} - \log I_{xs,ys}) + \log O_{xs,ys} \right]$ represents the product. Reset operation is performed to update the maximum intensity of the scene L_{max}^{scene} if $\left[\log I_{x,y} - \log I_{xs,ys} + \log O_{xs,ys} \right] > \log L_{max}^{scene}$. The $\log O_{x,y}^*$ is a result of averaging with $\log O_{x,y}$ and $O_{x,y}^*$ itself is an updated output produced in each iteration that will be used as an input for the next iteration.

A comparison of Retinex algorithms in terms of advantages and disadvantages of each method is summarised in Table 2-3.

Table 2-3 Advantages and disadvantages of several Retinex algorithms

Retinex algorithms	Advantages	Disadvantages
Single scale Retinex (SSR) [123]	Well-performed for dynamic range compression.	'Washed out' appearance, loss of good tonal rendition.
Multi-scale Retinex (MSR) [124]	Good tonal rendition and preserve image's details.	'Washed out' appearance (less than SSR).
MSR with dynamic range [131]	'Washed out' appearance is suppressed, preserve image's details, increase global contrast.	'Ringing' artefacts are not totally diminished.
Retinex-based adaptive filter [132]	Reduce artefacts.	Increased computational time.
Fast MSR [133]	Fast	Image and template must be in the same size, size of the image must be in the power of two.
Iterative Retinex methods [125-126]	Reduce artefacts, no need to determine image-dependent parameters, only number of iteration.	Number of iteration is fixed and pre-determined, increased computational time.

2.4.2 Applications of Retinex in Image Processing

Retinex technique has been widely used in image processing mostly to solve the problems of colour constancy [120, 122, 124, 134-135]. Other implementations of Retinex technique are on shadow removal [136] and illumination normalisation [137-138]. Retinex technique has also been widely employed for medical imaging. For

instance, Chen applied Retinex technique in chest radiographic image for dynamic range compression and contrast enhancement to improve the visibility of the dark regions on chest radiograph [139]. Chao *et al.* applied this technique on MRI images and showed that it is able to correct varied contrast and to enhance image contrast to clarifying the deep brain structures of MR images captured by surface coils [140]. A specific application of Retinex technique on retinal images has been proposed by Vázquez *et al.* for classification of retinal blood vessels that combines an image enhancement based on MSR Retinex and a clustering technique performed in a number of overlapped areas in the fundus image [141].

In this thesis, the iterative method based on McCann algorithm [125-126] is adapted since it only needs to determine the number of iteration for its operation. The operation of this iterative Retinex method is simpler than that of the non-iterative ones in which several parameters, such as the weighted scale, must be predetermined to obtain good dynamic range and tonal rendition. However, the number of iteration used by McCann algorithm is fixed and must be determined in prior. Therefore, in our developed algorithm, we improve McCann algorithm by setting up a parameter to determine the optimum number of iteration for the Retinex rather than to use a fixed and predetermined number of iteration.

2.5 Independent Component Analysis

Independent Component Analysis or ICA is a blind statistical and computational technique that belongs to a class of blind source separation (BSS) for separating the mixed signals and determining the underlying factors or components from mixtures of a set of random variables, measurements or signals [142]. Besides blind source separation, the main applications of ICA are blind deconvolution and feature extraction. Herault and Jutten [143-144] introduced mathematical theory behind ICA and then was improved by Common [145], Lee [115], Cardoso [146], and Hyvarinen [147]. In ICA, a generative model is defined for the observed multivariate data generally obtained from a large number of samples. Multivariate data assumedly are to be linear or nonlinear mixtures of some unknown hidden variables or sources while the mixing process or the distribution of sources is unknown. The uniqueness of ICA

from other methods is that it determines hidden variables called as the independent components (ICs) of the observed data that are both non-Gaussian (possible exception of only one component to be Gaussian) and statistically independent. ICA has been successfully applied to solve various problems, e.g. medical signal [148], image processing [149], face recognition [150], telecommunication [151] and so forth.

2.5.1 Linear ICA Model

A mathematical formulation of ICA model is described as follows. Given observed random data $v = [v_1, v_2, \dots, v_N] \in \mathfrak{R}^{m \times N}$ with m as the number of observations and N as the number of available samples, a linear combination of n random sources $s = [s_1, s_2, \dots, s_N] \in \mathfrak{R}^{n \times N}$ with mixing matrix $A \in \mathfrak{R}^{m \times n}$ is formulated as

$$v = As \tag{2-17}$$

This generative model of ICA shows how a process of mixing the components s generates the observed data v . It is assumed that v and s are centred or mean subtracted. In this basic model, the number of ICs is equal to the number of observed data ($m = n$), thus, mixing matrix A is square and invertible. Both the ICs, which are hidden variables and the mixing matrix A , cannot be directly observed. Only is the random data v being observed. Mixing matrix A and random sources s are estimated using v . If $A = W^{-1}$, the ICs can be determined using separating matrix W simply by

$$\hat{s} = Wv \tag{2-18}$$

where \hat{s} is defined as estimated sources. The goal of ICA is to get \hat{s} as close as possible to s , which is determined as original sources, by finding out the optimum separating matrix W based on various estimation methods of independence. In some cases, noise is included in the measurements. Thus, adding a noise term in the model of ICA yields

$$v = As + n \tag{2-19}$$

where n represents additive white Gaussian noise. The problem of ICA is

systematically illustrated in Figure 2.2.

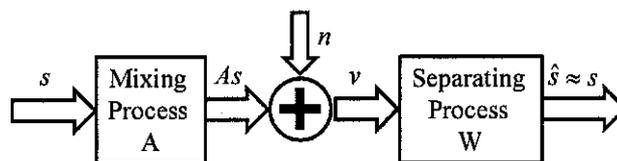


Figure 2.2 Diagram of ICA problem

In cases where the number of observed data is greater than the number of sources ($m > n$), the row dimension m of A can be reduced to n dimension using principle component analysis (PCA) to make the mixing matrix A square. If $m < n$, the number of observed data is smaller than the number of ICs, thus, the mixing matrix A is not invertible. This case is called as ICA with over-complete representations [152]. The possible way to estimate the ICs in over-complete cases is by using pseudo-inverse of mixing matrix. The mathematical formulation of this solution is described as

$$\hat{s} = A^T (AA^T)^{-1} v \quad (2-20)$$

Even though a simple pseudo-inverse offers a solution in some situations, many cases still need a more sophisticated estimate, for instance, using maximum likelihood and maximum a posterior estimation [153].

2.5.2 Limitations and Ambiguities in ICA

In generative ICA model shown in (2-17), the only assumptions needed are that (1) the ICs are statistically independent, (2) the mixing of the sources into the observations is linear, (3) the probability densities of the ICs are non-Gaussian and (4) the number of observations is larger than or equal to the number of sources [154].

Based on (2-17), some ambiguities may occur due to indeterminacies of the orders and the variances of the ICs. Since both s and A are unknown, the order of the ICs in (2-17) cannot be determined. Substituting a permutation matrix P and its inverse in the ICA model (2-17) gives

$$v = (AP^{-1})(Ps) = A's' \quad (2-21)$$

where P_s are the original ICs but in another order while AP^{-1} is the new unknown mixing matrix A' to be solved. Moreover, any scalar multiplier in one of the sources s_i can always be wiped out by dividing the corresponding column a_i of A by the same scalar, for instance k_i :

$$v = \sum_i \left(\frac{1}{k_i} a_i \right) (s_i k_i) \quad (2-22)$$

Fortunately, both of these ambiguities are insignificant in most applications [155].

2.5.3 Statistical Independence and Non-Gaussianity

Statistically, random variable x and y are considered to be independent if and only if the joint probability density function (pdf) can be factorised as

$$p_{x,y}(x,y) = p_x(x)p_y(y) \quad (2-23)$$

where $p_{x,y}(x,y)$ is the joint pdf of x and y , $p_x(x)$ and $p_y(y)$ are marginal pdf of x and y , respectively. Marginal density function of x is defined as

$$p_x(x) = \int p_{x,y}(x,y) dy \quad (2-24)$$

Applying this equation to random variables $s = [s_1, s_2, \dots, s_N]$, the components are statistically independent if the joint pdf $p(s)$ can be factorised as

$$p(s) = \prod_{i=1}^N p(s_i) \quad (2-25)$$

where $p(s_i)$ is the pdf of the i^{th} source.

For instance, in the case of two ICs, if s_1 and s_2 are independent, the density of s_1 is unaffected by s_2 . It is important to note that, different from principal component analysis (PCA), ICA uses statistical independence rather than only de-correlations.

Statistical independence shows stronger property than de-correlations, which simply considers the second order statistics. In other words, if the variables are independent, they must be uncorrelated. Nevertheless, the uncorrelated variables are not always independent.

Non-Gaussianity, which is of importance for estimation of the ICA model is the other parameter to show the statistical independence. It is defined as the deviation of pdf from Gaussian distribution. Based on the central limit theorem (CLT) [156], distribution of a sum of independent random variables tends to be more Gaussian (normal) than the distribution of each independent random variable. Thus, independence is non-Gaussianity. In the linear ICA model (2-17), v , which is the linear mixture of a number of ICs, has distribution closer to Gaussian than that of the ICs s .

2.5.4 Measuring Non-Gaussianity

A quantitative measure of non-Gaussianity of a random variable is to estimate the ICs. The first quantitative measure of non-Gaussianity is kurtosis, which in statistics shows a peaked measure of a probability distribution. Kurtosis or the fourth-order cumulant of random variable y denoted by $kurt(y)$ is defined as

$$kurt(y) = E\{y^4\} - 3(E\{y^2\})^2 \quad (2-26)$$

where $E = \{\cdot\}$ is the statistical expectation operator. The normalised kurtosis of a random variable y is then formulated as

$$kurt(y) = \frac{E\{x^4\}}{(E\{x^2\})^2} - 3 \quad (2-27)$$

Kurtosis of a Gaussian (normal) random variable is equal to zero; conversely, for most non-Gaussian random variables, it is nonzero. With negative kurtosis, a random variable is called sub-Gaussian or leptokurtic, while with positive one it is called as a super-Gaussian or platykurtic. Due to its simplicity, both theoretical and

computational, kurtosis has been widely used to measure the non-Gaussianity of a random variable. However, it has a limitation for being sensitive to outliers in data set; leading it to be not a robust measure of non-Gaussianity.

The second quantitative measure of non-Gaussianity is negentropy, which is calculated based on the information theoretic differential entropy. Entropy of a random variable corresponds to the degree of information given by the observed variable. The more random (i.e. unstructured or unpredictable) the variable is, the larger the entropy is. Entropy H of a discrete random variable Y is defined as [157]

$$H(Y) = -\sum_i P(Y = a_i) \log P(Y = a_i) \quad (2-28)$$

where a_i are the possible values of Y . Generalisation of the above formula for continuous random variables is known as differential entropy. The differential entropy H of a random variable y with probability density function $p(y)$ is defined as [157]

$$H(y) = -\int p(y) \log p(y) dy \quad (2-29)$$

It has been proved that Gaussian variable has the greatest entropy among all random variables of equal variance [157]. Conversely, the entropy of a random variable is small for random variables with non-Gaussian distribution. For this, the entropy apparently can be used as a measure of non-Gaussianity. A slight modification of differential entropy, called negentropy is defined as

$$J(y) = H(y_{gauss}) - H(y) \quad (2-30)$$

where J is negentropy of y and y_{gauss} is a Gaussian random variable of the same covariance matrix as y . Negentropy is always non-negative. It is zero if and only if y has a Gaussian distribution. The use of negentropy as a quantitative measure of non-Gaussianity has both advantages and disadvantages in that negentropy or differential entropy is the optimal estimator for non-Gaussianity and is well justified by statistical theory. However, it is very difficult computationally for requiring an

estimate of the pdf to calculate the negentropy.

The third quantitative measure of non-Gaussianity is by using approximations of negentropy. Some approximations of negentropy have been proposed to overcome the difficulty in calculating negentropy for the application of ICA. Classical method in approximating negentropy is by using the following higher-order moments [158]

$$J(y) \approx \frac{1}{12} E\{y^3\}^2 + \frac{1}{48} kurt(y)^2 \quad (2-31)$$

However, the above classical approximation of negentropy suffers from the non-robustness due to the use of kurtosis. An approximation of negentropy has been proposed by Hyvarinen [159] and is defined as

$$J(y) \approx \sum_{i=1}^p k_i [E\{G_i(y)\} - E\{G_i(v)\}]^2 \quad (2-32)$$

where k_i are some positive constants and v is a Gaussian variable. Both y and v are normalised to zero mean and unit variance. The function of G_i are some non-quadratic functions that should not be sensitive to outliers and must not grow too fast to get robust estimators. In a case where only one non-quadratic function G is used, the approximation will be

$$J(y) \approx [E\{G(y)\} - E\{G(v)\}]^2 \quad (2-33)$$

The most common choices of function G that have been proved to be useful are

$$G_1(y) = \frac{1}{a_1} \log \cosh a_1 y, \quad G_1'(y) = g_1(y) = \tanh(a_1 y) \quad (2-34)$$

$$G_2(y) = -\frac{1}{a_2} \exp\left(-a_2 \frac{y^2}{2}\right), \quad G_2'(y) = g_2(y) = -y \exp(-a_2 y^2 / 2) \quad (2-35)$$

where a_1 and a_2 are some suitable constants where $1 \leq a_1 \leq 2, a_2 \approx 1$. The statistical properties of the ICA method such as consistency and robustness will depend on the

choice of the objective function, meaning that different contrast functions offer different advantages. As pointed out by Hyvarinen [147], G_1 is good general-purpose contrast function whilst G_2 is suitable when the ICs are highly super-Gaussian or when the robustness is very important.

2.5.5 Pre-processing Data for ICA

Before applying ICA algorithm, the data set usually undergoes some pre-processing steps to make the problem of ICs estimation simpler and better conditioned.

2.5.5.1 Centring

Centring data v is performed by subtracting the data v with its mean $m = E\{v\}$ to make data v a zero-mean variable. The formula is defined as follows:

$$v = v - E\{v\} \tag{2-36}$$

In (2-17), if data v is a zero-mean variable, it can be inferred that s is also zero-mean. The mixing matrix A is estimated with the centred data and the estimation process is completed by adding the mean of s to the centred estimates of s .

2.5.5.2 Whitening

Whitening is decorrelation followed by scaling of the observed random variables. In ICA it can be performed using PCA in which the observed data v is linearly transformed to obtain a whitened data \tilde{v} whose components are uncorrelated and their variances are equal unity (variance normalisation). A simple PCA algorithm uses eigen value decomposition (EVD) of the covariance matrix. For instance, given a random variable v containing a large samples, the covariance matrix of the whitened random variable \tilde{v} is obtained from the sample and expressed as

$$C_{\tilde{v}} = E\{\tilde{v}\tilde{v}^T\} = ED^T E = I \quad (2-37)$$

with $D = \text{diag}[d_1 \dots d_n]$ is the diagonal matrix of its eigen values of $C_{\tilde{v}}$, I is an identity matrix and E is an orthogonal matrix of eigen vectors of $E\{\tilde{v}\tilde{v}^T\}$. Whitening transform is formulated as

$$R = ED^{-1/2}E^T \quad (2-38)$$

Therefore, applying whitening transform on the observed random variable v is expressed as

$$\tilde{v} = Rv = ED^{-1/2}E^T v \quad (2-39)$$

The ICA is now performed on whitened data \tilde{v} instead of original observed data v . The PCA technique estimates the whitening matrix R and the ICA technique finds the separating matrix W , which its schematic diagram is shown in Figure 2.3.

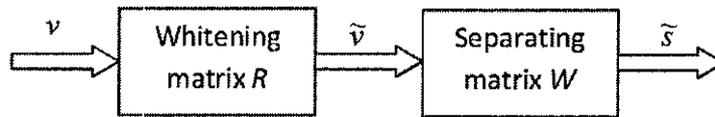


Figure 2.3 Estimating the ICs using whitening and separating processes

From (2-17), the mixing matrix A is considered as an inverse matrix of the concatenation of whitening matrix R and the separating matrix W .

2.5.6 ICA Algorithms

The estimation of ICs of the ICA model shown in (2-18) can be solved by using optimisation algorithm to determine a proper linear transform that makes s_i as independent as possible. The choice of the optimisation algorithm affects the algorithmic properties of the ICA such as convergence speed, memory requirement and numerical stability. The ICs are obtained using a separating matrix W . Several optimisation algorithms such as Newton-like methods and gradient –based methods

are used to optimise the chosen contrast functions, also known as cost functions or objective function for determining the separating matrix W . ICA algorithms to estimate the ICs can be derived from several different principles, such as maximisation of non-Gaussianity [147], maximum likelihood estimation [160] and minimisation of mutual information [161].

2.5.6.1 Maximisation of Non-Gaussianity

Assuming that ICs have non-Gaussian distribution, ICA methods are applied to separate the components from their mixture by maximising non-Gaussianity of each component. A flowchart showing the ICA process by maximisation of non-Gaussianity is depicted in Figure 2.4.

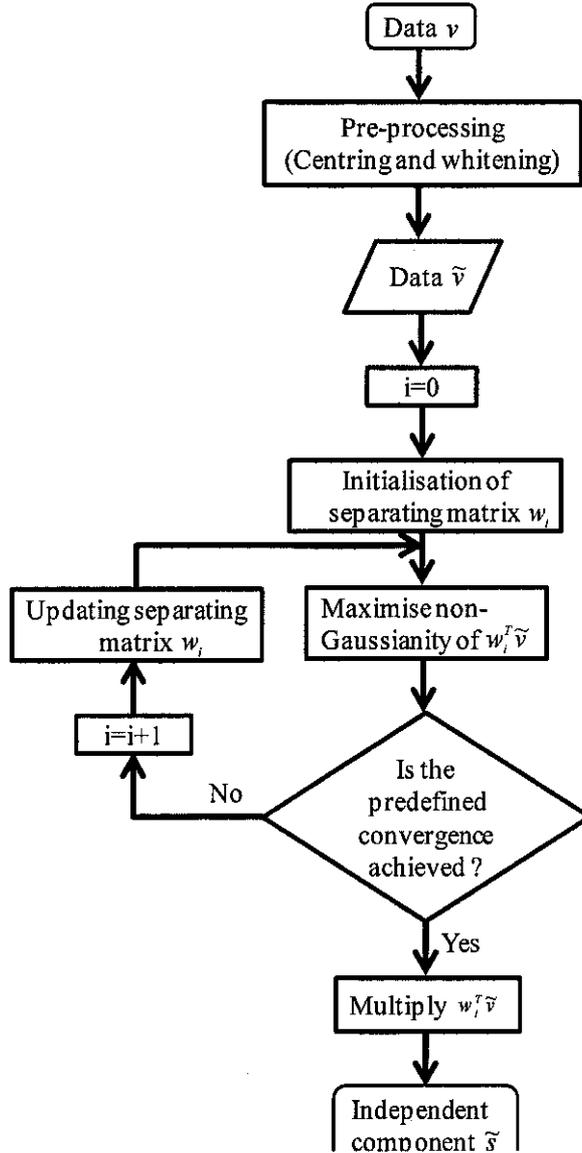


Figure 2.4 Flowchart of ICA by maximisation of non-Gaussianity

One well-known method in applying maximisation of non-Gaussianity is fast fixed-point algorithm (FastICA) developed by Hyvarinen *et al.* [147]. The FastICA is based on a fixed-point iteration for maximisation of non-Gaussianity of $w^T \tilde{v}$ to obtain the estimated IC \tilde{s} as indicated in (2-18). Since the FastICA uses approximation of negentropy, the maxima of the approximation of $w^T \tilde{v}$ are obtained at certain optima $E\{G(w^T \tilde{v})\}$. The optima of $E\{G(w^T \tilde{v})\}$ under the constraint $E\{(w^T \tilde{v})^2\} = \|w\|^2 = 1$ are obtained at points where

$$E\{\tilde{v}g(w^T \tilde{v})^2\} - \beta w = 0 \quad (2-36)$$

where β is a constant that gives $\beta = E\{w_0^T \tilde{v} g(w_0^T \tilde{v})\}$ and w_0 is the value of w at the optimum.

Using Newton's iteration method, matrix w is determined by the following equations.

$$w^+ = w - [E\{\tilde{v} g(w^T \tilde{v})\} - \beta w] / [E\{g'(w^T \tilde{v})\} - \beta] \quad (2-37)$$

$$w^* = w^+ / \|w^+\| \quad (2-38)$$

where w^* is the new value of w and $\|w^+\|$ is the norm of w^+ . By multiplying both sides of the (2-37) with $(\beta - E\{g'(w^T \tilde{v})\})$, the fixed-point algorithm can be formulated as

$$w^+ = E\{\tilde{v} g(w^T \tilde{v})\} - E\{g'(w^T \tilde{v})\} w \quad (2-39)$$

In summary, the algorithm of the FastICA for one IC estimation can be described as follows:

1. Determine an initial random weight vector (matrix) w .
2. Calculate $w^+ = E\{\tilde{v} g(w^T \tilde{v})\} - E\{g'(w^T \tilde{v})\} w$
3. Determine w^* as the new value of w denoted by $w^* = w^+ / \|w^+\|$
4. Check the criteria for convergence. If $\|w - w^*\| \leq \varepsilon$ is not fulfilled, the process will be back to step 2. The convergence parameter ε is set to some values, e.g. 0.0001.

For estimation of several ICs, the FastICA implements two approaches, i.e. deflationary and symmetrical approaches. In deflationary approach, the ICs are estimated one by one, while in the symmetrical one, the ICs are obtained in a parallel process. Detailed steps for deflationary approach are as follows:

1. Pre-process data to make zero-mean and whitened data \tilde{v} .

2. Choose m ICs.
3. Initialise random $w_i, i=1, 2, \dots, m$ to unit form,
4. $w_i^+ = E\{\tilde{v}g(w_i^T \tilde{v})\} - E\{g'(w_i^T \tilde{v})\}w_i$.
5. Orthogonalisation of $w_{io}^+ = w_i^+ - \sum_{a=1}^{i-1} (w_i^{+T} w_a) w_a$.
6. Normalisation of $w_{io}^* = w_{io}^+ / \|w_{io}^+\|$.
7. Check the criteria for convergence. If $|w_i - w_i^*| \leq \varepsilon$ is not fulfilled, the process will be back to step 4. The convergence parameter ε is set to some values, e.g. 0.0001.
8. Increase the iteration $i = i+1$ until $i=m$.
9. The iteration process ends when the convergence is achieved or the iteration has reached its maximum number of iteration.

For symmetrical orthogonalisation, detailed steps are described as follows:-

1. Pre-process data to make zero-mean and whitened data \tilde{v} .
2. Choose m ICs and set iteration $i=1$.
3. Initialise random $w_i, i = 1, 2, \dots, m$ to unit form and orthogonalise the matrix w .
4. For each $i: w_i^+ = E\{\tilde{v}g(w_i^T \tilde{v})\} - E\{g'(w_i^T \tilde{v})\}w_i$ and update each column of the separating matrix w from the previous iteration.
5. Orthogonalisation of $w^+ = (ww^T)^{-1/2} w$.
6. Check the criteria for convergence. If $|w - w^+| \leq \varepsilon$ is not fulfilled, the process will be back to step 4. The convergence parameter ε is set to some values, e.g. 0.0001.

7. The iteration process ends when the convergence is achieved or the iteration has reached its maximum number of iteration.

2.5.6.2 Maximum Likelihood Estimation

Maximum likelihood (ML) is a statistical approach for estimating the ICA model based on the assumption that the unknown parameters to be estimated are constants. If the pdf of the ICs are known, an application of a simple gradient-based algorithm enables to obtain these ICs. However, rarely does the situation where the pdf are known occur. Bell and Sejnowski introduced the infomax principle based on maximising information flow (entropy) of a neural network using non-linear scaling function [114]. This scaling function must be well chosen to allow the application of ICA. A stochastic gradient method [114] for maximising likelihood can be formulated as

$$w^+ = w + \mu [I + g(\tilde{s})\tilde{s}^T]w \quad (2-40)$$

where $\tilde{s} = w\tilde{v}$, μ is the learning rate and g is a function of the pdf of the IC: $g = f_i' / f_i$ where the f_i is the pdf of an IC.

Besides gradient-based methods, the FastICA could be an alternative to estimate the maximum likelihood and formulated as

$$w^+ = w + \text{diag}(\alpha_i) [\text{diag}(\beta_i) + E\{g(\tilde{s})\tilde{s}^T\}]w \quad (2-41)$$

with $\beta_i = -E\{\tilde{s}_i g(\tilde{s}_i)\}$ and $\alpha_i = -1/(\beta_i + E\{g'(\tilde{s}_i)\})$. The matrix w needs to be symmetrically orthogonalised iteratively.

By comparing (2-40) and (2-41), the FastICA can be considered as a fast fixed-point algorithm for maximum likelihood estimation. The choice of the matrices $\text{diag}(\alpha_i)$ and $\text{diag}(\beta_i)$ optimises the convergence speed in the FastICA. In ML, the problem may arise when the densities are not properly estimated and leading the overall estimation to be incorrect [154]. However, different from the gradient-based methods merely working for a given class of distribution (either it is super-Gaussian

or sub-Gaussian), the FastICA offers advantages for being able to estimate both sub and super-Gaussian ICs.

2.5.6.3 Minimisation of Mutual Information

Another approach based on information theory is the minimisation of mutual information among random variables. Mutual information I refer to a dependence measure among m random variables that can be formulated as

$$I(s_1, s_2, \dots, s_m) = \sum_{i=1}^m H(s_i) - H(s) \quad (2-42)$$

where H is the entropy of random variable s . The term $H(s_i)$ refers to the measured entropy of each variable s_i and $H(s)$ refers to measured entropy of all variable s . Hence, mutual information shows information reduction that is obtained by subtracting the entropy of the whole vectors from that of the separated components. The mutual information can be minimised by maximising $H(s)$ and that can be obtained if all s_i are independent. If all s_i are independent, no information is given from one to another, thus, $H(s)$ will be the same as $H(s_i)$. Mutual information is always non-negative and it is zero if and only if the variables are statistically independent. The formula stated in (2-42) is similar to negentropy given in (2-30) that also aims to find non-Gaussian components. In general, ICA algorithms by minimisation of mutual information are fundamentally equivalent to the ones for maximum likelihood estimation or maximising the sum of non-Gaussianities of the estimates of the ICs [154].

Compared to the other ICA algorithms, such as gradient-based methods, the FastICA offers several advantages, such as its simplicity, high computational speed and good accuracy for high dimensional data [162]. The main drawback of gradient-based algorithms is however on their slow convergence and dependence on a good choice of the learning rate sequence. Inaccurate choice of the learning rate can annihilate the convergence of the gradient-based algorithms. The FastICA, unequal to gradient-based algorithms for ICA, does not need adjustable parameters such as

learning rate. The convergence of the FastICA additionally is fast. On an independent experiment, the performance of FastICA was found to be up to 100 times faster than conventional gradient-based methods for ICA [163]. Moreover, comparison study on ICA algorithms given by [164] also showed that FastICA [147, 165] outperformed other ICA algorithms, such as Infomax [114], extended Infomax [166], neural gradient algorithm [167], EASI algorithm [168] with its shortest processing time, fastest convergence speed with small residual error. This is predictable since FastICA is not gradient descent but an approximative Newton method that can provide cubic or at least quadratic speed of convergence. In terms of floating-point operations per second (flops), the required amount computation for FastICA to converge is the smallest at around 10^7 flops in comparison to EASI [168] that has converged at around 1.5×10^8 flops and neural gradient algorithm [167] along with Infomax [114] at approximately 2.0×10^8 flops. Short computation time is becoming important in the development of a medical system related its use for mass screening such as DR mass screening.

2.5.7 Applications of ICA in Image Processing

In image processing, as well as in the field of medical imaging, ICA has been applied to solve the problems of image feature extraction [169-170], edge detection [171], texture analysis and classification [172] and blind deconvolution [115]. Wu and Liu [149] used ICA on dynamic contrast-enhanced imaging data for assessment of cerebral blood perfusion without any prior knowledge of arterial input function and underlying tissue. Promising results show that ICA is able to extract physiologically significant components from the DCE imaging data and the acquired IC maps allow for a reliable reference to identify venous and arterial structures. These results are able to provide better demarcation of the tumour territories. In mammographic imaging, ICA further has been used to improve the quality of digital mammographic images contributing to more accurate diagnosis [173].

An ICA-based method with selective filtering has been proposed by Li *et al.* to estimate functional activation regions in functional MRI (fMRI) [174]. Boroomand *et*

al. [175] also applied two most frequent ICA algorithms, i.e. FastICA [147, 165] and Infomax [114] to extract true activated temporal and spatial sources on simulated fMRI datasets in the presence of several different noise levels. In skin imaging, Tsumura *et al.* showed that spatial distributions of haemoglobin and melanin from a skin colour image can be separated by using ICA [176-177]. Moreover, Nugroho *et al.* successfully applied a technique based on PCA and ICA to convert the RGB skin image into a skin image that represents skin areas merely due to melanin and haemoglobin [178].

2.6 Summary

A general evaluation on the literature review concludes four problems in medical images. First, it is found that varied contrast is a problem in medical images due to the geometrical surface of the objects and configuration of the acquisition system. Varied contrast is defined as smooth variation of image intensity that needs to be normalised as part of image enhancement. In retinal image, the varied contrast occurs due to the spherical surface of the retina and the geometrical configuration of the light source and camera. Second, low contrast tiny objects of interest in medical images are related to biological structure of the objects and the amount of light being absorbed or reflected by these particular objects. This low contrast tiny objects need to be extracted and selectively enhanced to facilitate diagnosis based on direct observation or automated image analysis. These problems are very crucial when the diagnosis process involves an observation of these particular low contrast tiny objects to diagnose or to grade the severity level of a disease. Third, the best method to enhance the low contrast is based on invasive method. In retinal image, fundus fluorescein angiography (FFA) is used to enhance the retinal blood vessels and pathologies. However, this invasive method is not preferable due to its side effects that may cause physiological problems and even death for the worst case.

Fourth, the problem of increasing noise and creating artefacts may appear in most of existing enhancement methods based on filtering and histogram. Surface fitting and segmentation-based methods need to define objects as reference prior to enhancement process. For defining nonparametric model of object classes from the data themselves

and employing an iterative optimisation approach to estimate both smooth multiplicative illumination component and the distribution of the true object classes, statistical-based methods are found to be the best technique for enhancement in contrast normalisation. For contrast enhancement, adaptive contrast enhancement in turn are found to be the best; however, these histogram manipulation-based methods face the problem of increasing noise and creating artefacts.

Current image contrast measurements are only suitable to find the contrast between two or more images without involving specific image features. Image contrast measurement by Rubin and Siegel [53] given in (2-5) is basically the same as to find the variance of the pixels intensity distribution in the image. Even though, it is suitable to compare the contrast between two images in general, it does not correctly measure the contrast between two or more specific features. Using an image model, specific image features can be identified and the contrast between two specific image features, i.e. object of interest and the background can be determined by the ratio of the average of intensities between these two specific features. Instead of measuring contrast enhancement, the formulation given in (2-5) can however be used to measure the varied contrast normalisation since the lower the variance is, the more uniform the intensities are.

Retinex theory is initially developed to solve the problem of colour constancy that corresponds to characteristics of the objects, i.e. reflectance and makes the perceived colour of the objects relatively constant regardless the illumination condition. The use of the Retinex theory in which image intensity is a product of illumination and reflectance, enables to minimise the problem of varied contrast due to illumination by separating the illumination part from the reflectance part of the image. The reflectance part is obtained by estimating the illumination part of the original image and subsequently subtracting this estimated illumination from the original image. The objective of the Retinex theory is to optimise both dynamic range compression and tonal rendition. Retinex algorithm is applied to achieve optimal results for contrast normalisation indicated by the maximum compression of image intensity dynamic range without losing the details of the objects. In this thesis, the iterative method based on McCann algorithm [125-126] is adapted since it only needs to determine the

number of iteration for its operation. The operation of this iterative Retinex method is simpler than that of the non-iterative ones in which several parameters, such as the weighted scale, must be predetermined to obtain good dynamic range and tonal rendition. However, the number of iteration used by McCann algorithm is fixed and must be determined in prior. Therefore, in our developed algorithm, we improve McCann algorithm by setting up a parameter to determine the optimum number of iteration for the Retinex rather than to use a fixed and predetermined number of iteration.

ICA, which is a blind statistical method used to determine the underlying components, can be applied as an algorithm to separate the features or objects from their mixtures. The ICA searches for a linear transformation of a random variable that minimises the statistical dependence between its components. In order to define suitable search criteria, some parameters, such as maximisation of non-Gaussianity, maximum likelihood estimation and minimisation of mutual information can be utilised. In the case of image processing, ICA can be applied to extract the features from their mixtures observed from the image. It is believed that each of these features will have distribution which is more non-Gaussian than that of their mixtures. Extracting a specific feature in the image and separating it from the others by maximising non-Gaussianity of each feature result in the contrast enhancement of this specific feature. Nevertheless, before applying ICA algorithms, several steps can be applied to reduce the complexity of the separation process. The most common ICA pre-processing steps are centring and whitening. Centring is useful to normalise data variability, whilst whitening is useful either to decorrelate the mixed components or to reduce data dimension and noise in the observed data. However, any pre-processing steps can be added depending on the complexity of the problem. In this thesis, since the problem faced is varied and low contrast image, contrast normalisation based on Retinex is proposed to overcome the problem of varied contrast image prior to applying ICA for contrast enhancement. Due to its simplicity, high computational speed and good accuracy for high dimensional data [162], the FastICA algorithm [147], which is an efficient fixed-point iterative algorithm is adapted in this research to maximise the non-Gaussianity of the components to achieving contrast enhancement.

CHAPTER 3
MODELING OF VARIED AND LOW CONTRAST COLOUR RETINAL
FUNDUS IMAGES

3.1 Introduction

The objective of the research is to develop a non-invasive image enhancement method for varied and low contrast colour retinal fundus images. Varied and low contrast retinal fundus image models are developed to evaluate the performance of the proposed image enhancement method. The work involves the use of colour retinal fundus images that may suffer from problems of both varied and low contrast. Varied contrast may occur in within a colour fundus image and between two colour fundus images of the same retina. Figure 3.1 shows an example of varied contrast within an image in which retinal blood vessels may have different contrast.

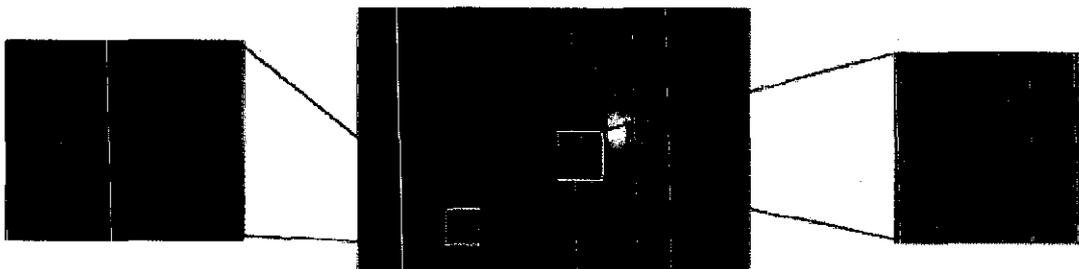


Figure 3.1 Varied contrast occurs in the colour fundus image

Another example of varied contrast between two images is shown in Figure 3.2. Although using the same fundus camera to acquire these two colour fundus images, the results show varied contrast between them.

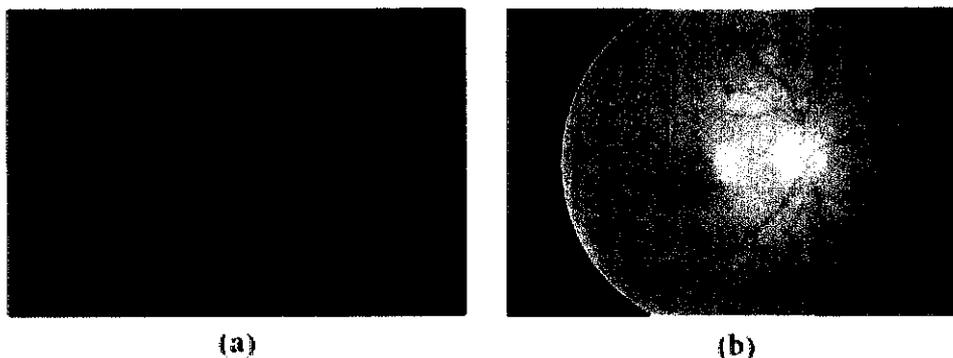


Figure 3.2 Varied contrast between two colour retinal fundus images of the same eye acquired using the same fundus camera

Besides varied contrast, colour retinal fundus images also suffer from low contrast particularly between very fine retinal capillaries and the background in the macular region as shown in Figure 3.3. The appearance of retinal blood vessels and capillaries in the macular region are important for diagnosing several retinal diseases, such as diabetic retinopathy (DR) and diabetic maculopathy (DM).

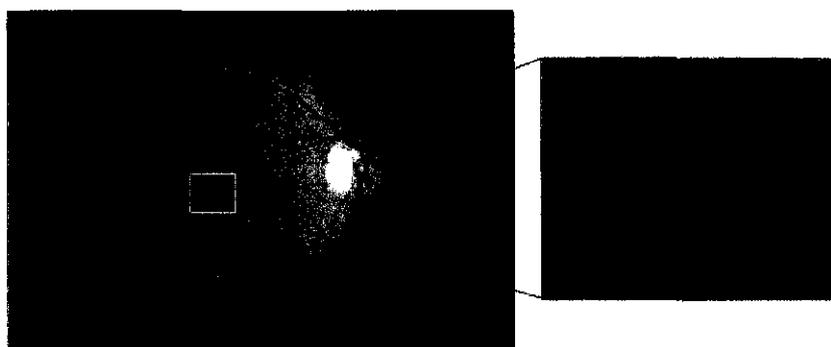


Figure 3.3 Low contrast of retinal vessels and capillaries in the macular region

Three retinal fundus image parametric models, i.e. varied contrast image, low contrast image, and varied and low contrast image are developed based on the probability distribution functions of macular pigment, haemoglobin and melanin to represent macular region, retinal vasculature and background, respectively. Data for modelling were collected from a clinical observational study NMRR-08-842-1997 (Appendix B) that had been approved by the Clinical Research Centre, Ministry of Health, Malaysia and was conducted at Hospital Selayang, Malaysia from July 2008 to March 2009. This database called as Fundus Image for Non-invasive Diabetic Retinopathy System (FINDeRS) consists of 315 colour retinal fundus images [179]

which forty-four of them, for this modelling, are randomly selected.

3.2 Structure of the Eye and the Retina

In general, the structure of the eye shown in Figure 3.4 can be classified into two main groups, namely ocular media and ocular fundus [19].

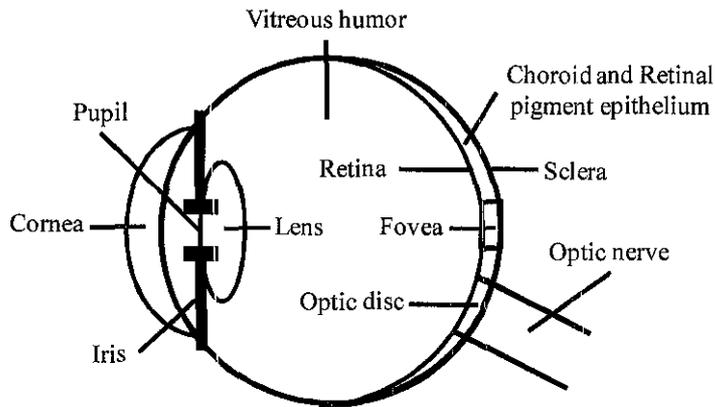


Figure 3.4 Schematic diagram of structure of the eye

Ocular media, which is located between the ocular fundus and the observer, consists of cornea, lens and vitreous humour; the ocular fundus meanwhile consists of the retina, retinal pigment epithelium, choroid and sclera. A diagrammatic cross-section of the eye inferred from [19, 180-181] is illustrated in Figure 3.5.

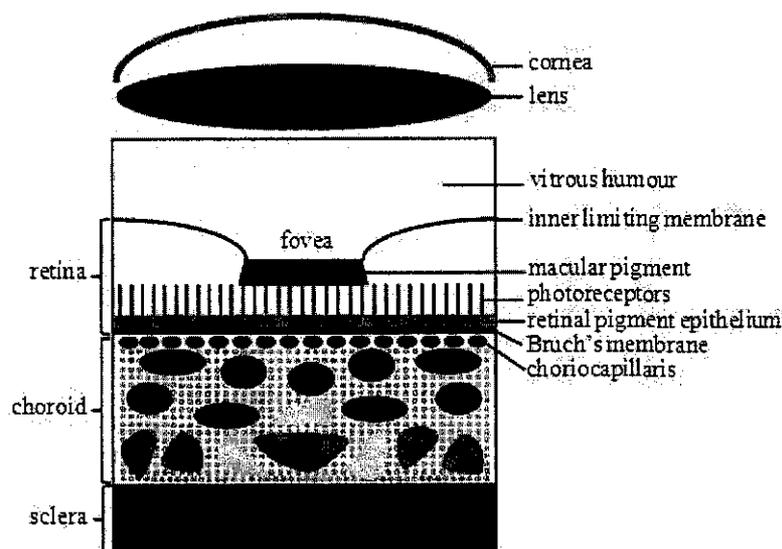


Figure 3.5 Diagrammatic cross-section of the eye

Figure 3.5 illustrates the eye in terms of layers. Whilst the ocular media consists of cornea, lens and vitreous humour; the ocular fundus comprises three main different layers - the retina, choroid, and sclera. The centre of the retina is called the macula that has a pale yellow pigmentation and is visible through an ophthalmoscope. The macula contains macular pigment (xanthophyll) - a mixture of three carotenoids, namely lutein, zeaxanthin and meso-zeaxanthin [182]. The distribution of xanthophyll is correlated to the concentration of photoreceptors which are composed of light-sensitive cells called the rods and cones, and also characterised by different sensitivity to light. Photoreceptor cells convert light into nerve signals that are sent to the brain through the optic nerves. The cones are smaller than rods and highly concentrated in the fovea located at the very centre of macula and responsible for central vision. The layers of other cells and blood vessels covering the peripheral retina dilute and disappear over the fovea, allowing uninterrupted exposure of the image. The rods do not exist in the fovea but dominate peripheral (non-central) vision.

Under photoreceptors is a dark layer called retinal pigment epithelium (RPE). The RPE contains melanin granules that absorb excess light and transport oxygen, nutrients and cellular wastes between the photoreceptors and choroid. The choroid is a layer of blood vessels containing a large amount of blood or haemoglobin that

supplies oxygen and nutrients to the outer layers of the retina. The innermost choroid called the choriocapillaris is a dense net of flattened capillaries that forms a blood-filled shell lying parallel to the basal side of the RPE. Bruch's membrane in turn separates the blood vessels of the choroid from the retinal pigment epithelium layer. The rest of the choroid is filled with larger blood vessels and melanin-containing melanocytes. The melanin content of the retinal pigment epithelium varies among individuals. However, only the melanin content of the choroid depends on skin pigmentation resulting in different eye colours among different ethnic groups. The choroidal layer also scatters light that originates from the underlying collagen tissues. The final layer of significance is the sclera - the fibrous, thick, white outer layer of the eyeball. The scleral layer, located underneath the choroidal layer and composed by collagen tissues reflects around 50% of the incident light [183]. Characteristics of the ocular fundus are strongly influenced by the absorption of light by melanin pigment in the RPE and choroid, by macular pigment in the fovea and by blood throughout the ocular fundus part as shown in Figure 3.5 [180]. Therefore, the appearance of the retinal fundus image depends on the presence of melanin, macular pigment and blood, which is characterised by haemoglobin.

Retinal pigments, i.e. macular pigment, melanin, and haemoglobin are present in the macular region. Macular pigment exists in the retinal layer [184] and melanin is distributed in the retinal pigment epithelium and the choroidal layer [185]. Haemoglobin meanwhile is contained in the blood distributed in the retinal blood vessels, namely arteries, veins, and capillaries. Figure 3.6 shows the spectral absorbance or optical density of macular pigment, melanin and haemoglobin in the visible spectrum [186].

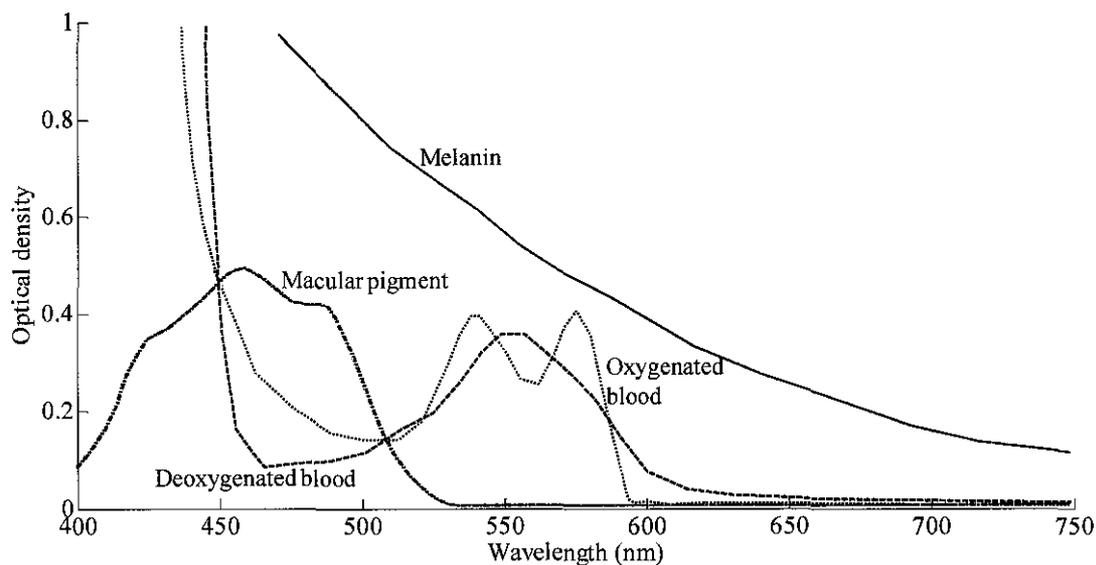


Figure 3.6 Optical density (spectral absorbance) of macular pigment, retinal blood (haemoglobin) and melanin based on data obtained from [186]

Figure 3.6 shows that the macular pigment optical density is 0.5 at 460 nm. Haemoglobin is almost transparent for wavelength $\lambda > 600$ nm. It causes the retinal blood vessels to present the greatest contrast from the surrounding retinal tissue in the spectral region from 540 to 580 nm. Haemoglobin in the blood can be oxygenated or deoxygenated. While oxygenated blood is closely related to arteries, deoxygenated blood corresponds to veins that are darker than arteries of similar calibre. However, the veins present low intensity reflectance throughout this spectral range. In the visible spectrum, oxygenated blood shows local maxima at 416, 542 and 577 nm and local minima at 510 and 560 nm, while deoxygenated blood shows a local minimum at 470 nm and a local maximum 559 nm. Contrast is diminished below 540 and for wavelengths it is greater than 580 nm. On its way through in the fundus, light is absorbed by blood in the retinal vessels, retinal capillaries and choroid. Yet, the light absorption in the capillaries is minimal due to their thickness, only 71.5 μm [186]. The melanin density is 0.8 at 500 nm in which its absorption spectrum decreases consistently with the increasing value of wavelength.

In general, melanin, macular pigment and haemoglobin that present in the ocular fundus affect the appearance of the fundus image due to light absorption by these components. As shown in Figure 3.6, these three components have different spectral

reflectance and do not interfere with each other. It means that the spectral reflectance or absorbance of these components is independent to each other. This characteristic is advantageous for the development of our non-invasive image enhancement technique in which the haemoglobin that relates to retinal blood vessels is separated from the other two components, i.e. melanin and macular pigment to obtain a high contrast of retinal blood vessels. To the best of our knowledge, this approach has never been implemented to solve the problem of low contrast of retinal blood vessels in colour retinal fundus image.

3.3 Light Interaction

The eye's optics limits the view of the fundus. In general, the retina is mostly invisible since most of the incident light is absorbed by the retinal tissues; only 5% is reflected [187]. To capture the retinal surface, the light must enter the eye and the reflected light must leave the retinal through the pupil. However, the cornea and lens have surface reflections that must be avoided.

The retinal fundus image is acquired using a fundus camera, a specialised low power microscope with an attached camera to capture the interior surface of the eye (i.e. fundus), consisting of the retina, optic disc, macula, and posterior pole. Optometrists, ophthalmologists, and trained medical professionals utilise fundus cameras to obtain retinal fundus images for monitoring progression, diagnosing and treating eye-related diseases, such as DR and DM.

A digital fundus camera acquires retinal fundus images by capturing the illumination reflected from the retinal surface. The principle of fundus cameras as shown in Figure 3.7 is similar to that of indirect ophthalmoscopy in which the illumination and imaging systems follow dissimilar paths surface [188]. The only difference is that the observer's eye in indirect ophthalmoscopy is now replaced by a camera as a sensor to photograph the fundus on a film or to capture as a digital image.

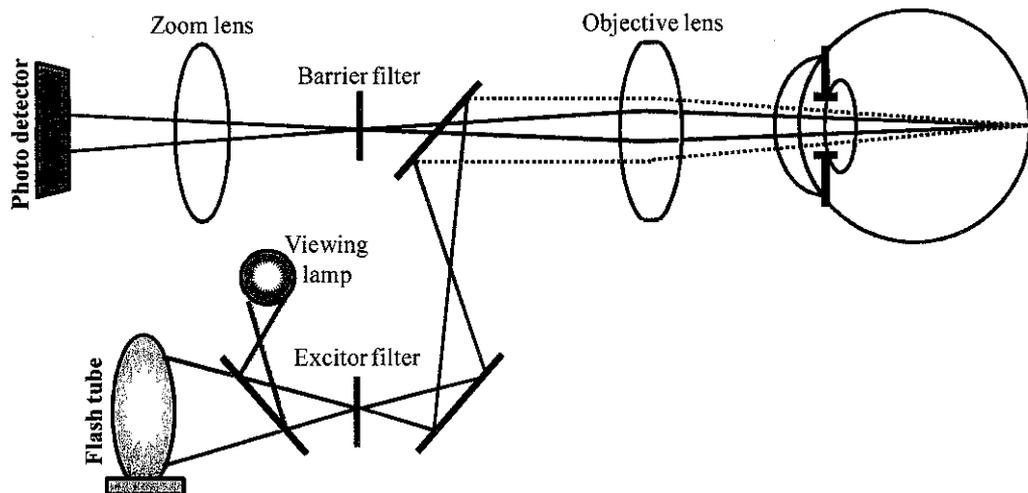


Figure 3.7 diagram of principle of fundus camera reproduced from [188]

A fundus camera is a complex optical system that provides an upright, magnified view of the retina of the eye. Unlike indirect ophthalmoscope which uses only one source of illumination, the fundus camera is equipped with two illumination systems, i.e. flash tube for flash photography and viewing lamp for observation. Both of these lights follow the same path through any further optics in the illumination system. The sources of these two light are required since the intensity of light used for visual observation of the retinal surface is not sufficient for photographing the image of retinal surface. In comparison to fundus camera, the use of only one source of illumination in indirect ophthalmoscope has become a major drawback, i.e. prolonged exposure to high intensity indirect ophthalmoscope illumination. Applying prolonged exposure of sufficient intensity for taking an image however can cause patient's discomfort and possibly lead to the damage of the retina. The illumination system passes the light from the source to the retinal surface through a condensing lens.

The condensing lens has two main objectives. First, it projects the illuminated light to form a ring-like illumination at the pupil allowing the retinal surface to be illuminated through the outer part of the pupil. The ring-like illumination shown in Figure 3.8 has the imaging pupil or exit aperture used for imaging path and illumination annulus or entrance aperture used for illumination path that are separated by a buffer. Moreover, the entrance aperture with radius R_{il} is larger than the exit aperture with radius R_{im} .

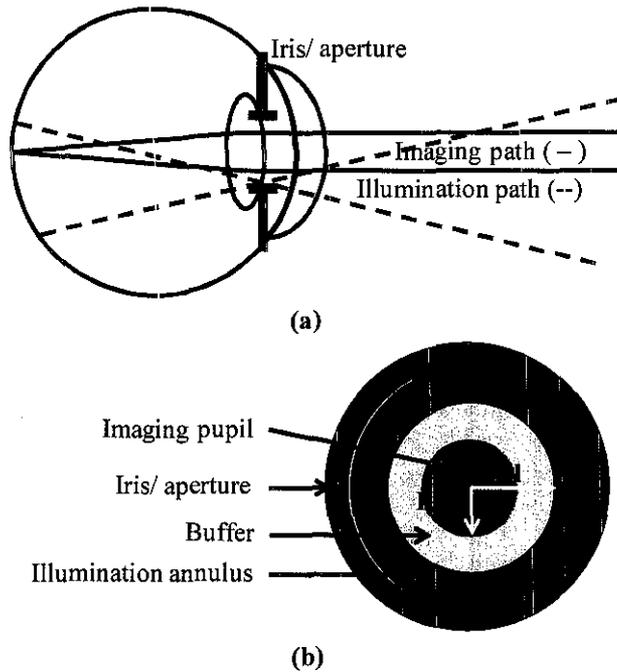


Figure 3.8 Fundus illumination and imaging paths using a fundus camera from (a) side view and (b) front view

Second, the converging lens collects the reflected diverging light from the retinal surface and passes it to further optics to form an image. The field of view (FOV) of the retinal surface is determined by the ratio of the condensing lens and its focal length. A typical fundus camera can cover a FOV of retinal area from 20 to 60 degrees with a magnification of around 2.5 times. A modification can be made via additional zoom lens such as wide angle lens to extend the FOV from 15 to 140 degrees with a magnification of around 5 times.

Dissimilar paths between illumination and imaging are necessary to provide optimum illumination to the retina as well as to minimise the reflection of the light sources captured in the acquired image. Two filters, i.e. barrier and excitor, are used to eliminate back reflections from the zoom lens and the condensing lens, respectively by absorbing the back reflected light.

As shown in the principle of fundus camera from Figure 3.7, the light pathways in the human fundus is determined when a light ray enters the eye, passes the ocular media and a series of layers in the retina and eventually strikes the opaque white sclera in the back of the eye. The acquired retinal fundus image shows a different

intensity of reflectance that depends on the wavelength, architecture of fundus' layer, optical densities and quantities of retinal pigments in the ocular fundus. Optical density or absorbance, $A(\lambda)$ at a given wavelength λ is defined as a log expression of a ratio between the intensity of incident light I_0 and the intensity of light $I(\lambda)$ at a specified wavelength λ that passed through a substance. Opposed to the definition of the absorbance, transmittance, $T(\lambda)$ of an optical element for a given wavelength λ is defined as a fraction of incident light I_0 that passed through a substance. These aforementioned definitions can be formulated as

$$A(\lambda) = \log_{10} \left(\frac{I_0(\lambda)}{I(\lambda)} \right) \quad (3-1)$$

$$T(\lambda) = \frac{I(\lambda)}{I_0(\lambda)} \quad (3-2)$$

The higher the optical density (absorbance) is, the lower the transmittance is. The incident light from a fundus camera can be reflected, absorbed, scattered or transmitted by the retinal tissues. The differences in the light interaction of any fundus' pigment or tissue can be quantified to determine the components of ocular fundus based on their reflectance.

Berendschot *et al.* [186] comprehensively summarised several important works in fundus reflectance and provided the simplest model for the fundus reflectance where the entire incident light is transmitted by the retinal and choroidal layers, reflected by the sclera and retransmitted by the choroid and retina. This reflected light is captured by the fundus camera and forms the colour retinal fundus image. The reflectance, $R(\lambda)$, is given by

$$R(\lambda) = R_{sclera}(\lambda) 10^{-2D_{tot}(\lambda)} \quad (3-3)$$

$R_{sclera}(\lambda)$ is the reflectance of the sclera and $D_{tot}(\lambda)$ is the total optical density of all the absorbers, through which the light has passed.

One of the important works on light interaction of the ocular fundus was

conducted by van Norren and Tiemeijer [189]. Van Norren and Tiemeijer modelled a light interaction in the ocular fundus for foveal fundus reflection with two spectrally neutral reflectors (the sclera and a reflector) located anteriorly to the retinal pigment epithelium but posteriorly to the macular pigment. A schematic presentation of van Norren and Tiemeijer model is shown in Figure 3.9.

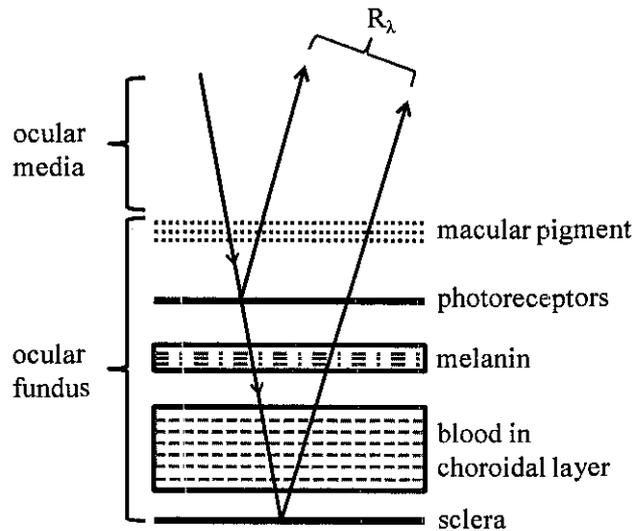


Figure 3.9 Schematic presentations of the van Norren and Tiemeijer model

As shown in Figure 3.9, incident light enters the eye from the top passing through several layers in the ocular media and in the ocular fundus. The incident light is reflected by different layers emerging from the eye represented by upward pointing arrows and is subsequently detected by a sensor. The model used four parameters acting as spectral absorbers, i.e. the lens which is part of ocular media, macular pigment, melanin and blood.

A modification to van Norren and Tiemeijer model has been proposed by Delori and Pflibsen [180]. Delori and Pflibsen model includes light scattering in the choroid and comprises a scleral reflector, an absorbing-scattering layer simulating the choroid, a blood layer for the choriocapillaris, a melanin layer for the retinal pigment epithelium, and a spectrally neutral reflector. In this model, the choroid was simulated by a homogeneous scattering layer, in which blood and melanin are uniformly distributed. The results gave more realistic data for melanin and blood in a physiological sense than the van Norren and Tiemeijer data. Moreover, Orihuela *et*

al. showed that fundus colour are related to spectral reflectance of the ocular fundus [190].

Based on the aforementioned explanation, in van Norren and Tiemeijer model, incident light passing through the ocular fundus is absorbed by three components, namely macular pigment, melanin and blood. This model of light interaction with several fundus layers has been improved in the Delori and Pflibsen model by taking into account the presence of these three components in every possible layer mainly in the ocular fundus. In general, both these models describe the reflectance of the fundus in the terms of the retinal layers. Figure 3.10 depicts a model of ocular fundus showing possible pathways of the remitted light based on the presence of melanin, macular pigment and haemoglobin, which is related to the blood in the ocular fundus layers. As a result, slight changes of the biological structure and retinal pigment construction lead to variation in colour of the fundus [191]. Therefore, it is necessary to understand the colour retinal fundus image based on the structure and pigment construction to model fundus spectral absorbance image.

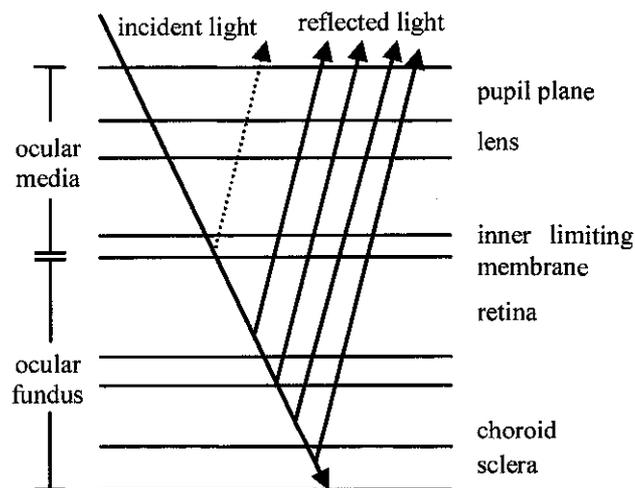


Figure 3.10 A model of ocular fundus showing light propagation

From the principle of fundus camera, providing adequate illumination is the main limiting factor of the fundus camera. The illuminating light goes through a small pupillary aperture (which sometimes needs to be fully dilated) reaching the retinal layers until the bottom layer of the retina called the sclera. The light is then reflected

passing through several fundus layers and finally captured by the sensor. However, the size of the pupil affects the amount of the illuminating light that can reach the retinal layers and the reflected light from the retinal surface varies due to spherical surface of the retina. Both pupil size and spherical surface of the retina therefore influence the characteristic of the reflected light and lead to varied contrast of the acquired colour retinal fundus image.

Moreover, as previously discussed in the light interaction with several ocular fundus layers based on the presence of macular pigment, haemoglobin and melanin, it can be inferred that the colour of the retinal fundus image is a mixture between three retinal pigments, i.e. macular pigment, haemoglobin and melanin as illustrated in Figure 3.11. The differences in the optical density between these retinal pigments influence the reflected light and significantly affect the colour of the acquired retinal fundus image. This subsequently results in the low contrast of a specific retinal pigment, i.e. haemoglobin that exists in the retinal capillaries and distributed in the choroidal layers.

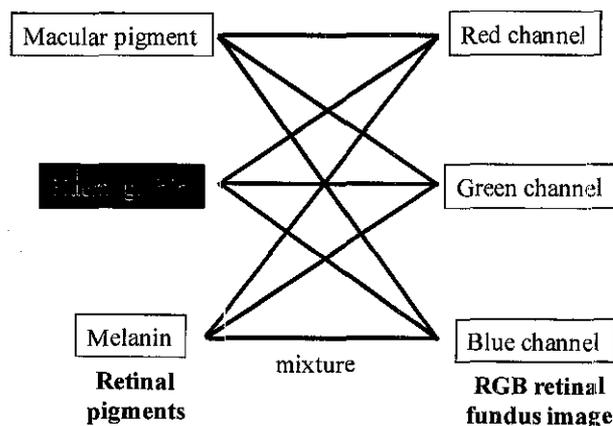


Figure 3.11 Retinal pigments are mixed in the colour retinal fundus image

3.4 Retinal Fundus Image Models

In this research, 44 fundus images from FINDeRS database, taken using nonmydriatic fundus camera *Kowa nonmyd 7* as shown in Figure 3.12 and containing macular region, are used to develop three fundus image models. Compared with several other image enhancement algorithms, those image models are used to test the performance

of the proposed image enhancement method algorithm. In each fundus image, areas of macular pigment, retinal vessels and melanin are sampled and their normalised intensity distributions are used to model retinal fundus image.



Figure 3.12 Nonmydriatic fundus camera Kowa 7 used to capture colour retinal fundus images

The objective of this sampling is to develop an intensity distribution of the components, i.e. melanin, macular pigment and haemoglobin for the colour fundus image model. The sampling method is conducted by selecting several random colour fundus images. In each image, areas of macular pigment, retinal vessels and melanin are sampled and their intensity distributions are used to model retinal fundus image. Ideally, the greater the number of sample size, the better the sample in representing the population. Therefore, it is important to determine the minimum sample size for a specific parameter required. The sample size is determined to a specific level of significant and margin of error using Cochran's formula as follows [192-193],

$$n = \left(\frac{Z_{\alpha/2} \sigma}{E} \right)^2 \quad (3-4)$$

where n is the sample size, σ is the estimated population standard deviation and α is the required significant level. In the case of the standard normal distribution, $Z_{\alpha/2}$ is the critical sample value that will produce the required significant level, α . The error (E) between population and sample mean is set to a maximum of 1% of the intensity range of a specific class. Each point of sample is determined as pixel intensity of the

corresponding component in each channel. Whilst the minimum sample size is calculated using (3-4), the sample size obtained shows the number of pixels collected to develop the colour retinal fundus image model. These pixel intensities are collected from 44 random colour retinal fundus images. A calculation of minimum sample size along with their corresponding sample size obtained for modelling of retinal fundus image model is shown in Table 3-1.

Table 3-1 Comparison between minimum sample size and sample size obtained of the component in each colour channel

Component	Colour channel	Significant level	$Z_{\alpha/2}$	Error (E)	Standard dev. (σ)	Min. sample size (N)	Sample size obtained
Melanin	Red	0.025	2.241	0.50	25.660	13318.50	108203
	Green	0.025	2.241	0.50	22.129	9982.90	108203
	Blue	0.025	2.241	0.50	20.358	8399.60	108203
Macular pigment	Red	0.025	2.241	0.50	32.547	21574.40	34769
	Green	0.025	2.241	0.50	15.644	4865.60	34769
	Blue	0.025	2.2414	0.50	6.32	803.30	34769
Haemoglobin	Red	0.025	2.2414	1.00	29.79	4457.50	4462
	Green	0.025	2.2414	1.00	18.09	1643.50	4462
	Blue	0.025	2.2414	0.75	11.09	1070.50	4462

As shown in Table 3-1, each component has different minimum sample size. Based on these minimum numbers, the collected sample can now be determined whether its sample size is sufficient. The comparison in Table 3-1 shows that the sample size obtained is greater than the minimum sample size calculated; hence, the data sample size is sufficient for modelling of colour retinal fundus image. Therefore, these 44 random colour retinal fundus images are considered to be sufficient for statistical measurement.

In colour retinal fundus images, the lowest contrast of retinal blood vessels is shown by retinal capillaries in the macular region that will be used to determine the foveal avascular zone. For this, the optical angle of the fundus camera was set to capture 45° colour fundus image with an internal fixation target on the central showing the centre on the macula. The quality of the captured images depends on the attached external digital camera. This fundus camera is equipped with external Nikon D-80 digital camera that can capture images with resolution of 3872 x 2592 pixels or up to 10 mega pixels. However, in this research work, the image resolution used is

1936 x 1296 pixels to reduce the processing time.

Theoretically, the diameter of retinal blood vessel ranges from 60 μm to 1600 μm , the largest diameter of which belongs to the inferior temporal vein [194]. Based on our direct observation on the colour retinal fundus image with resolution 1936 x 1296, the largest diameter of inferior temporal vein estimated could be around 25 pixels as shown in Figure 3.13. Assuming that the 25 pixel of retinal blood vessels equals to 1600 μm , it is found that one pixel represents 64 μm which is 4 μm different from its expected value. Hence, the use of colour retinal fundus image at this current resolution yields 0.93 for accuracy. The accuracy can be increased by increasing image resolution; however, it predictably will increase the processing time. Nikon D-80 attached to the fundus camera is able to produce resolution up to 10 mega pixels - four times larger than the current resolution.

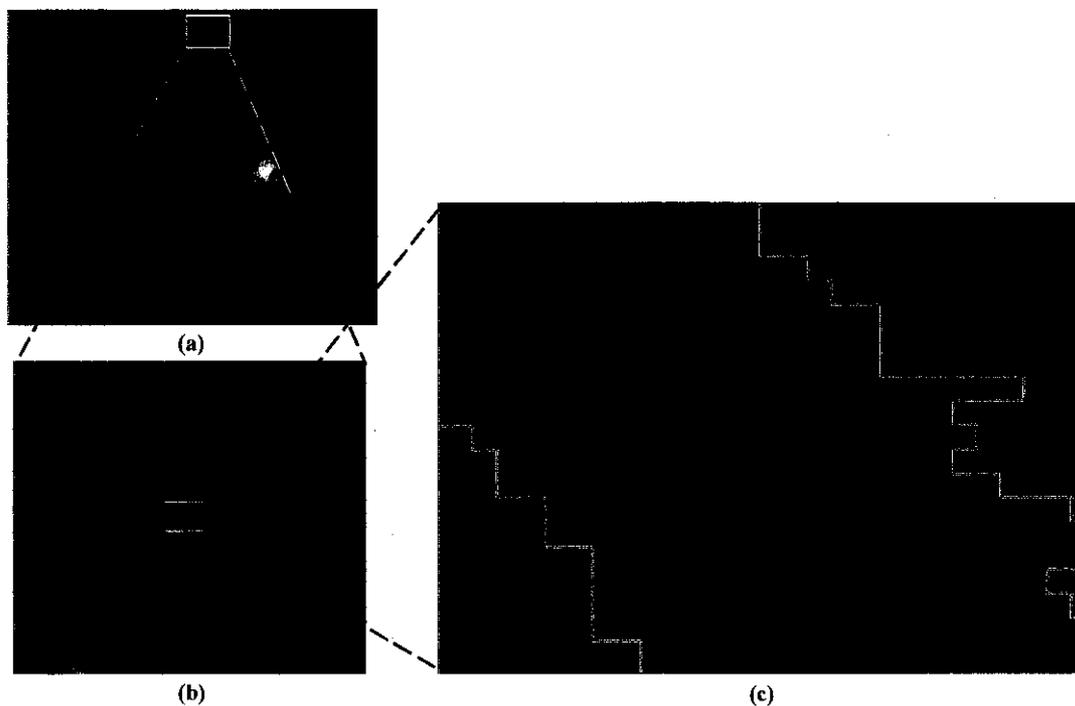


Figure 3.13 (a) An example of retinal colour fundus image with (b) a sample of inferior temporal retinal blood vessels and (c) pixel's intensities of the corresponding areas

Assuming that the 25 pixel of retinal blood vessels equals to 1600 μm , it is found that one pixel represents 64 μm which is 4 μm different from its expected value. Hence, the use of colour retinal fundus image at this current resolution yields 0.93 for

accuracy. The accuracy can be increased by increasing image resolution; however, it predictably will increase the processing time. Nikon D-80 attached to the fundus camera is able to produce resolution up to 10 mega pixels - four times larger than the current resolution.

A simulation has been conducted to calculate the processing time of the enhancement of two image models with different resolution at several numbers of iteration. The objective of the simulation is to show the effect of increasing resolution to the processing time. Adapted from typical size of macular region, the first image model has a resolution of 320x320 pixels and the second one has four times larger resolution that is 1280 x 1280 pixels. Figure 3.14 shows two image models being subjected to the proposed image enhancement method and a comparison of processing time.

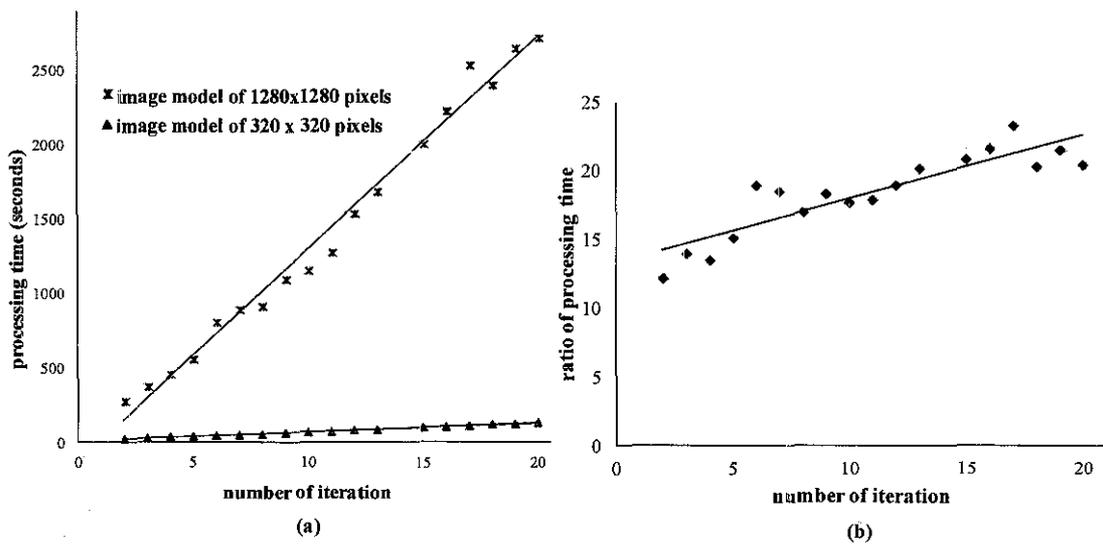


Figure 3.14 (a) Processing time of two images with different resolution at several numbers of iteration, (b) ratio between processing time of the two image models

As illustrated in Figure 3.14(a), an increase of the number of iteration of the proposed enhancement method results in a linear increase in processing time for both image models. However, image model with higher resolution has significantly higher processing time of around fifteen to twenty times than that of the lower resolution as shown in Figure 3.14(b). Considering more calculation in the proposed image enhancement method and the speed of computer to process, a significant increase in processing time comes to be expected. In this research, the computer uses Intel Core

i5-460 2.53 GHz and 4 GB DDR3 as its processor and memory respectively. Based on the aforementioned results, the four-time increase in resolution is not proportional for the increase in the processing time, i.e. fifteen times at the minimum. Therefore, to increase the resolution for higher accuracy in detecting retinal blood vessels is not efficient.

Another experiment to measure the width of retinal blood vessels (in pixels) specifically in macular region from a colour retinal fundus image with resolution of 1936 x 1296 shows that the current resolution is sufficient to reveal the smallest width of retinal blood vessels. The example of colour fundus image shown in Figure 3.15(a) underwent the proposed image enhancement method on its macular region (Figure 3.15 (b)) with samples of pixel's intensities of the corresponding areas (Figure 3.15 (c), (d) and (e)).

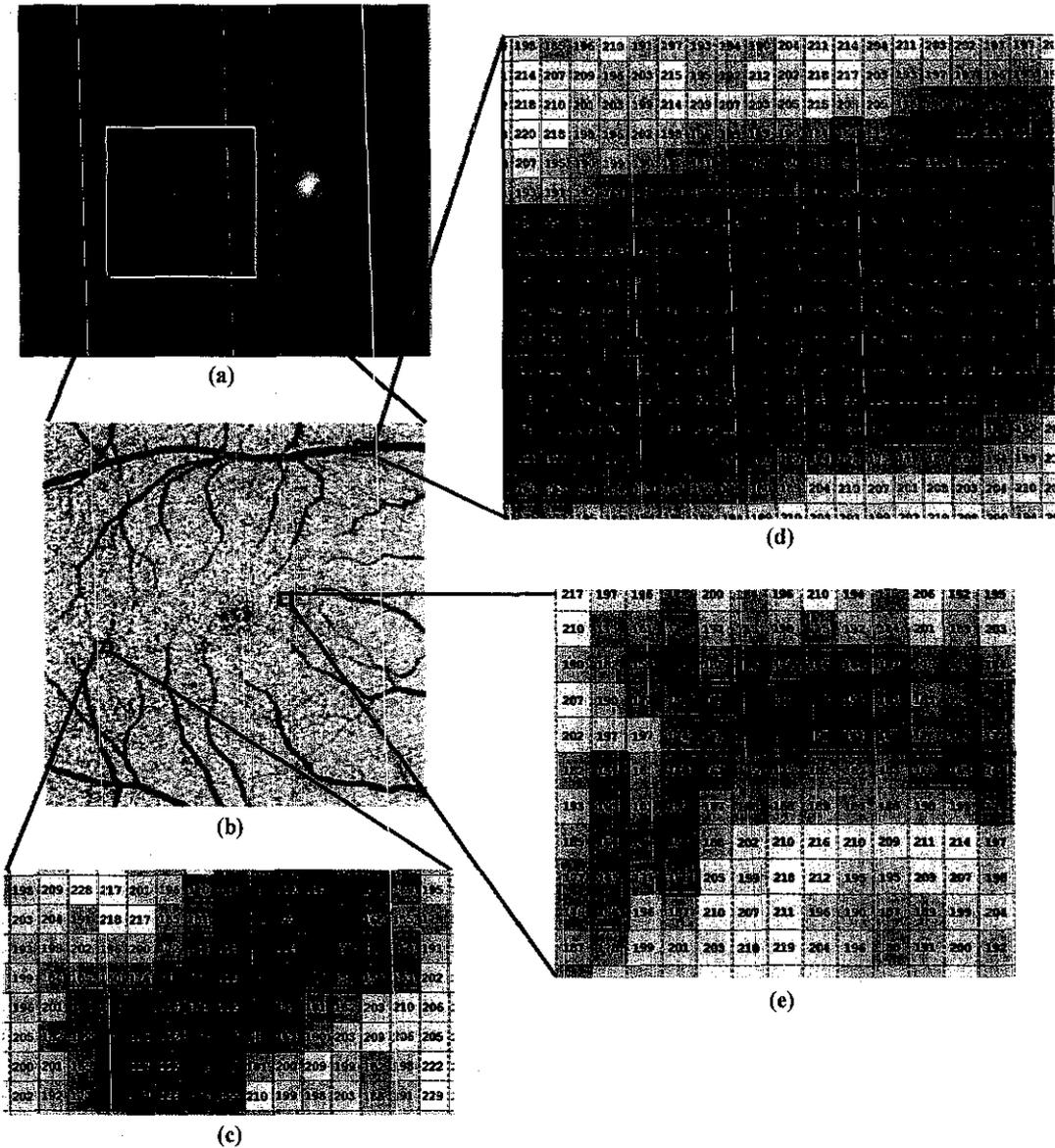


Figure 3.15 (a) An example of retinal colour fundus image with (b) its cropped macular region and (c), (d) and (e) show pixel's intensities of the corresponding areas

From the three different selected retinal blood vessels in the macular region (Figure 3.15 (b)) with their corresponding pixel intensities, the width of retinal blood vessels is estimated to be from 1 to 13 pixels in range as shown in Figure 3.15(c) to Figure 3.15(e). This range will be used in the development of colour fundus image models. The increase of the current resolution will also increase the width of retinal blood vessels. In this case, the range of width of retinal blood vessels is expected to expand from 4 to 52 pixels. The advantage is that the small objects, i.e. retinal capillaries can be more clearly noticed resulting in greater accuracy in detecting

retinal blood vessels. However, it also causes a major disadvantage for, as previously discussed, the significantly increasing processing time. Besides its long processing time, the smallest width of retinal blood vessels has already been able to be detected as small as one pixel with this current resolution. As the smallest width of retinal blood vessels equals to one pixel, the use colour fundus image with this current resolution comes to be sufficient. In other words, it is not efficient to increase the current resolution (1936 x 1296 pixels) into the higher or even the highest resolution that can be produced by Nikon D-80 in order to increase the accuracy in detecting retinal blood vessels. Moreover, in the proposed image enhancement method, the number of iteration is automatically determined and will be discussed in Chapter 4 (Section 4.2).

There are three fundus image models, i.e. (1) varied contrast image model, (2) low contrast image model and (3) varied and low contrast image model to be developed to deal with the problem of varied and low contrast. The problem of varied contrast and low contrast is investigated separately using the first and the second image models respectively. The third image model is used to deal with the problem of both varied and low contrast.

To model fundus images, 44 fundus images are randomly selected from FINDeRS database. As previously discussed, there are three components – macular pigment, melanin and haemoglobin – that significantly influence the appearance of colour retinal fundus images. For modelling, these three components are estimated from the real colour retinal fundus images. Whilst the macular pigment is estimated from the centre area of the retina, the haemoglobin and the melanin are estimated from the sample of retinal blood vessels and the background, respectively. An example of colour retinal fundus images showing the selection of these three components is shown in Figure 3.16.

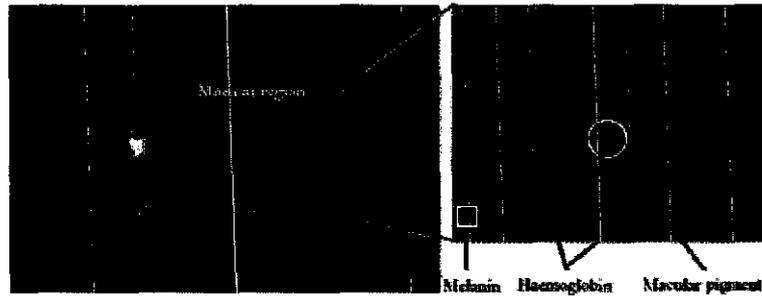


Figure 3.16 A colour retinal fundus image with enlarged macular region

The statistics of macular pigment, haemoglobin and melanin from three channels, i.e. red, green and blue are shown in Table 3-2.

Table 3-2 Statistical data of macular pigment, haemoglobin and melanin intensities in RGB channels

	Macular pigment			Haemoglobin			Melanin		
	R	G	B	R	G	B	R	G	B
mean	93.40	46.21	7.77	120.88	62.21	15.64	158.16	95.93	35.29
stdev	37.76	17.656	6.21	34.23	20.37	11.45	29.44	25.20	22.07
min	0	0	0	18	0	0	35	0	0
max	228	124	33	227	115	55	255	197	120
skewness	0.048	0.0796	0.695	-0.036	-0.066	0.416	-0.045	-0.026	0.232
kurtosis	-0.107	0.056	-0.016	-0.018	0.025	-0.363	0.022	0.167	-0.416

From Table 3-2, it can be seen that the intensity means of the three components are different in each colour channel. The macular pigment and melanin have the lowest and the highest mean respectively. The difference in intensity mean of macular pigment, haemoglobin and melanin is expected due to difference in spectral absorbance of these three components as previously discussed in Section 3.2. The difference is advantageous for further confirming the possibility to separate these three components. Standard deviation and minimum-maximum intensities vary among these three components. Standard deviations and intensity ranges shown in Table 3-2 indicate the homogeneity of intensity distribution of each component in each channel. A low standard deviation implies that intensity distribution tends to centre on the mean indicating a more homogeneous intensity distribution. Conversely, a high standard deviation implies that data intensities are spread out over a large range of values indicating a more inhomogeneous intensity distribution. The variation of standard deviation and intensity range is expected and implies that the contrast of the retinal fundus image is varied. Like standard deviation, the highest

intensity range belongs to the red channel followed by the green and the blue channel. It implies that intensity variation mostly occurs in the red channels rather than in the other two colour channels. Nevertheless, the overlap of intensity ranges between the components is one of the problems in the separation process that will be discussed in Chapter 4 (Section 4.3). The minimum and maximum of intensity are important to set up the intensity range of the varied contrast fundus image model that will be developed in the next section. Moreover, skewness and kurtosis of the components show that the intensities of the three components tend to have normal (Gaussian) distribution. This is expected since the data intensities of the three components are sampled from real colour fundus images. Probability density functions (pdfs) of the components are used to develop the low contrast fundus image model that will be discussed in Section 3.4.2. Statistics of the components shown in Table 3-2 is important to characterise the intensity distribution of samples used in the development of varied contrast and low-contrast image models based on the real colour fundus images.

3.4.1 Varied Contrast Image Model

Varied contrast image model is developed to evaluate the proposed algorithm in dealing with the problem of varied contrast. Varied contrast in an image is characterised by spurious smooth variation of image intensities. Variation of image intensities is mainly due to the effect of illumination. Illumination will determine the lightness of an image. Land showed that the relationship between reflectance and lightness is not linear but, generally can be approximated with cube root, square root and logarithmic functions [119]. In this research, smooth variation of image intensities is modelled using a mathematical function

$$Y = k.X^{\alpha} \tag{3-5}$$

with k and α are some constants. The above function is a general function in which cube root and square root are obtained for α equal to $\frac{1}{3}$ and $\frac{1}{2}$. A smooth image intensity variation $i(x)$ as a function of pixel's position x is mathematically

formulated as

$$i(x) = k \cdot x^\alpha \quad (3-6)$$

Using the statistics of the samples as shown in Table 3-2, the mean \bar{I} and the standard deviation σ of image intensities are used to model smooth variation of image intensity $i(x)$ so that $i_{\min} = \bar{I} - 2\sigma$ and $i_{\max} = \bar{I} + 2\sigma$. The value of $\bar{I} \pm 2\sigma$ is chosen for i_{\min} and i_{\max} instead of minimum and maximum intensity values due to the problem of extreme values (outliers) raised by the use of minimum and maximum intensity values. Moreover, the range $\bar{I} \pm 2\sigma$ covers 95% of all possible values [195]. Whilst the value of x represents the position of specific pixel in the image, the value of i has the range as follow:-

$$[i_{\min}, i_{\max}] = [k \cdot x_{\min}^\alpha, k \cdot x_{\max}^\alpha] \quad (3-7)$$

Having known i_{\min} , i_{\max} , x_{\min} and x_{\max} , the constants k and α can be obtained for the three components on each red, green and blue channel based on the collected data from 44 retinal fundus images as shown in Table 3-3.

Table 3-3 Constants k and α obtained for macular pigment, haemoglobin and melanin in RGB channels

	Macular pigment		Haemoglobin		Melanin	
	k	α	k	α	K	α
Red	17	0.453	53	0.263	100	0.152
Green	10	0.415	22	0.3177	46	0.228
Blue	1	0.590	1	0.753	1	0.861

A difference in constants of k and α obtained for macular pigment, haemoglobin and melanin in RGB channels is expected considering a difference in statistical values (mean, standard deviation and intensity range) among the three components. These constants in turn will affect the intensity variation of the components in the varied contrast fundus image model. Applying the obtained constants on (3-6), the function $i(x)$ showing variation of image intensities based on pixel's position x for macular pigment, melanin and haemoglobin in each colour channel can be generated as shown in Figure 3.17.

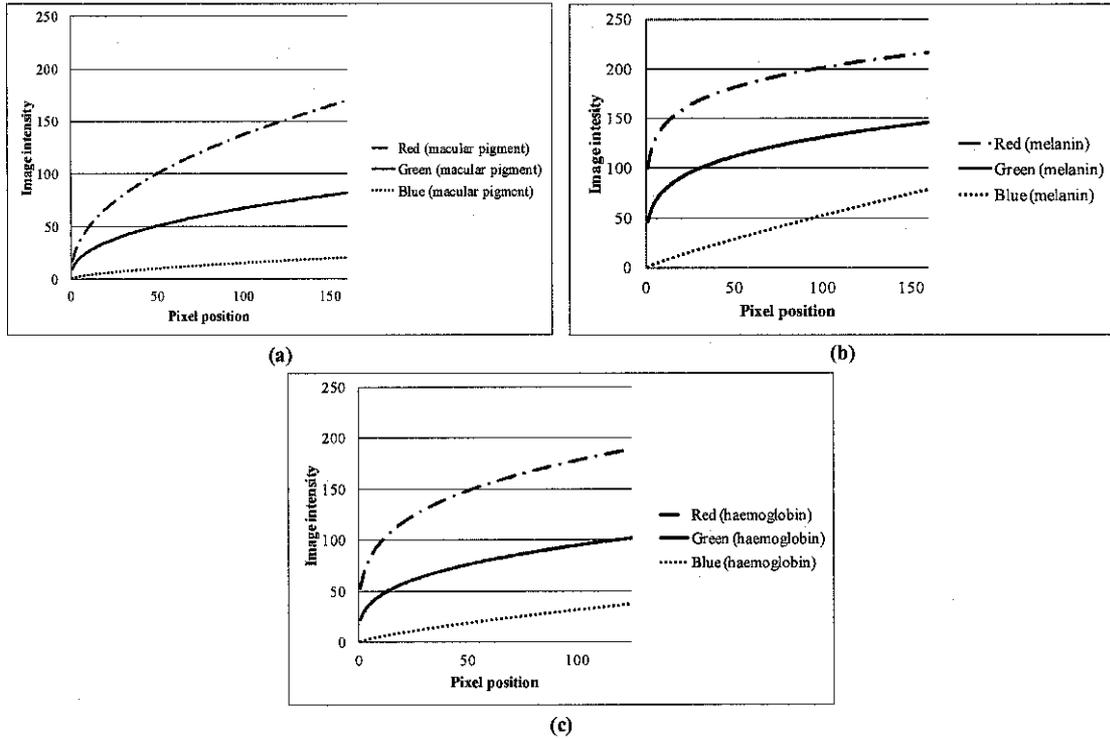


Figure 3.17 Image intensity variation $i(x)$ as a function of pixel's position x for (a) Macular pigment, (b) Haemoglobin and (c) Melanin on each red, green and blue channel

As shown in the graphs from Figure 3.17, image intensities increase as the pixel position increases. The increase in intensity variation is expected due to intensity ranges of the sample distribution and a result of applying (3-6). The greater the intensity range is, the greater the increase of intensity will be. The variation of image intensities occurs in a vertical profile line in the image model. In the image model, a pixel position is vertically set up from 0 started at the top of the image to 160 at the bottom of the image for macular pigment and melanin. For haemoglobin, the pixel position at the bottom of the image is set up to 125. The choice of these lengths is determined by the size of the related components, i.e. macular pigment, melanin and haemoglobin in the developed fundus image model. Two fundus image models of 160x160 pixels showing the variations of image intensities for macular pigment and melanin and one fundus image model of 125x125 pixels showing the variations of image intensities for haemoglobin are depicted in Figure 3.18.

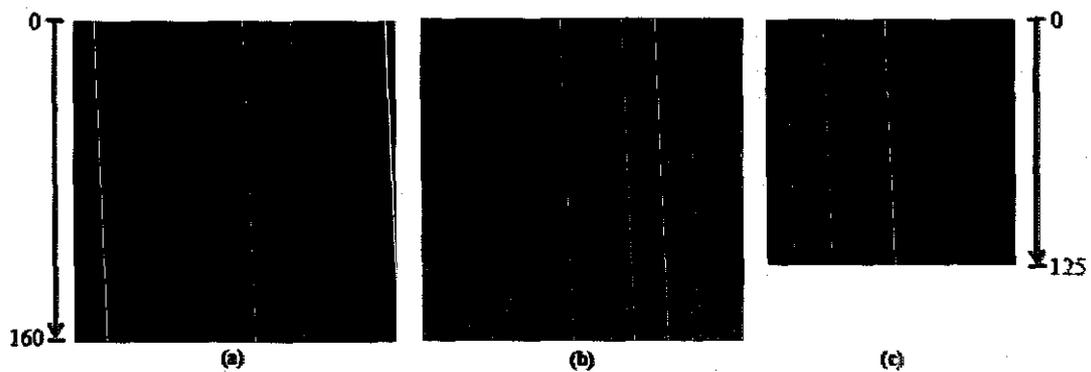


Figure 3.18 Variation of image intensities in fundus image models for (a) Macular pigment, (b) Melanin and (c) Haemoglobin with the referred vertical pixel position

As shown in Figure 3.18, the image intensities increase as the pixel position increases vertically. In the image model, each vertical line shows an equal variation of intensities. Since the image model is square, for instance, in the image model of macular pigment, there are 160 equal vertical lines containing 160 pixels each used to form the image model. In other words, each horizontal profile line consists of 160 same pixel intensity values. The highest intensity value belongs to the pixels positioned at the top of the image. Reversely, the lowest intensity value belongs to the pixels laid at the bottom of the image. Therefore, the image models look darkest at the top and brightest at the bottom of the image. The variation of these image intensities for macular pigment, melanin and haemoglobin is then used to model the varied contrast fundus image model where all of these components appear in one image.

The varied contrast image model of 320 x 320 pixels represents the macular region and its surrounding. As previously mentioned, the selection of resolution for the fundus image model – 320 x 320 pixels – is determined based on the resolution of typical macular region in colour fundus image with resolution of 1936 x 1296 pixels. The image model consists of three components, i.e. macular pigment, haemoglobin and melanin. In the real fundus image, retinal blood vessels where the haemoglobin is fairly distributed exist in both the fovea where the macular pigment are fairly distributed and the background where the melanin is fairly distributed. The area of the fundus image model is divided into two, i.e. top half of the image model

representing the fovea and bottom half of the image model representing the background. Retinal blood vessels are modelled in 9 straight lines with the same height parallel to each other with the width ranges from 1 to 13 pixels representing the width of retinal blood vessels from the real retinal fundus image. Whilst the thin lines represents the retinal capillaries where mostly exists in the macular region, the wider lines represents wider blood vessels where mainly exist in the background. A varied contrast fundus image model is shown in Figure 3.19.

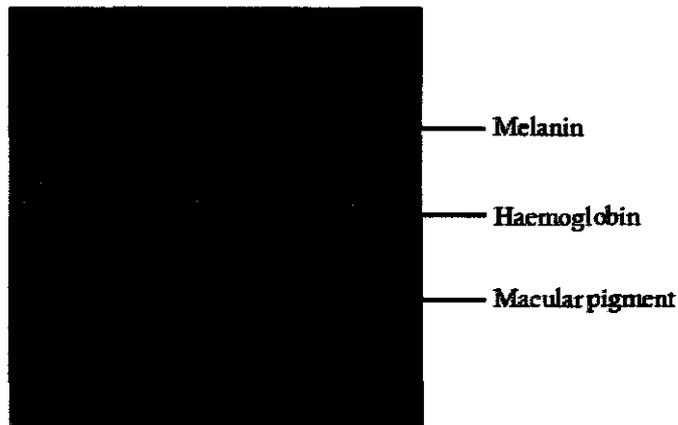


Figure 3.19 Varied contrast fundus image model

The varied contrast fundus image model as illustrated in Figure 3.19 is developed by applying (3-5) to generate the function of image intensity variation of macular pigment, haemoglobin and melanin. In the varied contrast image model, the melanin has the lowest intensity value at the top of the image. The melanin intensity increases as the pixel position moves down and reaches the highest value towards the middle of the image where the pixel position is 160 as depicted in Figure 3.20.

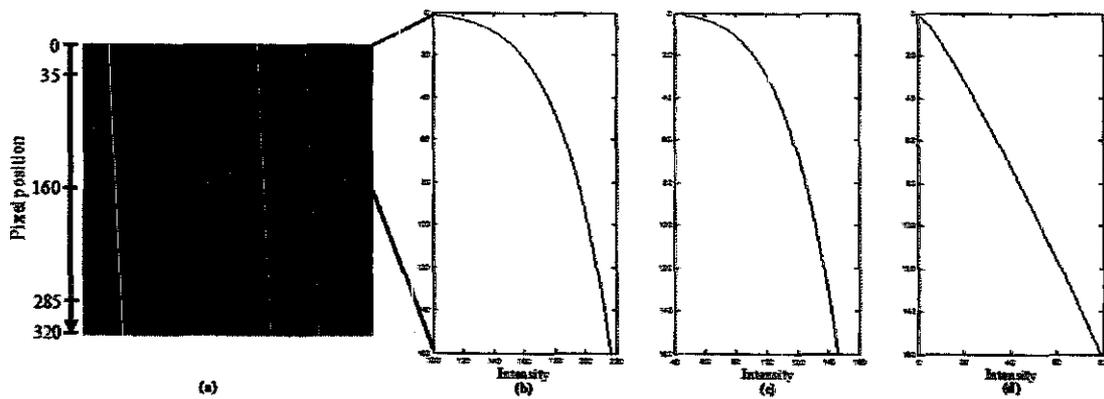


Figure 3.20 (a) Varied contrast fundus image model and its related intensity variation of melanin in (b) red, (c) green and (d) blue channels

The three graphs shown in Figure 3.20 illustrate the variation of image intensities of melanin in a vertical profile line for each colour channel. The same as that of shown in Figure 3.20(c), these graphs show the lowest intensity value at the top of the image model where the pixel position is 0 as referred in Figure 3.20(a). In this image model, each horizontal profile line of the image is filled with the equal pixel intensity values; hence, the variation of image intensity appears vertically from the top of the image to the middle of the image.

For the haemoglobin that represents the blood vessels model, its intensity in the retinal fundus image model is varied leading both melanin and macular pigment as the backgrounds to contain 12 lines of blood vessel model. The total length of each blood vessel model is 250 pixels and divided into two so that each background contains 125 pixel length of blood vessel model. For the blood vessels, the highest intensity value belongs to the pixels of the haemoglobin that are laid in the middle of the image where the pixel position is 160. The intensity value decreases as the pixel position vertically moves both up and down. The lowest intensity value meanwhile belongs to the pixels position at 35 as it moves up and to that of at 285 as it moves down. The details of the intensity variation for haemoglobin are shown in Figure 3.21.

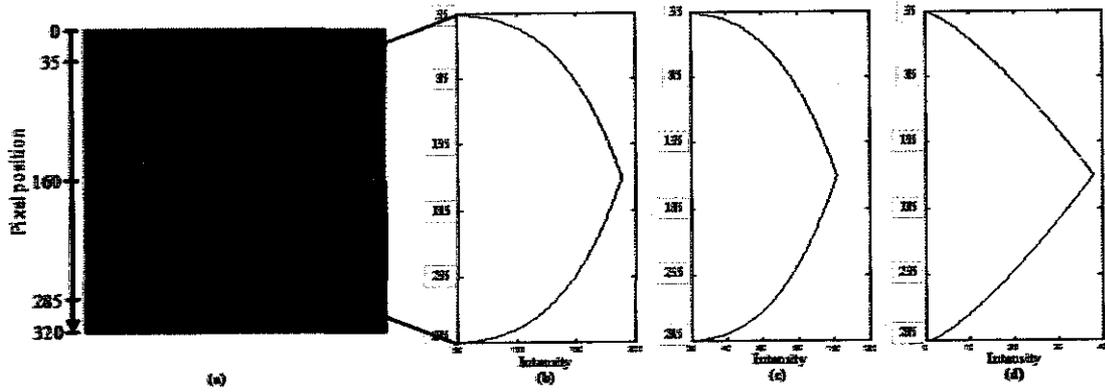


Figure 3.21 Varied contrast fundus image model and its related intensity variation of haemoglobin in (b) red, (c) green and (d) blue channels

Unlike that of the melanin, the intensity of the macular pigment has the highest value at the middle of the image model. The intensity value decreases as the pixels position vertically increases and reaches its maximum value for the pixels located at the bottom of the image model as depicted in Figure 3.22.

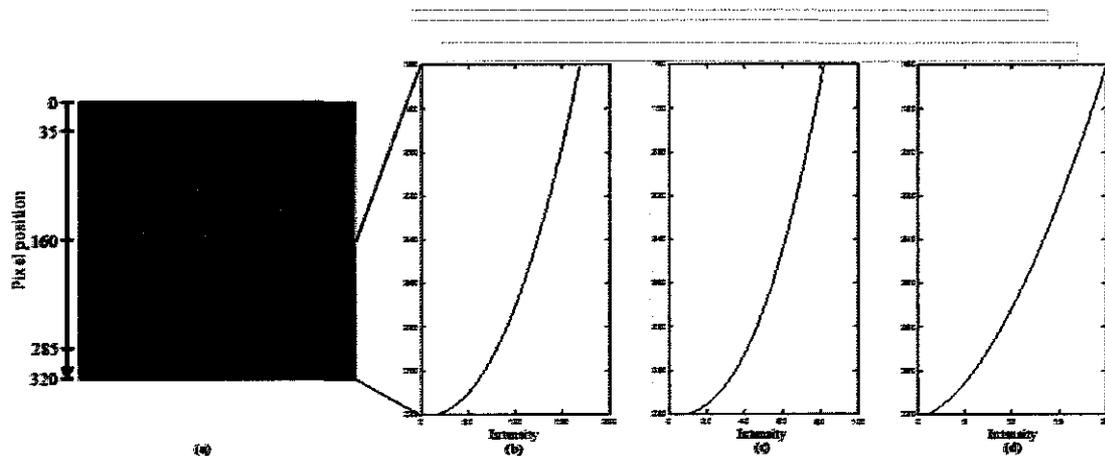


Figure 3.22 Varied contrast fundus image model and its related intensity variation of macular pigment in (b) red, (c) green and (d) blue channels

3.4.2 Low Contrast Image Model

Based on the 44 collected image samples and the statistics shown in Table 3-2, normalised intensity distributions of the samples, i.e. macular pigment, haemoglobin and melanin are shown in Figure 3.23.

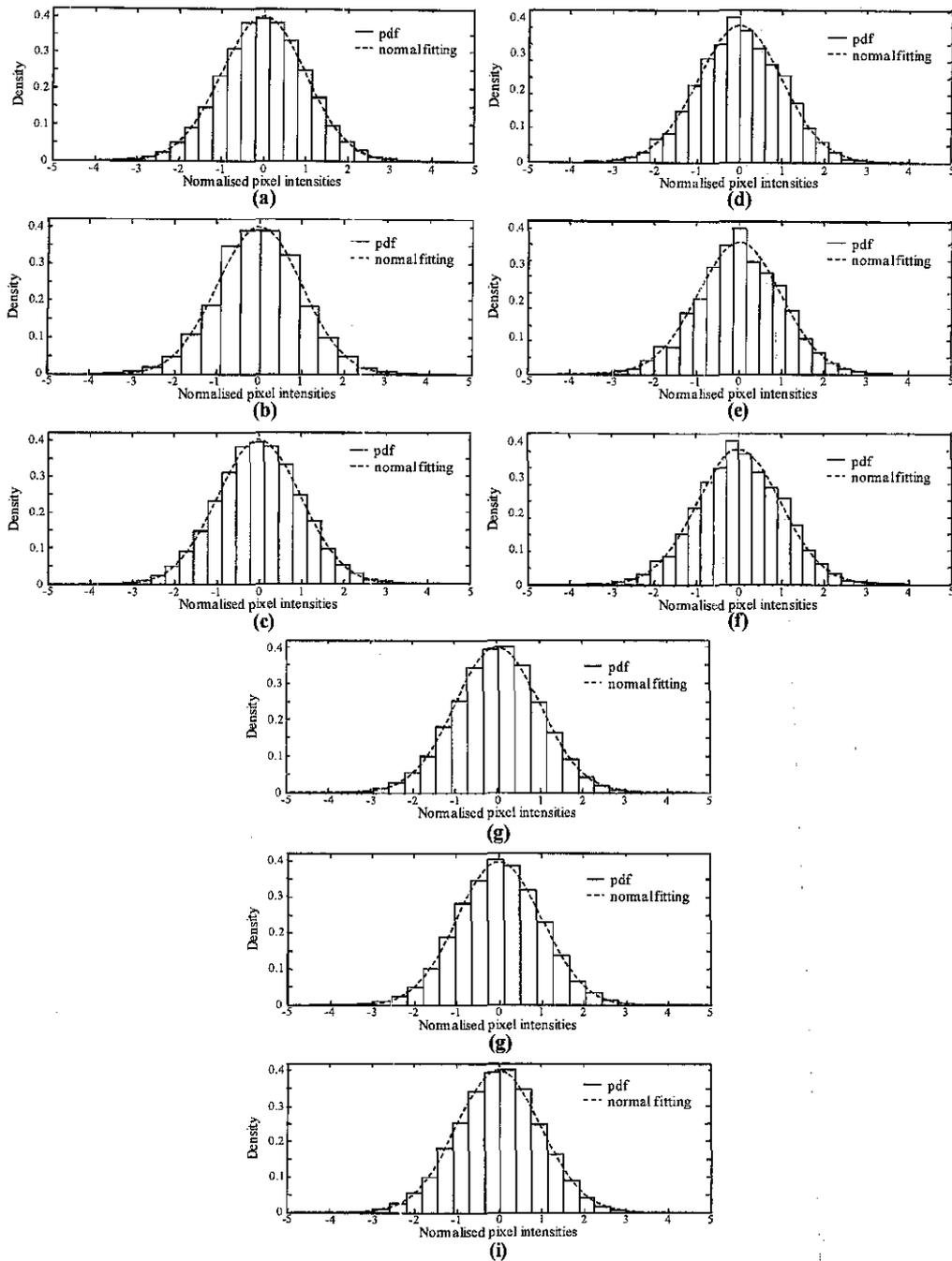


Figure 3.23 Probability distribution function of the normalised pixel intensities of Macular Pigment of (a) Red channel, (b) Green channel, (c) Green channel, Haemoglobin of (d) Red channel, (e) Green channel, (f) Green channel and Melanin of (g) Red channel, (h) Green channel, (i) Green channel

These normalised intensity distributions are obtained from the estimated samples of macular pigment, haemoglobin and melanin in each colour channel. Based on these normalised intensity distributions, pixel values are generated to model the three

related components used in the low contrast retinal fundus image model. A diagram of the development of low contrast fundus image model is illustrated in Figure 3.24.

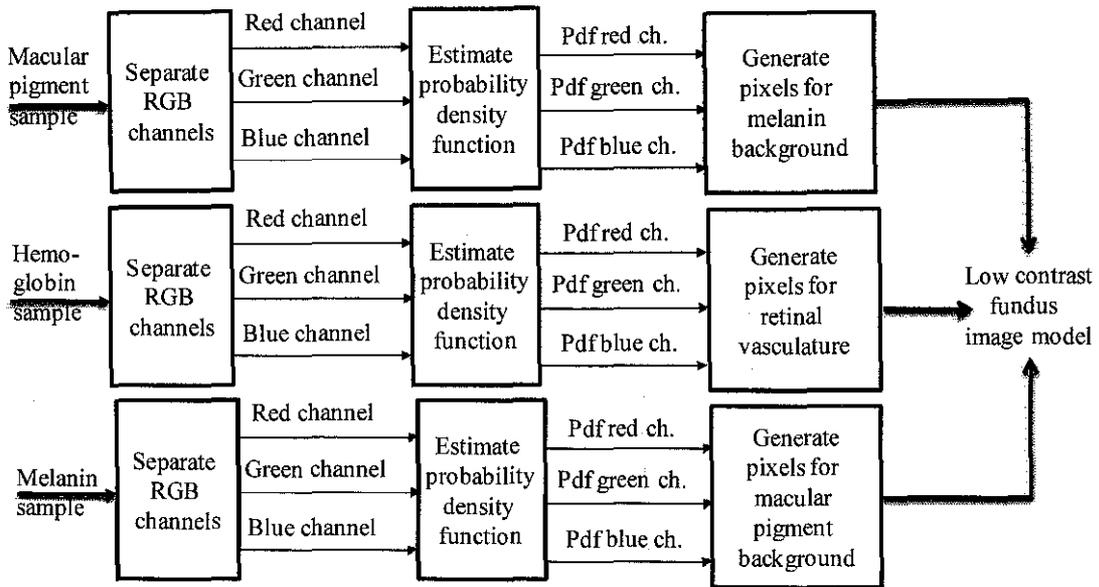


Figure 3.24 Development of low-contrast retinal fundus image model

Based on the obtained probability density functions (pdfs) and the mean of the components, colour distribution of each component are generated as shown in Figure 3.25.

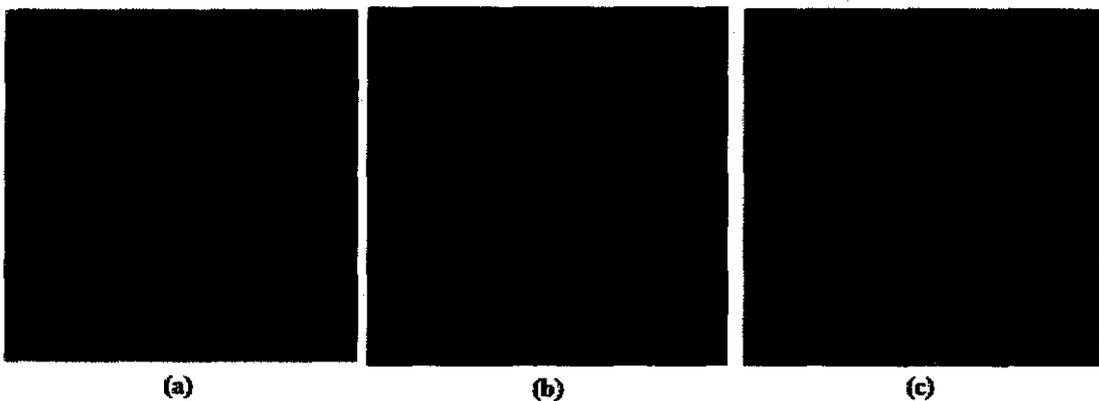


Figure 3.25 Colour distribution of (a) Macular pigment, (b) Haemoglobin and (c) Melanin generated in an image model of 320 x 320 pixels

These three different colour distributions representing macular pigment, haemoglobin and melanin are used to develop the low contrast retinal fundus image that contains these three components. Similar to the varied contrast image model, the low contrast image model of 320 x 320 pixels as depicted in Figure 3.26 represents

the macular region and its surrounding.

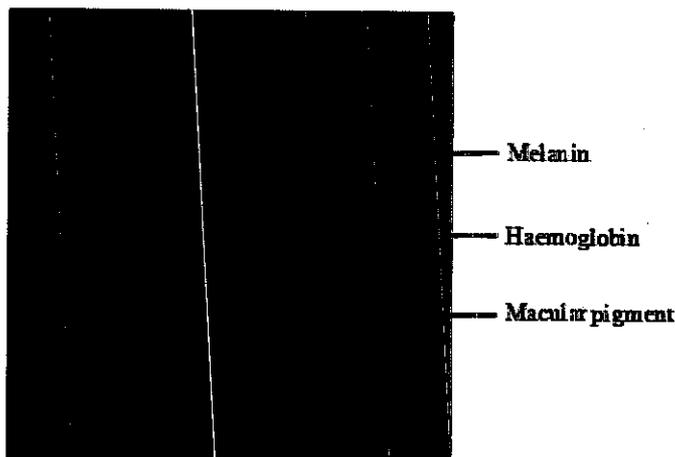


Figure 3.26 Low contrast fundus image model

In this image model, macular region containing the fovea is taken to identify the enhancement of retinal capillaries, which have a very low contrast of retinal blood vessels - also known as the retinal vasculature. The area of the image model is divided into two, i.e. top-half and bottom-half to represent the melanin and the macular pigment, respectively. Again, 9 parallel straight lines with the width varied from 1 to 13 pixels are used to represent the retinal blood vessels. These three components are filled up by the generated pixels with the intensity values that are determined from the normalised pdfs obtained from the sample.

3.4.3 Varied and Low Contrast Image Model

In the physics of light, brightness of a point (x, y) , which in the image plane also known as the image intensity and is independent for viewer direction, is defined as the amplitude of a function of illumination and surface properties at a particular wavelength λ [196-198]. In the image formation model, the function of $i(\lambda, x, y)$ is formed as a product of these two components – illumination (l) and reflectance (r) – that can be formulated as [46]

$$i(\lambda, x, y) = l(\lambda, x, y) \cdot r(\lambda, x, y) \quad (3-8)$$

A varied contrast in the image mostly occurs because of uneven illumination and

low contrast is due to presence of the tiny objects or other objects in the image that have some similar characteristics resulting in a subtle difference in the reflectance. Responding this, the varied and low contrast image model is then developed based on a combination of the two previous image models on varied contrast image model and low contrast image model. At this point, the varied contrast image model represents an illumination part and the low contrast one represents a reflectance part. Hence, the varied and low contrast image model can be developed as a product of these two image models using (3-8). Since the varied and low contrast image model is developed based on colour image, matrix element-by-element multiplication between illumination and reflectance parts – represented by the varied contrast and low contrast image models – is conducted in each colour channel. As shown in Figure 3.27, results of three multiplications between varied contrast image model and low-contrast image model in each channel are combined to obtain the varied and low-contrast retinal fundus image model. The obtained varied and low-contrast image model is shown in Figure 3.28.

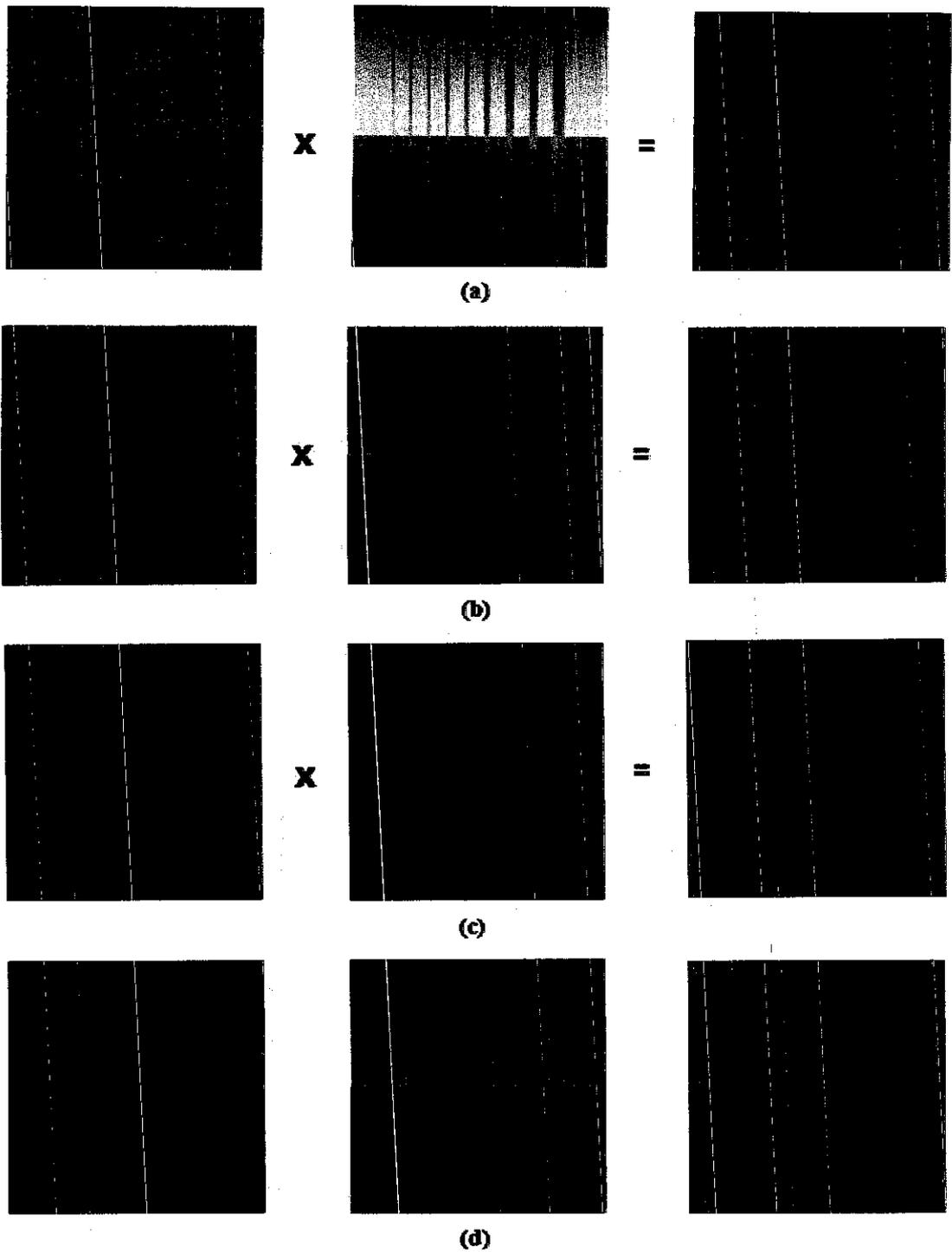


Figure 3.27 Varied and low contrast fundus image model is obtained from multiplication between low contrast and varied contrast image models in (a) Red channel, (b) Green channel and (c) Blue channel. (d) Colour fundus image models for low-contrast, varied contrast, and varied and low-contrast.

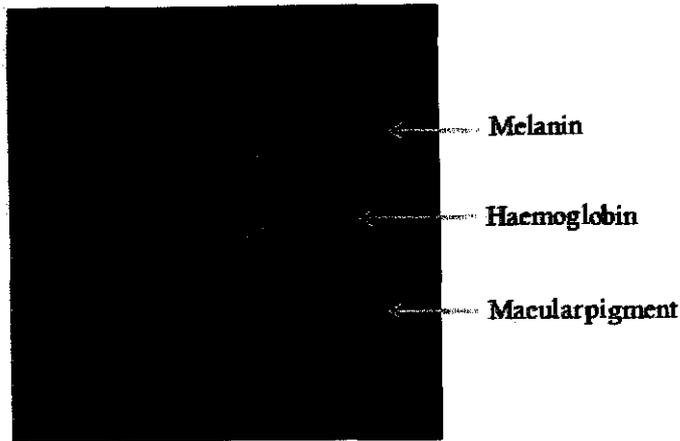


Figure 3.28 Varied and low-contrast fundus image model

3.5 Retinal Fundus Spectral Absorbance

The reflected light from the ocular fundus are strongly affected by the absorption of light by blood throughout the fundus, melanin pigment in the choroid, retinal pigmented epithelium (RPE), and macular pigment in the fovea. The spectral absorbance image provides useful information to identify the absorbance components. Analysing the spectral absorbance image further is advantageous to reduce the effect of luminance [177]. In this research, distribution of macular pigment, haemoglobin and melanin is used to model spectral absorbance of the retinal fundus.

The information of the retinal fundus image is contained in its colour. The light reflection from tissues with different optical density results in the differences in the colour of the image. Having acquired the colour retinal fundus image, the information can be extracted from its colour channel to obtain the characteristics of the reflectance by analysing the spectral absorbance. A linear model is developed based on the absorption coefficients of melanin, haemoglobin and macular pigment from three absorbencies; namely $\mu_a(\lambda_1)$, $\mu_a(\lambda_2)$ and $\mu_a(\lambda_3)$ at three wavelengths of λ_1 , λ_2 and λ_3 . These three wavelengths represent three colour channels: red, green and blue. Fundus spectral absorbance image shows spectral characteristics of the absorbance components in the retinal fundus. Two conditions are assumed when analysing fundus spectral absorbance. First, the colour observed in the fundus image is due to distributions of three main components, namely haemoglobin, melanin and

macular pigment. Second, the quantities of these components are spatially independent of each other. The spectral absorbance in the fundus image represents a linear combination of the absorption coefficients of melanin, haemoglobin and macular pigment. Figure 3.29 depicts the absorbance of the retinal fundus which consists of pure spectral vectors of melanin, haemoglobin, and macular pigment.

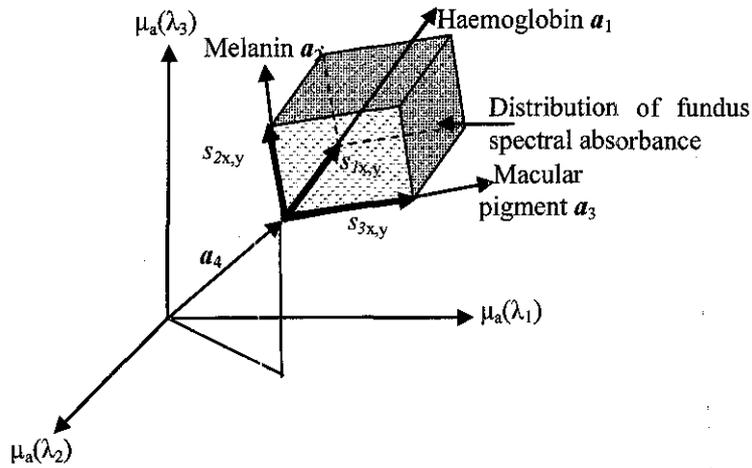


Figure 3.29 Model of spectral absorbance of the ocular fundus

As shown in Figure 3.29, Let $s_{x,y}$ and $v_{x,y}$ designate the three-dimensional (3-D) quantity vector and composite colour vector on the image coordinate (x, y) of the digital colour image. The mixing matrix A with a_1 , a_2 and a_3 represents pure colour vectors of the three components per unit quantity. It is assumed that linear combination of mutually independent pure colour vectors with the quantities of $s_{1x,y}$, $s_{2x,y}$ and $s_{3x,y}$ result in the composite colour vectors of $v_{1x,y}$, $v_{2x,y}$ and $v_{3x,y}$ on the image coordinate (x, y) . The following equation illustrates the transformation matrix, where T denotes the transpose.

$$v_{x,y} = A s_{x,y} \quad (3-9)$$

$$s_{x,y} = [s_{1x,y}, s_{2x,y}, s_{3x,y}]^T \quad (3-10)$$

The pixel value of each channel corresponds to each element of the colour vector. The reason for using the fundus spectral absorbance model is to find a suitable transformation from the RGB colour channels leading the sources constituted in the retinal colour fundus image to be extractable. As shown in Figure 3.29, distribution

of fundus spectral absorbance is illustrated as a mixture of three components. However, as previously discussed, those components have their own different spectral reflectance and do not interfere with each other; in a word, each of them is independent. In a central limit theorem [156], distribution of a sum of independent random sources tends to be more Gaussian (normal) than the distribution of each independent random source. Hence, a transformation to maximise the non-Gaussianity is necessary to obtain the original sources, which, in this case, are macular pigment, melanin and haemoglobin – as independent as possible from their mixture in RGB image. Having separated the components from their mixture, the haemoglobin-related component is hypothesised to have the highest contrast of retinal blood vessels of the other two components and also any RGB images. The proposed method to separate the components from their mixture by maximising their non-Gaussianity will be discussed in Chapter 4 (Section 4.3).

3.6 Summary

As the objective of the research is to develop a non-invasive image enhancement method for varied and low contrast image, this chapter explains about the development of varied and low contrast image models used to validate the proposed image enhancement technique and to evaluate the performance of the proposed method. Three image parametric models, i.e. varied contrast image, low-contrast image, and varied and low-contrast image are developed based on colour retinal fundus images that may suffer from problems of both varied and low contrast. Data for modelling are randomly selected from a colour fundus image database called FINDeRS.

As the structure of eye is divided into two, i.e. ocular media and ocular fundus, a colour retinal fundus image depicts the ocular fundus part, which is the structure of the back of the eye. Characteristics of the ocular fundus are strongly influenced by the light absorption by melanin pigment in the RPE and choroid, macular pigment in the fovea and haemoglobin throughout the ocular fundus part. Hence, the appearance of the retinal fundus image will highly depend on the presence of melanin, macular pigment and blood characterised by haemoglobin. These three components have

different spectral absorbance (and reflectance) and are independent to each other. This characteristic in turn is advantageous for the development of our non-invasive image enhancement technique in which the haemoglobin related to retinal blood vessels is separated from the other two components – melanin and macular pigment – to obtain a high contrast of retinal vessels.

To capture the retinal surface, the light must enter the eye, pass the ocular media and a series of layers in the retina, and strike the opaque white sclera in the back of the eye. The reflected light then must leave the retina through the pupil. A fundus camera acquires retinal fundus images by capturing the illumination reflected from the retinal surface. The acquired retinal fundus image shows a different intensity of reflectance that depends on the wavelength, architecture of fundus' layer, optical densities and quantities of the biological structure and retinal pigment construction retinal pigments in the ocular fundus. Slight changes lead to variation in colour of the fundus.

The retinal fundus image model is composed from three colour channels as a mixture of three main sources, i.e. macular pigment, haemoglobin and melanin. These three main sources with different quantities and locations in the retinal layers reflect the incident light from the illumination source and also form the colour retinal fundus image. The 44 fundus images randomly selected from FINDeRS are used to develop the three fundus image models – varied contrast, low-contrast and varied and low-contrast – representing the problems occurred in most of medical images, particularly in retinal fundus images. The problem of varied contrast and low contrast is investigated separately using the first and second image models respectively. The third image model meanwhile is used to cope with the problem of both varied and low contrast. Whilst the varied contrast fundus image model is developed to represent the problem of illumination, the low contrast one is developed to represent that of reflectance. Again, different from the low contrast image developed from the normalised pdfs obtained from the collected samples, the varied contrast image model is developed by applying a smooth variation of intensities. A product of these image models is subsequently used to develop the varied and low-contrast image model.

Assuming that the colour observed in the retinal fundus image is due to the distributions of three main sources spatially independent to each other, the sources can be analysed from the fundus spectral absorbance. The spectral absorbance in the fundus image represents a linear combination of the absorption coefficients of melanin, haemoglobin and macular pigment. A suitable transformation technique can be applied to obtain these main sources from the observed RGB channels. Based on central limit theorem, a transformation, purposively used to separate a mixture of components, can be applied by maximising non-Gaussianity distribution of the components that consequently will be as independent as possible. If the components can be separated, the haemoglobin-related component is predicted to have a higher contrast of retinal blood vessels than that of the contrast measured from any of the RGB images.

CHAPTER 4

DEVELOPMENT OF NON-INVASIVE IMAGE ENHANCEMENT METHOD (RETICA)

4.1 Introduction

In this research, varied and low contrast nature of colour retinal fundus images is addressed. The objective is to develop a non-invasive digital imaging enhancement scheme capable of enhancing varied and low-contrast medical images to be similar to, or better than the contrast produced by an invasive method without introducing noise or artefacts. In this chapter, the detail of the proposed method is discussed and applied to the varied and low-contrast fundus images. It is validated using developed retinal fundus image models in which its performance is evaluated and compared against other selected non-invasive image enhancement methods.

Image intensity according to the hypotheses (as discussed in Chapter 1) is a product of illumination and reflectance. In the image, the varied contrast occurs due to slowly varied illumination, whereas the low contrast in some objects of interest is related to the reflectance. If the varied contrast can be determined in a local neighbourhood, it is possible to normalise the contrast by some specialised methods such as Retinex. Meanwhile, by determining the actual sources that resulted in the observed (low contrast) RGB image using methods such as ICA, the objects or areas due the source that is of interest, can then be enhanced separately without introducing some unwanted artefacts. The advantage of contrast normalisation and enhancement is an increase in accuracy, sensitivity and specificity of the diagnosis through either a direct observation or a computer assisted diagnosis system.

In general, the proposed method called as RETICA enhances the varied and low contrast colour retinal fundus images using two processes, i.e. contrast normalisation based on Retinex and contrast enhancement based on ICA. The input of RETICA

refers to colour image that has been separated into three channels, i.e. red, green and blue channels. RETICA first normalises the varied contrast using an improved iterative Retinex, a method to separate the illumination from the reflectance part of the image. The improved iterative Retinex – one of the contributions of this research work to body of knowledge – uses kurtosis to determine the optimum number of iteration and overcomes the problem of standard iterative Retinex in which the number of iteration is fixed and pre-determined. . Normalisation of varied contrast is followed by separating the retinal pigments makeup, namely macular pigment, haemoglobin and melanin, using Independent Component Analysis (ICA). Independent component image due to haemoglobin exhibits higher contrast of retinal vessels. The use of ICA to enhance the contrast of retinal vessels by revealing the underlying sources in colour retinal fundus images is another contribution of this work since most of the image enhancement methods use pixel manipulation. A block diagram of RETICA is depicted in Figure 4.1.

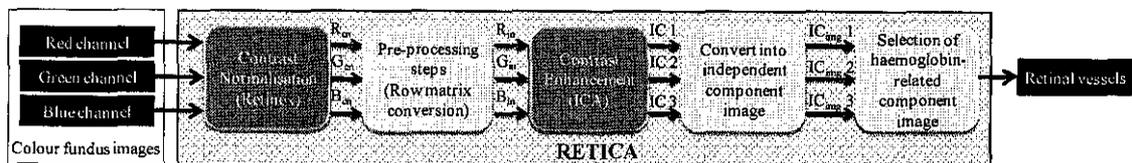


Figure 4.1 Proposed method (RETICA) for contrast normalisation and contrast enhancement of retinal blood vessels on colour fundus image

As illustrated in Figure 4.1, the three channels, i.e. red, green and blue channels are inputted to the first stage of RETICA, i.e. contrast normalisation based on Retinex. These images are processed to obtain three contrast-normalised output images. Prior to inputting these images into the second stage, a pre-processing step that converts the image matrix into row matrices is required to speed up the computation at the second stage.

The ICA at the second stage is performed for contrast enhancement by separating the independent components from their mixture. The outputs of the second stage, which are the independent components, are then converted back from row matrices to image matrix. Details of the process in each stage are explained in the following subsections.

4.2 Contrast Normalisation

The contrast normalisation stage is based on the Retinex algorithm (presented in Chapter 2) purposively to normalise the varied contrast of the retinal fundus image by predicting the sensory response of lightness in the image. The contrast-normalised image is advantageous for the subsequent image processing techniques, e.g. contrast enhancement, as it will enable an effective enhancement on the overall image. Among the Retinex algorithms, the iterative method based on McCann algorithm [125-126] which is an improvement of the random walks Retinex algorithm [118], is chosen. Unlike non-iterative methods in which several parameters, such as the weighted scale, must be predetermined to obtain good dynamic range and tonal rendition, the iterative Retinex method only needs to determine the number of iteration. A typical number of iteration for natural image is 4 as been suggested by Funt *et al.* [127]. However, in our developed algorithm, a parameter to measure contrast normalisation based on kurtosis is used to determine the optimum number of iteration for the Retinex rather than to use a fixed number of iteration. A flowchart showing the algorithm for contrast normalisation based on the iterative Retinex is depicted in Figure 4.2.

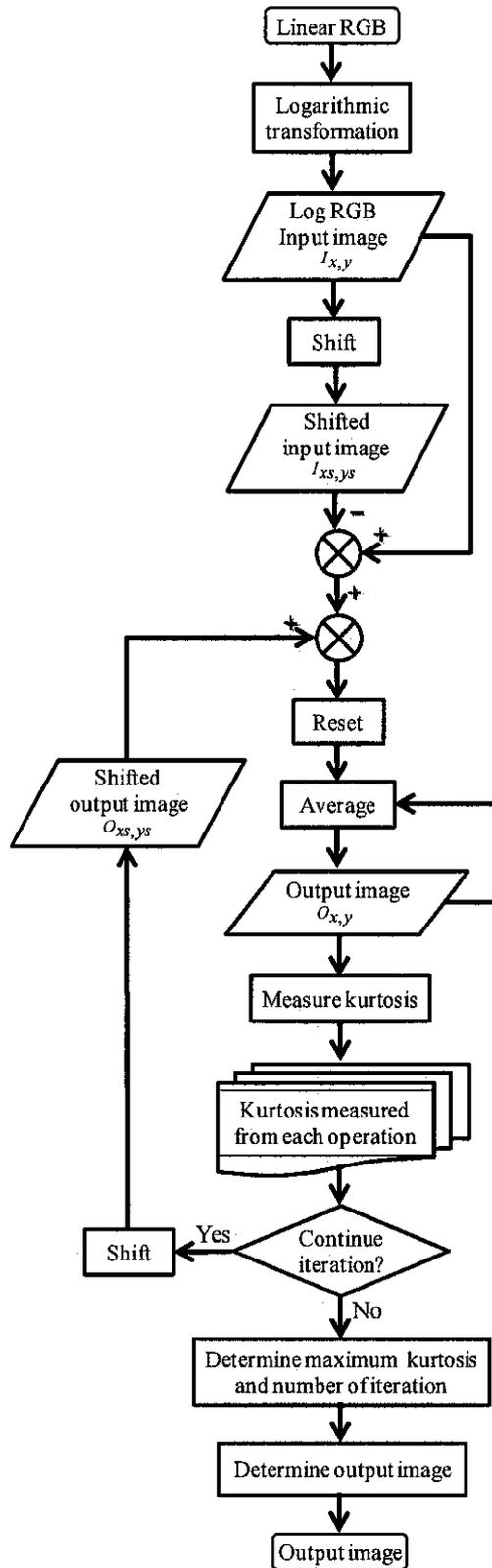


Figure 4.2 Flowchart for contrast normalisation based on Retinex algorithm

Referring to Figure 4.2, the RGB input image is initially separated into three

channels, each of which undergoes Retinex algorithm. For each colour channel, the input image is transformed from linear to logarithmic form to simplify the process from multiplication to addition or from division to subtraction. In the iterative Retinex, a multi resolution pyramid from the input is created by averaging fundus image. These iterative Retinex methods [125-126] calculates the long-distance interactions and then gradually moves to short-distance interactions among pixels. The method then compares the pixel at the most highly averaged or top level of the pyramid.

In each step, the spacing between the pixels being compared decreases. The direction among pixels also alters at each step in a clockwise order. In each step, the comparison of pixels is implemented to estimate the reflectance part using the ratio-product-reset-average operation, which is iteratively computed in a certain amount of times. This number of iteration turns out to be an important image-dependent parameter of the algorithm. After estimating the reflectance part of the image at the longest-distance, the resulting values are used as an initial estimation of reflectance for the next level of interaction. Subsequent comparisons between pixels are continually performed to refine the estimated reflectance until the spacing decreases to one pixel and the final product is obtained.

Ratio and product are processes of accumulating and comparing resulting in the revision of a newer product in each process of pixel comparison. Reset operation is to normalise the newer product exceeding the sustainable maximum. Averaging aims to estimate and update one pixel's luminance. The ratio-product-reset-average operation is performed by calculating the ratio between images I (in a specific channel) and its spatially shifted version and offset by some displacement distances formulated as

$$\log O_{x,y}^* = \frac{Reset \left[(\log I_{x,y} - \log I_{xs,ys}) + \log O_{xs,ys} \right] + \log O_{x,y}}{2} \quad (4-1)$$

where $(\log I_{x,y} - \log I_{xs,ys})$ is the ratio and $\left[(\log I_{x,y} - \log I_{xs,ys}) + \log O_{xs,ys} \right]$ represents the product. Reset operation is performed to update the maximum intensity of the image scene L_{\max}^{scene} if $\left[\log I_{x,y} - \log I_{xs,ys} + \log O_{xs,ys} \right] > \log L_{\max}^{scene}$. The term

$\log O_{x,y}^*$ is a result of averaging with $\log O_{x,y}$ and $O_{x,y}^*$ itself is an updated output produced iteratively that will be used as an input for the next iteration.

The kurtosis of the data, melanin, macular pigment and haemoglobin is measured and saved iteratively. After all iterations have been performed, the maximum kurtosis can be found and the related number of iteration is determined as the optimum number of iteration for the Retinex.

4.3 Contrast Enhancement

The proposed method for contrast enhancement is based on ICA, a technique to determine the original signals from mixtures of several independent sources [145, 154]. It is purposively to enhance the contrast of a specific object or component, which, in this case, is the contrast of retinal blood vessels by separating each of the components, namely macular pigment, haemoglobin and melanin from their mixtures. The ICA is applied on fundus spectral absorbance model that shows spectral characteristics of the absorbance components in the ocular fundus and provides useful information to identify the absorbance components [199]. Basis of linear combination of the absorption coefficients of melanin, haemoglobin and macular pigment is modelled from three absorbance $\mu_a(\lambda_1)$, $\mu_a(\lambda_2)$ and $\mu_a(\lambda_3)$ at three wavelengths λ_1 , λ_2 and λ_3 . These wavelengths represent the red (R), green (G) and blue (B) channels. A model of spectral absorbance of the ocular fundus has been explained in the previous chapter and is shown in Figure 4.3 to illustrate the idea of using ICA in separating the spatial distributions of melanin, haemoglobin, and macular pigment in the ocular fundus.

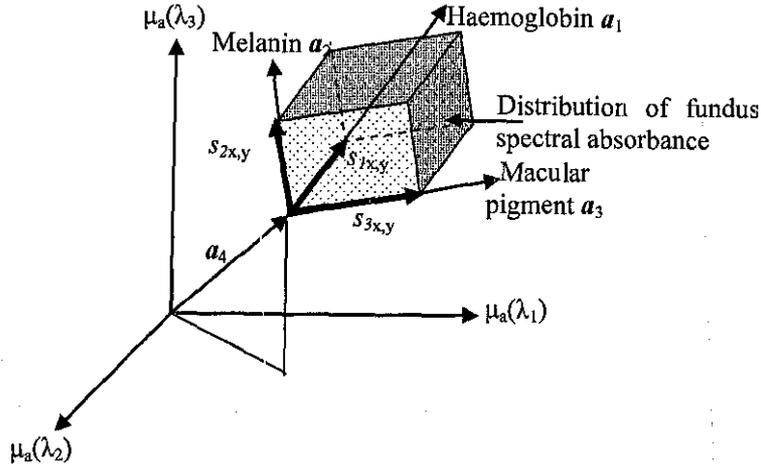


Figure 4.3 Model of spectral absorbance of the ocular fundus

According to the model of spectral absorbance of the ocular fundus from Figure 4.3, the colour density vector of the fundus can be stated as

$$v_{x,y} = A\tilde{s}_{x,y} + a_4 \quad (4-2)$$

$$\tilde{s}_{x,y} = [\tilde{s}_{1x,y}, \tilde{s}_{2x,y}, \tilde{s}_{3x,y}]^T \quad (4-3)$$

with the mixing matrix $A = [a_1, a_2, a_3]$ and $\tilde{s}_{x,y}$ representing pure colour vectors of the three components (melanin, haemoglobin and macular pigment) per unit quantity. It is assumed that a linear combination of mutually independent pure colour vectors of $\tilde{s}_{1x,y}$, $\tilde{s}_{2x,y}$ and $\tilde{s}_{3x,y}$ with the mixing matrix A results in the composite colour vectors of $v_{1x,y}$, $v_{2x,y}$ and $v_{3x,y}$ on the image coordinate (x, y) . The composite colour vector $v_{x,y}$ is determined based on the output of the Retinex algorithm in which the input images to the ICA is contrast-normalised. The input for the ICA is determined as

$$[\mu_a(\lambda_1), \mu_a(\lambda_1), \mu_a(\lambda_1)] = [Rr_{x,y}, Rg_{x,y}, Rb_{x,y}] \quad (4-4)$$

Here, the values of $Rr_{x,y}$, $Rg_{x,y}$ and $Rb_{x,y}$ correspond to pixel intensity in the channels of red, green and blue respectively as the outputs of the Retinex for contrast normalisation. The composite colour vector is denoted as

$$\tilde{v}_{x,y} = [\mu_a(\lambda_1), \mu_a(\lambda_1), \mu_a(\lambda_1)] \quad (4-5)$$

By applying the ICA to the composite colour vectors in the image, the relative quantity and pure colour vectors of each independent component are determined with no prior information on both the quantity and colour vector. The quantities of the melanin, haemoglobin and macular pigment are assumed to be mutually independent for the image coordinate. The separating matrix W is defined to separate vector $\tilde{s}_{x,y}$ using the following equations.

$$\tilde{s}_{x,y} = W\tilde{v}_{x,y} \quad (4-6)$$

The estimated independent components $\tilde{s}_{1x,y}$, $\tilde{s}_{2x,y}$ and $\tilde{s}_{3x,y}$ may be similar to $s_{1x,y}$, $s_{2x,y}$ and $s_{3x,y}$, respectively. A flowchart showing the ICA algorithm is depicted in Figure 4.4.

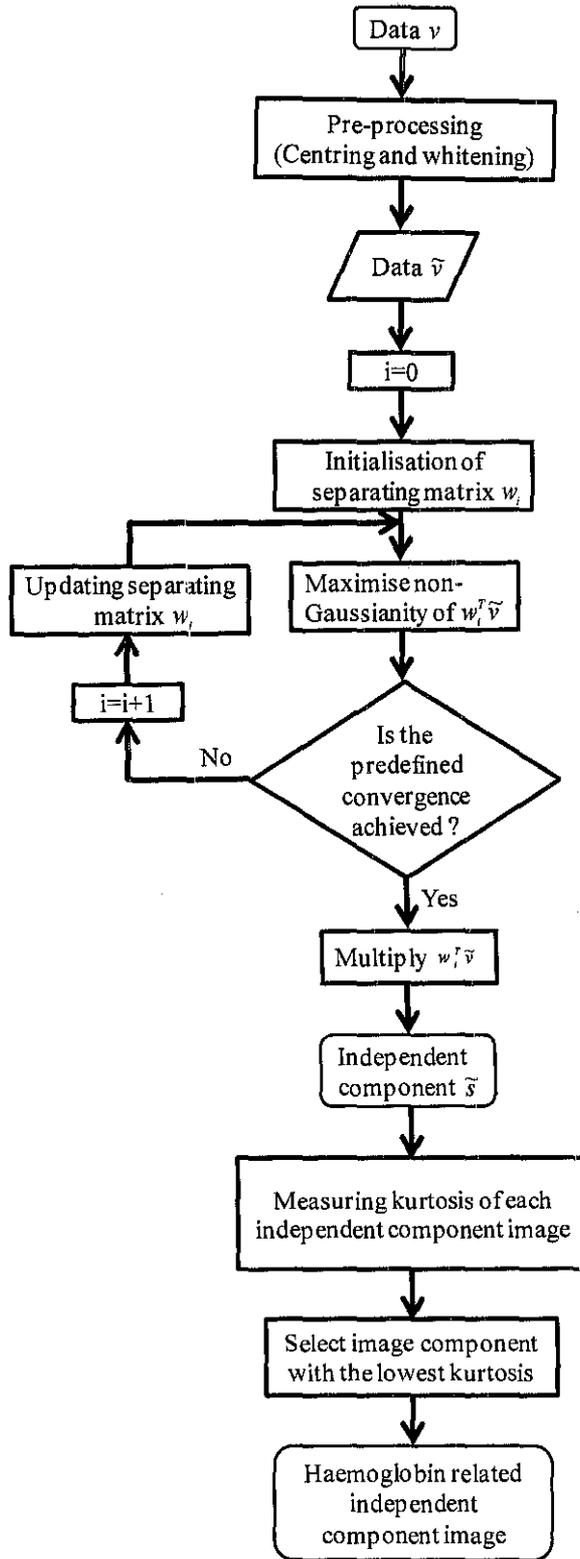


Figure 4.4 A flowchart of contrast enhancement of retinal vessels based on ICA

Data v as the input for ICA consists of three colour channels that have been previously processed by Retinex for contrast normalisation. The outputs of the

Retinex are three images from three different colour channels, i.e. red, green and blue. Each of these images is transformed from matrix of $m \times n$ into a row matrix $1 \times (mn)$. Since there are 3 colour channels, data v will be $3 \times (mn)$. Data v is initially centred and whitened prior to performing the ICA algorithm. The result of this process is zero-mean and whitened data \tilde{v} . Following this, data \tilde{v} undergoes the ICA algorithm. The algorithm uses the FastICA [147], which is based on a fixed-point iteration for maximisation of non-Gaussianity of $w\tilde{v}$ to obtain the estimated IC \tilde{s} as indicated in (4-6). Since FastICA uses approximation of negentropy, the maxima of the approximation of $w^T\tilde{v}$ are obtained at certain optima $E\{G(w^T\tilde{v})\}$.

For estimation of several independent components (ICs), a symmetrical orthogonalisation that obtains the ICs in a parallel process is used and detailed steps are described as follows:

1. Choose h ICs and set iteration $i=1$. In this study, number of ICs h is equals to 3, i.e. melanin, macular pigment and haemoglobin.
2. Initialise random $w_i, i=1,2,3$ to unit form and do orthogonalisation of the matrix w .
3. For each $i: w_i^+ = E\{\tilde{v}g(w_i^T\tilde{v})\} - E\{g'(w_i^T\tilde{v})\}w_i$ and update each column of the separating matrix w from the previous iteration.
4. Orthogonalisation of $w^+ = (ww^T)^{-1/2}w$.
5. Check the criteria for convergence. If $|w - w^+| \leq \varepsilon$ is not fulfilled, the process will be back to step 3. The convergence parameter ε is set to 0.0001.

The iteration process ends when the convergence is achieved or the iteration has reached its maximum number of iteration, which is 1000. Once the optimum separating matrix W is obtained, the estimated ICs can be determined.

However, since the order of the ICs cannot be determined, the haemoglobin-related IC cannot be automatically selected. Therefore, the fourth order statistics, i.e. kurtosis, is used to differentiate the haemoglobin-related IC from the other

components. Kurtosis is a measure of how peaked or flat the distribution of the data is. Kurtosis is formulated as

$$kurtosis = \frac{\sum_{i=1}^M (I_i - \bar{I})^4}{(M-1)\sigma^4}, \quad (4-7)$$

where I_i refers to the intensity value of data point i from the total data point M , \bar{I} is the mean of the intensity and σ is the standard deviation of the data. For normal distribution, the kurtosis of the data equals to 3. In both the melanin-related IC and the macular pigment-related IC images, the contrast of retinal blood vessels comes to be low for the intensity distribution dominated by the intensities of the melanin and that of the macular pigment respectively. Whilst in the haemoglobin-related IC image, the contrast of retinal vessels is significantly higher than that of the other two IC images since the intensity distribution of haemoglobin represented by the nine parallel lines is maximised to be as non-Gaussian as possible leading the haemoglobin to be distinct. However, due to significantly smaller area of haemoglobin (retinal blood vessels) compared to that of macular pigment and melanin in the fundus image model (as discussed in Chapter 3), the kurtosis measured from the haemoglobin-related IC therefore comes to be smaller than that of the other two ICs. The haemoglobin-related IC is distinguished from the other two ICs since it has the least value of kurtosis. As the fundus image model is developed based on real fundus images, the use of kurtosis to differentiate the haemoglobin-related from the other two ICs can be applied not only in the fundus image model but also in the real colour fundus images in which both macular pigment and melanin are also significantly dominant compared to haemoglobin (retinal blood vessels).

4.4 Validation of RETICA

The objective of the validation is to prove that RETICA really normalises and enhances the contrast of the image, in particular the enhancement of the retinal blood vessels in fundus images. Validation of RETICA in this study purposively is conducted in three parts; those are for (1) contrast normalisation, (2) contrast

enhancement and (3) contrast normalisation and enhancement. Three developed retinal fundus image models as described in the previous chapter are going to be used.

Two problems are addressed in this validation study, i.e. contrast normalisation and contrast enhancement. Firstly, to measure the contrast normalisation, the kurtosis of the components, i.e. the melanin, the macular pigment and the haemoglobin is used. As previously described, the kurtosis is used as a parameter to determine the optimum number of iteration of the Retinex. The highest kurtosis of the data corresponds to the optimum number of iteration of the Retinex and leads to the most homogenous intensity of the image. Secondly, to measure the contrast enhancement of the retinal blood vessels, the contrast between the retinal blood vessels and the background needs to be determined. There are two kinds of background namely melanin and macular pigment in which the retinal blood vessels are fairly distributed. Hence, to validate RETICA, four reference masks as shown in Figure 4.5 are used to extract the region of interest (ROI) of a processed image. The mask is created in a binary form in which the value of 1 and that of 0 represent the ROI and the background respectively. Hence, when the mask is multiplied with the enhanced image model, the result will be the extraction of ROI from the enhanced image model. From the extracted ROI, contrast normalisation and enhancement are validated.

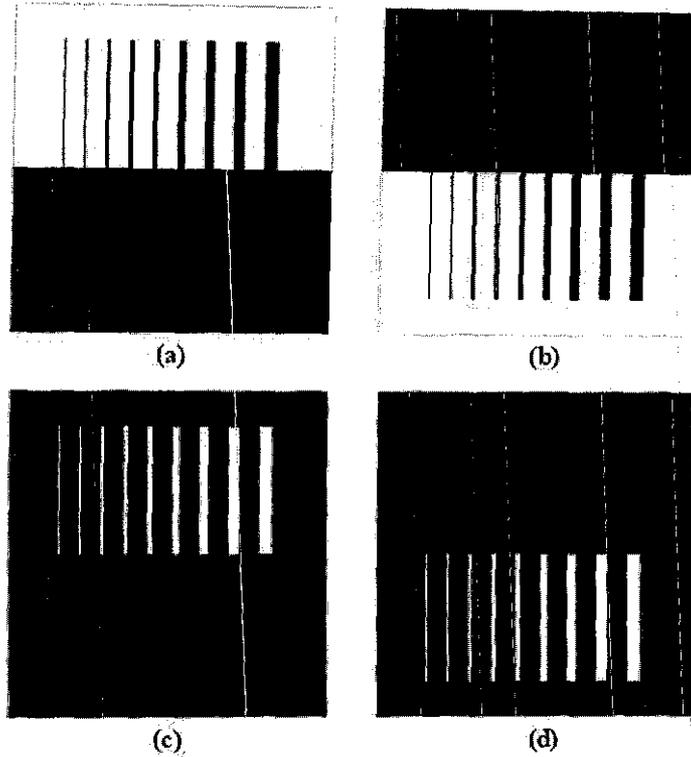


Figure 4.5 Reference masks for (a) Melanin, (b) Macular pigment, (c) Haemoglobin (retinal blood vessels) on melanin and (d) Haemoglobin (retinal blood vessels) on macular pigment

The first mask (Figure 4.5(a)) shows the area of melanin and the second mask (Figure 4.5(b)) shows the area of macular pigment. The third (Figure 4.5(c)) and the fourth (Figure 4.5(d)) masks show the retinal blood vessels (haemoglobin) in the melanin and in the macular pigment respectively.

After performing RETICA on the fundus image model, the enhanced image is multiplied with each of the masks to obtain the four areas of interest, i.e. the melanin, the macular pigment, the retinal blood vessels in the melanin and the retinal blood vessels in the macular pigment. By identifying these areas, the contrast between the retinal blood vessels and each background can be determined. The contrast between retinal blood vessels and the background ($C_{|bv-bg|}$) is defined as the absolute mean intensity difference between retinal blood vessels and the background and is formulated as

$$C_{|bv-bg|} = \left| \frac{1}{u} \sum_{i=1}^u Ibv_i - \frac{1}{v} \sum_{j=1}^v Ibg_j \right| \quad (4-8)$$

with Ibv and Ibg are the intensities of the retinal blood vessels and the background respectively. The values of u and v indicate the number of pixels of the retinal blood vessels and the background in the fundus image model. The higher the value of the $C_{|bv-bg|}$, the better the contrast of retinal blood vessels in the image will be. Since there are two kinds of background where the retinal blood vessels are located, the contrast of retinal blood vessels is then defined as the average of contrast between retinal blood vessels in the macular pigment and retinal blood vessels in the melanin. The contrast of retinal blood vessels (C_{av}) in the fundus image model is formulated as

$$C_{av} = \frac{\left| \frac{1}{a} \sum_{i=1}^a Ivml_i - \frac{1}{b} \sum_{j=1}^b Imel_j \right| + \left| \frac{1}{c} \sum_{k=1}^c Ivmc_k - \frac{1}{d} \sum_{l=1}^d Imac_l \right|}{2} \quad (4-9)$$

$Ivml$ and $Ivmc$ are the intensities of retinal blood vessels in melanin and in macular pigment, whilst $Imel$ and $Imac$ are intensities of melanin and macular pigment respectively. The values of a and c indicate the number of pixels of the retinal blood vessels both in melanin and in macular pigment correspondingly; whilst the values of b and d indicate the number of pixels both in melanin and in macular pigment of the fundus image model. The higher the C_{av} , the better the contrast of retinal blood vessels will be.

4.5 Algorithms for Comparative Study

There are so many algorithms for image enhancement. However, not only does each algorithm offer its own advantages but also does suffer from some disadvantages. The algorithms that are selected for comparison must fulfil some criteria to set up; namely (1) they should include the classical and state-of-the-art ones in the area of image enhancement, (2) they are not a combination of two or more principal algorithms and (3) their implementation should not be highly complicated with lots

of parameters that need to be adjusted. These criteria are set up for the simplicity of choosing the algorithms for comparison due to many existing image enhancement algorithms in which each of them offers its own benefit in a specific application. Nevertheless, our proposed non-invasive image enhancement method has already a gold standard one, i.e. the invasive FFA, to compare as stated in the objective of this research.

In this study, six algorithms, i.e. contrast stretching (CS) [46], histogram equalisation (HE) [39], adaptive histogram equalisation (AHE) [40], adaptive contrast enhancement (ACE) [41], contrast limited adaptive histogram equalisation (CLAHE) [88] and homomorphic filtering (HF) [46] commonly used for image enhancement for general application, are selected to evaluate the performance of the proposed algorithm. In the application of retinal image enhancement, Yousiff *et al.* [35] particularly show that adaptive histogram equalisation is the most effective method among the other seven algorithms being compared.

The objective of this comparative study is to measure the quality of the contrast-enhanced image produced by the proposed method compared to that of the selected algorithms. Three criteria are set up to compare the results of image enhancement process. The first criterion is image contrast that is represented by the contrast of retinal blood vessels (C_{av}) as explained in (4-9). The second one is the image contrast normalisation (R_{sdc}) that is defined as the ratio between standard deviation σ and the average contrast C_{av} of an image with the size of $m \times n$. The second criterion is derived from the standard deviation that has been widely used to measure image contrast [52-54, 200-201]. Rubin and Siegel showed that images with an equal standard deviation will have an equal contrast [53].

Theoretically, a standard deviation shows a spread of data from its mean value in which a low standard deviation indicates that most of the data concentrated on their mean value and vice versa. In term of image intensities, low standard deviation indicates that most of the intensity values are close to the mean value. Whereas a high standard deviation indicates that the intensity values are spread out over a large range of values. Hence, the standard deviation can be used to indicate the

homogeneity of intensity distribution. A low standard deviation obtained from an image area represents more homogeneous image intensities compared to the high one. This is in line with the objective of contrast normalisation in which the intensity distribution is made to be as homogeneous as possible. However, to use only one standard deviation is not sufficient if several objects in the image present.

As our objective is also to enhance the contrast between an object and its background, we use not only standard deviation σ but also average contrast C_{av} to measure contrast normalisation of the image since the average contrast shows the average of intensity difference between different objects, which in the fundus image model is the average of contrast between retinal blood vessels in the macular pigment and retinal blood vessels in the melanin. If the average contrast C_{av} is significantly high compared to the intensity variation indicated by its standard deviation σ , the image will be considered to have more homogeneous intensities. Conversely, if the average contrast C_{av} is significantly low compared to the intensity variation represented by its standard deviation σ , the image is considered to have more non-homogeneous intensities. Hence, the lower the R_{sdc} is, the better the contrast normalisation of the image will be.

Having incorporated both standard deviation σ and average contrast C_{av} between objects in an image, the R_{sdc} actually measures not only pure contrast normalisation, but also contrast enhancement. However, both the aforementioned criteria can only be implemented in the image model where the objects have been determined in prior. Whereas in the real image, the objects cannot be determined and separated one and another in prior by such a system; hence, the average contrast that shows the average of intensity difference between different objects cannot be practically measured.

For the second criterion - image contrast normalisation (R_{sdc}) - , standard deviation is formulated as

$$\sigma = \frac{1}{mn} \sum_{i=1}^{(mn)} I_i - \bar{I} \quad (4-10)$$

Therefore, the image contrast normalisation (R_{sdc}) can be formulated as

$$R_{sdc} = \frac{1}{mn} \frac{\sum_{i=1}^{(mn)} I_i - \bar{I}}{C_{av}} \quad (4-11)$$

where I and \bar{I} denote image intensity and its average correspondingly. The lower the R_{sdc} is, the more homogeneous the intensity is; the more normalised the contrast thus is obtained. This criterion can also be used to measure noise reduction because of performing a specified image enhancement process. Noise can be characterised by the standard deviation of the image intensities. Ideally, the image without any noise will have one value of intensities or uniform intensity distribution, which is almost impossible to get from the real image. The idea of using R_{sdc} can be seen if the value of R_{sdc} obtained is small enough, meaning that the standard deviation is also small. The smaller the standard deviation is, the smaller the intensity variation will be. It also means that the more homogenous the intensity distribution will be.

The third one is the contrast improvement factor (CIF) that is defined as a ratio between the contrast of retinal blood vessels obtained by a specified algorithm (C_{sp}) and that of the reference (C_{ref}). In this case, C_{ref} uses the contrast of the retinal blood vessels in the green band image. The CIF is therefore formulated as

$$CIF = \frac{C_{sp}}{C_{ref}} \quad (4-12)$$

The higher the CIF , the better the performance of the algorithm will be.

4.6 Results and Analysis

Three fundus image models, i.e. the varied contrast image model, the low-contrast image model and the varied and low-contrast image model are used to validate each stage and the whole stage of RETICA. Using the fundus image model, the performance of RETICA is evaluated and compared to several image enhancement

algorithms. A smaller region containing the macular area is taken to see the enhancement of retinal capillaries, which usually has a very low contrast between retinal vasculature and the background. As explained in the previous chapter, the area of the fundus image model is divided into two, i.e. the melanin and the macular pigment that are located at the top half and the bottom half of the image model respectively. Retinal blood vessels are modelled in 9 straight lines paralleling in height and ranging from 1 to 12 pixels in width, representing the width of retinal blood vessels from the real retinal fundus image. The thin lines are to represent the retinal capillaries where mostly exist in the macular region; while the wider lines are to represent wider retinal blood vessels where mainly exist in the background.

4.6.1 Contrast Normalisation

The first model, namely the varied-contrast fundus image model as shown in Figure 4.6(a) is used to validate the first stage of RETICA known as contrast normalisation.

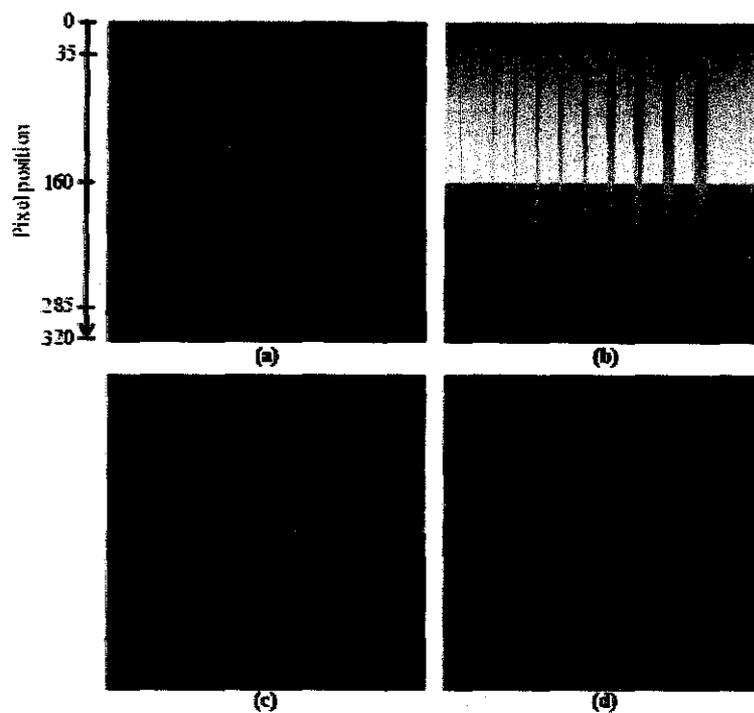


Figure 4.6 Varied contrast fundus image and its (b) Red, (c) Green and (d) Blue channel images

As shown in Figure 4.6, the varied-contrast fundus image is separated into three

channels, i.e. red, green and blue channels that are inputted to the first stage of RETICA, which is based on the Retinex. Validation of the Retinex on the varied-contrast fundus image model is performed by observing the distribution of each component (melanin, macular pigment and haemoglobin) and determining the optimum iteration of the Retinex-based algorithm that results in the most homogenous pixel intensity distribution of each component.

The varied-contrast fundus image model is developed by varying the intensity from low to high values as the position changes vertically. By performing the Retinex-based algorithm, the variation of intensities is reduced resulting in more homogeneous intensity distribution. Using the mask from Figure 4.5, each component of the fundus image model is separated.

A vertical line profile is then selected from the area of each component to show its homogeneity of the intensity variation. Referred to the pixel position in the varied contrast image model shown in Figure 4.6, the original melanin intensity shows the lowest value at the top of the image and increases as the pixel position moves down and reaches the highest value towards the middle of the image where the pixel position is 160. Figure 4.7, Figure 4.8 and Figure 4.9 depict the comparison of melanin's intensity variation on a vertical line profile taken from red, green and blue channel images after performing Retinex algorithm with several different numbers of iterations. The optimum number of iteration of the Retinex is determined when the most homogenous intensity distribution is achieved.

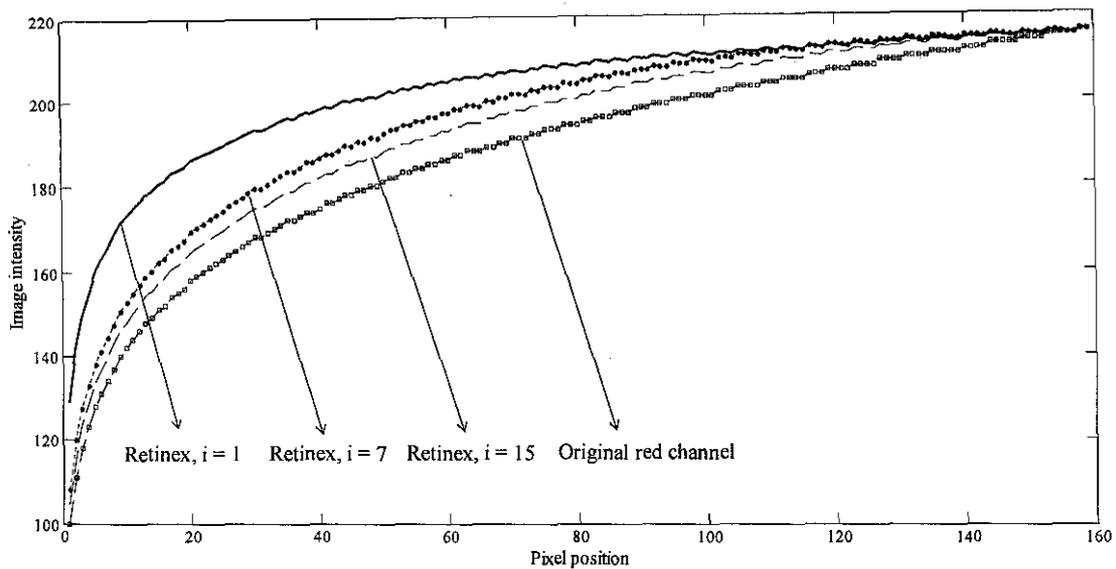


Figure 4.7 Comparison of melanin's intensity variation on an image profile between red channel image model and its Retinex output images with several iterations

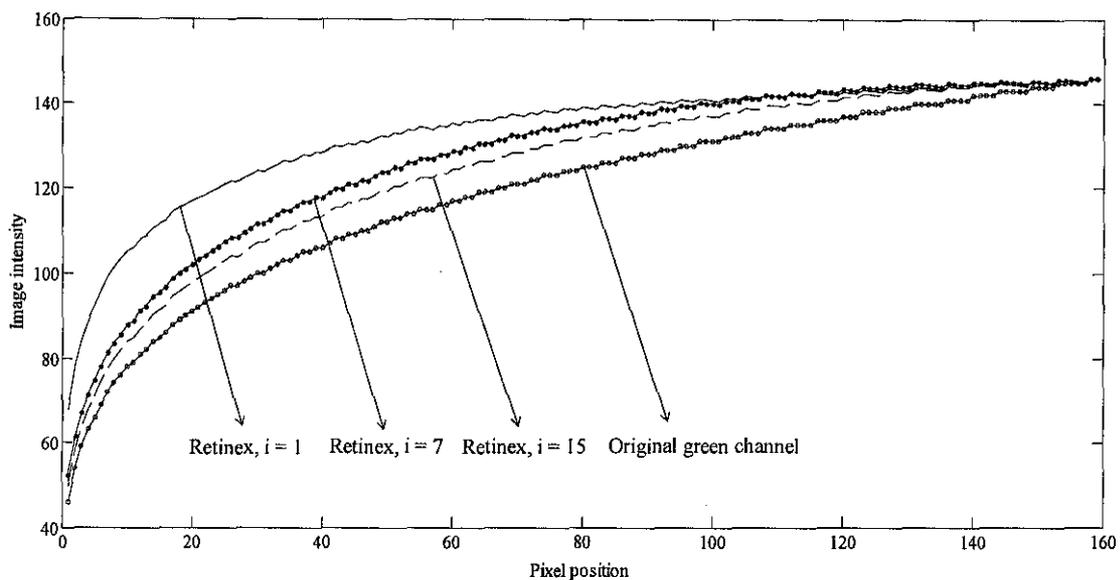


Figure 4.8 Comparison of melanin's intensity variation on an image profile between green channel image model and its Retinex output images with several iterations

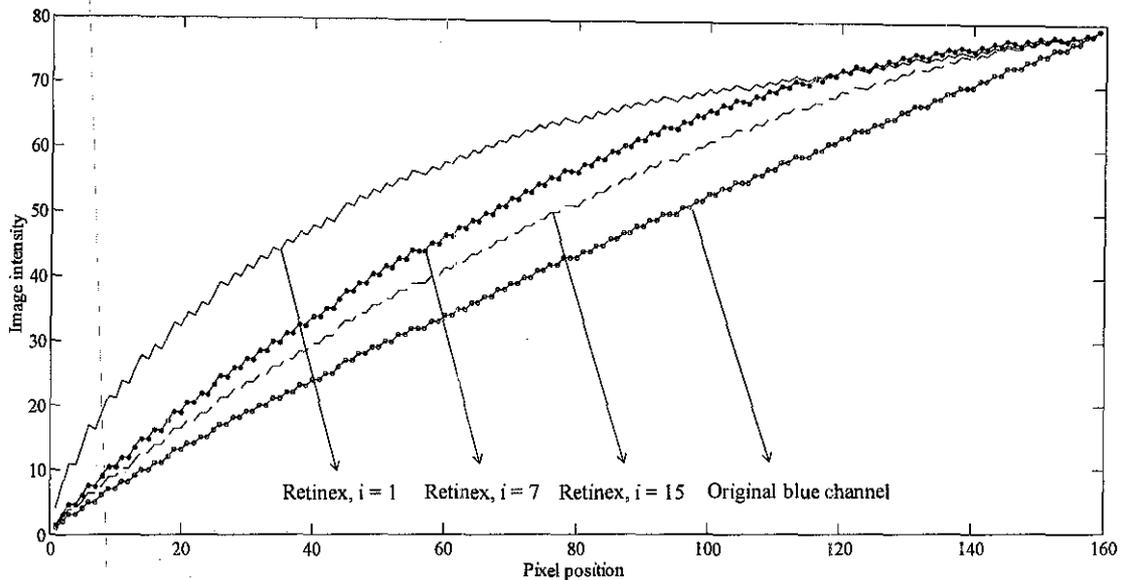


Figure 4.9 Comparison of melanin's intensity variation on an image profile between blue channel image model and its Retinex output images with several iterations

It can be seen from the graphs that different number of iteration gives a different intensity variation. Ideally, a homogenous intensity distribution is indicated by a completely flat line - meaning that all values of intensity are the same. However, it is difficult or even not possible to have a completely flat line in the real situation due to presence of several different objects and/or a varying illumination. From the three aforementioned figures, the more homogeneous the intensities is, the flatter the line will be. Qualitatively, all the three graphs show a similar pattern in which the melanin has the highest intensity when the number of iterations of the Retinex equals to 1. This result is expected since the Retinex-based proposed algorithm is applied on the varied-contrast fundus image model in which the intensity variation is regular and not random. The intensities of pixels in the operated image will be updated iteratively based on the ratio-product-reset-average operation of the Retinex as previously discussed in Section 4.2. The more random the intensity variation is, the higher the optimum number of iterations of Retinex is. Performing Retinex on the varied-contrast fundus image model, as the number of iteration of the Retinex increases, the melanin's intensity values tend to decrease. It means that the most homogeneous melanin's intensity distribution is obtained when the number equals to 1 that makes this as the optimum number of iteration of the Retinex for the melanin in red, green and blue channels.

Opposed to that of the melanin, the intensity of the macular pigment has the highest value at the middle of the image model (Figure 4.6). The intensity value decreases as the pixels position increases and reaches its minimum intensity value for the pixels located at the bottom of the image model where the position is 320 as shown in Figure 4.6. Similar results occur with the macular pigment's intensity variation for red, green and blue channels in which the highest intensity is obtained by the Retinex with the number of iteration equal to 1 as shown in Figure 4.10, Figure 4.11 and Figure 4.12.

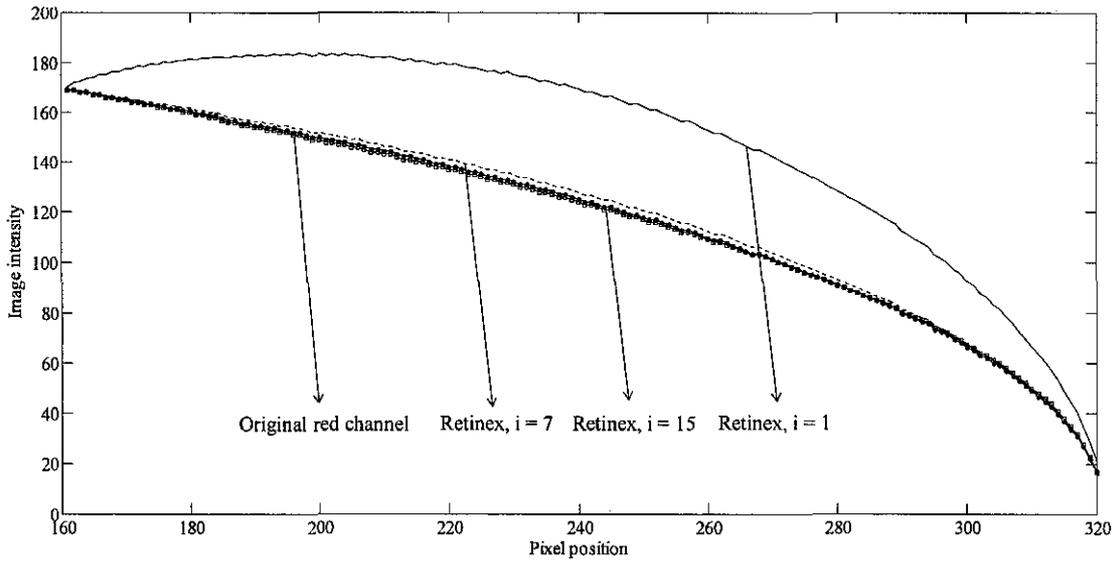


Figure 4.10 Comparison of macular pigment's intensity variation on an image profile between red channel image model and its Retinex output images with several iterations

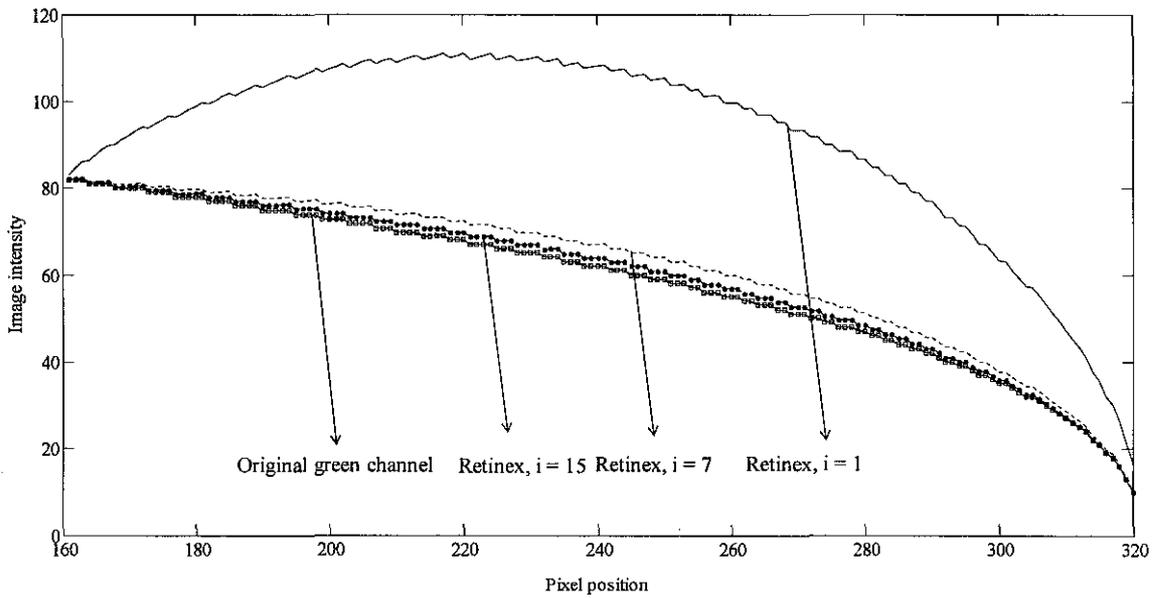


Figure 4.11 Comparison of macular pigment's intensity variation on an image profile between green channel image model and its Retinex output images with several iterations

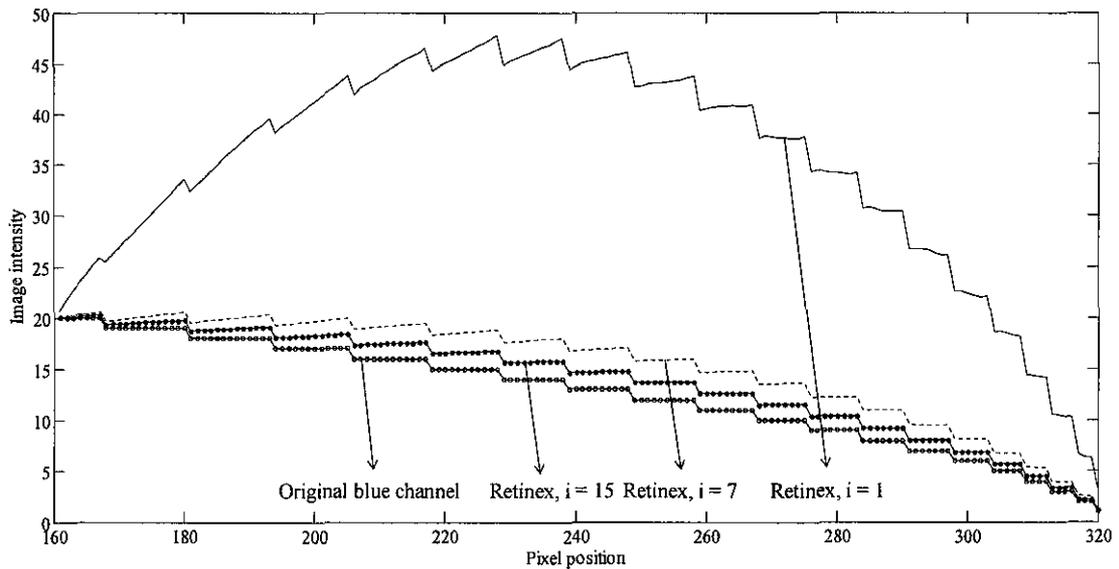


Figure 4.12 Comparison of macular pigment's intensity variation on an image profile between blue channel image model and its Retinex output images with several iterations

In all cases of its variation, the macular pigment's intensity values tend to decrease as the number of iteration of the Retinex increases. These similar results to that of the melanin are expected since the Retinex-based proposed algorithm is applied on the varied-contrast fundus image model in which the intensity variation is regular (not random). Moreover, in the fundus image model, the melanin and the macular pigment have some similar characteristics such as the size of area and regular intensity variation. The increase of the number of iterations of Retinex results in the change of intensities of the operated image according to the ratio-product-reset-average operation of the Retinex. Nevertheless, the objective is to get the most homogeneous intensity distribution. The more random the intensity variation is, the higher the optimum number of iteration of Retinex will be. Qualitatively, the image undergoing Retinex will look brighter indicated by the increase of intensity values. Quantitatively, the optimum number of iteration of Retinex is obtained when the operated image has the highest kurtosis measured from its intensity distribution. Quantitative results based on kurtosis will be further discussed in this section. Moreover, similar to the melanin, the macular pigment obtained by the Retinex with the number of iteration equal to 1 has the most homogeneous melanin's intensity distribution and appears brighter than that of the Retinex with more numbers of iteration. Hence, the optimum number of iteration of the Retinex for the macular

pigment in red, green and blue channels is equal to 1. The increase of the number of iteration greater than the optimum one will result in more non-homogeneous intensity distributions. It is because the ratio between one image scene and the previous one used in the ratio operation is getting closer to one and the maximum intensity used in the reset operation is also getting smaller due to the regular intensity variation of the fundus image model. Hence, in the fundus image model, increasing the number of iteration of Retinex greater than the optimum one makes the image darker indicated by the reduction of image intensity values.

Moreover, a small difference in the optimum number of iteration of the Retinex is found in the case of the haemoglobin's intensity variation compared to that of the melanin and the macular pigment. Referred to the fundus image model shown in Figure 4.6, the haemoglobin is modelled by 9 vertical straight lines of retinal blood vessel model parallel with varied width from 1 to 12 pixels and the same length that is 250 pixels. The retinal blood vessel model has the highest intensity value at the middle of the image where the pixel position is 160 and its intensity values decrease as the pixel position vertically moves both up and down. The lowest intensity value meanwhile belongs to the pixels position at 35 as it moves up and to that of at 285 as it moves down. Results for applying different number of iteration of the Retinex on the haemoglobin are shown in Figure 4.13, Figure 4.14 and Figure 4.15.

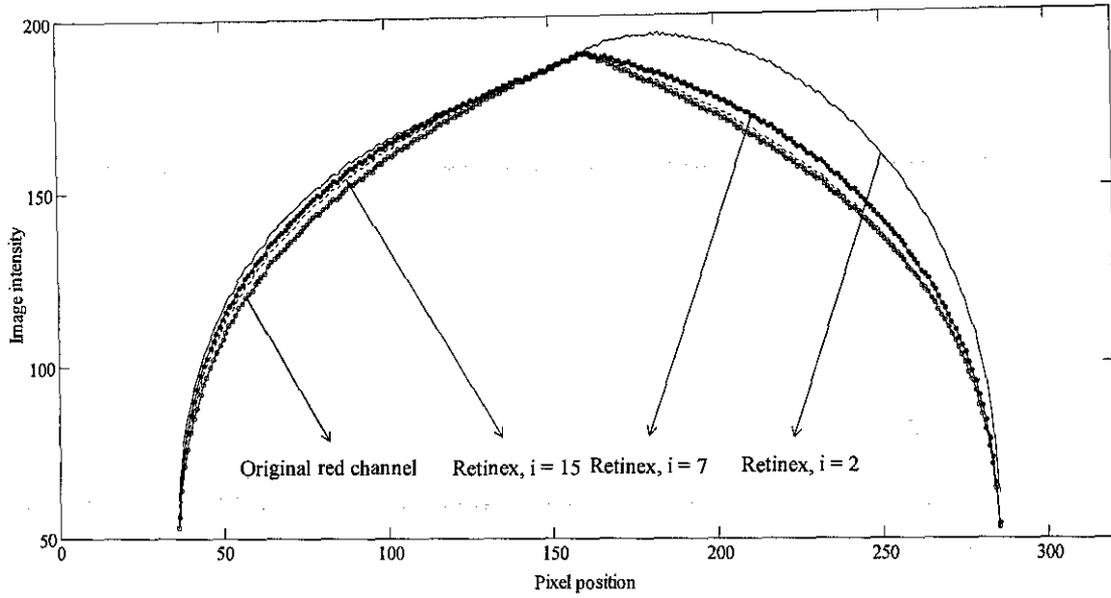


Figure 4.13 Comparison of haemoglobin's intensity variation on an image profile between red channel image model and its Retinex output images with several iterations

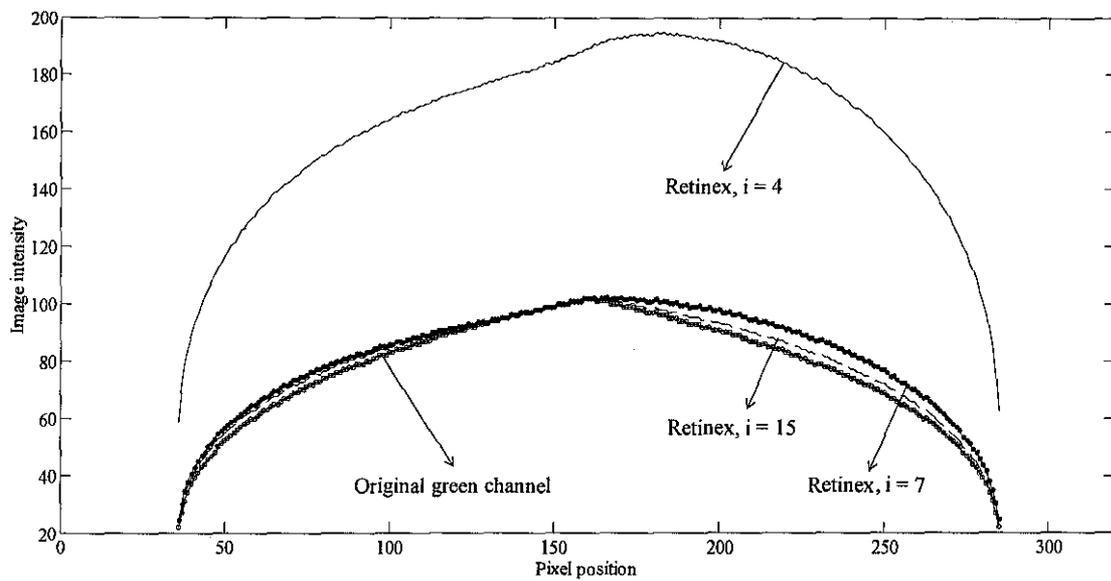


Figure 4.14 Comparison of haemoglobin's intensity changes on an image profile between green channel image model and its Retinex output images with several iterations

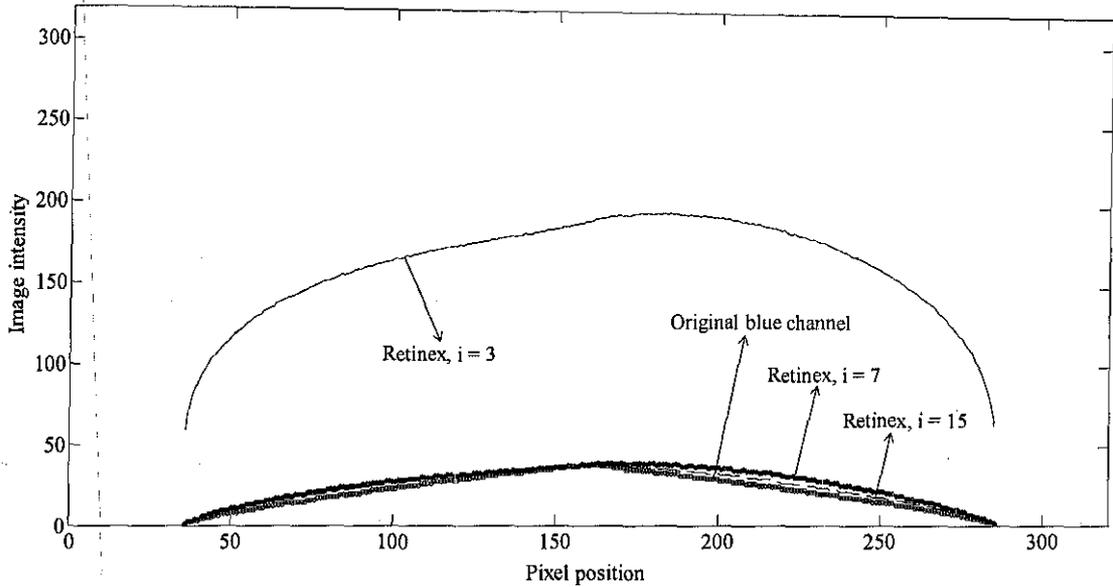


Figure 4.15 Comparison of haemoglobin's intensity changes on an image profile between blue channel image model and its Retinex output images with several iterations

Unlike that of the melanin and the macular pigment that have the same optimum number of iteration for all the included channels, the optimum number of iteration of the Retinex for the haemoglobin is different in each channel. It is found that the optimum numbers of iteration of the Retinex in red, green and blue channels are 2, 4 and 3 respectively. These results obtained by the haemoglobin are a little bit different from that of the previous two. It is because the size and structure of the retinal blood vessel (haemoglobin) represented by nine vertical lines is different from that of the melanin and macular pigment. However, since the intensity variation of the haemoglobin is regular (not being random), the optimum number of iteration of Retinex is relatively small then.

Qualitatively, it is easy to determine the optimum number of iteration by observing the graphs in which the line showing the image intensity distribution tends to be flatter. However, in such an automated algorithm, a specified parameter is needed to determine this optimum number of iteration. Since the optimum number of iteration of the Retinex is related to the homogeneity of the intensity distribution, kurtosis is then used as a parameter to determine this number. The higher the kurtosis is, the more homogenous the intensity will be. In other words, the highest kurtosis that can be obtained after performing several iterations corresponds to the most

homogenous intensity distribution that can be achieved. Once the highest kurtosis is determined, the related number of iteration is selected as the optimum number and its corresponding Retinex output image can be used as the best output images. Table 4-1 shows the highest kurtosis of melanin, macular pigment and haemoglobin data obtained from red, green and blue channel in relation to the optimum number of iteration of the Retinex.

Table 4-1 Kurtosis and related optimum number of iteration for Retinex algorithm for melanin, macular pigment and haemoglobin in each colour channel

	Melanin			Macular pigment			Haemoglobin		
	Red	Green	Blue	Red	Green	Blue	Red	Green	Blue
Kurtosis	7.76	8.26	7.75	6.98	8.06	8.20	6.25	6.58	7.23
Optimum number of iteration	1	1	1	1	1	1	2	4	3

However, in the application, the optimum number of iteration is possibly different between one and another component. For instance, as shown in Table 4-1, even though the optimum number of iteration of the Retinex between the melanin and the macular pigment is the same, it does not occur for the haemoglobin. In the case of the fundus image model, even though these three components, i.e. the melanin, the macular pigment and the haemoglobin present all together, it is easy to separate these components using the reference masks shown in Figure 4.5. Hence, it is possible to use different optimum number of iteration for each of the components in the fundus image model. However, in the real application, there is no reference mask; thus, only one of the components is used as the reference in order to determine the optimum number of iteration.

In the real fundus images, the problem of varied contrast, particularly in the macular region, is due to the macular pigment. Therefore, the highest kurtosis obtained from the macular pigment data is used to determine the optimum number of iteration of the Retinex in each channel. These Retinex output images consisting of three colour channels are subsequently used as the input for the contrast enhancement process based on ICA. Figure 4.16 shows the original red, green and blue channels of the retinal fundus image model and their corresponding Retinex output images in red, green and blue channels based on the optimum number of iteration obtained from the macular pigment.

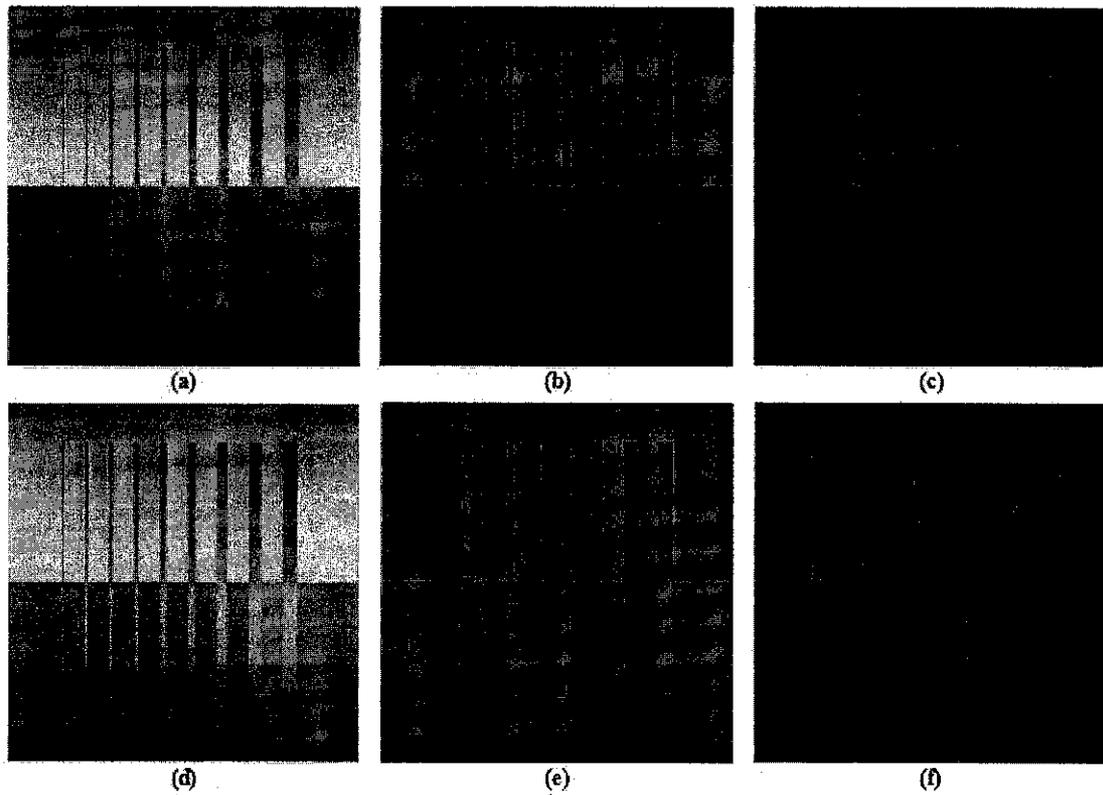


Figure 4.16 Retinal fundus image model in (a) Red, (b) Green and (c) Blue channel images and their corresponding Retinex outputs in (d) Red, (e) Green and (f) Blue channel images

As depicted in Figure 4.16, the Retinex output images shows better visualisation than that of the original images as the image intensity is more homogenous. The lower intensity values of the original input images that make the image seemingly to be darker have been brought up to higher intensity values in the output images that in turn make the output image seemingly to be brighter. As a result, the retinal blood vessel model in the output image is more clearly visible than that of the input image. A significant improvement can be seen from blue channel image of the Retinex (Figure 4.16(f)) with more homogeneous intensity than that of the original blue channel input images (Figure 4.16(c)). Retinal blood vessel model particularly in the macular pigment from the blue channel image that cannot be clearly seen is better visualised in the corresponding Retinex output image because of more homogenous intensity of the macular pigment.

The more homogenous intensity obtained implies that the varied contrast of the

image model has been reduced. Retinex is able to convert the darker area or sometimes referred to as shadow area into a brighter appearance. With the objective of contrast normalisation, the dynamic contrast of the image has been significantly reduced by applying the Retinex algorithm.

In some cases, noise present in the image is represented as the standard deviation or the variance of image pixels. The more homogeneous intensity then could lead to a lower standard deviation. This implies that the noise of the image is also reduced. Hence, the normalisation of the varied contrast significantly improves the quality of the image by reducing the intensity variation as well as the noise present in the image. With the normalised intensity and reduced noise, the contrast of the image can be further enhanced without enhancing the noise (artefacts).

The result of a more homogeneous intensity distribution is expected since the use of the Retinex algorithm with its ratio-product-reset-average operation reduces the dynamic contrast of the image intensities. With the reference of the maximum intensity of the image scene, the lower intensities are brought up into higher values, which result in a reduction of dynamic contrast. If a maximum intensity value is found in the iteration process, it will be used in the reset operation to update the reference. Therefore, not only does the dynamic range of intensity values reduce but also the lower intensities are brought up into the higher ones resulting in a brighter appearance of the image.

This contrast-normalised image is advantageous for the contrast enhancement process since the intensity distribution of an image component is set to be as more homogeneous as possible and the noise present in the image has been reduced. Hence, the subsequent contrast enhancement process will enhance the contrast among the image components.

4.6.2 Contrast Enhancement

The validation of RETICA for the contrast enhancement stage is performed on the low-contrast fundus image model as shown in Figure 4.17.

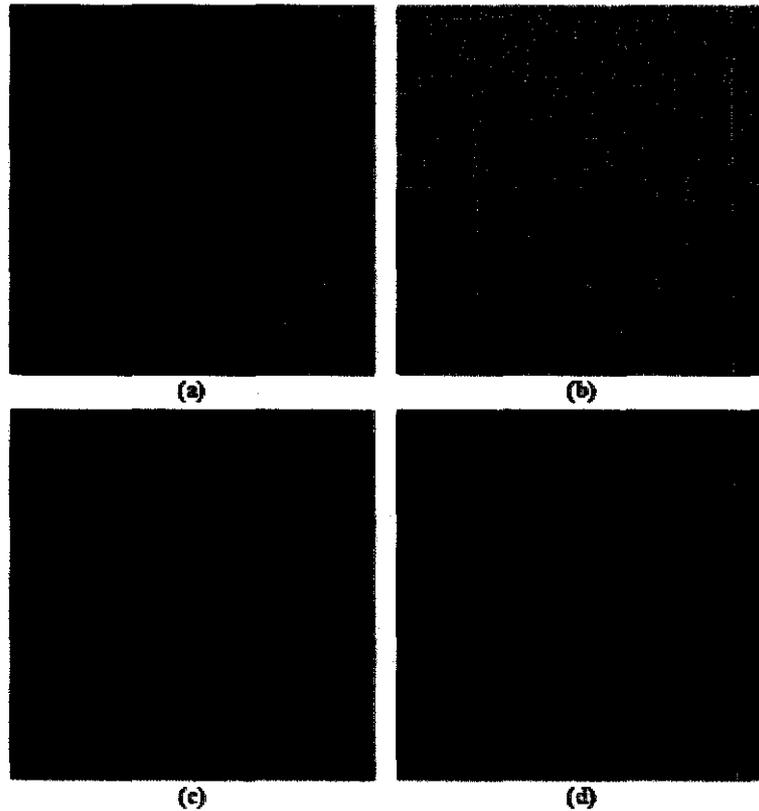


Figure 4.17 (a) Low-contrast fundus image model and its (b) Red, (c) Green and (d) Blue channel images

The low-contrast fundus image model (Figure 4.17(a)) is separated into three, i.e. red (Figure 4.17(b)), green (Figure 4.17(c)) and blue (Figure 4.17(d)) channel images and these images are inputted to the second stage of RETICA for contrast enhancement based on the ICA. The validation of the ICA on the low-contrast fundus image model is performed by separating the components (melanin, macular pigment and haemoglobin) that are mixed in the red, green and blue channel images and determining the haemoglobin-related independent component that gives the best contrast of the retinal blood vessels.

The ICA algorithm works based on an assumption that the independent components are mixed in the input images. The output images that show the separation of the independent components are obtained by maximisation of the non-Gaussianity of the components since non-Gaussianity is related to the independence. In this work, the objective is to enhance the contrast of the retinal blood vessels. Therefore, the haemoglobin-related independent component is selected since the best

contrast of retinal blood vessels is obtained from the haemoglobin-related IC image. Results of performing the ICA on the low-contrast fundus image model with the comparison to the green band image are shown in Figure 4.18.

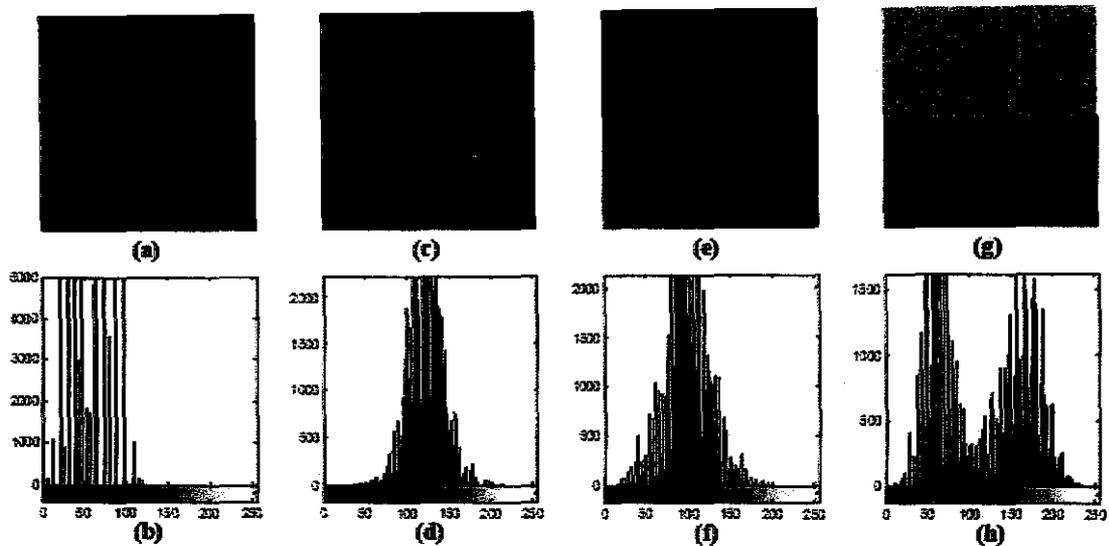


Figure 4.18 (a) Green band image with (b) its corresponding histogram, (c) ICA 1st component image with (d) its corresponding histogram, (e) ICA 2nd component image with (f) its corresponding histogram, (g) ICA 3rd component image with (h) its corresponding histogram

It can be seen from Figure 4.18 that the proposed algorithm successfully separates the components into three independent components. The 1st and 2nd independent components are related to the melanin and the macular pigment respectively. The 3rd independent component is related to the haemoglobin. The order of the components is not unique meaning that if the fundus image model undergoes the ICA for the second, third and so forth, the order of the components might be different. However, it is not a problem since the independent components can be identified either qualitatively or quantitatively.

Qualitatively, the IC image is identified by visual inspection. Moreover, the histogram of the green band image (Figure 4.18(b)) has been shifted from lower to higher intensity values and more fairly distributed as shown by histograms of the IC images. In Figure 4.18(d) and Figure 4.18(f), the histograms tend to be normal having specific mean values. Nevertheless, unlike the previous two histograms of 1st and 2nd IC images, the histogram of 3rd IC shown in Figure 4.18(h) has two peaks and fairly

distributed in the whole intensity ranging from 0 to around 250. These two peaks are related to the mean values of the intensity of the melanin and the macular pigment. Furthermore, the mean of haemoglobin's intensity is predicted to lie between these two peaks. The higher the difference between the mean of haemoglobin's intensity and that of the melanin is, the higher the contrast of retinal blood vessels will be. This situation also occurs for the haemoglobin and the macular pigment in which the higher the difference between the mean of intensity of the haemoglobin and that of the macular pigment is, the higher the contrast of retinal blood vessels will be.

Quantitatively, the IC image meanwhile is identified based on the statistics of intensity distribution of the related components as shown in Table 4-2. The parameter of contrast of retinal blood vessels (C_{av}) as defined in equation (4-9) is used to select the haemoglobin-related IC image, which has the highest C_{av} .

Table 4-2 Statistics of green band of low-contrast image model and ICA component images

	Green band		ICA 1 st component		ICA 2 nd component		ICA 3 rd component	
	Mean	St.dev	Mean	St.dev	Mean	St. dev	Mean	St. dev
Melanin (Mel)	78.84	13.14	134.23	18.73	99.04	27.53	168.18	22.38
Macular pigment (MP)	35.18	9.73	133.73	16.11	98.58	12.82	63.21	15.67
Haemoglobin (BV)	62.13	20.17	128.50	30.62	99.91	36.16	133.70	32.35
BV - Mel	16.71	7.02	5.73	11.89	0.86	8.62	34.48	9.97
BV - MP	26.95	10.43	5.23	14.51	1.33	23.34	70.49	16.68
Contrast of retinal blood vessels (C_{av})	21.83		5.48		1.10		52.78	

As can be seen from Table 4-2, among the IC images, the best contrast of retinal blood vessels indicated by the highest C_{av} belongs to the 3rd IC image with C_{av} of 52.78. The 3rd IC image which is also the haemoglobin-related IC image has significantly higher contrast of retinal blood vessels than that of the green band. Expectedly, the best contrast of retinal blood vessels belongs to the haemoglobin-related IC image since the haemoglobin, which is related to retinal blood vessels, is extracted from its mixture with melanin and macular pigment and results in the

contrast enhancement of retinal blood vessels. With the extraction of the retinal blood vessels, the contrast of retinal blood vessels with two kinds of background, namely the melanin and the macular pigment, is also enhanced. Using the contrast of retinal blood vessels in the green band as the reference, the haemoglobin-related IC image achieves *CIF* of 2.42. This haemoglobin-related IC image is advantageous for showing the most-contrasted retinal blood vessels.

From the validation result for the contrast enhancement, the ICA successfully separates the independent components, i.e. the melanin, the macular pigment and the haemoglobin. The haemoglobin-related IC image shows higher contrast of retinal blood vessels than that of the green band image with *CIF* of 2.42 for the low-contrast fundus image model.

4.6.3 RETICA for Image Enhancement

The third validation of RETICA for image enhancement that contains both contrast normalisation and contrast enhancement is conducted on the varied and low-contrast fundus image model as shown in Figure 4.19(a).

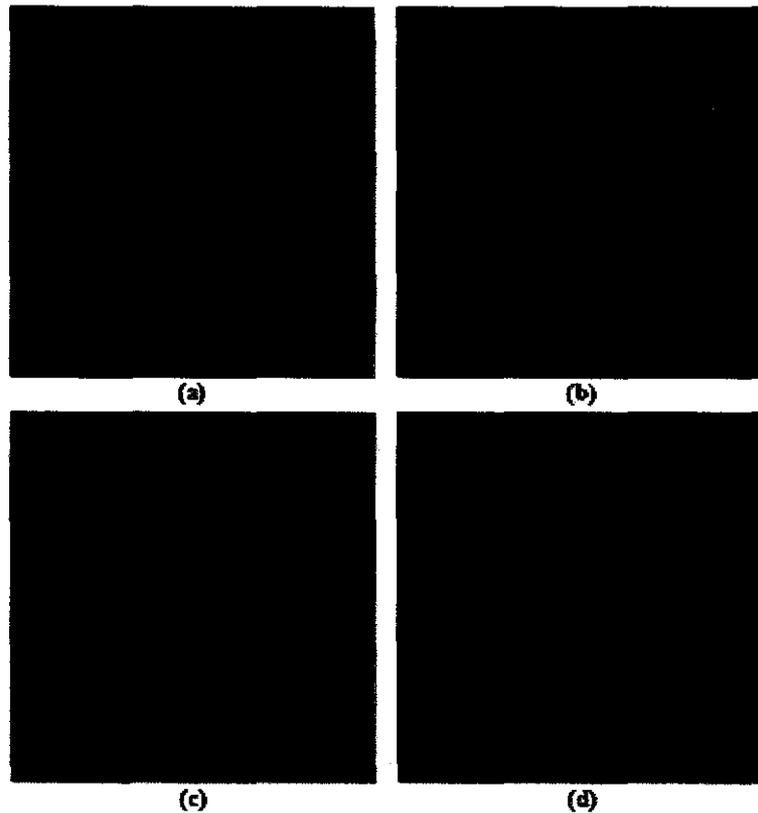


Figure 4.19 Varied and low-contrast fundus image model and its (b) Red, (c) Green and (d) Blue channel images

As shown in Figure 4.19, the varied and low-contrast fundus image model is separated into three, i.e. red (Figure 4.19(b)), green (Figure 4.19(c)) and blue (Figure 4.19(d)) channel images inputted to RETICA. In RETICA, the first stage is for contrast normalisation based on the Retinex and followed by the second stage i.e. contrast enhancement based on the ICA. The same technique for contrast normalisation, as previously explained, is applied for this varied and low-contrast image model. Maximum kurtosis and its related optimum number of iteration obtained from the macular pigment are shown in Table 4-3 and the Retinex output images are shown in Figure 4.20.

Table 4-3 Kurtosis and related optimum number of iteration of RETICA for melanin, macular pigment and haemoglobin in each colour channel of the varied and low-contrast image model

	Melanin			Macular pigment			Haemoglobin		
	Red	Green	Blue	Red	Green	Blue	Red	Green	Blue
Kurtosis	6.30	5.76	5.36	5.06	4.23	3.66	5.60	7.14	2.38
Optimum number of iteration	1	1	1	1	2	29	1	7	1

The Retinex output images as shown from Figure 4.20(d) to Figure 4.20(f) are obtained based on these optimum numbers of iteration of the Retinex. They are subsequently inputted to the second stage of RETICA, namely contrast enhancement based on the ICA. As previously explained, the same technique for contrast enhancement is applied to separate the components (melanin, macular pigment and haemoglobin) that are mixed in the contrast-normalised red, green and blue channel images. The haemoglobin-related IC that gives the best contrast of the retinal blood vessels is then determined. Figure 4.20(g) to Figure 4.20(i) show the output images of contrast enhancement based on the ICA.

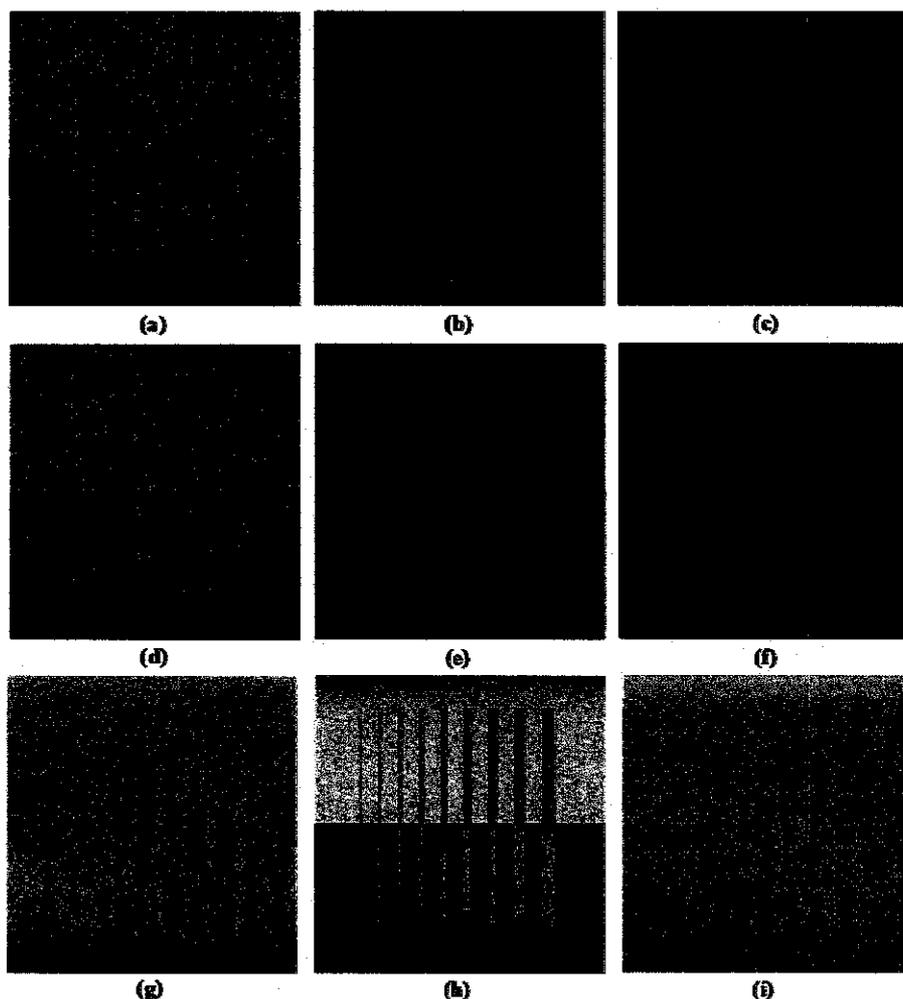


Figure 4.20 Varied and low-contrast fundus image model in (a) Red, (b) Green and (c) Blue channel images and their corresponding contrast normalisation outputs in (d) Red, (e) Green and (f) Blue channel images and contrast enhancement outputs showing (g) 1st IC image, (h) 2nd IC image and (i) 3rd IC image

RETICA successfully separates the components into three independent components. It was mentioned earlier that the order of the components is not unique; the order of the components for this reason might be different if the related input image undergoes RETICA for the second, third and so forth. Referring to the results obtained, the haemoglobin is shown by the 2nd IC, while the 1st and 3rd independent components are related to the melanin and the macular pigment respectively. Even though the haemoglobin-related IC can be qualitatively determined by visual inspection, quantitative results are required so that RETICA is applied in such a computerised medical diagnosis system. RETICA determines the haemoglobin-related IC by measuring the kurtosis of each IC and determining the least value of

kurtosis among the related ICs. Table 4-4 shows the statistics of the green band of the varied and low-contrast fundus image model with its corresponding ICA images. The intensity I is measured in two forms, i.e. I_{norm} and I , in which I_{norm} shows normalisation of I . I_{norm} ranges from 0 to 1, whilst I ranges from 0 to 255.

Table 4-4 Statistics of green band of varied and low-contrast image model and ICA images

	Green band (Intensity I)		ICA 1 st comp. (Intensity I)		ICA 2 nd comp. (Intensity I)		ICA 3 rd comp. (Intensity I)	
	I_{norm}	I	I_{norm}	I	I_{norm}	I	I_{norm}	I
Melanin (Mel)	0.14	36.40	0.63	159.51	0.72	183.78	0.61	154.45
Macular pigment (MP)	0.03	7.87	0.59	149.93	0.32	80.70	0.64	163.66
BV (Mel)	0.07	18.95	0.62	157.09	0.40	101.43	0.62	157.38
BV (MP)	0.07	18.94	0.64	164.04	0.60	152.01	0.64	163.04
Contrast of BV (C_{av})	0.06	14.26	0.03	8.27	0.30	76.83	0.01	1.77
St. dev	0.06	15.11	0.11	28.12	0.23	57.86	0.11	27.48
Contrast norm. (R_{sdc})	1.060		3.403		0.753		15.486	

As shown in Table 4-4, the highest C_{av} belongs to the 2nd IC image which is also the haemoglobin-related IC image with C_{av} of 76.83. Moreover, the 2nd IC image has R_{sdc} of 0.753 which is the lowest among the IC images. It means that the 2nd IC has the best contrast of retinal blood vessels as well as the least varied contrast among the IC images. As expected, the contrast of the retinal blood vessel is enhanced since the haemoglobin IC, which is related to retinal blood vessels, can be extracted from its mixture with the melanin and the macular pigment. This contrast normalised and enhanced image is advantageous as a pre-processed image to be further segmented and analysed in a computerised medical diagnosis system.

4.6.4 Comparative Study

To evaluate the performance of RETICA, the varied and low-contrast fundus image model undergoes the proposed algorithm and the other six selected algorithms as well. The parameters, i.e. the contrast of retinal blood vessels (C_{av}), the image contrast

normalisation measured as the ratio between standard deviation and average contrast (R_{sdc}), and the contrast improvement factor (CIF), are used for the comparative study.

The six selected algorithms for comparative study work only at one channel out of three channels. Therefore, the channel showing the best image quality in relation to optimum contrast of retinal blood vessels and the less noise present in the image must be selected prior to undergoing the algorithms. To select the optimum image quality, three parameters, i.e. C_{av} as defined in (4-9), standard deviation of component's intensity (σ) and R_{sdc} as defined in (4-11) are measured. Even though the C_{av} shows the contrast of retinal blood vessels measured from a specific channel, it is not enough to determine which channel has to be selected. The other parameters, such as σ and R_{sdc} are required since these parameters represent the quality of the image in relation to the noise present in the image. The more the noise present in the image is, the worse the quality of the image will be. Moreover, performing selected image enhancement algorithm on the image with noise leads to the enhancement of noise in the enhanced image. Hence, the selected algorithms must be performed on the image channel with as high contrast as possible but with as less noise as possible. A comparison of contrast of retinal blood vessels among three channels of the varied and low-contrast fundus image model is shown in Table 4-5.

Table 4-5 Statistics of Red, Green and Blue channels of the varied and low-contrast fundus image model

	Red channel (Intensity I)		Green channel (Intensity I)		Blue channel (Intensity I)	
	I_{norm}	I	I_{norm}	I	I_{norm}	I
Melanin (mean)	0.40	100.63	0.14	36.40	0.015	3.77
Macular pigment (mean)	0.13	32.07	0.03	7.87	0.004	1
BV in melanin (mean)	0.28	71.03	0.07	18.95	0.007	1.89
BV in macular pigment (mean)	0.28	71.16	0.07	18.94	0.007	1.87
Contrast of retinal vessels (C_{av})	0.14	34.35	0.06	14.26	0.005	1.38
Standard deviation (σ)	0.15	37.04	0.06	15.11	0.009	2.32
Contrast normalisation (R_{sdc})	1.078		1.060		1.686	

According to the statistics shown in Table 4-5, the highest C_{av} belongs to the red channel image with C_{av} of 34.35 followed by the green channel image with C_{av} of 14.26. However, the red channel has a significantly higher σ than that of the other

two channels. The lowest σ , which is 2.32, belongs to the blue channel; yet the contrast of retinal blood vessels of the blue channel is significantly low with C_{av} of only 1.38. Ideally, the image will be selected for that with the standard deviation σ is as low as possible and the contrast of retinal blood vessels C_{av} is as high as possible. Nevertheless, those two conditions are not agreeable in this situation. Thus, the ratio R_{sdc} is used to further determine the best enhanced image. As previously discussed in Section 4.5, instead of specifically measuring contrast normalisation of the image, the ratio R_{sdc} also indirectly measures image contrast enhancement since it incorporates both σ and C_{av} . The ratio R_{sdc} is derived from the standard deviation σ , which measures the variation of data from its mean value and thus, specifically indicating the homogeneity of image intensity variation. The more homogeneous the intensities is, the more normalised the image contrast will be. Nevertheless, the use of mere standard deviation σ is suitable to measure the homogeneity of one object or area in the image. If there are more than one object, each of which has a different intensity variation, measuring contrast normalisation based on mere standard deviation σ is no longer appropriate. Therefore, the average contrast C_{av} , which measures the average of intensity difference between different objects, is incorporated in the ratio R_{sdc} that specifically measures the contrast normalisation of the image and indirectly measures the contrast enhancement of the image. Moreover, the ratio R_{sdc} of the green channel is the lowest among the others. The lower the ratio R_{sdc} is, the better the contrast normalisation will be as well as the contrast enhancement. Therefore, the green channel is selected to undergo the algorithms for comparative study. In the real application, the green channel is usually selected for enhancement of retinal blood vessels. Here, it is proved from the image model that the contrast of retinal blood vessels in the green channel is actually lower than that of the red one. However, the green channel has the lowest R_{sdc} (1.060) that shows the best contrast normalisation among the three colour channels. The green channel image undergoes six selected algorithms, i.e. CS, HE, AHE, ACE, CLAHE and HF and the results are shown in Figure 4.21.

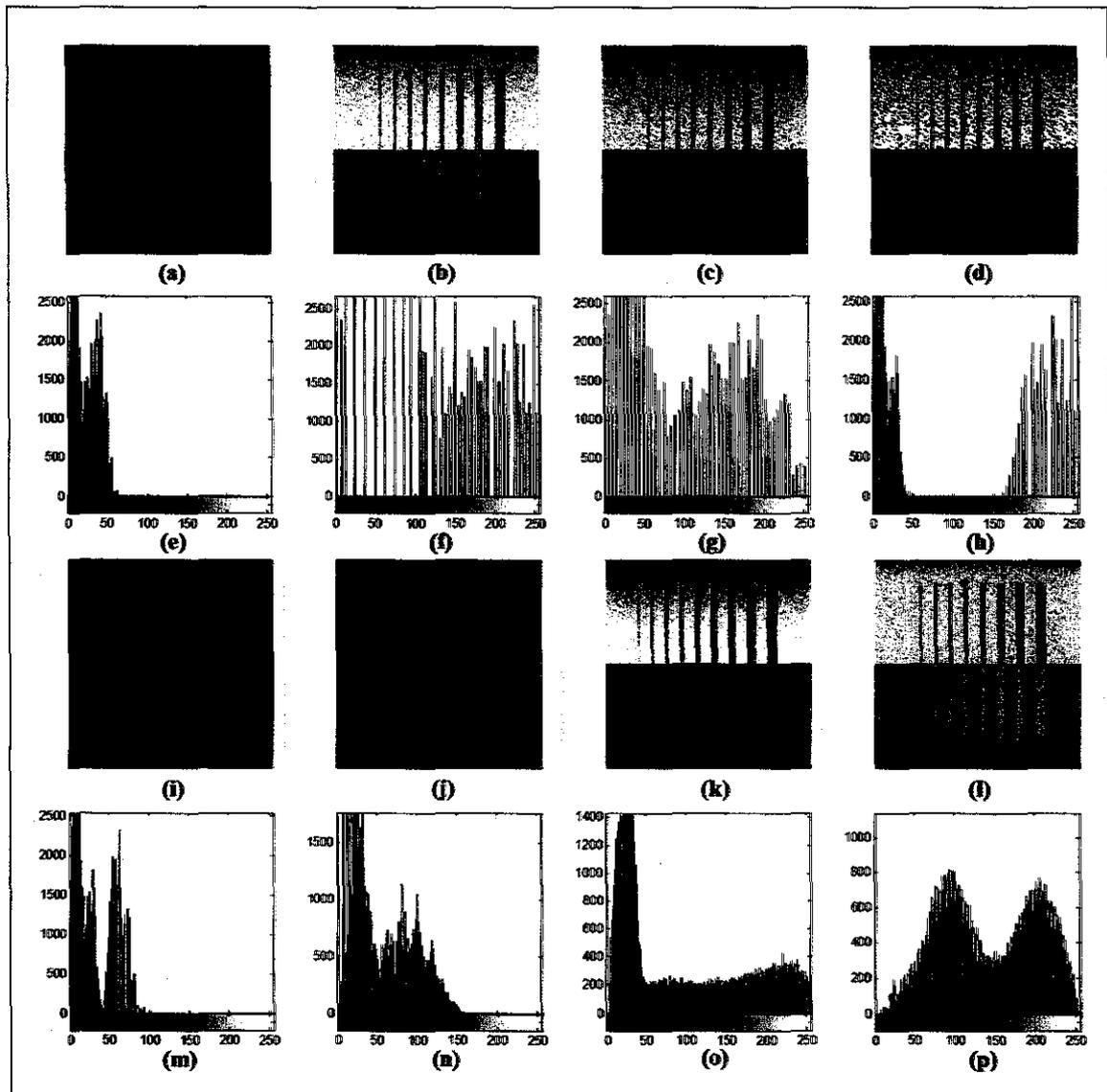


Figure 4.21 (a) Green band image with (e) its corresponding histogram, (b) green band image after HE with (f) its corresponding histogram, (c) green band image after CS with (g) its corresponding histogram, (d) green band image after AHE with (h) its corresponding histogram, (i) green band image after ACE with (m) its corresponding histogram, (j) green band image after CLAHE with (n) its corresponding histogram, (k) green band image after HF with (o) its corresponding histogram and (l) haemoglobin-related component image with (p) its corresponding histogram

As depicted in Figure 4.21, the green band image suffers from both varied and low-contrast. The contrast of the retinal blood vessel model in the macular pigment especially at the bottom of the image is very low. Its histogram (Figure 4.21(e)) also shows that the intensity distribution is concentrated at the low intensities values, meaning that the contrast of the image is low. Applying different image enhancement methods on the varied and low image model changes the histogram of the image

model. Enhanced images obtained by HE (Figure 4.21(b)) and CS (Figure 4.21(c)) have similar pattern of histograms (Figure 4.21(f-g)). These histograms show moderately and the equalised intensity distribution from 0 to 255 results in better contrast of retinal blood vessel model. Unlike CS and HE, AHE does not qualitatively produce better enhanced image (Figure 4.21(d)) even though the contrast of retinal vessel model is further enhanced due to amplification of noise. Although the contrast of retinal vessels model in the melanin backhroud is significantly enhanced, AHE fails to enhance the low contrast of retinal vessels in the macular pigment due to low and varied contrast occurred in the image model. Furthermore, ACE produces slightly better contrast of retinal vessels model (as shown in Figure 4.21(i)) with no significant noise amplification as suffered by AHE. In general, these techniques – CS, HE, AHE and ACE – effectively enhance the contrast of the objects in the image model, but they do not overcome the problem of varied contrast occurred in the image model.

Unlike the aforementioned comparative selected algorithms, CLAHE and HF are better in solving the problem of varied contrast since it does not cause over-enhancement in the image models (Figure 4.21(j-k)). Nevertheless, the contrast enhancement of the object obtained by CLAHE is not as good as CS and HE as seen from the histogram of the image model by CLAHE (Figure 4.21(n)). However, CLAHE succesfully increases its dynamic contrast resulting in better contrast of retinal blood vessel model than that of the green band image. In qualitative, HF produces better contrast of retinal vessels model (as shown in Figure 4.21(k)) than that of CLAHE. This result is further confirmed by its histogram (Figure 4.21(o)) showing more equalised intesity distribution than that of CLAHE. Nevertheless, it fails to overcome the problem of over-enhancement resulting in the 'washed-out' appearance of the image moodel.

RETICA overcomes both the problems of varied and low-contrast of the image model as in the haemoglobin-related IC image (Figure 4.21(l)). The haemoglobin-related IC image qualitatively shows a better contrast of retinal blood vessel model than that of the enhanced images produced by other selected enhancement methods.

Moreover, the histogram of the haemoglobin-related IC image (Figure 4.21(p)) shows better dynamic range than that of the green band and the CLAHE due to its more equalised histogram; yet, the histogram of the haemoglobin-related IC image is more concentrated than that of other comparative selected algorithms resulting in higher contrast of retinal blood vessel model.

Histogram of an image with better contrast will normally have a non Gaussian distribution. Ideally, if there are two or more objects appearing in the image, the histogram will have the number of peaks that are the same as the number of objects. Each peak relates to the mean intensity value of the corresponding object that is represented by some specific intensity distribution. The further the distance between these peaks is, the better the contrast of the image will be and the more non-Gaussian distribution the intensity of the object has, the less varied contrast the image is. In the case of the haemoglobin-related IC image, the histogram of 3rd IC as previously explained has two peaks that are related to the mean values of the melanin's and the macular pigment's intensity. A higher difference between the mean of haemoglobin's intensity that is predictably located between these two peaks and that of the melanin or the macular pigment, will result in a higher contrast of retinal blood vessels. Quantitative results represented by three parameters, i.e. contrast of retinal blood vessels (C_{av}), standard deviation (σ) and contrast normalisation (R_{sdc}) are used to measure the quality of the enhanced image as shown in Table 4-6.

As shown in Table 4-6, RETICA achieves the best contrast of retinal blood vessel model with the highest C_{av} of 76.83 among the selected image enhancement methods followed by AHE and CS in the second and the third column respectively. However, to determine the quality of the enhanced image needs not only the contrast of the retinal blood vessels, but also the contrast normalisation of the image represented by the reduction of the varied contrast including noise that results from the enhancement process. Hence, σ and R_{sdc} are used to measure the contrast normalisation of the image.

Table 4-6 Comparative results of several image enhancement algorithms on the varied and low-contrast fundus image model

		Melanin	Macular pigment	BV (mel)	BV (mac)	C_{av}	σ	R_{sdc}
Green band (Intensity I)	I_{norm}	0.143	0.031	0.074	0.074	0.056	0.059	1.060
	I	36.40	7.87	18.95	18.94	14.26	15.11	
HE (Intensity I)	I_{norm}	0.777	0.237	0.499	0.499	0.270	0.293	1.086
	I	198.16	60.50	127.28	127.24	68.81	74.71	
CS (Intensity I)	I_{norm}	0.660	0.119	0.329	0.329	0.271	0.289	1.067
	I	168.37	30.24	83.83	83.83	69.11	73.73	
AHE (Intensity I)	I_{norm}	0.599	0.031	0.092	0.093	0.285	0.368	1.292
	I	152.73	7.87	23.49	23.95	72.66	93.86	
ACE (Intensity I)	I_{norm}	0.196	0.031	0.076	0.076	0.083	0.93	1.127
	I	50.00	7.87	19.46	19.50	21.08	23.77	
CLAHE (Intensity I)	I_{norm}	0.357	0.095	0.151	0.225	0.168	0.147	0.876
	I	91.02	24.16	38.62	57.39	42.81	37.51	
HF (Intensity I)	I_{norm}	0.720	0.097	0.349	0.253	0.264	0.329	1.248
	I	183.59	24.80	88.87	64.63	67.27	83.97	
ICA (Intensity I)	I_{norm}	0.577	0.177	0.388	0.388	0.200	0.210	1.051
	I	147.23	45.15	98.84	98.98	51.11	53.67	
RETICA (Intensity I)	I_{norm}	0.721	0.316	0.398	0.596	0.301	0.227	0.753
	I	183.78	80.70	101.43	152.01	76.83	57.86	

The green band image has the value of σ which is 15.11 and after performing several enhancement methods, the minimum value of σ belongs to the enhanced image after ACE followed by CLAHE. Even though the enhanced images obtained by AHE, CS, HE and HF show better contrast of retinal blood vessels model than that of CLAHE and ACE, they have significantly higher value of σ than that of CLAHE and RETICA. It means that the varied contrast and noise are more in AHE, CS and HE than that in CLAHE and RETICA. It occurs due to the nature of the AHE, CS and HE in which they enhance not only specific objects, but also noise that presents in the image. It can be seen from their histograms in which the distribution is made more equalised and spread out. Therefore, not only objects of interest, but also noise and the varied contrast are being enhanced resulting in the over-enhanced image. Parameter R_{sdc} as previously explained is used to measure image quality in terms of contrast normalisation and enhancement by considering the ratio between σ and C_{av} . Moreover, as shown in the Table 4-6, ICA with C_{av} of 51.11 produces higher contrast of retinal vessels model than that of CLAHE with C_{av} of 42.81; however, σ of

CLAHE is less than that of ICA. It means, merely applying ICA to the green band image can produced better contrast of retinal vessels model in the enhanced image but still enhance the noise.

RETICA achieves the lowest R_{sdc} , which is 0.753 among the selected image enhancement methods and the green band image. It means that RETICA can enhance image with the optimum contrast normalisation and enhancement compared to other image enhancement methods. Moreover, using the green band image as the reference, a contrast improvement achieved from the selected image enhancement methods can be measured. A comparative result is illustrated in Figure 4.22.

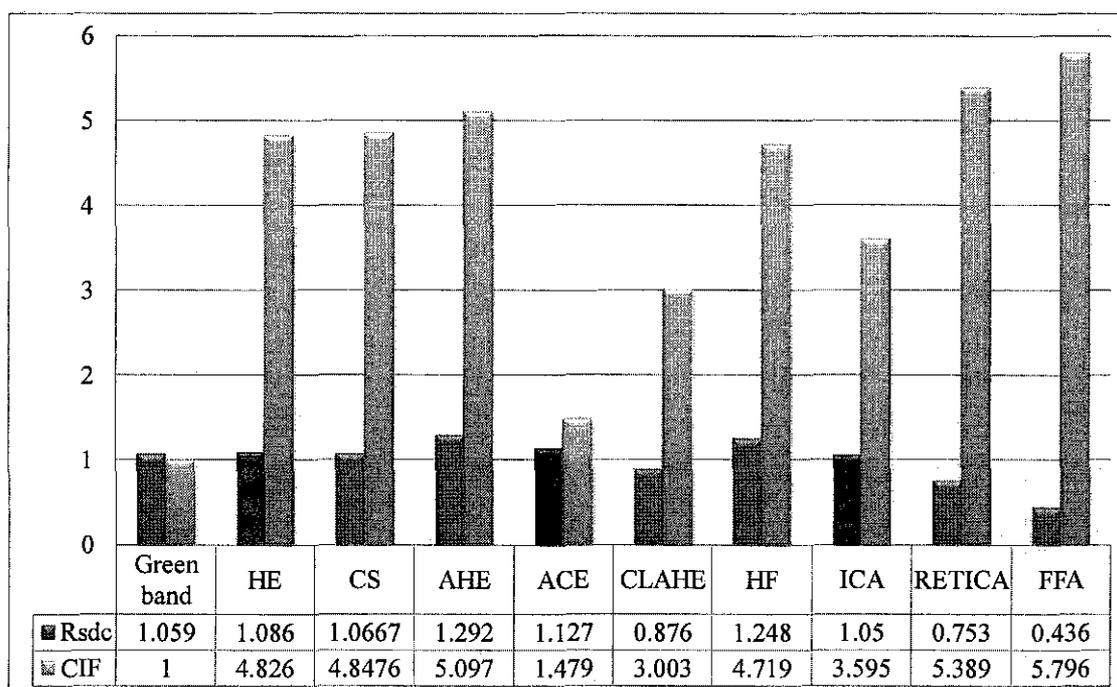


Figure 4.22 Contrast improvement factor (CIF) and ratio (R_{sdc}) between standard deviation and average contrast of the varied and low fundus image model after performing seven different algorithms

Figure 4.22 shows that among the selected non-invasive digital imaging enhancement methods, RETICA is the one achieving the highest contrast of the retinal blood vessels in the varied and low-contrast fundus image model with CIF of 5.389 which is slightly lower than that of the FFA with CIF of 5.796. The highest contrast improvement obtained by RETICA compared to other non-invasive image enhancement methods, such as AHE with 5.097, CS with 4.848, HE with 4.826, HF

with 4.719, followed by ICA with 3.595 and CLAHE with 3.003 and the ICA with 3.595 is predicted. Since the fundus image model is varied and low in contrast, RETICA first addresses the problem of varied contrast using the contrast normalisation based on the Retinex and is followed by contrast enhancement based on the ICA. Contrast normalisation significantly reduces the intensity variation and minimises the noise present in the image so that the image can be further enhanced without enhancing the noise. Noise in the image is represented as a standard deviation or a variance of image intensities, which moreover can also be used to compare the contrast of two different images [52-53].

The two common problems, i.e. varied contrast and low contrast have been addressed by RETICA, and expectedly, the result of image enhancement is better than that of the other selected non-invasive image enhancement methods that address mostly only the problem of low contrast. The common image enhancement methods such as AHE, CS and HE fail to produce better-enhanced images in that they do not specifically address the problem of noise present in the image. They are mainly focused to enhance the contrast of the image. For this reason, if the image being enhanced contains noise, it will also result in an enhancement of the noise during the process.

The improvement of contrast achieved by RETICA is significantly important to reduce the use of invasive procedure such as the FFA that has the best contrast of retinal blood vessels. Nevertheless, due to its invasiveness by injecting contrasting agent into the blood vessels, this method may also lead to physiological problems such as nausea, vomiting and dizziness [25]. The worst case of adverse reactions following fluorescein injection could be fatal anaphylactic shock, which eventually leads to death [26]. Furthermore, RETICA can be implemented as part of computerised medical diagnosis system to process the image prior to segmenting and analysing the results. The use of RETICA as an image enhancement method is advantageous to increase sensitivity, specificity and accuracy of the system in diagnosing retina-related eye diseases, e.g. Diabetic Retinopathy (DR).

4.7 Summary

A non-invasive image enhancement scheme called RETICA has been developed. RETICA addresses the problem of varied and low contrast image, accommodated by using the Retinex for contrast normalisation and ICA for contrast enhancement. The three developed fundus image models are used to validate RETICA. The performance of RETICA is evaluated and compared to three common image enhancement methods.

The first stage of RETICA is to normalise the varied contrast and to be developed based on the Retinex. Among the various Retinex algorithms, the iterative Retinex method is selected since only one parameter needs to be determined, that is the number of iteration. The existing iterative Retinex method uses a predetermined number of iteration, which does not always yield the optimum results. Since the optimum number of iteration of the Retinex is related to the homogeneity of the intensity distribution, an iterative Retinex based on the kurtosis is developed to normalise the varied contrast by determining an optimum number of iteration. The higher the kurtosis is, the more homogenous the intensity will be. The contrast-normalised images are subsequently inputted to the second stage of RETICA.

The second stage of RETICA is to enhance the low contrast and to be developed based on the ICA, which in turn enhances the contrast of a specific object or component by separating each of the components that are mixed in the input images. The FastICA algorithm with symmetrical orthogonalisation is used to get the estimated independent components because of its good accuracy and high computational speed. One of the problems in the ICA is that the order of the components is not unique. In the case of fundus image model in which the related independent components are the melanin, the macular pigment and the haemoglobin, the fourth order statistics, i.e. kurtosis, is used to differentiate the haemoglobin-related IC from the other components. The haemoglobin-related IC image gives the best contrast of retinal blood vessels among the IC images and higher contrast of retinal blood vessels than that of the green band image.

Three fundus image models, i.e. varied contrast image model, low-contrast image

model and varied and low-contrast image models are developed to validate RETICA. Validation is performed in each stage of RETICA, i.e. contrast normalisation and contrast enhancement and RETICA as an entire process. Three parameters, namely contrast of retinal blood vessels (C_{av}), image contrast normalisation (R_{sdc}) and contrast improvement factor (CIF) are set up to measure quality of the contrast-enhanced image. Furthermore, the varied and low-contrast fundus image model undergoes RETICA and six selected image enhancement methods, i.e. CS, HE, AHE, ACE, CLAHE and HF to evaluate the performance of RETICA.

Results of validation study for contrast normalisation show that the Retinex successfully normalises the varied contrast of fundus image model. Different numbers of iteration yield different results of contrast normalisation. Since three components are involved; the use of kurtosis may result in different number of iteration of the Retinex in each component. However, only one optimum number of iteration needs to be used. The optimum number of iteration obtained from the macular pigment is used in that the macular region in the application of RETICA for computerised DR system is selected for determination of FAZ and the varied contrast mainly occurs in the macular pigment. For contrast enhancement, the ICA successfully separates the components into three independent components, i.e. melanin, macular pigment and haemoglobin. Even though the order of the component is not unique, the use of kurtosis is able to determine the haemoglobin-related IC that gives the best contrast of retinal blood vessels among the IC images.

Results of comparative study show that RETICA successfully normalises the varied contrast with R_{sdc} of 0.756 better than that of the other selected non-invasive image enhancement methods. RETICA outperforms other enhancement methods in producing higher contrast of retinal blood vessels with C_{av} of 76.83 followed by AHE, CS, HE, HF, CLAHE and ACE with C_{av} of 72.66, 69.11, 68.81, 67.27, 42.81 and 21.08, respectively. Using C_{av} of the green band image (i.e. 14.25) as the reference, RETICA achieves CIF of 5.389 that is slightly lower than that of the invasive FFA with CIF of 5.796. It means that without doing invasively, the contrast of retinal blood vessels can be enhanced at similar level to that obtained by the

invasive procedure, which possibly causes some physiological side effects.

In short, RETICA is able to reduce the varied contrast and significantly enhance the low contrast of the varied and low-contrast fundus image model. The contrast normalised and enhanced image produces a higher contrast of retinal blood vessels and is advantageous for the diagnosis of the retina-related eye diseases, such as Diabetic Retinopathy (DR) through a direct observation or computerised medical diagnosis system. RETICA can be beneficial for retinal vasculature segmentation and determination of foveal avascular zone (FAZ) for grading of DR. This improvement in contrast avoids the need of applying contrasting agent on patients. In the next chapter, RETICA is applied on the computerised DR system to increase sensitivity, specificity and accuracy in grading of DR severity level.

CHAPTER 5
RETICA FOR A COMPUTERISED DIABETIC RETIONOPATHY
MONITORING AND GRADING SYSTEM (RETINO)

5.1 Introduction

Diabetic Retinopathy (DR), a complication threatening the sight due to diabetes mellitus affecting the retina, has become one of the leading causes of blindness in the world [202]. According to the National Eye Database 2007, of 10,856 cases with diabetes in Malaysia, 36.8% has some forms of DR, 7.1% of which comprises proliferative diabetic retinopathy (PDR) as depicted in Figure 5.1 [203]. International Diabetes Federation (IDF) 2009 also reported that approximately 285 million people worldwide have suffered from diabetes [204] with a prediction of the increasing number to be 438 millions within 20 years at the rate of 7 million people developing diabetes per year [204].

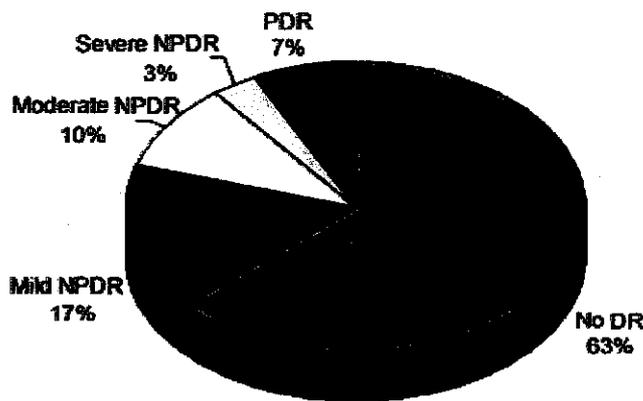


Figure 5.1 DR statistics of registered diabetic patients in Malaysia [203]

A determination of DR severity is deemed essential in treating disease. In grading DR, an International Clinical Diabetic Retinopathy Disease Severity Scale shown in Table 3-2 is now used [205] in which an ophthalmologist using this scale needs to observe and determine DR-related abnormalities in the retinal fundus image. The

above pathology-based method, however, is time-consuming for approximately taking 20 to 30 minutes and often requires fundus fluorescein angiography (FFA) for an accurate diagnosis as well as highly trained and skilled clinicians to perform the DR severity grading method. Fundus fluorescein angiography (FFA) refers to an invasive imaging procedure to highlight the retinal and choroidal circulation by injecting a contrasting agent (sodium fluorescein) into blood vessels to obtain an angiogram of well-contrasted retinal blood vessels for diagnosis of retinal and choroidal pathologies [206]. Pathologies such as micro-aneurysms in a same eye and captured in both colour fundus and FFA images are shown in Figure 5.2.

Table 5-1 International Clinical DR Disease Severity Scale [205]

Proposed Disease Severity Level	Findings Observable upon Dilated Ophthalmoscopy
No apparent Retinopathy	No abnormalities
Mild Non-Proliferative DR	Micro-aneurysms only
Moderate Non-proliferative DR	More than just micro-aneurysms but less than Severe NPDR
Severe Non-Proliferative DR	Any of the following: 1. >20 intra-retinal haemorrhages in each of 4 quadrants. 2. Definite venous beading in 2+ quadrants. 3. Prominent intra-retinal micro-vascular abnormalities in 1+ quadrant. 4. No signs of proliferative retinopathy.
Proliferative DR	One or more of the following: 1. Neo-vascularisation 2. Vitreous/ pre-retinal haemorrhage

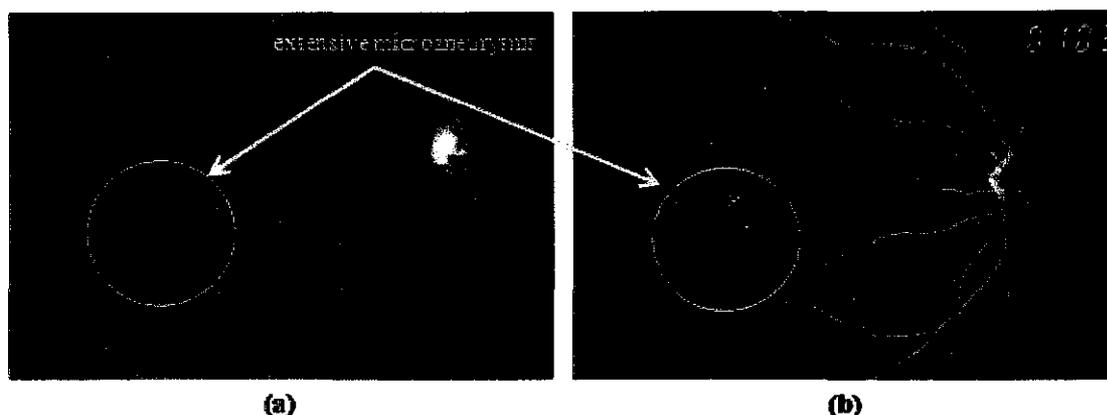


Figure 5.2 Extensive micro-aneurysms in both (a) colour fundus and (b) FFA images [179]

As reported in several scientific literatures [207-212], a number of automatic detecting systems for DR is based on one or more features including retinal blood vessels, exudates, micro-aneurysms, texture, and distances (between the exudates and foveae). These systems use different classifiers for different types of feature. Yun *et al.* [209] for instance reported the use of area and perimeter features of the RGB components of retinal blood vessels in retinal fundus images with feed-forward neural network classifiers to determine DR stages - normal, mild moderate NPDR, severe NPDR and PDR. The system then achieved 84% for average efficiency, 90% for sensitivity and 100% for specificity. Nayak *et al.* [208] meanwhile proposed a neural network system based on area of exudates, retinal blood vessels and texture parameters to be classified into normal, NPDR and PDR stages. The system then achieved 93% of detection accuracy, 90% and 100% of sensitivity and specificity respectively. In Kahai *et al.* [213] a Bayes' decision support system with optimality criteria is used to identify early stages of DR based on micro-aneurysms with 100% of sensitivity and 67% of specificity.

An enlargement of the foveal avascular zone (FAZ), as reported in medical literature, also can biologically occur in diabetic retinopathy (DR) cases due to loss of capillaries in the perifoveal capillary network [214-216]. FAZ is the fovea devoid of capillaries in the macula and can be represented as a dark circle zone without vessels at the centre of macula as shown in Figure 5.3 [206]. Even though being various in sizes for healthy subjects, FAZ usually has roughly 500 μm [217-219] in diameter and

about 0.4 mm^2 in size [220-223]. The enlargement of FAZ is not readily observable in colour retinal fundus images, but its effects are identifiable in invasive fundus fluorescein angiograms for both non-proliferative DR (NPDR) and proliferative DR (PDR) cases [224]. Determination of FAZ area on FFA that have been studied tends to use either Bayesian statistical methods [225] or thresholding techniques based on morphological operators and Sobel edge detector area [226]. However, no studies on the measurement of FAZ from digital colour fundus images have been found so far. An early detection of FAZ enlargement at NPDR stage will enable clinicians to advise their patients on better metabolic control to prevent progression of the disease to PDR stage and loss of vision. Several studies in addition have shown that early treatment on DR patients can reduce the risk of severe loss vision by 57% [227-228].

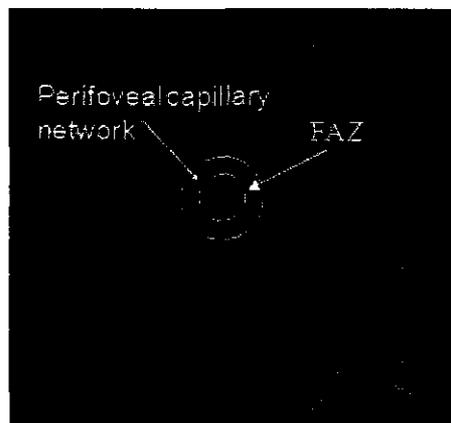


Figure 5.3 FFA shows the perifoveal capillary network in FAZ

A non-invasive computerised DR system, RETINO, is developed to implement a DR grading protocol based on FAZ enlargement using colour retinal fundus images [229-231]. The system uses an external fundus camera (KOWA Non-Myd 7) that allows the capture of non-mydratiac retinal images, which is connected to an image-processing computer that digitises and analyses the retinal images (Figure 5.4).

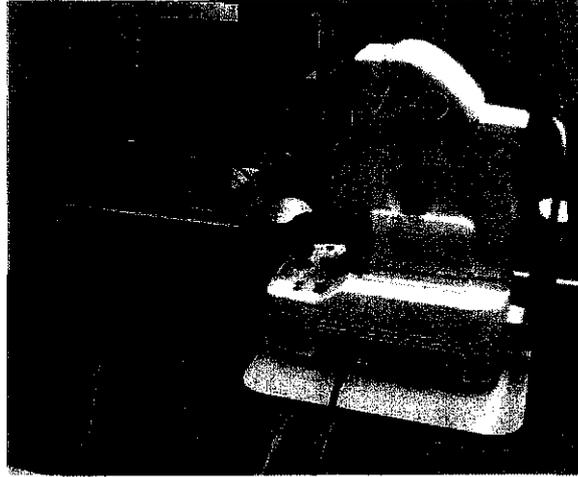


Figure 5.4 Computerised DR Monitoring and Grading System (RETINO)

In this DR grading system, the 1936 x 1296 pixel fundus images captured at 45 degrees are stored in a file format of JPEG (Joint Photographic Experts Group) that is chosen for several practical reasons such as storage media capacity, time processing and limitation of an external camera in producing ready-processed raw images. An external fundus camera is equipped with a digital camera (Nikon D80) capable of capturing a raw image in Nikon's file format, i.e. NEF (Nikon Electronic Format). The NEF contains metadata including information about lens, settings, camera's identification and image information received from a camera sensor. However, it cannot be directly processed and must be converted into ready-processed image format such as JPEG and TIFF. Nikon D80 directly converts the raw NEF images into ready-processed image in JPEG as Fine (1:4 jpeg), Normal (1:8 jpeg), and Basic (1:16 jpeg). Conversion of NEF format to another ready-processed image format such as lossless TIFF (Tagged Image File Format) is also possible to avoid actual quality loss due to compression level as in JPEG. For this, since Nikon D80 does not directly convert it, additional specific software is needed. The size of the TIFF files produced is four times greater than that of the original NEF files. For instance, using the Nikon D80, the size of NEF file of around 8 megabytes is directly reduced to around 2 megabytes in ready-processed JPEG image. Nevertheless, using the additional specific software could make the size of the image produced four times greater (around 30 megabytes) when converted from NEF to TIFF. Hence, JPEG image format is used in this application.

To grade DR severity level, two algorithms, i.e. semi-automated and fully automated are developed. Initially, the semi-automated algorithm is developed based on CLAHE and ICA for image enhancement. For the improvement of the DR grading system, a fully automated algorithm is then developed based on RETICA. In this chapter, these two developed algorithms are explained along with their results and analyses.

For effectiveness in DR grading, two clinical studies, i.e. observational and interventional clinical studies, have been conducted clinically to test and evaluate the performance of the computerised DR monitoring and grading system. An observational clinical study is to evaluate the performance of DR grading system by using digital analysis of colour retinal fundus images. An interventional clinical study meanwhile is to determine the accuracy of the new DR grading protocol by comparing FAZ values obtained either from ground truth or from DR system using both colour retinal fundus and FFA images.

5.2 Semi-Automated RETINO DR Grading System

The algorithm of the semi-automated computerised DR grading system based on FAZ analysis as shown in Figure 5.5 performs four main tasks, i.e. image enhancement of retinal blood vessels, segmentation of retinal vessels, determination of FAZ and analysis of FAZ for DR grading.

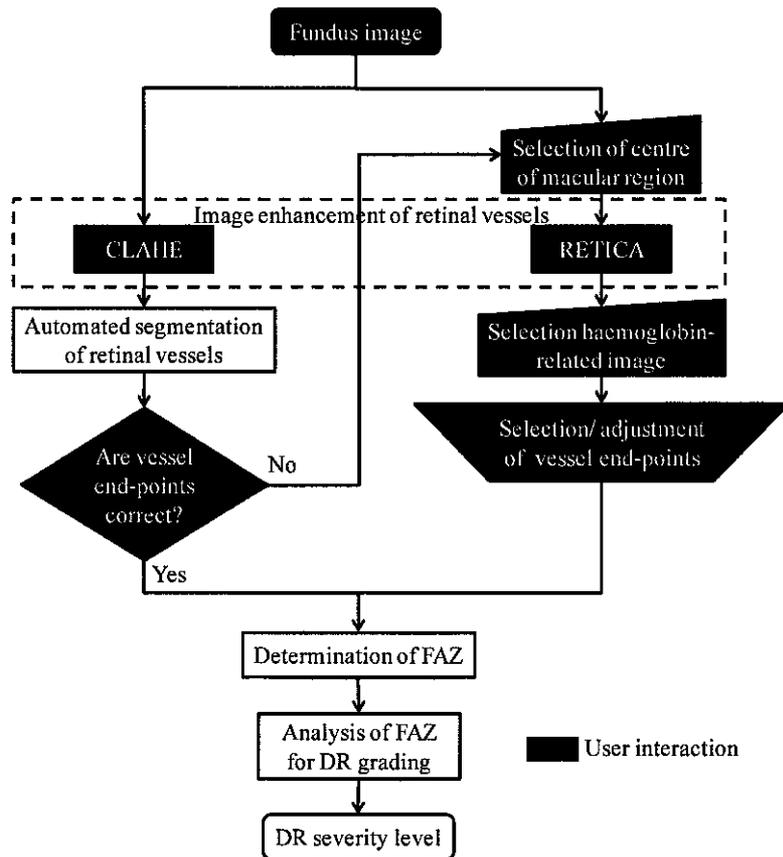


Figure 5.5 Flowchart of the semi-automated DR algorithm

After the fundus camera acquires a colour retinal image, the image is initially enhanced using two image enhancement methods - CLAHE and RETICA. The first method is used to produce CLAHE-enhanced image that is subsequently used for the automated segmentation of retinal vessels and FAZ determination. The CLAHE-enhanced image undergoes segmentation of retinal blood vessels based on Otsu's threshold [232] before the FAZ area is determined based on the obtained retinal vessel end-points of retinal vessels in the macular region showing its exact area formed by joining these retinal vessel end-points. The latter method, i.e. RETICA aims to enhance the retinal vessels of the colour fundus image, which in turn will be used to assist the user to detect correctly retinal vessel end-points for FAZ determination. The RETICA method is applied as a part of the semi-automated DR algorithm considering that the CLAHE-based method does not always produce correct retinal vessel end-points due to poor image quality (dark or blur images and shadowy image) resulting from an improper acquisition process. Based on a direct observation and comparison between vessel end-points obtained from CLAHE-enhanced image and

RETICA-enhanced image, the user, if necessary, will manually determine the correct vessel end-points for a more accurate FAZ determination. Finally, the determined FAZ area is analysed using Gaussian Bayes classifier [233] for DR grading. A cross-validation technique as mentioned in [234-235] is used to evaluate the performance of the classifier. Details of the techniques used are discussed in the following sections.

5.2.1 Enhancement of Retinal Blood Vessels

The first stage of enhancement of retinal blood vessels in colour fundus image involves a process called contrast enhancement of retinal blood vessels that, as its name implies, is to enhance the contrast of the retinal blood vessels against the background image. This process involves two methods - Contrast Limited Adaptive Histogram Equalisation (CLAHE) [88] and RETICA (as discussed in Chapter 4).

CLAHE, a window or tile based enhancement technique, is applied to increase the contrast of retinal blood vessels to the background in both dark and bright regions for being more effective in enhancing vessels in varying surroundings evenly. It outperforms other global enhancement methods such as contrast stretching and normal histogram equalisation in turn [236]. Iznita found that the contrast improvement using CLAHE on colour retinal fundus images ranges between 1.7 and 3 [96]. Our initial experiment on retinal fundus image model developed using 20 test images from DRIVE [237] showed that CLAHE has the contrast enhancement factor of 3.15 [238].

CLAHE is primarily used to apply histogram equalisation within small windows in an image. Gray level values are then evenly distributed within the window to ensure hidden features in it more visible. Window size selection is crucial since it can affect the result of enhancement. The optimum size of window itself will be dependent on the image and the features. Hence, the optimum window size is determined based on the features being enhanced, which in this case are the retinal blood vessels. Applying large window size may also lose the enhancement of tiny features. Conversely, applying small window size may increase the possibility for noise enhancement.

An experiment to determine the optimum window size for CLAHE using varied and low contrast fundus image model has been conducted (as discussed in Chapter 3). Having the highest contrast among the three colour bands (as proven in Chapter 4), the green band of the varied contrast fundus model is selected for image enhancement using CLAHE. The contrasts of enhanced images obtained by applying CLAHE with different window size are measured. The contrast improvement factor (*CIF*) is measured as the contrast ratio between the CLAHE-enhanced image and its green band image. The results are shown in Table 5-2.

Table 5-2 Contrast and Contrast Improvement Factor (*CIF*) obtained from applying different window size for CLAHE

	Green band	Window size for CLAHE								
		2x2	3x3	4x4	5x5	6x6	7x7	8x8	9x9	10x10
Contrast	14.26	42.26	41.67	42.81	40.29	39.41	37.72	38.19	36.96	34.88
CIF	1	2.96	2.92	3.00	2.82	2.76	2.64	2.68	2.59	2.44

From Table 5-2, applying different window size in CLAHE results in a different contrast of the enhanced image with the highest contrast of 42.81 and CIF of 3.00 obtained using 4x4 pixel window. Therefore, the optimal 4x4 window size is used for CLAHE enhancement of retinal blood vessels for the semi-automated DR algorithm.

For vessel detection, the fundus image is initially enhanced using a mean filter followed by CLAHE and a bottom-hat morphological transformation to extract retinal vasculature (retinal blood vessels). Background noise removal followed by contrast stretching is then carried out to reduce the unwanted line features in the background due to morphological transformation.

RETICA (as discussed in Chapter 4), a developed non-invasive image enhancement based on Retinex and ICA [145, 154], meanwhile refers to a technique to normalise varied image contrast and to enhance low contrast. The contrast normalisation based on Retinex is performed by separating the illumination part from the reflectance part of the image. The reflectance part is used for the subsequent enhancement method using ICA. Enhancement of the low contrast of retinal blood vessels in the digital fundus image is performed by determining the retinal pigments

makeup consisting of haemoglobin, melanin and macular pigment using ICA. ICA images due to the obtained haemoglobin exhibit higher contrast retinal blood vessels. The details of the work have been published in [199, 239].

5.2.2 Segmentation of Retinal Blood Vessels

The aim of this second stage is to segment retinal blood vessels in the fundus image based on Otsu's threshold [232]. Otsu uses an inter-class variance as a measure of separability among classes by utilising the histogram information derived from the input image. In order to evaluate the threshold value for segmentation, the inter-class variance is used as a discriminant measure of class separability. The threshold value, which optimises the inter-class variance, here is chosen then.

5.2.3 Determination of Foveal Avascular Zone

The third stage is to detect and to select retinal blood vessel end-points at perifoveal capillary network for both determination and calculation of the FAZ area by connecting the end-points of retinal blood vessels. At this stage, all nearest points to the centre of macula are detected whereby the FAZ area is then formed by connecting the detected points encircling the perimeter of macula.

In practice, a point representing the centre of the macular region is initially chosen and a 600x600 pixel square area centred at this point is selected as the region of interest. The segmented pixels resulted from the second stage are then grouped into objects (object labelling) using 3x3 neighbourhood. The distances between the centre point and all of pixels of the labelled objects are then measured. The end-point is defined as a pixel nearest to the centre point for a particular labelled object. Eight equal radial segments from the centre point are created. In each radial segment, the end-points with the minimum distance from the centre, d_i , are selected. The end-points that are less than the mean distance of all selected end-points are then connected to form the FAZ area. Figure 5.6 shows a schematic diagram of vessel end-points selection for determination of FAZ based on its area.

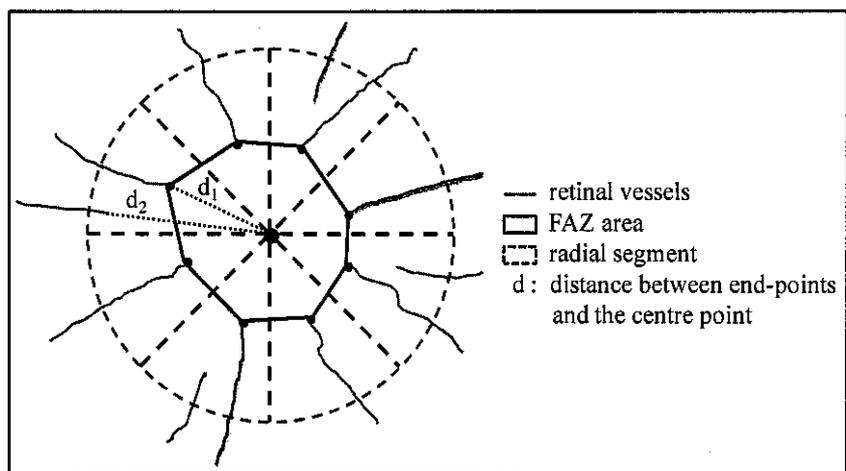


Figure 5.6 FAZ determination by connecting vessel end-points inside the circle (with the radius, which is the mean distance of all end-points from the centre point) from eight radial segments

The area of the determined FAZ is computed below.

$$A(S) = \sum_{i=0}^{i_{\max}} \sum_{j=0}^{j_{\max}} I(x_i, y_j) \quad (5-1)$$

$I(x, y)$ is 1 if the pixel is within the shape, $(x, y) \in S$, and 0 otherwise.

Using the CLAHE-enhanced image, the FAZ is determined by selecting centre point at the macula followed by automatically connecting the selected vessel end-points around the macula. The automatic algorithm is based on the nearest distance of retinal vessels end-points from the centre point.

5.2.4 Gaussian Bayes Classifier for Grading of DR

The distribution of FAZ area in pixels for each DR severity class is determined and modelled with Gaussian (normal) probability density function. Suitability of the data distribution with that of Gaussian distribution is qualitatively observed from its probability mass function and quantitatively measured using goodness-of-fit. One of the methods to measure goodness-of-fit is by using the coefficient of determination R squared (R^2) to indicate the strength of fit between two variables implied by a

particular value between 0 and 1. For Gaussian distribution, R^2 measure of goodness of fit is formulated as [240]

$$R^2 = 1 - \frac{RSS}{TSS} = 1 - \frac{\sum_i (y_i - \hat{y})^2}{\sum_i (y_i - \tilde{y})^2}, \quad (5-2)$$

RSS is residual sum-of-squares, TSS is total sum-of-squares, y_i is observed value for data i , \hat{y} is predicted value and \tilde{y} is mean of observed values. The value of R^2 lies from 0 to 1 in which 0 represents the worst and 1 represents the best goodness of fit.

A Gaussian Bayes classifier is developed to determine DR severity based on the measured FAZ area (in pixels) obtained from digital colour retinal fundus images. The classifier uses Bayes theorem for pattern classification and assumes that the classes have Gaussian distribution [241-244]. According to Bayes theorem, probability of continuous data x that belongs to class ω_c is determined as

$$\begin{aligned} P(\omega_c | x) &= \frac{p(x | \omega_c)P(\omega_c)}{p(x)} \\ &= \frac{p(x | \omega_c)P(\omega_c)}{\sum_{k=1}^C p(x | \omega_k)P(\omega_k)} \end{aligned} \quad (5-3)$$

$$P(\omega_c | x) \propto p(x | \omega_c)P(\omega_c) \quad (5-4)$$

To simplify the above equation, the logarithm of the equation is taken.

$$\log P(\omega_c | x) = \log p(x | \omega_c) + \log P(\omega_c) \quad (5-5)$$

$$LP(\omega_c | x) = LL(x | \omega_c) + LP(\omega_c) \quad (5-6)$$

Note that $LP(\omega_c | x)$ is the log posterior probability, $LL(x | \omega_c)$ is the log likelihood and $LP(\omega_c)$ is the log prior probability. The log posterior probability ratio (LPPR) is then defined as

$$\log \frac{P(\omega_a | x)}{P(\omega_b | x)} = LP(\omega_a | x) - LP(\omega_b | x) \quad (5-7)$$

$$\log \frac{P(\omega_a | x)}{P(\omega_b | x)} = (LL(x | \omega_a) - LL(x | \omega_b)) + (LP(\omega_a) - LP(\omega_b)) \quad (5-8)$$

For one-dimensional case, the Gaussian probability density function has a form of

$$p(x) = \frac{1}{\sqrt{2\pi}\sigma} \exp\left(-\frac{(x-\mu)^2}{2\sigma^2}\right) \quad (5-9)$$

If the probability density function is assumed as Gaussian, the log likelihood will become

$$\begin{aligned} LL(x | \mu, \sigma^2) &= \log p(x | \mu, \sigma^2) \\ &= -\log(\sqrt{2\pi}\sigma) - \frac{(x-\mu)^2}{2\sigma^2} \end{aligned} \quad (5-10)$$

$$LL(x | \mu, \sigma^2) = \frac{1}{2} \left(-\log \sigma^2 - \frac{(x-\mu)^2}{\sigma^2} \right) \quad (5-11)$$

Therefore, the log posterior probability will be

$$LP(\omega_c | x) = \frac{1}{2} \left(-\log \sigma^2 - \frac{(x-\mu)^2}{\sigma^2} \right) + \log P(\omega_c) \quad (5-12)$$

In the case of Gaussian Bayes classifier, if class ω_a and class ω_b are modelled by Gaussian distribution with mean μ_a and μ_b and variances σ_a^2 and σ_b^2 , the log posterior probabilities ratio (LPPR) can be written as

$$\begin{aligned} \log \frac{P(\omega_a | x)}{P(\omega_b | x)} &= \frac{1}{2} \left(\frac{(x-\mu_a)^2}{\sigma_a^2} - \frac{(x-\mu_b)^2}{\sigma_b^2} + \log \sigma_a^2 - \log \sigma_b^2 \right) \\ &\quad + (\log P(\omega_a) - \log P(\omega_b)) \end{aligned} \quad (5-13)$$

If the ratio is greater than 0, data x will belong to class ω_a . Otherwise, data x belongs to class ω_b [241].

In grading of DR severity, the FAZ area (in pixels) is measured for several identified DR related fundus images to obtain FAZ area ranges corresponding to the severity of DR. The overlapping ranges of FAZ area show a progression of the disease from a DR stage to the next. The categories of the ranges used in this work are as follows:-

- (a) Range 1 – No DR stage
- (b) Range 2 – Progression range from no DR to mild NPDR
- (c) Range 3 – Mild NPDR
- (d) Range 4 – Progression range from mild NPDR to moderate NPDR
- (e) Range 5 – Moderate NPDR
- (f) Range 6 – Progression range from moderate NPDR to severe NPDR/ PDR
- (g) Range 7 – Severe NPDR/ PDR

5.2.5 V-Fold Cross Validation for Performance Evaluation

Used to evaluate the performance of the classifier, a V-Fold Cross Validation (VFCV) [235, 245-246], due to the quite small number of samples (number of samples for moderate NPDR is only 32), is chosen. The VFCV algorithm randomly divides data set D into V disjoint subsets T_v , $v=1, 2, 3 \dots V$ with approximately equal size iteratively performs the cross-validation V times. $V-1$ of the subsets is used as a learning set and the rest is used as a test set. An average of the results is used to measure the performance of the developed system. The VFCV is also computationally feasible since V can be chosen (generally between 5 and 10). V is set to 5 (i.e. each subset consists of 20% of total number of data) since the smallest sample size of the DR severity level is 32 (i.e. moderate NPDR) in order to maintain sufficient training sample size.

5.3 Fully Automated RETINO DR Grading Algorithm

The fully automated DR algorithm is developed as a subsequent improvement from the semi-automated DR algorithm. In this fully automated DR algorithm, RETICA is applied for the image enhancement followed by the automated segmentation of retinal vessels and the analysis of FAZ for DR grading. Having the same image acquisition process with the semi-automated one, the fully automated DR algorithm offers a greater advantage than does the semi-automated one. The user through the fully automated DR algorithm simply selects the centre point of the macular region prior to running the algorithm. On the other hand, the user through the semi-automated DR algorithm needs to give inputs several times for the algorithm (Figure 5.5). Moreover, once the semi-automated DR algorithm does not produce the correct vessel end-points as produced by the CLAHE, the user needs to adjust these vessel end-points based on the direct observation on the RETICA-enhanced fundus image.

In addition to the fully automated process of FAZ determination and analysis, the main difference between semi-automated and fully automated DR algorithms is the indicator used to determine the FAZ. In the semi-automated DR algorithm, FAZ is indicated by the area of the obtained FAZ, whilst in the fully automated case, FAZ is indicated by the radius of the determined FAZ that both are measured in pixels. The radius functions to reduce the error between the FAZ obtained and the actual FAZ as a result as of performing square factor on the radius of the FAZ with an assumption that its area is a circle and is defined as half of the longest line connecting two detected points encircling the perimeter of macula. A flowchart of the algorithm of the fully automated DR algorithm based on FAZ analysis is depicted in Figure 5.7.

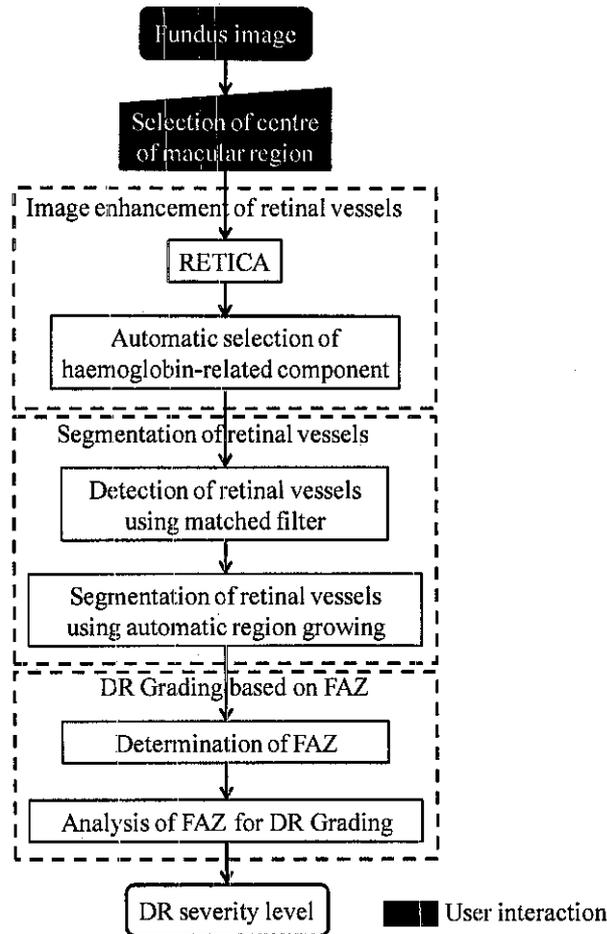


Figure 5.7 Flowchart of the fully automated DR algorithm

The process starts by inputting the colour retinal fundus-image into the system either by direct acquisition of the image using fundus camera or by manually selecting the retinal fundus image that is going to be processed. In this application, the resolution of the retinal fundus image is 1936x 1296 pixels. A user then selects a point representing the centre of the macular region and a 518x518 pixel square area centred at this point is subsequently cropped. Unlike the semi-automated DR algorithm that uses a fixed cropped image of 600 x 600 pixels; the fully automated one uses a ratio of resolution of the input image to determine the resolution of the cropped image, thus enabling it to be applied for any inputted image resolution. The process continues with the enhancement of retinal vessels as shown in Figure 5.7.

5.3.1 Enhancement of Retinal Blood Vessels

In the fully automated DR algorithm, the enhancement of retinal vessels is performed using RETICA. In general, the inputs of RETICA are the three colour channels and its outputs are the haemoglobin-related component image that has high contrast of retinal blood vessels.

5.3.2 Segmentation of Retinal Blood Vessels

The second process aims to segment automatically retinal blood vessels in the retinal fundus image. Several methods have been developed for vessel extraction. With the intentions on automated segmentation of retinal blood vessels in the retinal fundus image, the approaches can be categorised into three, i.e. matched-filter [44-45, 247-248], mathematical morphology [249] and region-growing [250]. Matched-filter technique aims to extract objects of interest, e.g. retinal blood vessels, by convolving the image with multiple matched-filters. Since retinal blood vessels are with different orientation and size, it is important to design several filters to match the profile of these retinal blood vessels. Chaudhuri *et al.* [45] noted that the gray-level intensity profiles of the cross-sections of the retinal blood vessels can be approximated by a Gaussian. For this, they proposed a Gaussian function as a model for retinal blood vessel profile by applying a set of 2-D segment profiles that consists of 12 different kernels. These kernels are designed by rotating the initial matched-filter at an angular resolution of 15° . The green band of the colour retinal fundus image is convolved with these 12 kernels. The corresponding responses are subsequently compared and the maximum response is retained for each pixel. This technique is able to achieve accuracy of 0.8773 in detecting retinal blood vessels from DRIVE [237] as has been reported in [251]. In practice, matched-filter is simple and good in detecting large retinal blood vessels, but it has a disadvantage in detecting retinal capillaries since the tiny vessels can be missed in detection.

Mathematical morphology approaches segment the objects of interest by filling holes and eliminating undesirable patterns. Structuring elements are applied to perform morphological operations such as dilation, erosion, closing and opening. A

method developed by Zana and Klein used the mathematical morphology followed by curvature estimation to segment retinal vasculature [252]. This method achieved an accuracy of 0.9377 indicating a better performance in detecting retinal blood vessels than that of Chaudhuri *et al.* [45] with accuracy of 0.8773 as has been reported in [251]. However, like the matched-filter by Chaudhuri *et al.* [45], the mathematical morphology approach by Zana and Klein [252] also fails to detect retinal capillaries.

The third approach, i.e. region growing offers advantages such as it is able to generate smooth parametric curves or surfaces and it is robust to noise. From some initial seed-points, surrounding pixels are incrementally recruited to define a region based on some criteria, e.g. spatial proximity and similarity of intensity values. In region growing, pixels close to each other are assumed to have similar intensity values and belong to the same object. Higgins *et al.* [250] applied an iterative seeded region growing to segment out the arterial tree from a 3-D angiogram. For each of iteration, a set of voxels adjacent to the confirmed seed regions is examined by comparing their intensity values to some predetermined values to classify whether these voxels – the candidate seeds – are to be included into the confirmed seed region. However, a major disadvantage of region growing approach is that it generally needs initial seed-points provided by the user for the starting points of the segmentation process. User interaction therefore is required and becomes a problem for such automated process. Hence, an automated process for generating initial seed-points is required. Moreover, due to variations in image intensities, region growing may result in holes and over-segmentation. Nevertheless, this problem can be overcome by minimising varied image intensities.

Our approach for segmentation of retinal blood vessels is based on the automated region growing that combines a series of digital filters used to detect retinal blood vessels and region growing used to segment the retinal blood vessels. First, a matched-filter technique by Chaudhuri *et al.* [45] is adapted to detect the retinal blood vessels by convolving a set of 12 kernels that have the 35x35 pixels with the retinal fundus image due to its simplicity; yet, it still produces high accuracy in detecting retinal blood vessels. The method of Chaudhuri *et al.* [45] has been implemented on the green band of retinal fundus image and achieved accuracy of 0.8773 in detecting

retinal blood vessels. Compared with our method, the matched filters are implemented on the RETICA-enhanced image, which has contrast 5.389 times better than that of the green band image according to our results described in Chapter 4. Hence, it leads to significantly better accuracy of retinal blood vessel detection. A sample of 1 kernel out of 12 kernels is shown in Appendix G.

The kernel (Appendix G) is used to cover retinal blood vessels on vertical orientation. In this work, the kernel is designed to have an angular resolution of 15° to make the total number of kernels needed to be 12 for covering all possible orientations of retinal blood vessels as suggested by Chaudhuri *et al.* [45]. The angular resolution can be made smaller; yet it would result in more processing time needed and possibly increase the noise. These 12 kernels are convolved with the RETICA-enhanced image to obtain matched-filter responses. The corresponding responses are compared and the maximum response for each pixel is retained. Output of this matched-filter technique is then processed with Higgins *et al.* filter [250] in which the detected retinal blood vessels, characterised by bright and connected regions, are extracted and these bright regions are isolated to form the initial seed-points for the region growing. The region growing, as previously explained, needs initial seed-points to start the process. Considering the automated process, determination of initial seed-points must also be automatically done. Hence, the first step of the segmentation of retinal blood vessels in the fully automated DR algorithm is important to provide automatically initial seed-points for the region growing.

Next step is to apply region growing to segment the retinal blood vessels. Region growing is chosen for being capable of maintaining connectivity among pixels that are close together and have similar intensity values. These connected pixels are related to the same objects, thus being suitable with the characteristics of the retinal blood vessels. In the region growing method, two homogeneity parameters, i.e. similarity of intensity values and spatial proximity are set up to determine whether a pixel should be included in the regions. For the first parameter, a similarity threshold value (ΔR) is needed to determine whether a candidate seed (x,y) should be included in the confirmed seed region (r_a) based on its intensity value. In this case, ΔR is defined as

the minimum intensity value of all selected seed-points obtained from applying a series of digital filters. The determined region because of region growing must have greater intensity values than the ΔR in the segmented image. The second parameter, i.e. spatial proximity, is determined by examining a set of 8 neighbouring pixels to the confirmed seed pixel $s_a(x, y)$ and checking whether these neighbouring pixels should be included in the confirmed seed region (r_a). Using the two aforementioned parameters, a candidate seed $c(x, y)$ having greyscale intensity value $i_r(x, y)$ is added into r_a if $i_r(x, y)$ is greater than ΔR and its location is within 8 neighbouring pixels centred on $s_a(x, y)$. The added pixels $c_a(x, y)$ will be the next confirmed seed $s_a(x, y)$ and the process continues until no further pixels are added to r_a . Region growing creates a segmented retinal vessel image that is subsequently used to detect retinal blood vessels end-points at perifoveal capillary.

5.3.3 Determination and Analysis of Foveal Avascular Zone

Similar to that of the semi-automated DR algorithm, determination of FAZ is by detecting all the nearest points to the centre of macula and the FAZ area is formed by connecting these detected points encircling the perimeter of macula. However, in determining the FAZ, two differences between the semi-automated and the fully automated ones exist. The first one deals with the method used in determining the retinal vessel end-points to form the FAZ and the second one is about the use of FAZ radius instead of the area as a parameter to measure the FAZ. Radius of FAZ is defined as half of the longest line, i.e. FAZ diameter, connecting two detected points encircling the perimeter of macula.

The segmented pixels resulted from the previous stage are grouped into objects (object labelling) using 3x3 neighbourhood. Then, the distances between the centre point and all of pixels in the labelled objects are measured. The end-point is defined as the pixel with the shortest distance to the centre point of a particular labelled object. However, unlike the semi-automated system that uses eight equal radial segments from the centre point, the fully automated one, determined based on an

experiment, uses 60 equal radial segments to determine retinal vessel end-points. The experiment purposively to find an acceptable and optimum number of radial segments is conducted by measuring 2 kinds of correlation. The first correlation is between radius and the FAZ area obtained by applying a specific number of radial segments and second correlation is between FAZ radii obtained by applying a specific number of segments and that of manually obtained to be used as the reference. Since the fully automated system has to select the retinal vessel end-points to determine the FAZ area prior to determining the FAZ radius, it is important to find an acceptable number of radial segments which correlation between the radius and the area of the FAZ is sufficiently high. The sufficiently high correlation indicates that the radius can be used as a parameter to indicate the FAZ besides the FAZ area. Whilst for the second correlation, the highest correlation factor obtained indicates the optimum number of radial segments. From eight samples of number of radial segments, the acceptable and optimum number of radial segments for the fully automated DR algorithm indicated by coefficient correlation is shown in Table 5-3.

Table 5-3 Correlation coefficients (CC) measured (1) between radius and area of FAZ obtained by applying a specific number of radial segments and (2) between FAZ radius obtained by applying a specific number of radial segments and FAZ radius obtained manually (reference)

	Number of equal radial segments							
	8	12	16	20	30	60	90	120
CC 1	0.19	0.73	0.86	0.73	0.79	0.85	0.72	0.91
Significance 1	0.590	0.018	0.001	0.018	0.006	0.002	0.019	0.0002
CC 2	0.15	0.27	0.21	-0.06	0.53	0.56	0.34	0.47
Significance 2	0.671	0.446	0.560	0.867	0.107	0.097	0.335	0.167

As shown in Table 5-3, different correlations are obtained with varying number of radial segments. For the first correlation coefficient (CC 1), it can be seen that 120 radial segments have the strongest correlation coefficient of 0.91 at significant level of 0.002 followed by 16 radial segments with correlation coefficient of 0.86 at significant level of 0.001 and 60 radial segments with correlation coefficient of 0.85 at significant level of 0.002 in the third. Of eight numbers of radial segments shown

in Table 5-3, only three (16, 60 and 120) have correlation coefficient greater than 0.80 while the rest are less than 0.80.

Different correlation coefficients and significance obtained by applying different number of radial segments was expected as it will result in a different FAZ. A higher correlation coefficient along with a lower significance indicates that the FAZ obtained by applying a specific number of radial segments is more accurate. At first, it was predicted that the more the number of radial segments is, the more accurate the determined FAZ will be for more retinal vessel end-points selected to form the FAZ. The more accurate the FAZ is, the more consistent the FAZ to be characterised in the form of its radius and area resulting in higher correlation coefficient and lower significance obtained will be. However, since the FAZ is formed based on retinal vessel end-points, applying more numbers of radial segments at certain value may result in a false selection of retinal vessel end-points leading to inaccuracy of FAZ determination. It is clearly shown in Table 5-3 that by increasing the number of radial segments at some points enables the correlation coefficient to increase, but at certain values the correlation coefficient goes down even after the number of radial segments is increased. It occurs due to the false selection of retinal vessel end-points used to determine the FAZ. According to results shown in Table 5-3, the three numbers of radial segments, i.e. 16, 60 and 120, by considering their correlation coefficient greater than 0.80 with significant level obtained less than 0.01, are to be used in the application. However, the optimum number of radial segments must also be determined.

Based on the second correlation coefficient (CC 2) as shown in Table 5-3, the strongest correlation coefficient belongs to the 60 radial segments, which, furthermore, also have the lowest significant level of 0.097 among other numbers of radial segments. In essence, the 60 radial segments have the most linear dependence to the reference. For the reference, the correlation coefficient between radius and area of the FAZ is found to be 0.99 at significant level of 0.00000146. The second correlation coefficient and significance are necessary to find the optimum number of radial segments from the three acceptable numbers of radial segments obtained from CC1. The optimum number of radial segments is selected if it has the highest

correlation coefficient (CC2) along with the lowest significance (Significance 2). As expected, the highest CC1 does not always produce the highest CC2. It is because in the case of CC2 the FAZ is specifically characterised by its radius. Whilst in the case of CC1, the FAZ is characterised by both radius and area. It is important to compare the radius of FAZ obtained by the system with that of manually obtained by the reference to know which number of equal radial segments needs to be selected - considering the manually obtained one is the most accurate one in determining the FAZ from its radius. Whereas the CC1 indicates the consistence of the DR system in obtaining the FAZ using both the radius and area, the CC2 indicates a relationship between the DR system and the reference in obtaining the FAZ based on its radius. Showing the consistence of the system (CC1) here also indirectly indicates the system's precision, whilst the relationship of the system (CC2) is indirectly indicates the system's accuracy. In other words, the higher the CC1 is, the more precise the system will be; and the higher the CC2 is, the more accurate the system is will be. Hence, the number of radial segment, i.e. 60 that has the highest correlation coefficient with the reference is used to select the retinal vessel end-points followed by the determination of FAZ indicated by its obtained radius.

Additionally, unlike the semi-automated DR algorithm, which only determines the FAZ area, the fully automated DR algorithm can determine both area and radius of the FAZ. The FAZ area is computed using (5-1) and the radius of FAZ is defined as half of the longest line connecting two detected points encircling the perimeter of macula. Nevertheless, at present, only the FAZ radius is analysed to grade DR severity levels for clinical practice.

In the last process, DR severity is determined based on the radius of FAZ (in pixels) using Gaussian Bayes classifier [233] similar to that of the semi-automated DR algorithm (as described in Section 5.2.4). The DR severity levels in the semi-automated DR algorithm are indicated by the range of FAZ area, whilst in the fully automated DR algorithm, they are indicated by the range of FAZ radii.

Results of determination of FAZ area and FAZ radius using both semi-automated and fully automated DR algorithms are analysed using statistical correlation analysis.

The correlation analysis shows the strength of linear relationship between two variables - the FAZ parameters (area and radius) obtained by the DR algorithms and the corresponding DR severity level graded by the ophthalmologists. The objective of the analysis is to prove if the FAZ measured from colour fundus images using the developed DR algorithms can be used to grade DR severity. If the correlation between the FAZ parameters and DR grades is high, FAZ determined from the colour retinal fundus image using the developed DR system inevitably can be effectively used to grade DR severity.

Furthermore, performance of the DR algorithms in grading of DR severity levels is evaluated based on agreement test [253] and performance test. In the agreement test, the DR severity graded by the fully automated DR algorithm is compared to that of the ophthalmologists used as a reference. Ideally, a new developed method should produce an identical result as the reference, yet, it might not be fulfilled. An agreement test will describe to what extent the new developed method is likely to differ from the reference. If the difference is sufficiently small such that it will not cause undesired problems in clinical practice, the developed DR system can be implemented to assist the ophthalmologists in monitoring and grading of DR.

The performance test on the other side is measured in terms of sensitivity, specificity and accuracy [254]. In medical application, sensitivity measures the ability of a system in detecting a patient actually suffering from a specific stage of disease. Moreover, specificity objectively measures the ability of a system in detecting a patient actually not suffering from a specific stage of disease. Accuracy furthermore combines sensitivity and specificity without specifically informing which of these two has a higher value. Therefore, both sensitivity and specificity are very important to describe the ability of system to detect separately a class as a class and a non-class as a non-class. In medical practice, an erroneous diagnosis is very dangerous and may lead to patient's death. Thus, it is not only accuracy to be important to measure, but also sensitivity and specificity of the developed system to be required for indicating the ability of such a medical system. Sensitivity is given by

$$\text{Sensitivity} = \frac{TP}{TP + FN} \quad (5-14)$$

True positive (TP) is when the system correctly classifies the particular desired DR stage, while false negative (FN) is when the system incorrectly classifies the particular desired DR stage. Specificity is formulated as

$$\text{Specificity} = \frac{TN}{TN + FP} \quad (5-15)$$

True negative (TN) is when the system correctly classifies the particular undesired DR stage while false positive (FP) is when the system incorrectly classifies the particular undesired DR stage. Accuracy is defined as

$$\text{Accuracy} = \frac{TP + TN}{TP + TN + FP + FN} \quad (5-16)$$

The values of sensitivity, specificity and accuracy lie from 0 to 1 representing the worst and the best performance of the system respectively.

5.4 Accuracy Analysis on Determination of FAZ

At present, ophthalmologists use FFA images to determine the FAZ due to high contrast of retinal blood vessels obtained from FFA images. With implementation of RETICA on the colour retinal fundus image that can produce contrast of retinal blood vessels at par to that of the FFA image, the FAZ can be determined from the colour retinal fundus image by detecting and connecting retinal end-points in the macular region. The objective of the accuracy analysis is to measure the accuracy of the DR system in determining the FAZ from the colour retinal fundus image. It is performed by comparing FAZ parameters obtained from ground truth and that of DR system. Two accuracy analyses are conducted.

The first analysis is performed by comparing FAZ parameters (area and radius) obtained from ground truth using FFA and those obtained by the DR system, which digitally analyses colour fundus image. Unlike the ground truth detecting the retinal

vessel end-points from the FFA image, the DR system obtains the retinal vessel end-points from colour fundus image. The DR system determines the area and radius of the FAZ from a colour retinal fundus image and compares the FAZ radius to that of the ground truth obtained by manual FAZ determination using the FFA image. A schematic diagram depicted in Figure 5.8 shows the difference of the FAZ determination between the ground truth and the DR system. Since the contrast of retinal blood vessels is higher in the FFA image than the one in the colour fundus image, more retinal capillaries could be detected in the FFA image. Hence, the FAZ obtained from the ground truth tends to be smaller than that of the DR system as shown in Figure 5.8.

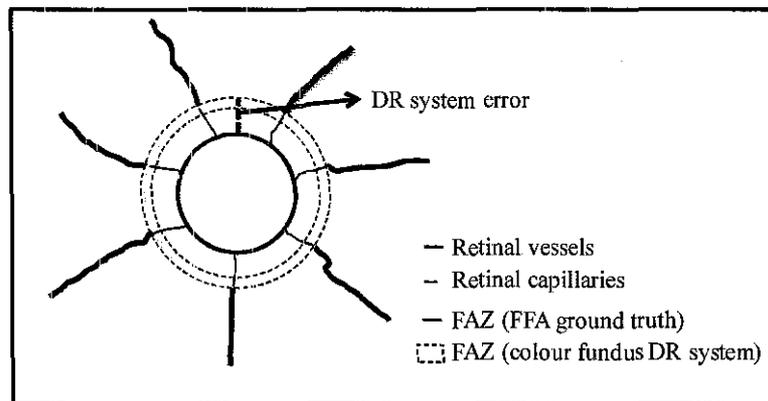


Figure 5.8 A schematic diagram of FAZ obtained by the ground truth and the DR system

Defined as an area that encircles the macular area devoid of retinal capillary networks, the FAZ assumedly refers to a circle in this analysis. In the case of DR system, the FAZ area is digitally analysed from normal colour fundus images using the automatically selected retinal blood vessel end-points. For ground truth measurements, the actual FAZ area is visually determined from FFA images by connecting the correct end-points of retinal vessels in the macular region. All unbiased retinal blood vessel end-points encircling the macula are determined by two trained research personnel. Like the DR system, a MATLAB[®] program then automatically selects two end-points that, when connected, give the longest diameter (and radius) for the FAZ. Microsoft Excel[®] and SPSS[®] software are used to analyse the FAZ obtained by the DR system against the ground truth. A flowchart showing accuracy analysis on determination of FAZ by comparing the FAZ radius obtained by

the ground truth and that of the DR system is depicted in Figure 5.9.

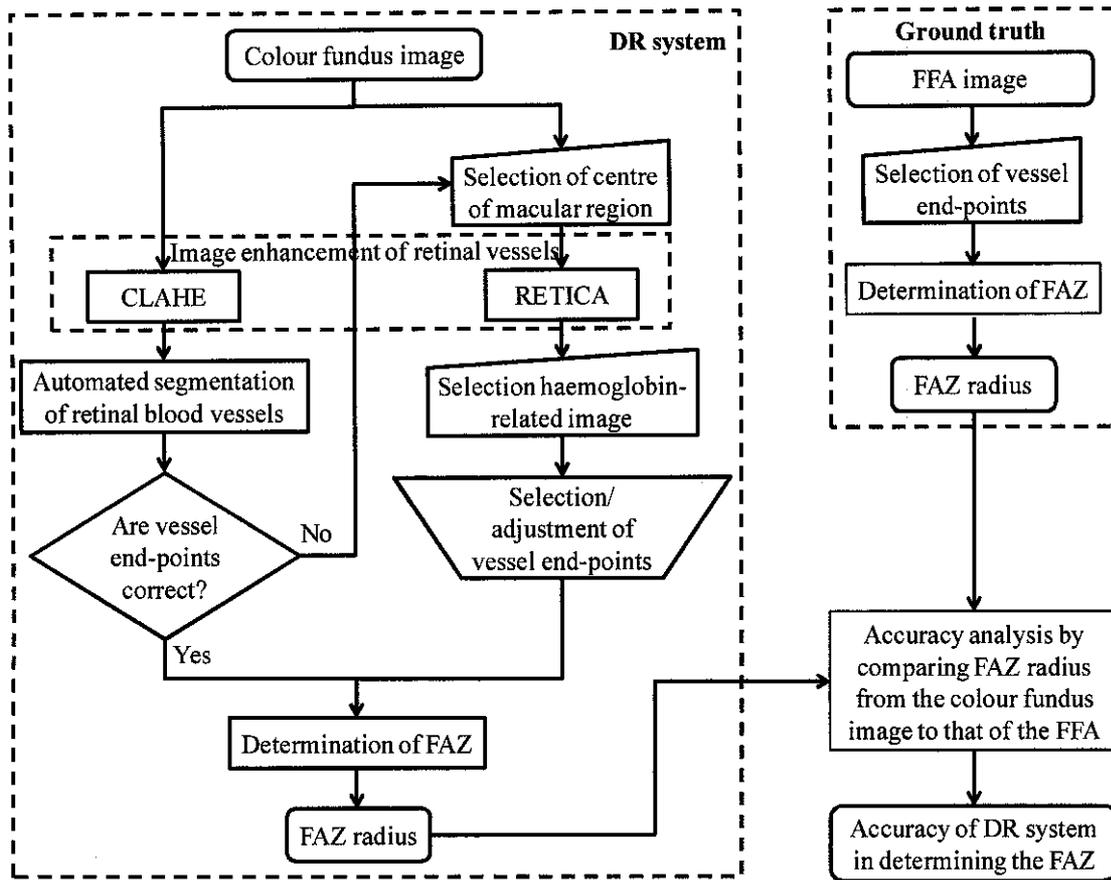
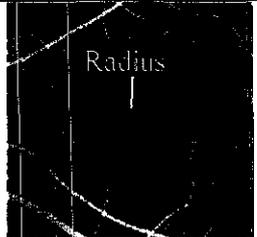
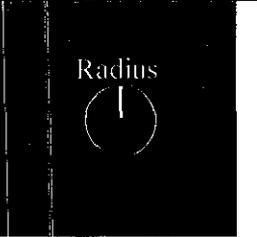


Figure 5.9 A flowchart of accuracy analysis on determination of FAZ

Illustrated in Figure 5.9, the DR system digitally processes and analyses the colour fundus image to determine the FAZ diameter (and radius). The DR system used for the accuracy analysis is the semi-automated one with modification on the final output. Instead of the use of area as the parameter of the FAZ, the DR system for accuracy analysis determines the FAZ diameter and radius. Even though both area and diameter of FAZ can be used to grade DR severity level as proven in several studies [214-215, 223, 255], ophthalmologists in daily practice generally use the FAZ diameter rather than FAZ area measured from FFA images to indicate DR severity level for simplicity in direct observation. This fact has been confirmed with consultant ophthalmologists at Selayang Hospital, Malaysia as our collaborators in this research study. Hence, the FAZ diameter and radius are used for accuracy analysis of DR system on FAZ determination. As previously explained (in Section 5.2) the semi-automated DR algorithm has four main steps to process the inputted

colour retinal fundus image. However, for accuracy analysis, it only uses three steps, i.e. enhancement of retinal blood vessels (as described in Section 5.2.1), segmentation of retinal blood vessels (as described in Section 5.2.2), and determination of FAZ (as described in Section 5.2.3). The output of the third step is the retinal vessel end-points. A MATLAB® program then automatically chooses two of selected end-points that, when connected, give the longest diameter (and radius) for the FAZ. Table 5-4 illustrates a comparison of the FAZ radius determination between the ground truth and the DR system.

Table 5-4 FAZ determination (radius) based on ground truth and DR system measurements

	Ground truth	DR system
Type of image	FFA image	Colour fundus image
Software	MATLAB®	MATLAB®
FAZ radii		

Finally, to obtain the DR system error (E_{GT-DR}) the radius of the determined FAZ by the DR system ($RFAZ_{DR}$) is compared to the ground truth ($RFAZ_{GT}$).

$$E_{GT-DR} = RFAZ_{GT} - RFAZ_{DR} \quad (5-17)$$

The second analysis is aimed only for the fully automated DR algorithm to determine the accuracy and precision of the algorithm in determining the FAZ radius compared to that of in determining the FAZ area. However, unlike the first analysis using FAZ obtained from FFA images as ground truth, the second analysis uses the average of FAZ radii measured from several observations on one image as ground truth. It is related to the characteristics of the fully automated DR algorithm in which the user has to determine only one point, i.e. the centre of macular region at the beginning of the process. Moreover, a user unlikely will select an identical point at the next use of the algorithm. Therefore, it is important to determine the accuracy and precision of the fully automated DR algorithm in determination of FAZ radius. The FAZ radius obtained for a particular colour retinal fundus image in an observation is

compared to its reference (ground truth) and error between them is analysed. Due to the use of FAZ radius in the fully automated DR algorithm, it also comes to be important in the second analysis to show whether FAZ radius is more reliable to use than FAZ area as FAZ parameter.

5.5 Study Protocol

Two clinical studies, i.e. interventional and observational clinical studies, have been conducted to clinically test and evaluate the performance of the computerised DR monitoring and grading system. In these studies, inclusion and exclusion criteria for the patient were set. The inclusion criteria are as follows:

1. The participant ranges from 21 to 60 years old.
2. The participant has clear ocular media

The exclusion criteria are as follows:

1. The participant is less than 21 years old and not more than 60 years old.
2. The participant has media opacity.
3. The participant has allergy to any dye, seafood and asthma
4. The participant has any medical illness.
5. The participant has maculopathy.

The interventional clinical study MOH/CRC/CTA004/100209-rvd130309 (Appendix A) was approved by the Ministry of Health Ethics Committee and conducted at Selayang Hospital, Malaysia from August 2009 to April 2010. Figure 5.10 shows the interventional clinical study that was designed based on several activities.

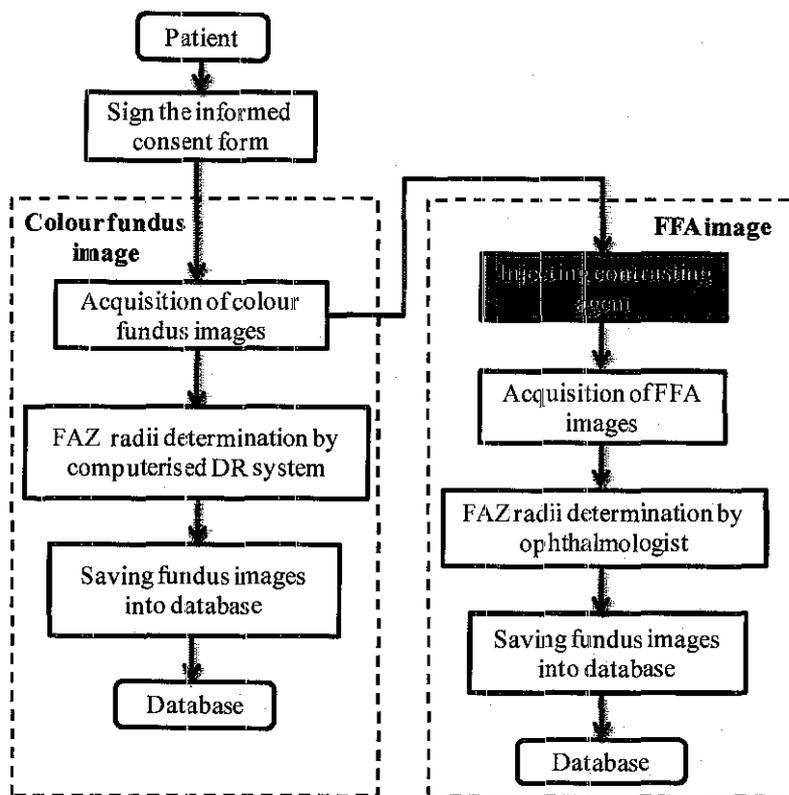


Figure 5.10 Flowchart of the interventional clinical study protocol

All participants initially are given information sheet and required to sign the consent form. Their retinal images in the second step are captured using KOWA VX-10 mydriatic and non-mydriatic camera attached to an image-processing computer for both colour fundus image and FFA image acquisition. The FAZ of the participant is afterward measured using the DR system from colour fundus images. FFA images are acquired by ophthalmologists of Selayang Hospital using FA standard procedure, i.e. patients are injected with a contrasting agent to obtain well-contrasted retinal blood vessels. The acquired colour fundus images and FFA images are at last saved into a database.

Meanwhile, the observational clinical study NMRR-08-842-1997 (Appendix B) was approved by the Clinical Research Centre, Ministry of Health and conducted at Selayang Hospital, Malaysia from August 2008 to March 2009. The study protocol that also followed the tenets of Declaration of Helsinki was designed based on the following activities shown in Figure 5.11.

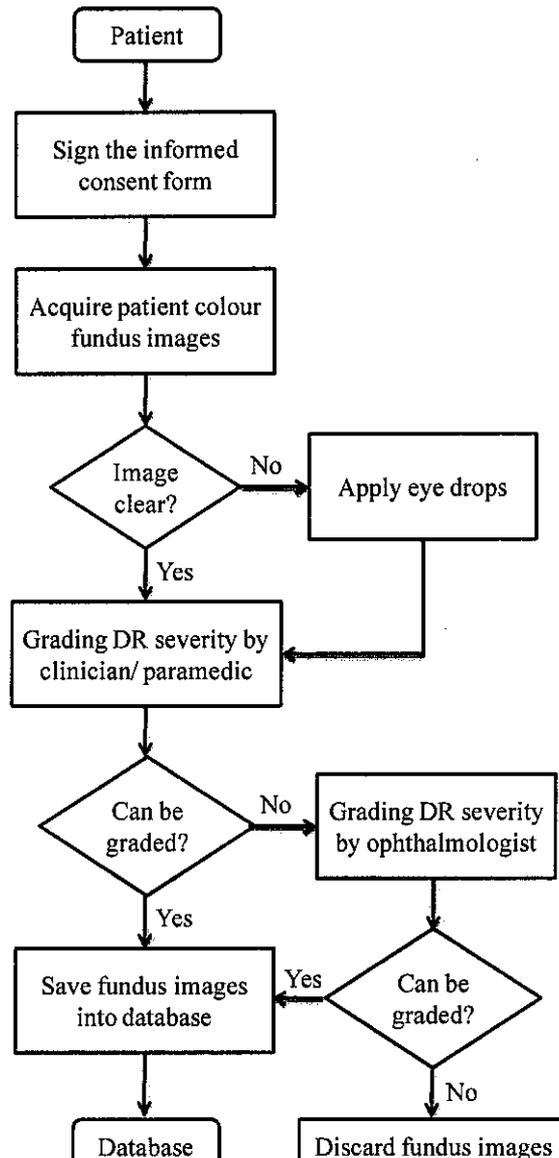


Figure 5.11 Flowchart of the observational clinical study protocol

Firstly, the informed consent forms were obtained from all the participating patients and then the retinal fundus images of the patients were taken using non-mydratic fundus camera Kowa non-mydr 7 attached with Nikon D80. Performed by trained personnel, the optical angle was set to capture 45° colour retinal fundus image with internal fixation target on the central showing the centre on the macula. Patients with small pupil preventing a clear and good colour retinal fundus image to be captured have their pupil dilated using one drop of 1% of gutt tropicamide. Thirdly, the state of DR was graded using the International Clinical Diabetic Retinopathy Disease Severity Scale by two clinicians, who, when in doubt, could consult two senior ophthalmologists at Selayang Hospital. Finally, the graded retinal fundus

images were then stored into a database. These retinal fundus images were then analysed by the computerised DR system. The grading ranges of the computerised DR monitoring and grading system were calibrated for optimum accuracy needed for medical practice.

5.6 Results and Analysis

5.6.1 Analysis of FAZ

A digital colour retinal fundus image undergoes both semi-automated and fully automated DR algorithms according to the flowcharts illustrated in Figure 5.5 and Figure 5.7, respectively. Results of the developed semi-automated DR algorithm performance on an example of colour fundus image are shown in Figure 5.12.

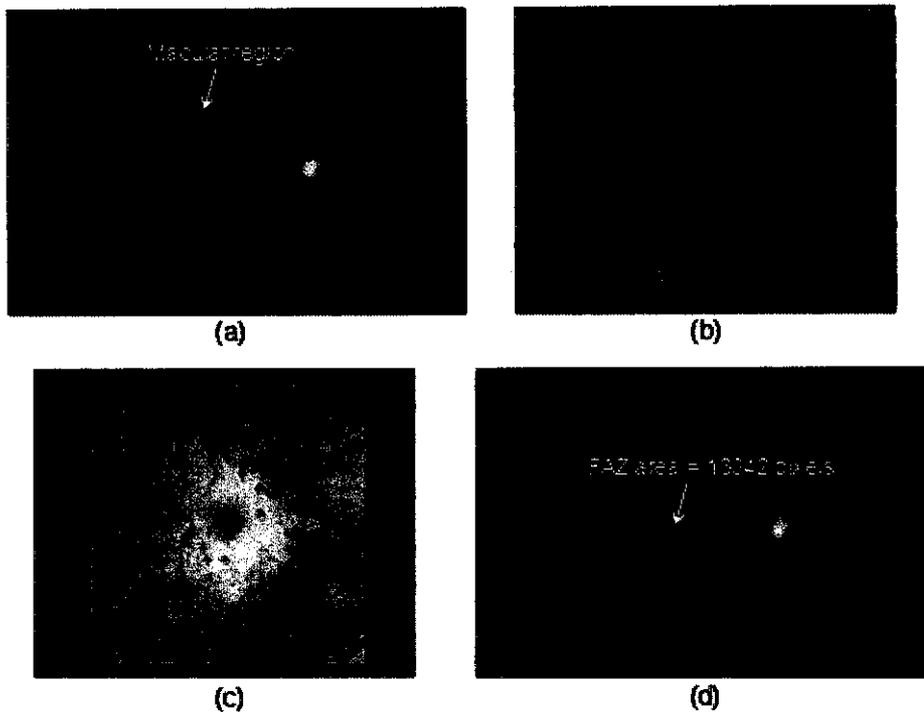


Figure 5.12 Fundus image analysis of FAZ using semi-automated DR algorithm, (a) Digital retinal fundus image showing macular region, (b) Extracted retinal vessels with end points in macular region using CLAHE-based method, (c) Vessel end points in macular region are overlaid with the RETICA-enhanced image, (d) More accurate estimation of vessel end points shown by FAZ area

Figure 5.12 illustrates the result of segmenting the macular regions of a digital retinal fundus image (Figure 5.12(a)) using the CLAHE-based method (Figure 5.12(b)). Since the automated segmentation on CLAHE-based image does not always give accurate vessel end-points and pathologies close to macula, the selected end-points are then overlaid on the RETICA-based image to be manually processed to obtain a more accurate estimation and better visualization of retinal vessel end-points in the perifoveal area (Figure 5.12(c)). It is then followed by connecting the obtained retinal vessel end-points to each other for FAZ determination and analysis (Figure 5.12(d)). In other word, the determination of FAZ in the semi-automated DR algorithm could be considered as a combination of automated process using CLAHE-enhanced image and manual process using RETICA-enhanced image.

In the fully automated DR algorithm, the determination of FAZ is improved from combination of automated and manual process to fully automated process. RETICA

is incorporated into the fully automated DR algorithm for image enhancement followed by automated segmentation of retinal blood vessels and FAZ determination. Results of performing the fully automated DR algorithm on a colour retinal fundus image are shown in Figure 5.13.

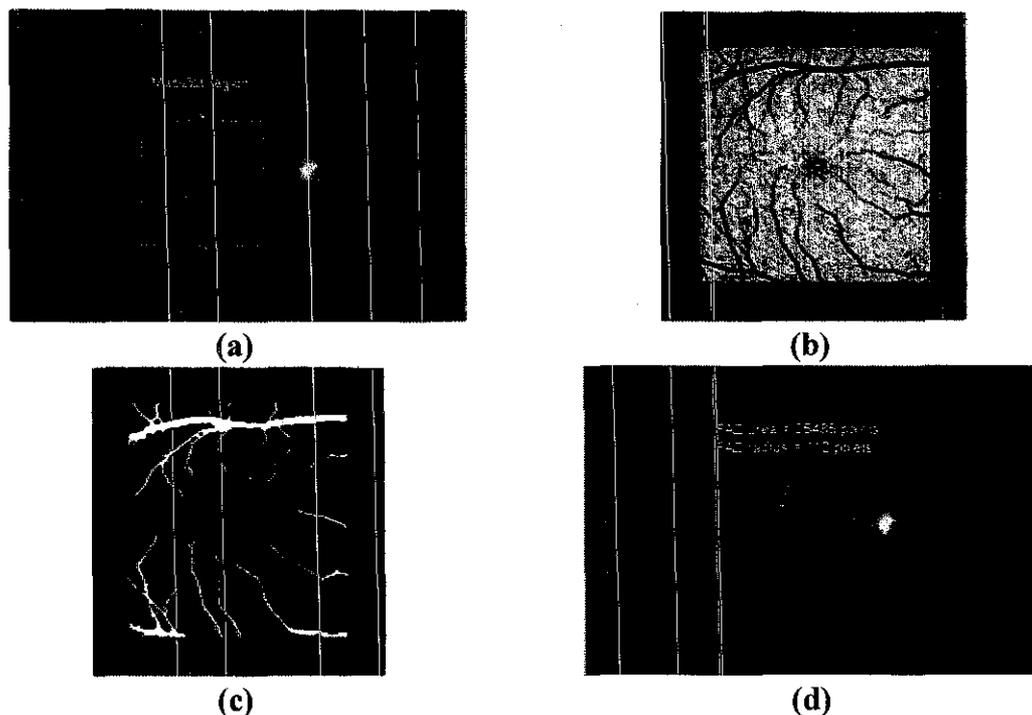


Figure 5.13 Fundus image analysis of FAZ using fully automated DR algorithm, (a) Digital retinal fundus image showing macular region, (b) RETICA-enhanced image on macular region overlaid with the colour fundus image, (c) Segmented retinal vessels and detected vessel end-points on macular region, (d) The determined FAZ area and radius

An example of colour retinal fundus image (Figure 5.13(a)) is cropped at the macular region. The cropped area undergoes RETICA for image enhancement and the enhanced image is overlaid on the colour fundus image (Figure 5.13(b)). This RETICA-enhanced image is subsequently processed by automated segmentation in which the segmented retinal blood vessels obtained (Figure 5.13(c)) are then analysed to obtain retinal vessel end-points. The FAZ area and radius are determined based on the selected retinal vessel end-points as depicted in Figure 5.13(d).

Comparing the results obtained from the two developed DR algorithms, it is found that the FAZ area obtained in the semi-automated DR case is smaller than that of obtained by the fully automated case. Predictably, this is because retinal capillary end-points that are more clearly seen through direct observation in the RETICA-

enhanced image can be adjusted during manual process in the semi-automated DR algorithm. Even though using the same image (RETICA-enhanced image), the automated retinal blood vessels segmentation of the fully automated DR algorithm cannot produce the identical retinal vessel end-points as that of manually adjusted using the semi-automated one. It makes the FAZ area obtained by the fully automated DR algorithm greater than that of obtained by the semi-automated one. Therefore, FAZ radius, which is defined as half of the longest line connecting two detected points encircling the perimeter of macula, is used as FAZ parameter instead of the area. The use of FAZ radius is predicted to be more consistent in characterising the FAZ and this will be discussed in details in the next section of accuracy analysis.

5.6.2 Statistics of Diabetic Patients

Two clinical studies – interventional and observational – have been conducted. In the interventional clinical study MOH/CRC/CTA004/100209-rvd130309, 21 patients were involved. The patient distribution based on DR severity and the corresponding number of usable fundus and FFA images is tabulated in Table 5-5.

Table 5-5 Colour fundus image and FFA image distribution

DR Grades	Patients involved in the study	Colour fundus image	FFA images
No DR	6	10	10
Mild	4	6	6
Moderate	3	6	6
Severe	4	7	7
PDR	4	7	7
Total	21	36	36

In the observational clinical study NMRR-08-842-1997, a total of 256 patients were involved. The FAZ area is analysed for 315 fundus images (175 no DR, 52 mild NPDR, 32 moderate NPDR, 18 severe NPDR and 38 PDR) and the statistics of the FAZ areas according to DR severity is shown in Table 5-6. Having an equal clinical treatment, severe NPDR and PDR cases, as suggested by the ophthalmologists, are grouped into one in the analysis. The collected 315 fundus images are saved into a database called Fundus Image for Non-invasive Diabetic Retinopathy System (FINDeRS) [179].

Table 5-6 Statistics of FAZ areas for semi-automated DR algorithm

	FAZ areas			
	No DR	Mild	Moderate	Severe/ PDR
Sample size	175	52	32	56
Mean (pixels)	13644.20	21041.17	27198.31	33933
Std. dev (pixels)	2727.29	3709.95	3180.89	6787.10
Median (pixels)	13817.00	20177.50	27271.00	32211.50
Min (pixels)	6124	14002	21132	27051
Max (pixels)	18667	28202	33358	66558

As seen in Table 5-6, statistically speaking, the sample size is sufficient in each of DR stages to consider the distribution of the FAZ area as a normal distribution that will be analysed in the following section. The mean and median of the FAZ area increase as the DR stage progresses to a more severe level. Standard deviation that indicates most of the distribution of FAZ area around its mean for a particular stage varies among DR stages. Moreover, based on the standard deviation, the distribution of FAZ area in each DR stage is generally separated leading to possibility of classification of DR stages. However, based on the maximum and minimum values of FAZ areas of each DR stage, the ranges of FAZ area for the DR stages are overlapping. Hence, to handle this, an effective and reliable DR severity classification technique has to be developed and implemented as a part of the semi-automated DR algorithm based on the obtained FAZ areas.

Less than the image number used in the analysis of the semi-automated DR algorithm, the fully automated one selects a total of 133 colour retinal fundus images consisting of 85 images of no DR, 25 images of mild NPDR, 13 images of moderate NPDR and 10 images of severe NPDR and PDR. This is because not all images from FINDeRS can be used by the fully automated DR algorithm for improper acquisition process (dark or blur images and shadowy image) and pathologies near the macula (exudates, haemorrhages, micro-aneurysms, and drusens) that may lead to incorrect detection of retinal blood vessel end-points in the macular region. The selected images undergo the fully automated DR algorithm to obtain the FAZ radii; the statistics of which is shown in Table 5-7.

Table 5-7 Statistics of FAZ radii for fully automated DR algorithm

	FAZ radii			
	No DR	Mild	Moderate	Severe/ PDR
Sample size	85	25	13	10
Mean (pixels)	101.28	104.58	123.37	103.12
Std. dev (pixels)	11.34	10.56	10.57	23.62
Median (pixels)	101.18	105.31	123.86	106.97
Min (pixels)	67.31	75.90	106.90	58.05
Max (pixels)	120.51	120.18	143.69	133.83

Based on the results tabulated in Table 5-7, the sample size is statistically sufficient only for no DR and mild NPDR stages, while the rest i.e. moderate NPDR, severe and PDR are statistically lacking. It comes to be important to draw a general conclusion based on data with statistically sufficient sample size, yet, in order to present all DR stages, data from moderate, severe and PDR are still included in the analysis and performance evaluation of fully automated DR algorithm. The mean of FAZ radius for severe and PDR in addition is lower than that of mild and moderate NPDR. The standard deviation of severe and PDR is also more than twice as large as the other three DR stages. Nevertheless, since the sample size of severe and PDR is statistically insufficient, it cannot be said that their FAZ radii are normally lower than that of mild NPDR. Referring to the results shown in Table 5-6 in which the mean and median of FAZ area increase as the DR stage progresses to a more severe level, in general, the increase of FAZ radius also shows a similar trend. A statistical correlation analysis between FAZ area obtained by the semi-automated DR algorithm and FAZ radius obtained by the fully automated DR algorithm will further show quantitative results to prove a similar trend between these two DR algorithms. Overlapping between two adjacent stages also occurs according to the maximum and minimum values of FAZ radii of each DR stage. A classification technique similar to that of the semi-automated DR algorithm is implemented in the fully automated DR algorithm based on the obtained FAZ radii.

5.6.3 DR Grading Using Gaussian Bayes Classifier

Prior to applying Gaussian Bayes Classifier for grading of DR severity level, the suitability of the data distribution with that of Gaussian distribution is determined

both qualitatively and quantitatively. Qualitatively, the probability mass functions for most of the DR stages are shown in Figure 5.14.

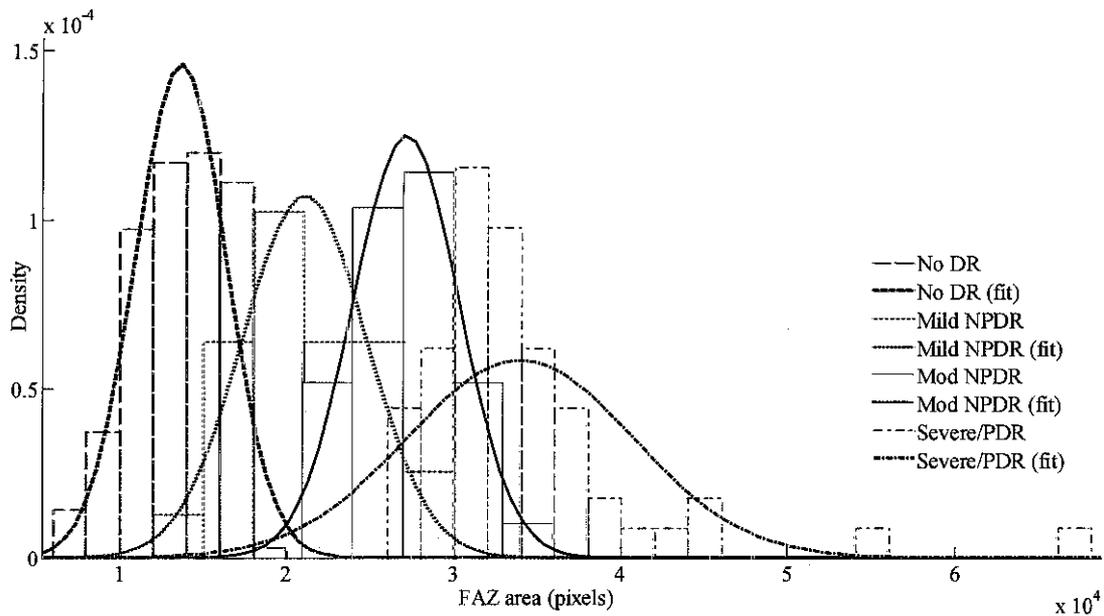


Figure 5.14 Probability mass function of FAZ area for each DR severity level and its estimated Gaussian distribution

The R^2 measure of goodness of fit test that quantitatively determines the suitability of the data distribution with the Gaussian distribution also yields the results as shown in Table 5-8.

Table 5-8 Measure of goodness of fit for Gaussian distribution on FINDeRS

	FAZ area			
	No DR	Mild	Moderate	Severe/ PDR
Sample size	175	52	32	56
R^2	0.9299	0.9003	0.6772	0.9948

As illustrated in Figure 5.14, though the probability mass functions for most of the DR stages show similar characteristics of a Gaussian distribution, most of the DR stages overlap between one and another. Gaussian Bayes classifier, for being able to classify DR stages based on probability, comes to be suitable for grading of DR severity level. Moreover, as depicted in Table 5-8, the results for most of the DR stages showing sufficiently high R^2 values are expected. Except moderate NPDR that has R^2 of 0.6772, the other DR stages have R^2 greater than 0.90. It may occur since the sample size of moderate NPDR is smaller than that of the other DR stages.

Increasing the sample size of moderate NPDR in turn may lead to an increase in R^2 . In general, the results of R^2 measure of goodness of fit are in line with the probability mass function of FAZ area as illustrated in Figure 5.14. Since the distribution of FAZ follows a Gaussian distribution, the Gaussian Bayes classifier is suitable to classify DR severity levels in this application and subsequently is designed to classify DR severity levels based on the measured FAZ area using the LPPR.

The LPPR between two selected stages can be computed using the corresponding mean and standard deviation data from Table 5-6 and applying (5-13). From the LPPR, the thresholds of FAZ area ranges for DR grading are determined as shown in Figure 5.15. The selected two stages are as follows: no DR and mild NPDR, mild NPDR and moderate NPDR, moderate NPDR and severe NPDR/ PDR. If LPPR between no DR and mild NPDR, for example, is greater than 0, the DR grade will be categorised as no DR. Otherwise, the DR grade will be categorised as mild NPDR. The LPPR is also calculated for other DR stages.

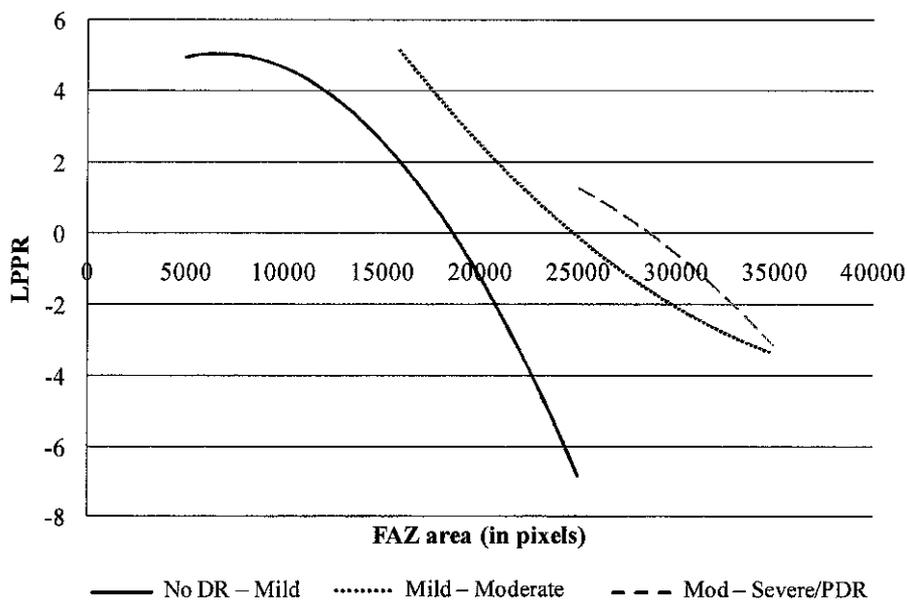


Figure 5.15 LPPRs for DR grading

Table 5-9 shows the range of FAZ area (in pixels) for the DR grade for different LPPR settings for the Gaussian Bayes classifier. If $LPPR = 0$, the Gaussian Bayes classifier does not include progression (in between) stages of DR grades. Progression stages, which in the Gaussian Bayes classifier can be obtained by setting $LPPR \neq 0$,

are important to give early indication to patients of the DR progression to more severe stages. Here, the receiver operating characteristic (ROC) analysis is used to find the optimum non-zero LPPR setting.

Table 5-9 DR Gaussian Bayes classifier based on FAZ area with progression stages for different LPPRs

DR stage	FAZ area range (pixels)			
	LPPR = 0	-0.25<LPPR<0.25	-0.5<LPPR<0.5	-0.75<LPPR<0.75
No DR	1-18702	1-18405	1-18101	1-17789
Progression no DR to mild NPDR	-	18406-18731	18102-19278	17790-19558
Mild NPDR	18703-25002	18732-24513	19279-24036	19559-23569
Progression mild to moderate NPDR	-	24514-25503	24037-26109	23570-26549
Moderate NPDR	25003-29939	25504-29177	26110-28224	26550-26734
Progression moderate to severe NPDR	-	29178-30593	28225-31175	26735-31703
Severe NPDR/PDR	29940-45431	30594-100000	31176-100000	31704-100000

For receiver operating characteristic (ROC), the sensitivity and specificity must be determined [254, 256-257]. Sensitivity measures the proportion of actual positives, which is correctly identified, while specificity measures the proportion of negatives, which is correctly identified. ROC curve is a plot of sensitivity against 1-specificity across a range of possible thresholds. In addition, accuracy gives an overall performance of the classifier.

Using ROC analysis, an optimum threshold is determined for the system by choosing a threshold, which gives an operating point nearest to the reference point. Based on the nearest distance between an operating point and the reference point in the ROC curve, the optimum classifier for each DR stage can be determined. For each of iteration of VFCV method, ROC analysis is applied on training data to evaluate the performance of the DR system. Using VFCV, data is divided into 5 subsets to perform 5 iterations in which four subsets are used to train the system and the rest is used to test the system. An example of optimal Gaussian Bayes classifiers obtained from one of the iterations is shown in Table 5-10.

Table 5-10 Optimal Gaussian Bayes classifiers for all DR stages

Optimum Gaussian Bayes classifiers for DR Stages	(1-Specificity)	Sensitivity
No DR ($-2 < LPPR < 2$)	0.02	1
Mild ($-2 < LPPR < 2$)	0.07	0.93
Moderate ($-0.75 < LPPR < 0.75$)	0.23	0.77
Severe/ PDR ($-0.75 < LPPR < 0.75$)	0.03	0.98

Based on the above settings, the corresponding FAZ area range of DR stages as shown in Table 5-11 can be clearly defined.

Table 5-11 DR Gaussian Bayes classifier with progression range

Stage	FAZ area range (pixels)
No DR	1 – 16204
Progression no DR to mild NPDR	16205 – 20912
Mild NPDR	20913 – 20654
Progression mild NPDR to moderate NPDR	20655 – 26866
Moderate NPDR	26867 – 27054
Progression moderate NPDR to severe/PDR	27055 – 31673
Severe/ PDR	31674 – 100000

As shown in Table 5-11, the DR grading system is able to identify DR severity even though the FAZ area lies in the progression range (highlighted rows). To doctors and patients, these ranges can be used to indicate if the DR condition is progressing to a severe level or at the borderline between two stages.

The results of DR grading based on FAZ area enlargement are analysed using non-parametric statistical correlation analysis based on Spearman's rank correlation coefficient [258]. This analysis shows significance and correlation of the FAZ indicated by area for the semi-automated DR algorithm and by radius for the fully automated one with DR severity levels graded by ophthalmologists. The strongest correlation is represented by value of 1 and the weakest one is represented by value of 0. Non-parametric analysis is conducted on the DR data because of a statistically insufficient sample size of one or two DR stages indicated by less than 25 samples. For the analysis of semi-automated DR algorithm, the insufficient sample size is from severe NPDR with only 18 images and for the analysis of fully automated DR algorithm, only two DR stages - no DR and mild NPDR stages - meet statistically sufficient sample size with 87 images and 25 images respectively. The other two DR stages, i.e. moderate NPDR with 13 images and severe PDR with 10 images do not

have a sufficient sample size. Therefore, non-parametric statistical analysis to measure correlation coefficient between FAZ area and DR severity is conducted. Correlation coefficient measures the strength of the linear dependence between two variables. Table 5-12 shows the results of statistical correlation analysis measured for two situations, i.e. (1) the correlation measured for no DR and all DR stages and (2) the correlation measured for DR stages only (without no DR) for both semi-automated and fully automated DR algorithms.

Table 5-12 Correlation between FAZ area and (1) DR severity 1 (no DR, mild NPDR, moderate NPDR, severe NPDR and PDR), (2) DR severity 2 (mild NPDR, moderate NPDR, severe NPDR and PDR)

	Semi-automated			Fully-automated		
	Correlation coefficient	Significance (2-tailed)	N	Correlation coefficient	Significance (2-tailed)	N
No DR – DR	0.877	1.40×10^{-101}	315	0.805	1.62×10^{-31}	133
Mild – mod – severe/ PDR	0.845	2.12×10^{-39}	140	0.744	3.1×10^{-9}	46

As shown in Table 5-12, in the first situation, i.e. correlation measured for no DR and all DR stages (mild NPDR, moderate NPDR, severe NPDR and PDR), both semi-automated and fully automated DR algorithms have a strong correlation more than 0.80 at significance (P) less than 0.01. In the second situation, which measures a correlation for DR stages only, the FAZ area determined by the semi-automated DR algorithm strongly correlates with DR stages graded by ophthalmologists with correlation coefficient of 0.845 higher than that of obtained by the fully automated DR algorithm with correlation coefficient of 0.744 at significance (P) less than 0.01. As expected, the correlation between FAZ parameters (area and radius) obtained by both semi-automated and fully automated DR grading systems and their corresponding DR severity level graded by the ophthalmologists for no DR and all DR stages is higher than that of DR stages only. This is because of the limitation of the sample size for specific DR stages. It can be seen that for DR stages only, the correlation between FAZ radii determined by the fully automated DR algorithm and their corresponding DR grades has the lowest correlation coefficient of 0.744 due to insufficient sample size of moderate NPDR, severe and PDR. It is believed that increasing the sample size of these specific DR stages will increase the correlation between FAZ radii and their corresponding DR stages.

In general, the findings from this study show a strong correlation between FAZ enlargements measured from colour fundus images and DR severity with correlation factor up to 0.877 for the semi-automated DR algorithm and 0.805 for the fully automated DR algorithm both at a very high significance (P) of less than 0.01. This strong correlation indicates that the FAZ obtained by the developed DR algorithms using colour fundus images can be used to grade DR severity. These findings further confirm FAZ enlargement in DR measured from fluorescein angiograms as previously reported by Bresnick *et al.* [214], Arend *et al.* [255], Sander *et al.* [223] and Conrath *et al.* [215]. In addition, several detection and segmentation methods on FAZ determination have been developed by Ballerini [259], Conrath *et al.* [216], Zheng *et al.* [260] and Haddouche *et al.* [261]. However, all the aforementioned reports on FAZ enlargement in DR and the developed methods on FAZ determination were applied only on FFA images and not on colour fundus images. So far as we know, early papers on determination of FAZ using colour fundus image merely were published by Fadzil *et al.* [262-265]. One of the main reasons is due to the high contrast of retinal blood vessels and capillaries in the FFA image that makes FAZ detection in FFA images easier. Conversely, FAZ determination in colour fundus image may come to be more difficult for the low contrast of retinal blood vessels and capillaries but it is possible still that the contrast of retinal blood vessels can be significantly enhanced. Our developed method, RETICA, is proven to successfully enhance the contrast of retinal blood vessels in the colour fundus image and even achieves *CIF* of 5.389 slightly lower than that of the FFA image with *CIF* of 5.796 (as described in Chapter 4).

In evaluating the performance of the DR algorithms in grading of DR severity, agreement test and performance test are conducted. An agreement test using Cohen's kappa coefficient measures the strength of inter-observer agreement that in this case is between the ophthalmologists and both semi-automated and fully automated DR algorithms in grading of DR severity. Kappa coefficient equals to 1 if there is a complete agreement between observers when giving response to a variable of *N* subjects. Results of agreement test are shown in Table 5-13.

Table 5-13 Measure of agreement using Kappa coefficient between ophthalmologist and DR algorithms in grading of (1) DR severity 1 (no DR and DR – all stages), (2) DR severity 2 (no DR and mild) and DR severity 3 (no DR, mild and moderate) and DR severity 4 (no DR, mild, moderate and severe/ PDR)

	Ophthalmologists vs. Semi-automated			Ophthalmologists vs. Fully-automated		
	Kappa coefficient	Significance (2-tailed)	N	Kappa coefficient	Significance (2-tailed)	N
No DR – DR	0.994	1.34×10^{-69}	315	0.901	2.48×10^{-25}	133
No DR – mild	0.973	4.05×10^{-48}	224	0.840	1.10×10^{-18}	110
No DR – mild – mod	0.918	4.21×10^{-83}	256	0.889	9.80×10^{-36}	121
No DR – mild – mod – severe PDR	0.918	1.62×10^{-146}	315	0.787	2.68×10^{-40}	133

As shown in Table 5-13, the agreement test between ophthalmologists and each semi-automated and fully automated DR algorithm is measured in four situations, i.e. (1) no DR and DR, (2) no DR and mild NPDR, (3) no DR, mild and moderate NPDR and (4) no DR, mild, moderate, severe NPDR and PDR. In the first situation, the class is categorised into two, i.e. (1) no DR and DR and (2) all DR stages (i.e. mild, moderate, severe NPDR and PDR) are combined into one category. Results show that both semi-automated and fully automated DR algorithms have Kappa coefficient of 0.994 and 0.901 indicating a strong agreement with ophthalmologists in grading of DR severity. Importantly, it shows the effectiveness of the developed DR algorithms for DR mass screening.

Having categorised into two classes, the second situation shows similar results. However, instead of no DR and DR as in the first situation, the class is divided into no DR and mild NPDR as its adjacent class. A strong agreement obtained from the second situation with Kappa coefficients of 0.973 and 0.840 for semi-automated and fully automated DR algorithms points out that the developed algorithms are able to differentiate between no DR and the early DR stage, i.e. mild NPDR. This important result indicates that the developed DR system is suitable for early detection of DR.

Furthermore, results obtained from the third and fourth situations confirm those obtained from previous situations. Whilst in the third situation the class is categorised into three (i.e. no DR, mild and moderate NPDR), the fourth situation is divided into four representing no DR and all specific DR stages. In both of these situations, Kappa coefficient obtained by semi-automated DR algorithm is 0.918 at a very high significance (P) of less than 0.01. For the fully automated algorithm, Kappa coefficients obtained are lower than that of the semi-automated algorithm. However, these values (i.e. 0.889 and 0.787) obtained by the fully automated algorithm are still considered as high and represent a strong agreement between observers, which in this case are the ophthalmologists and the developed algorithm. This strong agreement indicates that both semi-automated and fully automated DR algorithms are suitable for monitoring and grading of DR severity.

Generally, in all of the compared situations, Kappa coefficients obtained by the fully automated DR algorithm are consistently lower than that of the semi-automated one. As expected, it is because the sample size of colour fundus image used in the analysis of the fully automated DR algorithm is smaller than the one in the analysis of the semi-automated one. Increasing the sample size of DR images data perhaps will increase the strength of agreement between observers. Unlike the semi-automated DR algorithm which uses all 315 colour fundus images in FINDeRS, the fully automated DR algorithm only uses a total of 133 colour fundus images from FINDeRS to be analysed. It is due to improper acquisition process (dark or blur images and shadowy image) and presence of pathologies close to the macula (exudates, haemorrhages, micro-aneurysms, and drusens) that lead to inaccurate FAZ determination. The stronger agreement in the semi-automated DR algorithm comes to be reasonable due to its manual process. The manual process itself is useful to handle colour fundus images with low image quality and possible presence of pathologies in the macular region. However, the fully automated DR algorithm still has a significantly strong agreement with the ophthalmologists in grading of DR severity, thus enabling it to be effectively used to assist ophthalmologists for early DR detection, DR mass screening, and monitoring and grading of DR severity.

The performance of each semi-automated and fully automated DR algorithm is

evaluated in terms of sensitivity, specificity and accuracy. In the semi-automated DR algorithm, it is measured based on the average values of sensitivity, specificity and accuracy from the total of 5 subsets taken from all 315 fundus images from FINDeRS. For the fully automated, the performance is analysed from the total of 133 fundus images from FINDeRS (87 images of no DR, 23 images of mild NPDR, 13 images of moderate NPDR and 10 images of severe NPDR/ PDR). As previously mentioned, not all images from FINDeRS are analysed using the fully automated DR algorithm due to and presence of pathologies in macular region and improper acquisition process yielding dark or blur images and shadowy images leading to an inaccurate FAZ determination. The performance is measured by comparing a particular DR stage with its adjacent stages as, for instance, in the classifier of ‘mild NPDR versus adjacent DR stages’, the DR system classifies between mild NPDR and its adjacent DR stages, i.e. no DR and moderate NPDR. Results of performance analysis of both semi and fully automated DR algorithms are shown in Table 5-14.

Table 5-14 Performance analysis of the semi-automated and fully automated DR algorithms in classifying DR severity levels

Classifier	Sensitivity		Specificity		Accuracy	
	Semi-auto	Fully-auto	Semi-auto	Fully-auto	Semi-auto	Fully-auto
No DR – mild NPDR	1	0.954	0.979±0.310	0.905	0.991±0.140	0.944
Mild NPDR – adjacent stages	0.841±0.114	0.913	0.992±0.100	0.960	0.968±0.190	0.951
Moderate NPDR - adjacent stages	0.842±0.168	0.846	0.971±0.360	0.939	0.959±0.450	0.913
Severe/ PDR - adjacent stages	0.950±0.750	0.300	0.988±0.110	0.846	0.981±0.200	0.609

As shown in Table 5-14, the values of sensitivity, specificity and accuracy vary among DR stages for both semi-automated and fully automated DR algorithms. For the semi-automated DR algorithm, the values of sensitivity, specificity and accuracy for ‘no DR versus mild NPDR’ are significantly high (greater than 0.979). As expected, these high values are consistent with the strong agreement (Kappa coefficient of 0.973) obtained from the previous agreement test between the ophthalmologists and the semi-automated DR algorithm in the same situation (Table 5-13). This performance result further indicates the high ability of the semi-automated DR algorithm to differentiate between no DR and its adjacent stage, i.e. mild NPDR. A perfect value of sensitivity (i.e. 1) obtained by the classifier ‘no DR

versus mild NPDR' shows that the algorithm is able to diagnose correctly a patient having no DR when the patient is actually having no DR without any erroneous diagnoses. Moreover, a significantly high value of sensitivity (i.e. 0.979) shows that the algorithm is also able to correctly diagnose most of the patients actually suffering from mild NPDR. High sensitivity and specificity result in high accuracy obtained by the classifier for this particular class. Compared with the sensitivity, the value of specificity is a slightly lower indicating that some of patients are mistakenly classified as no DR when they are actually having mild NPDR. It may occur when the patient's stage is close to the progressing stage between no DR and mild NPDR.

Using the developed algorithm, when the patient is in the progression stage, both the most and the second probable DR stages the patient suffers from could be informed. The algorithm may mistakenly decide which of these two stages is the most probable due to slight difference in measuring FAZ area even if the difference is only one pixel. Hence, it is recommended for the user to decide carefully a stage when the algorithm classifies the patient's stage as progression stage. However, this value of specificity is considered as high (above 90%) and generally accepted for such a medical system. In case of the classifier 'no DR versus mild NPDR', high values obtained for both sensitivity and specificity indicate that the semi-automated DR algorithm is accurate and suitable for early DR detection and thus, the developed DR system is also effective for DR mass screening.

Moreover, the sensitivity value for the semi-automated DR classifier of mild NPDR has similar value to that of moderate NPDR (around 0.84). This indicates that the classifier has lower ability to correctly detect a patient actually suffering from mild or moderate NPDR compared to other DR stages (no DR and severe/ PDR stages). It occurs since the overlapping FAZ areas in mild and moderate NPDR are more than that of other DR stages. It can be minimised by increasing the number of training data for mild and moderate NPDR. Even though the semi-automated DR classifier for mild and moderate NPDR has lower sensitivity, the classifier shows high specificity for mild and moderate NPDR (0.971) that have been predicted since the classifiers for other DR stages, i.e. no DR and severe/ PDR have high values of sensitivity. That is to say, the classifier has high probability in detecting a specific

DR stage correctly rather than mild and moderate NPDR.

The high values of accuracy for all DR stages imply that the semi-automated DR classifier can detect a particular stage with high sensitivity and specificity. The accuracy indicates the ability of the classifier in correctly detect both a specific class as the class and a non-class as the non-class. Since the semi-automated DR algorithm shows high sensitivity and specificity in classifying all of DR stages, high accuracy values obtained for all DR stages have also been predicted. Hence, the semi-automated DR classifier having high sensitivity, specificity and accuracy has a potential to be used for early detection of DR, DR mass screening, monitoring and grading DR severity and for effective treatment of severe cases.

For the fully automated DR algorithm shown in Table 5-14, the values of sensitivity, specificity and accuracy for all DR classifiers are relatively high (≥ 0.846), except for the severe and PDR stages with only 0.30 of sensitivity and 0.609 of accuracy. It occurs as the number of selected severe and PDR fundus images is quite low, i.e. 10 images and the distribution of FAZ areas for severe and PDR overlaps more with its adjacent stage, i.e. moderate NPDR and even with mild NPDR. Based on statistics, the sample size of 10 is also considered as significantly low to draw a general conclusion. After all, in a most severe case, the ophthalmologists must be involved to determine and monitor a proper treatment for the patient. Therefore, general conclusion on performance analysis of the fully automated DR classifier will exclude the performance result of the system on detecting specific severe and PDR stage.

For moderate NPDR, the fully automated DR classifier obtains 0.846 of sensitivity, 0.939 of specificity and 0.913 of accuracy. Higher specificity compared to sensitivity indicates that the system has lower false positive rate detection than false negative rate. In other words, among the collected samples of moderate NPDR, the DR classifier more mistakenly diagnoses a patient not suffering from moderate NPDR when the patient is actually suffering from moderate NPDR compared to diagnose a patient suffering from moderate NPDR when the patient is actually not suffering from moderate NPDR. For such a medical system, it is quite dangerous to detect wrongly a

patient for not suffering from a particular disease when the patient is actually suffering from that disease rather than to detect its inverse situation. However, since this particular stage (moderate NPDR) is detected in corresponding to its adjacent stages (mild NPDR and severe/ PDR), two images out of only 13 images of moderate NPDR are misclassified as severe/ PDR contributing to false negative rate. Even though the DR classifier gives the wrong result of DR grade, the misclassification of the moderate NPDR to severe/ PDR should have given an early warning for ophthalmologist about the condition of the patient.

This can also be observed in the classifier ‘severe NPDR/PDR – adjacent stages’ in which adjacent stage is identified as moderate NPDR. In this case, the classifier has higher specificity (0.846) than sensitivity (0.30) indicating a similar situation as in the classifier ‘moderate NPDR – adjacent stages’. From a small sample size of only 10 for severe/ PDR, most of them are mistakenly diagnosed for not suffering from severe/ PDR. It happens due to presence of pathologies in the macular region mostly occurred in the severe stages. Even though colour retinal fundus images in this evaluation of the fully automated DR algorithm has been carefully selected, it is not possible to select colour fundus images without pathologies at this current DR stage due to the nature of severe and PDR stages. The more severe the stage is, the more the presence of pathologies is. Two samples of severe/ PDR images are shown in Figure 5.16.

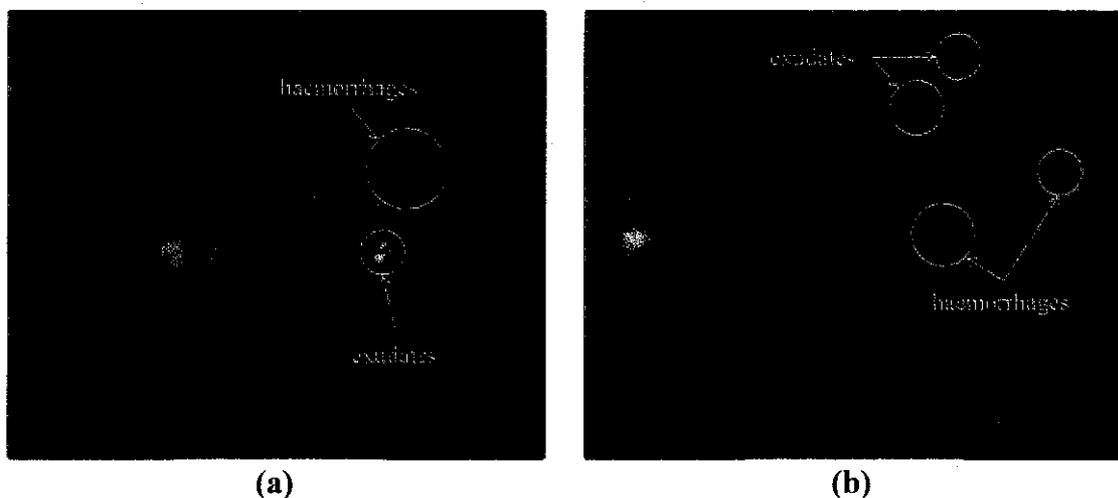


Figure 5.16 Two samples of colour fundus images (a) severe misclassified as moderate NPDR (b) PDR correctly classified as PDR

The colour retinal fundus image in Figure 5.16(a) was graded by the ophthalmologists as severe NPDR. However, the fully automated DR algorithm classifies this image as moderate NPDR due to presence of small parts of exudates in the macular region. These exudates indicated by yellowish patches have been wrongly detected as retinal vessel end-points; thus, it causes an inaccurate FAZ determination leading to misclassification of DR grade. Another colour retinal fundus image shown in Figure 5.16(b) was graded by the ophthalmologists as PDR similar with what has been successfully classified by the fully automated DR algorithm. Due to the presence of pathologies, such as exudates and haemorrhages out of the macular region, the retinal end-point at the macular region can be correctly detected. Thus, the fully automated DR algorithm is able to accurately determine the FAZ that leads to an accurate DR severity grading.

In general, excluding the specific severe and PDR stage, the fully automated DR algorithm consistently maintains high sensitivity (≥ 0.846), specificity (≥ 0.905) and accuracy (≥ 0.913) for most of DR stages. This indicates the potentiality of the fully automated DR system to be used for early DR detection, DR mass screening, monitoring and grading DR severity.

By comparing two developed DR algorithms, i.e. semi-automated and fully-automated, the semi-automated DR algorithm shows better performance and has a greater potential of the DR grading system according to its statistical correlation analysis and performance analysis. However, due to some practical reasons such as to allow untrained operators to use, the fully automated DR algorithm is developed with some reductions but still acceptable on its performance.

5.6.4 Accuracy Analysis of FAZ

Ahead of data analysis, outliers need to be determined and excluded from the data. Boxplot used as a graphical display to indicate outliers [266] uses the first and third quartiles, Q1 and Q3, with some constant k to determine outliers. Table 5-15 shows

details of quartile values in each type of error (E_{GT-OP} and E_{GT-DR}). Outliers are determined for being outside of the range:

$$[Q_1 - k(Q_3 - Q_1), Q_3 + k(Q_3 - Q_1)], \quad k=1 \quad (5-18)$$

Table 5-15 Quartile and Boxplot Range of DR Stages

	Ground truth – DR system (E_{GT-DR})
Quartile 1	13.30
Quartile 2	18.29
Quartile 3	21.99
Boxplot range minimum	4.61
Boxplot range maximum	30.67

From the Boxplot analysis, one outlier for ophthalmologist error (E_{GT-OP}) data is found while four outliers are for the DR system error (E_{GT-DR}) data. The statistical analysis in Table 5-16 uses 32 pairs of fundus images and FFA images for DR system error (E_{GT-DR}).

Table 5-16 Statistics of FAZ radii for accuracy analysis of DR grading system

	Ground truth – DR system (E_{GT-DR})
No. of data	32
Mean absolute error (pixels)	18.68
Std. deviation (pixels)	5.28
Skewness	-0.45
Kurtosis	-0.21
Lower bound (pixels)	6.37
Upper bound (pixels)	28.34
Range (pixels)	21.97

Shown in Table 5-16, the mean absolute error for DR system is relatively large predictably because the DR system uses colour fundus images, which have lower contrast resulting in large errors. It is observed that the standard deviation (i.e. 5.28) of the DR system error (E_{GT-DR}) data is significantly small. This can be further analysed using relationship plots of DR system against ground truth data as shown in Figure 5.17.

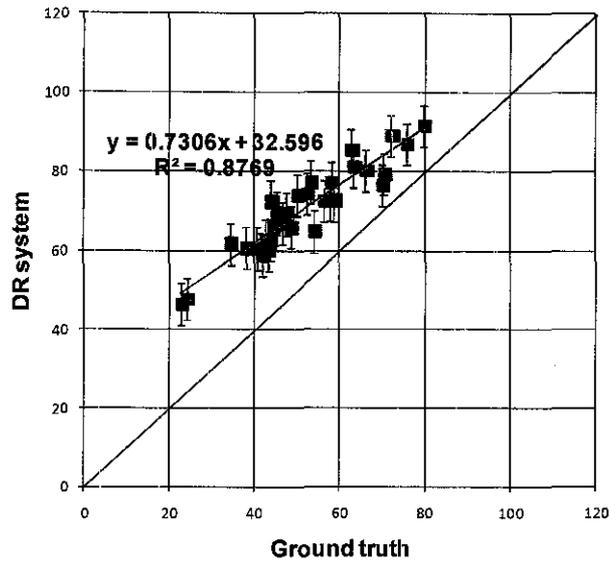


Figure 5.17 FAZ radii DR system against ground truth

The regression analysis of Figure 5.17 shows a strong linear relationship of DR system with ground truth data ($R^2 = 0.8769$) indicating a high precision of the system. In addition, the correlation analysis between ground truth and DR system shows how linear the relationship is. In Table 5-16, the error distributions are considered normal (skewness and kurtosis are close to 0) and the data samples are sufficient for parametrical statistical analysis such as Pearson correlation coefficient analysis to determine the linear relationships between ground truth and DR system for the radius measurement.

Table 5-17 describes a correlation between radius of the FAZ area obtained by the DR system and radius of the FAZ area obtained from the ground truth. There is a strong correlation, 0.936 (Pearson correlation) at a very high significant level ($P < 0.01$).

Table 5-17 Correlation between radius of FAZ obtained by DR system and ground truth

		FAZ radii obtained by DR system (pixels)
FAZ radii obtained from ground truth (pixels)	Correlation coefficient	0.936
	Significance (2-tailed)	3.48×10^{-15}
	N	32

Inferentially, the DR system is consistent and objective in determining the FAZ area. The above analysis that the DR system has a low standard deviation of error and strong linear relationship ($R^2 = 0.8769$) with ground truth and correlation coefficient analysis (0.936) also implies that the error can be considered as a systematic error. In the actual implementation of the DR grading system, the systematic error has been overcome by the Gaussian Bayes classifiers. The DR system based on colour fundus images, therefore, can provide an accurate and precise measurement of FAZ enlargement.

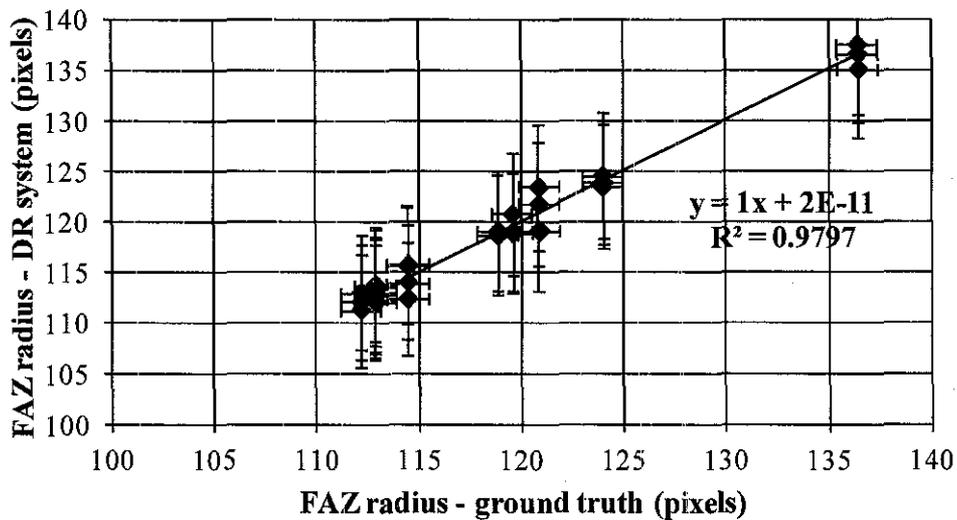
For the fully automated DR algorithm, the consistency of the algorithm in determining the FAZ radius is compared to that of in determining the FAZ area. As stated earlier (Section 5.3), the radius is preferred to reduce error of area in determining FAZ as a result of performing square factor on the radius of the FAZ assuming its area as a circle. To measure the consistency of the fully automated DR algorithm, two users ran the algorithm on eight colour retinal fundus images randomly selected from FINDeRS. Each of selected images underwent three to four simulations and average of FAZ radii was measured as the reference (ground truth) for each image. A total of 30 observations have been recorded. In each observation, the FAZ radius obtained for a particular colour retinal fundus image was compared to its reference (ground truth) and error between these two were analysed. Statistics of FAZ radii and areas' differences for the accuracy analysis of the fully automated DR algorithm is shown in Table 5-18.

Table 5-18 Statistics of error of FAZ radii and areas for the accuracy analysis of the fully automated DR algorithm

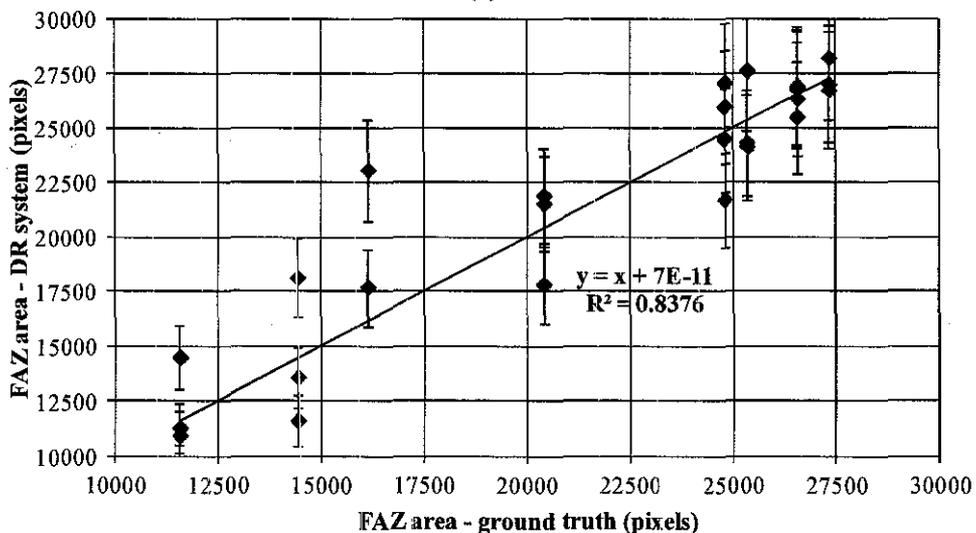
	Ground truth – DR system (FAZ radius)	Ground truth – DR system (FAZ area)
No. of data	30	30
Mean absolute	0.797	1707
Std. deviation	0.637	1923
Lower bound	0.023	216
Upper bound	2.572	8474
Range (pixels)	2.549	8258

From Table 5-18, the mean absolute error of the fully automated DR algorithm when using FAZ radius as parameter is significantly small (less than 1 pixel)

compared to that of when using FAZ area with mean absolute error of 1707 pixels. This indicates that the use of radius as parameter of FAZ results in high accuracy of the fully automated DR algorithm. Moreover, from a total of 30 observations, the maximum error produced by the fully automated DR algorithm when using FAZ radius is less than 3 pixels with a significantly small standard deviation (less than 1 pixel) compared to that of when using FAZ area with standard deviation of around 2000 pixels and maximum error of more than 8000 pixels. It indicates that the fully automated DR algorithm has not only high accuracy, but also high precision. This can be further analysed using relationship plots of DR system against ground truth data as shown in Figure 5.18.



(a)



(b)

Figure 5.18 (a) FAZ radii obtained by the fully automated DR algorithm against ground truth (b) FAZ areas obtained by the fully automated DR algorithm against ground truth

Illustrated in Figure 5.18, both radius and area obtained by the fully automated DR algorithm have a strong linear relationship with the ground truth data indicated by their most perfectly linear regression line. However, the fully automated DR algorithm with FAZ radius as parameter ($R^2 = 0.9797$) has a stronger relationship than that of with FAZ area as parameter ($R^2 = 0.8376$) according to their coefficients of determination R^2 . It further proves that the algorithm with radius as its FAZ parameter has a high precision as previously shown by its significantly small standard deviation. These results also indicate that the use of FAZ radius in the fully automated DR system is more reliable and consistent in determining the FAZ rather than the use of FAZ area. It is important to choose a parameter that measures FAZ as accurate and precise as possible since the result of measurement will be inputted into the DR classifier. The more accurate and precise the result of FAZ measurement is, the more accurate the DR grading is.

Compared to other FAZ analysis-based methods used to grade DR severity [216, 259-260], the developed computerised DR system offers two main advantages. Firstly, the developed DR system (both semi-automated and fully automated DR algorithms) is able to determine the FAZ only using colour fundus images whilst the others require invasive FFA. Ophthalmologists may argue that FAZ can only be determined using FFA image since the retinal vessel end-points are clearly seen from high contrast of retinal blood vessels produced by invasive FFA. However, RETICA applied on colour retinal fundus images provably is able to produce contrast of retinal blood vessels slightly lower than that of the FFA. Moreover, accuracy analysis of FAZ shows that the error between FAZ estimated from both colour fundus images and FFA images is equally considered as a systematic error. It means that the estimated FAZ obtained from colour fundus image using the developed algorithm is similar to the FAZ produced by the invasive FFA and indicates that the estimated FAZ obtained from colour fundus image can be used as effectively as the FAZ

obtained from FFA image.

Secondly, as an alternative to existing pathology-based DR grading systems, the FAZ which is determined and analysed using the developed DR system can be used as a parameter for a new protocol to grade DR severity. Based on the aforementioned performance analysis, sensitivity and specificity of the developed DR system (both semi-automated and fully automated DR algorithms) in differentiating between the normal fundus and the DR fundus images are above 0.954 and 0.905 respectively. A comparison of performance and description among these aforementioned DR grading systems is summarised in Table 5-19.

Table 5-19 Comparison of performance among several computerised DR grading systems

	Sensitivity	Specificity	Remarks
Olson <i>et al.</i> [267]	0.83	0.71	Automated detection of DR (without any specific levels) based on the presence of haemorrhages and or aneurysms using digital colour fundus images.
Singalavanija <i>et al.</i> [268]	0.748	0.827	Computerised system to differentiate between normal (no DR) and DR (without any specific severity levels) using digital colour fundus images by detection of DR pathologies (hard exudates, cotton wool spots, micro-aneurysms and retinal haemorrhages)
NMDSRI [269]	0.98	1	Grading of DR uses pathology-based method [270] conducted on non-mydratic stereoscopic fundus images that are manually examined by retina specialists. DR grading is categorised into five severity levels [205]. However, due to its manual assessment, the process is time-consuming (roughly 20 minutes per image).
RETINO	S-A: 1 F-A: 0.954	S-A: 0.979 F-A: 0.905	Automated monitoring and grading of DR severity levels based on FAZ analysis using digital colour fundus images. (<i>note: S-A is semi-automated DR algorithm and F-A is fully automated DR algorithm</i>)

Shown in Table 5-19, the performance of RETINO with minimum sensitivity and

specificity of 0.954 and 0.905 respectively is better than that of by Olson *et al.* [267] with sensitivity of 0.83 and specificity of 0.71 by also applying an automated grading protocol to the digital colour fundus images. Our findings are also better than that of Singalavanija *et al.* [268] with sensitivity of 0.748 and specificity of 0.827. Singalavanija *et al.* [268] developed an automated computerised DR screening program to analyse colour retinal images based on the presence of diabetic features such as exudates, haemorrhages, and micro-aneurysms. Both automated DR grading systems by Olson *et al.* [267] and Singalavanija *et al.* [268] aim only to differentiate DR from non-DR patients by analysing the pathologies, such as haemorrhages, aneurysms, exudates and cotton wool spots in colour retinal fundus image without informing a specific DR severity level the patient suffers from. Therefore, these two developed automated DR systems are effective only for DR screening. Moreover, the RETINO system specifically applying the semi-automated DR algorithm with sensitivity of 1 and specificity of 0.979 is comparable to Joslin Vision Network non-mydratic digital stereoscopic retinal imaging (NMDSRI) [269] with sensitivity and specificity of 0.98 and 1 respectively for grading of DR severity. Both these DR computerised systems are able to classify DR severity into five levels as categorised in [205]. However, the assessment of colour retinal fundus images in NMDSRI is conducted manually by retina specialists. Though the fully automated RETINO with sensitivity and specificity of 0.954 and 0.905 respectively has a lower performance than the NMDSRI, it still has a greater advantage since the whole process is of automated and the user needs to input once only at the beginning of the process when the centre of macular region is selected.

In general, the developed DR system (RETINO) either by semi-automated or by fully automated DR algorithms is sensitive enough to detect a particular DR stage and specific enough to exclude the non-affected individuals. For effectiveness in DR grading, the RETINO has been tested and evaluated in two clinical studies – interventional and observational – and achieved optimum accuracy, sensitivity and specificity in detecting DR severity needed for medical and thus enables an effective DR grading using colour fundus images. This new grading protocol based on FAZ analysis using the developed DR system can be implemented as an alternative to the current DR grading method using pathology-based direct ophthalmoscopy. Thus the

RETINO has a great potential to assist the ophthalmologists in early detection of DR, DR mass screening, as well as for monitoring and grading of DR severity.

For future research, the data used can be enlarged for further confidence of the results. The validity of the proposed DR grading method can be also established by performing cross-validation based on expert opinions. The performance of this DR grading method can be evaluated for different demographic data as well. For the fully automated DR algorithm, the automated segmentation of retinal blood vessels can be further improved so that the detection of retinal vessels end-points would be more accurate. Research of image quality can also be conducted to quantify the image that will be inputted into the system and to standardise the quality of the acquired image.

5.7 Summary

Diabetic Retinopathy, a complication threatening the sight due to diabetes mellitus affecting the retina, has become one of the leading causes of blindness in the world and has affected around 1.5 million populations in Malaysia (National Eye Database). DR severity consists of four levels: mild NPDR, moderate NPDR, severe NPDR and PDR in which to grade it ophthalmologists now use pathology-based direct ophthalmoscopy method using the International Clinical Diabetic Retinopathy Disease Severity Scale. This method, however, is time-consuming for requiring a direct observation and determination by ophthalmologists in the retinal fundus image and even being longer for employing fundus fluorescein angiography (FFA), an invasive procedure to get higher contrast of retinal blood vessels produced from fluorescein angiograms, for an accurate diagnosis due to varied and low contrast of colour retinal fundus image. Being invasive, the FFA is disadvantageous leading to physiological problems or even death to patients. Hence, a computerised DR system, RETINO, is developed to monitor and grade DR severity based on a FAZ analysis using colour retinal fundus image. This system has applied RETICA, proposed digital image enhancement towards the contrast of retinal blood vessels without any invasiveness. Two algorithms - semi-automated and fully automated - are developed to grade DR severity.

Initially, a semi-automated DR grading algorithm combining automated and manual processes of FAZ determination is developed based on CLAHE and RETICA for image enhancement. In grading DR, it performs four main tasks in sequence, i.e. image enhancement of retinal blood vessels, segmentation of retinal vessels, determination of FAZ and analysis of FAZ. Image enhancement is automatically processed based on CLAHE, followed by segmentation of retinal blood vessels based on Otsu's thresholding technique and FAZ determination using the obtained retinal blood vessel end-points. In FAZ determination, the manual process is incorporated using RETICA as CLAHE-based method does not always produce correct retinal vessel end-points due to poor image quality resulted from improper acquisition process. Thus, comparing vessel end-points obtained from both CLAHE and RETICA based on direct observation, the user, if necessary, will manually adjust these obtained vessel end-points for more accurate FAZ determination. Finally, the determined FAZ area is analysed using Gaussian Bayes classifier.

The fully automated DR algorithm is developed based on RETICA for improving the DR grading system in terms of minimising user intervention. Unlike the semi-automated DR algorithm requiring inputs several times for the algorithm by the user, the fully automated one offers a greater advantage enabling the user to input once only when selecting the centre point of the macular region prior to running the algorithm. Another difference between these two DR algorithms is on the indicator for the FAZ determination. While the semi-automated DR algorithm uses area to indicate the determined FAZ, the fully automated one uses radius to reduce the error between the FAZ obtained and the actual FAZ as a result of performing square factor on the radius of the FAZ assuming its area as a circle. Having been defined as half of the longest line connecting two detected points encircling the perimeter of macula, the radius of FAZ obtained eventually is analysed using Gaussian Bayes classifier to grade DR severity.

To determine the FAZ ophthalmologists at present use FFA images offering high contrast of retinal blood vessels. With implementation of RETICA on the colour retinal fundus image, contrast of retinal blood vessels can be enhanced at par to that of the FFA image, thus, enabling the FAZ to be determined from the colour retinal

fundus image by detecting and connecting retinal end-points in the macular region. Accuracy analysis of the DR system is important to measure the accuracy of the DR system in determining the FAZ from the colour retinal fundus image. Accuracy analysis comprises two analyses: - (1) comparing FAZ parameters (area and radius) obtained either from ground truth using FFA or from the DR system, and (2) aimed for the fully automated DR algorithm by determining the accuracy and precision of the algorithm in determining the FAZ radius compared to that of in determining the FAZ area. Importantly, it is to show whether FAZ radius is more reliable to use than FAZ area as FAZ parameter.

Observational and interventional clinical studies have been conducted to test clinically and evaluate the performance of the computerised DR grading system. The observational clinical study is to evaluate DR grading system by using digital analysis of colour retinal fundus images and the interventional one is to investigate an accuracy analysis of the new DR grading protocol.

Results from observational and interventional clinical studies are presented and analysed to clinically test and evaluate the performance of the computerised DR monitoring and grading system. From the observational clinical study, a database called Fundus Image for Non-invasive Diabetic Retinopathy System (FINDeRS) consisting of 315 fundus images (175 no DR, 52 mild NPDR, 32 moderate NPDR, 18 severe NPDR and 38 PDR) is created. Results of determination of FAZ area and FAZ radius by both semi-automated and fully automated DR algorithms are analysed using a statistical correlation analysis. Performance of the DR algorithms in grading DR severity is evaluated based on agreement test and performance test. Using the Gaussian Bayes classifier, the range of FAZ area for each DR severity stage is calibrated for an optimum performance. Findings from statistical correlation analysis show a strong correlation between FAZ enlargement measured by DR algorithms from colour retinal fundus images and corresponding DR severity level graded by ophthalmologists. This strong correlation indicates the usability of the FAZ by the developed DR algorithms using colour fundus images to grade DR severity. In addition, results of agreement test show a strong agreement between the DR system and the ophthalmologists in grading of DR severity indicated by Kappa coefficient.

Hence, the developed DR system can be effective to assist ophthalmologists for early DR detection, DR mass screening, and monitoring and grading of DR severity. Results of performance test on the developed DR system also support this statement in which the semi-automated DR algorithm achieves high sensitivity (> 0.84), specificity (> 0.97) and accuracy (0.95) for all DR stages. Moreover, high values of sensitivity (> 0.95), specificity (> 0.97) and accuracy (> 0.98) obtained for no DR and severe NPDR/ PDR stages indicate that the Gaussian Bayes classifier is suitable for an early detection of DR and effective for a treatment of severe cases. Moreover, the fully automated DR algorithm statistically achieves high sensitivity (≥ 0.846), specificity (≥ 0.905) and accuracy (≥ 0.913) for most of DR stages indicating the potentiality of the fully automated algorithm-based DR system for early DR detection, DR mass screening, monitoring and grading of DR severity.

From the interventional clinical study, of 36 fundus images (10 no DR and 26 any types of DR) used to analyse the accuracy of the computerised DR system, results show that the DR system error data has a small standard deviation (5.28) indicating a systematic error. In the actual implementation of the DR grading system, the systematic error has been overcome by the Gaussian Bayes classifiers. Moreover, a strong linear relationship between DR system and ground truth data ($R^2 = 0.8769$) is shown by regression analysis indicating a high precision. From the correlation analyses, the DR system has a significant and strong positive correlation coefficient up to 0.936 at a very high significant level (P) of less than 0.01. This further indicates accuracy and precision of the DR system in the FAZ measurement.

The accuracy analysis also shows the significantly small mean absolute error and standard deviation (less than 1 pixel) of the fully automated DR algorithm based on FAZ radius indicating high accuracy and precision of the radius-based DR algorithm. Similarly, the regression analysis shows that the fully automated DR algorithm has stronger relationship with FAZ radius as parameter ($R^2 = 0.9797$) than that of with FAZ area as parameter ($R^2 = 0.8376$) indicating a high precision of the DR algorithm in the FAZ determination. These high accuracy and precision are important as the measurement result will be inputted into the DR classifier. The more accurate and

precise the result of FAZ measurement is, the more accurate the DR grading is. Therefore, the DR system based on colour fundus images generally is able to provide an accurate and precise measurement of FAZ enlargement.

A non-invasive image enhancement, RETICA, has been applied on a developed computerised DR monitoring and grading system, RETINO. The DR system is developed based on two algorithms, i.e. semi-automated and fully-automated, clinically tested and evaluated on interventional and observational clinical studies, both to determine and analyse FAZ for an effective DR monitoring and grading. Results show capability of the DR system to classify the DR severity levels and evidentially to have a strong agreement with the ophthalmologists. Based on the collected colour retinal fundus images in FINDeRS and developed grading protocol, DR grading thresholds are successfully calibrated using the FAZ areas and radius. The DR system achieves optimum accuracy, sensitivity and specificity in detecting DR severity needed for medical practice and thus enables an effective DR grading using colour fundus images. This new grading protocol can also be applied as an alternative to the current DR grading method using pathology-based direct ophthalmoscopy and beneficial for early detection of DR, DR mass screening, and monitoring and grading of DR severity.

For future research, the data can be enlarged for further confidence of the results. The validity of the proposed DR grading method can be also established through cross-validation based on expert opinions as well as its performance to be evaluated for different demographic data. In the fully automated DR algorithm, the automated segmentation of retinal blood vessels can be further improved for a more accurate detection of retinal vessels end-points. A research can also be conducted to quantify and standardise the quality of the acquired image prior to inputting into the algorithm.

CHAPTER 6

CONCLUSION

6.1 Discussion

Most of medical images produced by various medical imaging modalities suffer from the problems of varied and low contrast due to geometrical surface of the objects and configuration of the acquisition system. These problems may lead to inaccurate detection of pathologies and cause wrong diagnosis. Colour retinal fundus image produced by a fundus camera is one of the examples of medical images in which, through analysis of this medical image, some diseases related to the retina such as Diabetic Retinopathy (DR) can be determined. The contrast between retinal blood vessels and the background in colour retinal fundus images however is varied and very low, leading the analysis of tiny retinal blood vessels (retinal capillaries) from such colour fundus images to be difficult. To overcome this problem, in medical practice, fundus fluorescein angiography (FFA) that produces fundus angiograms having higher contrast of retinal blood vessels with contrast improvement factor (*CIF*) of 5.796 is used. Unfortunately, for being an invasive procedure, FFA may lead to physiological problems and at worst can cause death to the patients.

The primary objective of this research is to develop a non-invasive digital imaging enhancement scheme that can enhance varied and low contrast medical images to be similar to or better than the contrast produced by invasive method (FFA) without introducing noise or artefacts. The significance of this research is to improve image quality for both direct observation and computer-based automated image analysis. The use of the enhanced images will increase the accuracy, sensitivity and specificity of the diagnosis through either direct observation or computer-assisted diagnosis system. In this research, a non-invasive image enhancement called RETICA was developed and applied in a developed computerised DR monitoring and grading

system called RETINO, a particular medical application to monitor and grade DR severity by enhancing the quality of digital colour retinal fundus image and analysing the FAZ.

This research work begins by developing a non-invasive digital image enhancement scheme (RETICA) to enhance the varied and low contrast of retinal fundus images that is by normalising varied contrast using Retinex. It is then followed by separating the retinal pigments make-up, namely macular pigment, haemoglobin and melanin, using Independent Component Analysis (ICA). Due to the haemoglobin, independent component image exhibits higher contrast retinal blood vessels. Three fundus image models, i.e. varied contrast image model, low contrast image model and varied and low contrast image models are developed to validate and evaluate the performance of RETICA. The varied and low contrast fundus image model subsequently undergoes the RETICA process and six selected image enhancement methods, i.e. contrast stretching (CS), histogram equalisation (HE), adaptive histogram equalisation (AHE), adaptive contrast enhancement (ACE), contrast limited adaptive histogram equalisation (CLAHE) and homomorphic filtering (HF) to evaluate the RETICA performance. Three criteria, namely contrast of retinal blood vessels (C_{av}), image contrast normalisation (R_{sdc}) and contrast improvement factor (CIF) are set up to measure quality of the contrast-enhanced image.

RETICA is applied as a part of a computerised DR system (RETINO), which is used to grade DR severity level based on the FAZ analysis. To implement RETICA for grading DR severity, two DR algorithms – semi-automated and fully-automated – are developed. The semi-automated DR algorithm applies CLAHE-based image enhancement method followed by automated segmentation of retinal blood vessels and determination of FAZ. However, since not all acquired colour retinal fundus images are of good quality in the implementation; RETICA is applied to further enhance the contrast of retinal blood vessels, especially the retinal capillaries in the macular region where the FAZ is located. In the semi-automated DR algorithm, RETICA-enhanced image which has better contrast of retinal blood vessels than that of the CLAHE is used to determine correct vessel end-points that have been obtained

by automated process using CLAHE-enhanced image. The semi-automated DR algorithm which elaborates manual and automated technique to determine FAZ is further improved by developing the fully-automated DR algorithm.

In the fully-automated DR algorithm, the manual correction of vessel end-points using RETICA-enhanced image applied in the semi-automated DR system is eliminated and the automated segmentation of retinal blood vessels based on thresholding technique is further improved by implementation of a series of digital filter and region-growing technique. RETICA is incorporated in the fully-automated DR algorithm for image enhancement prior to automated segmentation of retinal blood vessels and determination of FAZ. The user through the fully-automated DR algorithm simply selects the centre point of the macular region prior to the beginning and the rest of the process of FAZ determination automatically runs. Both the developed DR algorithms are tested and evaluated in two studies, i.e. interventional and observation clinical studies.

Results of validation study show that the proposed method successfully normalises the varied contrast in colour retinal fundus images with R_{sdc} of 0.756 better than that of the other non-invasive enhancement methods. RETICA outperforms other enhancement methods in producing better contrast of retinal blood vessels with C_{av} of 76.83 followed by AHE, CS, HE, HF, CLAHE and ACE with C_{av} of 72.66, 69.11, 68.81, 67.27, 42.81 and 21.08, respectively. Using of the green band image as the reference, RETICA achieves the highest contrast improvement among the other tested non-invasive image enhancement methods with CIF of 5.389, slightly lower than that of the FFA image with CIF of 5.796. Based on the results of the validation study, it is proven that the contrast of retinal blood vessels in the enhanced image obtained by RETICA has been significantly increased compared to the ordinary colour retinal fundus image. RETICA is then applied on a computerised DR system (RETINO) for grading of DR severity level based on FAZ analysis.

Findings from observational clinical study show a strong correlation between FAZ enlargement measured by both DR algorithms from colour retinal fundus images and corresponding DR severity level graded by ophthalmologists. This strong correlation

indicates the usability of the FAZ by the developed DR algorithms using colour fundus images to grade DR severity. In addition, this indication is confirmed by results of agreement test showing a strong agreement between the DR system and the ophthalmologists in grading of DR severity. Hence, the developed DR system can be effective to assist ophthalmologists for early DR detection, DR mass screening, and monitoring and grading of DR severity. Results of performance test on the developed DR system also support this statement in which the semi-automated DR algorithm achieves high sensitivity (> 0.84), specificity (> 0.97) and accuracy (0.95) for all DR stages. In particular, high values of sensitivity (> 0.95), specificity (> 0.97) and accuracy (> 0.98) obtained for no DR and severe NPDR/ PDR stages indicate that the Gaussian Bayes classifier is suitable for an early detection of DR and effective for a treatment of severe cases. For the fully-automated DR algorithm, high sensitivity (≥ 0.846), specificity (≥ 0.905) and accuracy (≥ 0.913) are achieved for no DR and mild NPDR. For moderate NPDR and severe/PDR, no conclusion is drawn due to lack of data images. In general, the achievement of the developed DR system based on both semi-automated and fully-automated DR algorithms indicates a potential use of RETINO for early DR detection, DR mass screening, monitoring and grading of DR severity.

Findings from interventional clinical study aimed for analysing the accuracy of the developed DR system for determining FAZ show a small standard deviation (5.28) of the DR system error data indicating a systematic error. In the actual implementation of the DR grading system, this systematic error has been overcome by the Gaussian Bayes classifiers. Moreover, a strong linear relationship between DR system and ground truth data ($R^2 = 0.8769$) shown by regression analysis indicates a high precision. This achievement on high accuracy and precision of the DR system in the FAZ measurement is further confirmed by results of correlation analyses in which the DR system has a significant and strong positive correlation coefficient up to 0.936 at a very high significant level (P) of less than 0.01. In particular, the analysis on accuracy also shows that the use of FAZ radius as parameter has better precision than that of FAZ area as parameter indicated by its significantly small mean absolute error and standard deviation (less than 1 pixel) and its high coefficient of determination R^2 .

Therefore, the fully-automated DR algorithm – an improvement of the semi-automated one – uses FAZ radius as its parameter for FAZ determination. High accuracy and precision are important as the measurement result will be inputted into the DR classifier. The more accurate and precise the result of FAZ measurement is, the more accurate the DR grading will be.

The developed method of non-invasive image enhancement method (RETICA) in general is to enhance the contrast of the very fine vessels in the macular region from varied and low colour retinal fundus images for an accurate determination of FAZ in monitoring and grading of DR severity level, especially at its early stage. An early detection of FAZ enlargement at NPDR stage will enable clinicians to advise patients on better metabolic control to prevent progression of the disease to PDR stage and loss of vision. Applying RETICA on the computerised DR system (RETINO) can establish a new non-invasive, simple and fast technique and can be done by non-eye trained healthcare providers, thus enabling a diabetic eye screening at primary healthcare setting.

6.2 Contribution and Future Works

Three major contributions could be achieved from this research. The first contribution is the development of the non-invasive image enhancement technique (RETICA), particularly for digital colour image obtained from non-invasive medical equipment to normalise varied contrast and increase the visible details and contrast of tiny biological tissues or objects of interest. This improvement in turn will avoid the need of applying contrasting agent on patients that can cause physiological problems to them. Having enhanced the contrast of retinal blood vessels in the colour retinal fundus image, RETICA is beneficial not only for diagnosis of retina-related diseases through direct observation, but also for segmentation of retinal vasculature using computer-based system. It moreover can be implemented as pre-processing step for medical image analysis to diagnose retina-related diseases.

The second one is the development of DR system for monitoring and grading of DR severity based on semi-automated and fully-automated algorithms of FAZ

analysis on colour retinal fundus image in which ophthalmologists today utilise FFA to obtain fundus angiograms that have high contrast of retinal blood vessels against the background to examine FAZ in diagnosing retina-related diseases. The developed DR system (RETINO) incorporates RETICA to enhance the contrast of the very fine vessels in the macular region from varied and low colour retinal fundus images for an accurate determination of FAZ.

Last but not least, the implementation of the developed technique on digital colour retinal fundus images and not fundus fluorescein angiograms for FAZ determination and measurement is also a major contribution in this research since no measurement of FAZ was studied based on digital colour fundus image so far. The developed DR grading algorithms based on FAZ analysis is a new protocol for grading of DR severity, which at present uses pathology-based direct ophthalmology for daily practice. The development of DR grading system will be advantageous to assist ophthalmologists for DR mass screening and monitoring and grading of DR severity.

For future research, the data can be enlarged for further confidence of the results. The validity of the proposed DR grading method can also be established through a cross-validation based on expert opinions as well as its performance to be evaluated for different demographic data. In the fully-automated DR algorithm, the automated segmentation of retinal blood vessels can further be improved for a more accurate detection of retinal vessels end-points. A research can also be conducted to quantify and to standardise the quality of the acquired image prior to inputting into the algorithm. RETICA at last can also be applied as a part of a medical system to solve other retina-related diseases.

REFERENCES

- [1] K. P. Andriole, "Medical Imaging Modalities and Digital Images," in *Practical imaging informatics: foundations and applications for PACS professionals*, B. F. Branstetter, Ed., ed New York: Springer, 2009, pp. 3-13.
- [2] U. Vovk, F. Pernus, and B. Likar, "A Review of Methods for Correction of Intensity Inhomogeneity in MRI," *Medical Imaging, IEEE Transactions on*, vol. 26, pp. 405-421, 2007.
- [3] E. Ardizzone, R. Pirrone, and O. Gambino, "Illumination Correction on MR Images," *Journal of Clinical Monitoring and Computing*, vol. 20, pp. 391-398, 2006.
- [4] T. Teng, M. Lefley, and D. Claremont, "Progress towards automated diabetic ocular screening: A review of image analysis and intelligent systems for diabetic retinopathy," *Medical and Biological Engineering and Computing*, vol. 40, pp. 2-13, January 12 2002.
- [5] M. Foracchia, E. Grisan, and A. Ruggeri, "Luminosity and contrast normalization in retinal images," *Medical Image Analysis*, vol. 9, pp. 179-190, June 2005.
- [6] T. O. Ozanian and R. Phillips, "Enhancement of fluoroscopic images with varying contrast," *Computer Methods and Programs in Biomedicine*, vol. 65, pp. 1-16, 2001.
- [7] A. Bhugaloo, B. Abdullah, and Y. S. K. Ng, "Diffusion weighted MR imaging in acute vertebral compression fractures: differentiation between malignant and benign causes," *Biomedical Imaging and Intervention Journal*, vol. 2, p. e12, December 2006.
- [8] V. Spyropoulou, N. Kalyvas, A. Gaitanis, C. Michail, G. Panayiotakis, and I. Kandarakis, "Modelling the imaging performance and low contrast

- detectability in digital mammography " *Journal of Instrumentation*, vol. 4, June 2009.
- [9] S. Makrogiannis, R. Bhotika, J. Miller, J. Skinner, and M. Vass, "Nonparametric Intensity Priors for Level Set Segmentation of Low Contrast Structures," in *Medical Image Computing and Computer-Assisted Intervention – MICCAI 2009*. vol. 5761, G.-Z. Yang, D. Hawkes, D. Rueckert, A. Noble, and C. Taylor, Eds., ed: Springer Berlin / Heidelberg, 2009, pp. 239-246.
- [10] S. W. Smith, R. F. Wagner, J. M. Sandrik, and H. Lopez, "Low Contrast Detectability and Contrast/Detail Analysis in Medical Ultrasound," *Sonics and Ultrasonics, IEEE Transactions on*, vol. 30, pp. 164-173, 1983.
- [11] A. Ciulla, G. Castronovo, G. Tomasello, A. Maiorana, L. Russo, E. Daniele, and G. Genova, "Gastric metastases originating from occult breast lobular carcinoma: diagnostic and therapeutic problems," *World Journal of Surgical Oncology*, vol. 6, p. 78, 2008.
- [12] S. Povoski, "The utilization of an ultrasound-guided 8-gauge vacuum-assisted breast biopsy system as an innovative approach to accomplishing complete eradication of multiple bilateral breast fibroadenomas," *World Journal of Surgical Oncology*, vol. 5, p. 124, 2007.
- [13] A. A. H. Abdel-Razik Youssif, A. Z. Ghalwash, and A. A. S. Abdel-Rahman Ghoneim, "Optic Disc Detection From Normalized Digital Fundus Images by Means of a Vessels' Direction Matched Filter," *Medical Imaging, IEEE Transactions on*, vol. 27, pp. 11-18, 2008.
- [14] A. A. A. Youssif, A. Z. Ghalwash, and A. S. Ghoneim, "A Comparative Evaluation of Preprocessing Methods for Automatic Detection of Retinal Anatomy," in *Proceedings of the Fifth International Conference on Informatics & Systems (INFOS'07)*, Cairo, Egypt, 2007, pp. 24-30.
- [15] M. Ebrahimi and A. Martel, "Image Registration under Varying Illumination: Hyper-Demons Algorithm," in *Energy Minimization Methods in Computer*

- Vision and Pattern Recognition*. vol. 5681, D. Cremers, Y. Boykov, A. Blake, and F. Schmidt, Eds., ed: Springer Berlin / Heidelberg, 2009, pp. 303-316.
- [16] W.-C. Kao, M.-C. Hsu, and Y.-Y. Yang, "Local contrast enhancement and adaptive feature extraction for illumination-invariant face recognition," *Pattern Recognition*, vol. 43, pp. 1736-1747, 2010.
- [17] J. Meier, R. Bock, G. Michelson, L. Nyúl, and J. Hornegger, "Effects of Preprocessing Eye Fundus Images on Appearance Based Glaucoma Classification," in *Computer Analysis of Images and Patterns*, ed, 2007, pp. 165-172.
- [18] A. D. Fleming, S. Philip, K. A. Goatman, J. A. Olson, and P. F. Sharp, "Automated microaneurysm detection using local contrast normalization and local vessel detection," *Medical Imaging, IEEE Transactions on*, vol. 25, pp. 1223-1232, 2006.
- [19] R. W. Knighton, "Quantitative reflectometry of the ocular fundus," *Engineering in Medicine and Biology Magazine, IEEE*, vol. 14, pp. 43-51, 1995.
- [20] A. Salvatelli and et al., "A comparative analysis of pre-processing techniques in colour retinal images," *Journal of Physics: Conference Series*, vol. 90, p. 012069, 2007.
- [21] B. Liesenfeld, E. Kohner, W. Piehlmeier, S. Kluthe, S. Aldington, M. Porta, T. Bek, M. Obermaier, H. Mayer, G. Mann, R. Holle, and K. D. Hepp, "A telemedical approach to the screening of diabetic retinopathy: digital fundus photography," *Diabetes Care*, vol. 23, pp. 345-348, March 1 2000.
- [22] W. K. Pratt, *Digital image processing*, 2nd ed. New York: Wiley, 1991.
- [23] C. Christiansen, "X-ray contrast media--an overview," *Toxicology*, vol. 209, pp. 185-187, 2005.

- [24] D. K. Wysowski and P. Nourjah, "Deaths Attributed to X-Ray Contrast Media on U.S. Death Certificates," *Am. J. Roentgenol.*, vol. 186, pp. 613-615, March 1 2006.
- [25] S. Dithmar, F. G. Holz, and SpringerLink, *Fluorescence angiography in ophthalmology*. Heidelberg: Springer Medizin Verlag, 2008.
- [26] M. Hitosugi, K. Omura, T. Yokoyama, H. Kawato, Y. Motozawa, T. Nagai, and S. Tokudome, "An Autopsy Case of Fatal Anaphylactic Shock Following Fluorescein Angiography," *Med Sci Law*, vol. 44, pp. 264-265, July 1 2004.
- [27] L. A. Yannuzzi, K. T. Rohrer, L. J. Tindel, R. S. Sobel, M. A. Costanza, W. Shields, and E. Zang, "Fluorescein angiography complication survey," *Ophthalmology*, vol. 93, pp. 611-7, 1986.
- [28] T. A. Ciulla, A. G. Amador, and B. Zinman, "Diabetic Retinopathy and Diabetic Macular Edema," *Diabetes Care*, vol. 26, pp. 2653-2664, September 1 2003.
- [29] J. R. Lindner, "Microbubbles in medical imaging: current applications and future directions," *Nat Rev Drug Discov*, vol. 3, pp. 527-533, 2004.
- [30] C. Burtea, S. Laurent, L. Elst, and R. N. Muller, "Contrast Agents: Magnetic Resonance," in *Molecular Imaging I*. vol. 185/1, W. Semmler and M. Schwaiger, Eds., ed: Springer Berlin Heidelberg, 2008, pp. 135-165.
- [31] R. Senior, H. Becher, M. Monaghan, L. Agati, J. Zamorano, J. L. Vanoverschelde, and P. Nihoyannopoulos, "Contrast echocardiography: evidence-based recommendations by European Association of Echocardiography," *European Journal of Echocardiography*, vol. 10, pp. 194-212, March 1 2009.
- [32] P. Marckmann, L. Skov, K. Rossen, A. Dupont, M. B. Damholt, J. G. Heaf, and H. S. Thomsen, "Nephrogenic Systemic Fibrosis: Suspected Causative Role of Gadodiamide Used for Contrast-Enhanced Magnetic Resonance Imaging," *J Am Soc Nephrol*, vol. 17, pp. 2359-2362, September 1 2006.

- [33] R. C. Gonzalez and R. E. Woods, *Digital image processing*. Upper Saddle River, NJ: Prentice Hall, 2007.
- [34] J. C. Russ, *The image processing handbook*. Boca Raton, FL: CRC/Taylor and Francis, 2007.
- [35] A. A. A. Youssif, A. Z. Ghalwash, and A. S. Ghoneim, "Comparative Study of Contrast Enhancement and Illumination Equalization Methods for Retinal Vasculature Segmentation," presented at the Proceedings of the Third Cairo International Biomedical Engineering Conference, Cairo, Egypt, 2006.
- [36] Clemson University, Clemson, SC., STARE project website [Online]. Available: <http://www.ces.clemson.edu/~ahoover/stare>
- [37] University Medical Center Utrecht, Image Sciences Institute, Research section, Digital Retinal Image for Vessel Extraction (DRIVE) database [Online]. Available: <http://www.isi.uu.nl/Research/Databases/DRIVE>
- [38] D. J. Cornforth, H. J. Jelinek, J. J. G. Leandro, J. V. B. Soares, J. R. M. Cesar, M. J. Cree, P. Mitchell, and T. Bossomaier, "Development of retinal blood vessel segmentation methodology using wavelet transforms for assessment of diabetic retinopathy," *Complexity International*, vol. 11, pp. 50-61, 2005.
- [39] R. C. Gonzalez, R. E. Woods, and S. L. Eddins, *Digital Image Processing Using MATLAB*: Pearson Education, 2004.
- [40] D. Wu, M. Zhang, J.-C. Liu, and W. Bauman, "On the adaptive detection of blood vessels in retinal images," *Biomedical Engineering, IEEE Transactions on*, vol. 53, pp. 341-343, 2006.
- [41] C. Sinthanayothin, J. F. Boyce, H. L. Cook, and T. H. Williamson, "Automated localisation of the optic disc, fovea, and retinal blood vessels from digital colour fundus images," *Br J Ophthalmol*, vol. 83, pp. 902-910, August 1, 1999 1999.

- [42] L. Tusheng and Z. Yibin, "Adaptive image enhancement for retinal blood vessel segmentation," *Electronics Letters*, vol. 38, pp. 1090-1091, 2002.
- [43] G. Yang, L. Gagnon, S. Wang, and M. C. Boucher, "Algorithm for Detecting Micros-Aneurysms in Low Resolution Color Retinal Images," in *Vision Interface 2001*, Ottawa, Canada, 2001, pp. 265-271.
- [44] A. D. Hoover, V. Kouznetsova, and M. Goldbaum, "Locating blood vessels in retinal images by piecewise threshold probing of a matched filter response," *Medical Imaging, IEEE Transactions on*, vol. 19, pp. 203-210, 2000.
- [45] S. Chaudhuri, S. Chatterjee, N. Katz, M. Nelson, and M. Goldbaum, "Detection of blood vessels in retinal images using two-dimensional matched filters," *Medical Imaging, IEEE Transactions on*, vol. 8, pp. 263-269, 1989.
- [46] R. C. Gonzalez and R. E. Woods, *Digital image processing*, 3rd ed. Upper Saddle River, NJ: Prentice Hall, 2008.
- [47] J. Shen, "On the foundations of vision modeling : I. Weber's law and Weberized TV restoration," *Physica D: Nonlinear Phenomena*, vol. 175, pp. 241-251, 2003.
- [48] A. Koschan and M. A. Abidi, *Digital color image processing*. Hoboken, N.J.: Wiley-Interscience, 2008.
- [49] A. A. Michelson, *Studies in optics*. Chicago: University of Chicago Press, 1962.
- [50] E. H. Weber, *Annotationes anatomicae et physiologicae*. Koehler, Leipzig, 1834.
- [51] G. Westheimer, "The oscilloscopic view: Retinal illuminance and contrast of point and line targets," *Vision Research*, vol. 25, pp. 1097-1103, 1985.
- [52] M. Pavel, G. Sperling, T. Riedl, and A. Vanderbeek, "Limits of visual communication: the effect of signal-to-noise ratio tin the intelligibility of American Sign Language," *J. Opt. Soc. Am. A*, vol. 4, pp. 2355-2365, 1987.

- [53] G. S. Rubin and K. Siegel, "Recognition of low-pass filtered faces and letters," *Investigative Ophthalmology and Visual Science (Suppl.)*, vol. 25, pp. 71-84, 1984.
- [54] E. Peli, "Contrast in complex images," *Journal of the Optical Society of America*, vol. 7, pp. 2032-2040, 1990.
- [55] Y. Wang, W. Tan, and S. C. Lee, "Illumination normalization of retinal images using sampling and interpolation," in *Medical Imaging 2001: Image Processing. Proc. of SPIE*, San Diego, CA, USA, 2001, pp. 500-507.
- [56] T. Walter and J.-C. Klein, "Automatic Detection of Microaneurysms in Color Fundus Images of the Human Retina by Means of the Bounding Box Closing," in *Medical Data Analysis*, ed, 2002, pp. 210-220.
- [57] M. Saleh, C. Eswaran, and A. Mueen, "An Automated Blood Vessel Segmentation Algorithm Using Histogram Equalization and Automatic Threshold Selection," *Journal of Digital Imaging*, pp. 1-9, 2010.
- [58] C. Sinthanayothin, V. Kongbunkiat, S. Phoojaruenchanachai, and A. Singalavanija, "Automated screening system for diabetic retinopathy," in *Proceedings of the 3rd International Symposium on Image and Signal Processing and Analysis, 2003. ISPA 2003.*, Rome, Italy, 2003, pp. 915- 920.
- [59] T. Shimahara, T. Okatani, and K. Deguchi, "Contrast enhancement of fundus images using regional histograms for medical diagnosis," in *SICE 2004 Annual Conference*, 2004, pp. 650-653 vol. 1.
- [60] K. Noronha, J. Nayak, and S. N. Bhat, "Enhancement of retinal fundus Image to highlight the features for detection of abnormal eyes," in *TENCON 2006. 2006 IEEE Region 10 Conference*, 2006, pp. 1-4.
- [61] J. V. B. Soares, J. J. G. Leandro, R. M. Cesar, H. F. Jelinek, and M. J. Cree, "Retinal vessel segmentation using the 2-D Gabor wavelet and supervised classification," *Medical Imaging, IEEE Transactions on*, vol. 25, pp. 1214-1222, 2006.

- [62] D. Tomaževič, B. Likar, and F. Pernuš, "Comparative evaluation of retrospective shading correction methods," *Journal of Microscopy*, vol. 208, pp. 212-223, 2002.
- [63] J. V. Manjón, J. J. Lull, J. Carbonell-Caballero, G. García-Martí, L. Martí-Bonmatí, and M. Robles, "A nonparametric MRI inhomogeneity correction method," *Medical Image Analysis*, vol. 11, pp. 336-345, 2007.
- [64] A. Simmons, P. S. Tofts, G. J. Barker, and S. R. Arridge, "Sources of intensity nonuniformity in spin echo images at 1.5 T," *Magnetic Resonance in Medicine*, vol. 32, pp. 121-128, 1994.
- [65] N. Gelber, R. Ragland, and J. Knorr, "Surface coil MR imaging: utility of image intensity correction filter," *Am. J. Roentgenol.*, vol. 162, pp. 695-697, March 1 1994.
- [66] B. H. Brinkmann, A. Manduca, and R. A. Robb, "Optimized homomorphic unsharp masking for MR grayscale inhomogeneity correction," *Medical Imaging, IEEE Transactions on*, vol. 17, pp. 161-171, 1998.
- [67] H. G. Adelman, "Butterworth equations for homomorphic filtering of images," *Computers in Biology and Medicine*, vol. 28, pp. 169-181, June 1 1998.
- [68] R. Guillemaud, "Uniformity correction with homomorphic filtering on region of interest," in *Image Processing, 1998. ICIP 98. Proceedings. 1998 International Conference on*, 1998, pp. 872-875 vol.2.
- [69] M. Styner, C. Brechbuhler, G. Szckely, and G. Gerig, "Parametric estimate of intensity inhomogeneities applied to MRI," *Medical Imaging, IEEE Transactions on*, vol. 19, pp. 153-165, 2000.
- [70] E. A. Vokurka, N. A. Watson, Y. Watson, N. A. Thacker, and A. Jackson, "Improved high resolution MR imaging for surface coils using automated intensity non-uniformity correction: Feasibility study in the orbit," *Journal of Magnetic Resonance Imaging*, vol. 14, pp. 540-546, 2001.

- [71] B. Likar, J. Derganc, and F. Pernus, "Segmentation-based retrospective correction of intensity nonuniformity in multispectral MR images," San Diego, CA, USA, 2002, pp. 1531-1540.
- [72] R. Guillemaud and M. Brady, "Estimating the bias field of MR images," *Medical Imaging, IEEE Transactions on*, vol. 16, pp. 238-251, 1997.
- [73] J. G. Sled, A. P. Zijdenbos, and A. C. Evans, "A nonparametric method for automatic correction of intensity nonuniformity in MRI data," *Medical Imaging, IEEE Transactions on*, vol. 17, pp. 87-97, 1998.
- [74] N. J. Tustison, B. B. Avants, P. A. Cook, Z. Yuanjie, A. Egan, P. A. Yushkevich, and J. C. Gee, "N4ITK: Improved N3 Bias Correction," *Medical Imaging, IEEE Transactions on*, vol. 29, pp. 1310-1320, 2010.
- [75] W. Zheng, M. W. L. Chee, and V. Zagorodnov, "Improvement of brain segmentation accuracy by optimizing non-uniformity correction using N3," *NeuroImage*, vol. 48, pp. 73-83, 2009.
- [76] C. Studholme, V. Cardenas, E. Song, F. Ezekiel, A. Maudsley, and M. Weiner, "Accurate template-based correction of brain MRI intensity distortion with application to dementia and aging," *Medical Imaging, IEEE Transactions on*, vol. 23, pp. 99-110, 2004.
- [77] M. S. Brown, S. Mingxuan, Y. Ruigang, Y. Lin, and W. B. Seales, "Restoring 2D Content from Distorted Documents," *Pattern Analysis and Machine Intelligence, IEEE Transactions on*, vol. 29, pp. 1904-1916, 2007.
- [78] J. P. Oakley and B. L. Satherley, "Improving image quality in poor visibility conditions using a physical model for contrast degradation," *Image Processing, IEEE Transactions on*, vol. 7, pp. 167-179, 1998.
- [79] B. M. Dawant, A. P. Zijdenbos, and R. A. Margolin, "Correction of intensity variations in MR images for computer-aided tissue classification," *Medical Imaging, IEEE Transactions on*, vol. 12, pp. 770-781, 1993.

- [80] L. Kubecka, J. Jan, and R. Kolar, "Retrospective Illumination Correction of Retinal Images," *International Journal of Biomedical Imaging*, vol. 2010, 2010.
- [81] B. Likar, M. Viergever, and F. Pernuš, "Retrospective Correction of MR Intensity Inhomogeneity by Information Minimization," in *Medical Image Computing and Computer-Assisted Intervention – MICCAI 2000*. vol. 1935, S. Delp, A. DiGoia, and B. Jaramaz, Eds., ed: Springer Berlin / Heidelberg, 2000, pp. 177-201.
- [82] W. M. Wells, III, W. E. L. Grimson, R. Kikinis, and F. A. Jolesz, "Adaptive segmentation of MRI data," *Medical Imaging, IEEE Transactions on*, vol. 15, pp. 429-442, 1996.
- [83] B. Likar, M. A. Viergever, and F. Pernus, "Retrospective correction of MR intensity inhomogeneity by information minimization," *Medical Imaging, IEEE Transactions on*, vol. 20, pp. 1398-1410, 2001.
- [84] S.-H. Lai and M. Fang, "A new variational shape-from-orientation approach to correcting intensity inhomogeneities in magnetic resonance images," *Medical Image Analysis*, vol. 3, pp. 409-424, 1999.
- [85] J. B. Zimmerman, S. M. Pizer, E. V. Staab, J. R. Perry, W. McCartney, and B. C. Brenton, "An evaluation of the effectiveness of adaptive histogram equalization for contrast enhancement," *Medical Imaging, IEEE Transactions on*, vol. 7, pp. 304-312, 1988.
- [86] M. Abdullah-Al-Wadud, M. H. Kabir, M. A. A. Dewan, and C. Oksam, "A Dynamic Histogram Equalization for Image Contrast Enhancement," *Consumer Electronics, IEEE Transactions on*, vol. 53, pp. 593-600, 2007.
- [87] Y. Jin, L. M. Fayad, and A. F. Laine, "Contrast enhancement by multiscale adaptive histogram equalization," in *Proc. SPIE, Medical Imaging*, San Diego, CA, USA, 2001, pp. 206-213.

- [88] S. M. Pizer, E. P. Amburn, J. D. Austin, R. Cromartie, A. Geselowitz, T. Greer, B. ter Haar Romeny, J. B. Zimmerman, and K. Zuiderveld, "Adaptive histogram equalization and its variations," *Computer Vision, Graphics, and Image Processing*, vol. 39, pp. 355-368, 1987.
- [89] R. Hummel, "Image enhancement by histogram transformation," *Computer Graphics and Image Processing*, vol. 6, pp. 184-195, 1977.
- [90] S. M. Pizer, J. B. Zimmerman, and E. V. Staab, "Adaptive grey level assignment in CT scan display," *Journal of computer assisted tomography*, vol. 8, pp. 300-5, 1984.
- [91] B. C. Stoel, A. M. Vossepoel, F. P. Ottes, P. L. Hofland, H. M. Kroon, and L. J. Schultze Kool, "Interactive histogram equalization," *Pattern Recognition Letters*, vol. 11, pp. 247-254, 1990.
- [92] S. M. Pizer, "Psychovisual issues in the display of medical images," presented at the Proceedings of the NATO Advanced Study Institute (NATO ASI Series) on Pictorial information systems in medicine, Braulage, Germany, 1986.
- [93] E. Pisano, S. Zong, B. Hemminger, M. DeLuca, R. Johnston, K. Muller, M. Braeuning, and S. Pizer, "Contrast Limited Adaptive Histogram Equalization image processing to improve the detection of simulated spiculations in dense mammograms," *Journal of Digital Imaging*, vol. 11, pp. 193-200, 1998.
- [94] M. H. Ahmad Fadzil, L. I. Izhar, P. A. Venkatachalam, and T. V. N. Karunakar, "Extraction and reconstruction of retinal vasculature," *Journal of Medical Engineering Technology*, vol. 31, pp. 435-442, November 6 2007.
- [95] A. M. Reza, "Realization of the Contrast Limited Adaptive Histogram Equalization (CLAHE) for Real-Time Image Enhancement," *The Journal of VLSI Signal Processing*, vol. 38, pp. 35-44, 2004.
- [96] L. Iznita, "Analysis of Retinal Vasculature and Foveal Avascular Zone for Grading of Diabetic Retinopathy," Master thesis, M.Sc. Thesis Electrical and

Electronics Engineering Programme, Universiti Teknologi PETRONAS, Bandar Seri Iskandar, Malaysia, 2006.

- [97] L. Yang, Y. Liang, and H. Fan, "Study on the methods of image enhancement for liver CT images," *Optik - International Journal for Light and Electron Optics*, vol. 121, pp. 1752-1755, 2010.
- [98] P. G. Tahoces, J. Correa, M. Souto, C. Gonzalez, L. Gomez, and J. J. Vidal, "Enhancement of chest and breast radiographs by automatic spatial filtering," *Medical Imaging, IEEE Transactions on*, vol. 10, pp. 330-335, 1991.
- [99] G. Ramponi, "A cubic unsharp masking technique for contrast enhancement," *Signal Processing*, vol. 67, pp. 211-222, 1998.
- [100] J.-S. Lee, "Digital Image Enhancement and Noise Filtering by Use of Local Statistics," *Pattern Analysis and Machine Intelligence, IEEE Transactions on*, vol. PAMI-2, pp. 165-168, 1980.
- [101] J. K. Kim, J. M. Park, K. S. Song, and H. W. Park, "Adaptive mammographic image enhancement using first derivative and local statistics," *Medical Imaging, IEEE Transactions on*, vol. 16, pp. 495-502, 1997.
- [102] Y. Xu, J. B. Weaver, D. M. Healy, and J. Lu, "Wavelet transform domain filters: a spatially selective noise filtration technique," *Image Processing, IEEE Transactions on*, vol. 3, pp. 747-758, 1994.
- [103] W. Jun, T. Xiaolin, S. Yankui, and T. Zesheng, "A New Wavelet-Based Adaptive Algorithm for MR Image Enhancement," in *Complex Medical Engineering, 2007. CME 2007. IEEE/ICME International Conference on*, 2007, pp. 600-603.
- [104] A. V. Bronnikov and G. Duifhuis, "Wavelet-Based Image Enhancement in X-Ray Imaging and Tomography," *Appl. Opt.*, vol. 37, pp. 4437-4448, 1998.

- [105] P. Heinlein, J. Drexler, and W. Schneider, "Integrated wavelets for enhancement of microcalcifications in digital mammography," *Medical Imaging, IEEE Transactions on*, vol. 22, pp. 402-413, 2003.
- [106] V. P. S. Rallabandi, "Enhancement of ultrasound images using stochastic resonance-based wavelet transform," *Computerized Medical Imaging and Graphics*, vol. 32, pp. 316-320, 2008.
- [107] A. F. Laine, S. Schuler, F. Jian, and W. Huda, "Mammographic feature enhancement by multiscale analysis," *Medical Imaging, IEEE Transactions on*, vol. 13, pp. 725-740, 1994.
- [108] S. G. Mallat, "A theory for multiresolution signal decomposition: the wavelet representation," *Pattern Analysis and Machine Intelligence, IEEE Transactions on*, vol. 11, pp. 674-693, 1989.
- [109] A. Salvatelli, G. Bizai, G. Barbosa, B. Drozdowicz, and C. Delrieux, "A comparative analysis of pre-processing techniques in colour retinal images," *Journal of Physics: Conference Series*, vol. 90, p. 012069, 2007.
- [110] Z. U. Rahman, G. A. Woodell, and D. J. Jobson, "A Comparison of the Multiscale Retinex With Other Image Enhancement Techniques," *IS AND T Annual Conference*, pp. 426-431, 1997.
- [111] Z. Bichao and W. Yiquan, "Infrared Image Enhancement Based on Wavelet Transformation and Retinex," in *Intelligent Human-Machine Systems and Cybernetics (IHMSC), 2010 2nd International Conference on*, 2010, pp. 313-316.
- [112] R. M. Haralick, S. R. Sternberg, and X. Zhuang, "Image Analysis Using Mathematical Morphology," *Pattern Analysis and Machine Intelligence, IEEE Transactions on*, vol. PAMI-9, pp. 532-550, 1987.
- [113] Likar, Maintz, Viergever, and Pernuš, "Retrospective shading correction based on entropy minimization," *Journal of Microscopy*, vol. 197, pp. 285-295, 2000.

- [114] A. J. Bell and T. J. Sejnowski, "An information-maximisation approach to blind separation and blind deconvolution," *Neural Computation*, vol. 7, pp. 1129-1159, 1995.
- [115] T.-W. Lee, M. Girolami, A. J. Bell, and T. J. Sejnowski, "A Unifying Information-Theoretic Framework for Independent Component Analysis," *Computers and Mathematics with Applications*, vol. 39, pp. 1-21, 2000.
- [116] P. Dinh-Tuan, "Fast algorithms for mutual information based independent component analysis," *Signal Processing, IEEE Transactions on*, vol. 52, pp. 2690-2700, 2004.
- [117] E. H. Land, "The retinex," *Am. Sci.*, vol. 52, pp. 247-64. Reprinted in McCann, vol. III, pp. 53-60. , 1964.
- [118] E. H. Land and J. J. McCann, "Lightness and retinex theory," *Journal of the Optical Society of America*, vol. 61, pp. 1-11, 1971.
- [119] E. H. Land, "The retinex theory of color vision," *Scientific American*, vol. 237, pp. 108-28. , 1977.
- [120] D. Marini and A. Rizzi, "A computational approach to color adaptation effects," *Image and Vision Computing*, vol. 18, pp. 1005-1014, 2000.
- [121] T. J. Cooper and F. A. Baqai, "Analysis and extensions of the Frankle-McCann Retinex algorithm," *Journal of Electronic Imaging*, vol. 13, pp. 85-92, 2004.
- [122] E. Provenzi, C. Gatta, M. Fierro, and A. Rizzi, "A Spatially Variant White-Patch and Gray-World Method for Color Image Enhancement Driven by Local Contrast," *Pattern Analysis and Machine Intelligence, IEEE Transactions on*, vol. 30, pp. 1757-70, 2008.
- [123] D. J. Jobson, Z. Rahman, and G. A. Woodell, "Properties and performance of a center/surround retinex," *Image Processing, IEEE Transactions on*, vol. 6, pp. 451-462, 1997.

- [124] D. J. Jobson, Z. Rahman, and G. A. Woodell, "A multiscale retinex for bridging the gap between color images and the human observation of scenes," *Image Processing, IEEE Transactions on*, vol. 6, pp. 965-976, 1997.
- [125] J. A. Frankle and J. J. McCann, "Method and apparatus for lightness imaging," U.S. Patent 4, 348,336, 1983.
- [126] J. McCann, "Lessons Learned from Mondrians Applied to Real Images and Color Gamuts," in *In Proc. IS&T/SID Seventh Color Imaging Conference: Colour Science, Systems and Applications*, Scottsdale, Arizona, 1999, pp. 1-8.
- [127] B. Funt, F. Ciurea, and J. McCann, "Retinex in MATLAB™," *Journal of Electronic Imaging*, vol. 13, pp. 48-57, January 2004.
- [128] E. Land, "An alternative technique for the computation of the designator in the retinex theory of colour vision," in *Proc. Nat. Acad. Sci*, 1986, pp. 3078-3080.
- [129] A. Moore, J. Allman, and R. M. Goodman, "A real-time neural system for color constancy," *Neural Networks, IEEE Transactions on*, vol. 2, pp. 237-247, 1991.
- [130] A. C. Hurlbert and T. A. Poggio, "Synthesizing a color algorithm from examples," *Science*, vol. 239, pp. 482-5, 1988.
- [131] M. Herscovitz, E. Artemov, and O. Yadid-Pecht, "Improving the global impression of brightness of the multi scale Retinex algorithm for wide dynamic range pictures," pp. 393-405, 2003.
- [132] L. Meylan and S. Süsstrunk, "Color image enhancement using a Retinex-based adaptive filter," in *Proc. IS&T Second European Conference on Color in Graphics, Image, and Vision (CGIV 2004)*, Aachen, Germany, 2004, pp. 359-363.
- [133] W. Wang, B. Li, J. Zheng, S. Xian, and J. Wang, "A fast Multi-Scale Retinex algorithm for color image enhancement," in *Wavelet Analysis and Pattern*

- Recognition, 2008. ICWAPR '08. International Conference on*, Hong Kong, 2008, pp. 80 - 85.
- [134] S. Chen and A. Beghdadi, "Natural Enhancement of Color Image," *EURASIP Journal on Image and Video Processing*, vol. 2010, p. 19 pages, 2010.
- [135] W. Jing, W. Ziwu, and F. Zhixia, "Application of Retinex in Color Restoration of Image Enhancement to Night Image," in *Image and Signal Processing, 2009. CISP '09. 2nd International Congress on*, 2009, pp. 1-4.
- [136] J. Sun, Y. Du, and Y. Tang, "Shadow Detection and Removal from Solo Natural Image Based on Retinex Theory," in *Intelligent Robotics and Applications*. vol. 5314, C. Xiong, H. Liu, Y. Huang, and Y. Xiong, Eds., ed: Springer Berlin / Heidelberg, 2008, pp. 660-668.
- [137] L. Cinque and G. Morrone, "Retinex Combined with Total Variation for Image Illumination Normalization," in *Image Analysis and Processing – ICIAP 2009*. vol. 5716, P. Foggia, C. Sansone, and M. Vento, Eds., ed: Springer Berlin / Heidelberg, 2009, pp. 958-964.
- [138] Y. K. Park, S. L. Park, and J. K. Kim, "Retinex method based on adaptive smoothing for illumination invariant face recognition," *Signal Processing*, vol. 88, pp. 1929-1945, 2008.
- [139] S. Chen and L. Zou, "Chest Radiographic Image Enhancement Based on Multi-Scale Retinex Technique," in *Bioinformatics and Biomedical Engineering , 2009. ICBBE 2009. 3rd International Conference on*, 2009, pp. 1-3.
- [140] W.-H. Chao, C.-W. Cho, Y.-Y. Shih, Y.-Y. Chen, and C. Chang, "Correction of Inhomogeneous MR Images Using Multiscale Retinex," *The International Journal of Image Processing*, vol. 1, pp. 1-16, 2006.
- [141] S. Vázquez, N. Barreira, M. Penedo, M. Saez, and A. Pose-Reino, "Using Retinex Image Enhancement to Improve the Artery/Vein Classification in Retinal Images," ed, 2010, pp. 50-59.

- [142] J. V. Stone, *Independent component analysis : a tutorial introduction*. Cambridge, Mass.: MIT Press, 2004.
- [143] J. Herault and C. Jutten, "Space or time adaptive signal processing by neural network models," *AIP Conference Proceedings*, vol. 151, pp. 206-211, 1986.
- [144] C. Jutten and J. Herault, "Blind separation of sources, part I: An adaptive algorithm based on neuromimetic architecture," *Signal Processing*, vol. 24, pp. 1-10, 1991.
- [145] P. Comon, "Independent component analysis, A new concept?," *Signal Processing*, vol. 36, p. 287, 1994.
- [146] J. F. Cardoso and A. Souloumiac, "Blind beamforming for non Gaussian signals," *IEE Proceedings-F*, vol. 140, pp. 362-370, December 1993.
- [147] A. Hyvarinen, "Fast and robust fixed-point algorithms for independent component analysis," *Neural Networks, IEEE Transactions on*, vol. 10, pp. 626-634, 1999.
- [148] J. Onton, M. Westerfield, J. Townsend, and S. Makeig, "Imaging human EEG dynamics using independent component analysis," *Neuroscience & Biobehavioral Reviews*, vol. 30, pp. 808-822, 2006.
- [149] X. Y. Wu and G. R. Liu, "Application of independent component analysis to dynamic contrast-enhanced imaging for assessment of cerebral blood perfusion," *Medical Image Analysis*, vol. 11, p. 254, 2007.
- [150] K. Jongsun, C. Jongmoo, Y. Juneho, and M. Turk, "Effective representation using ICA for face recognition robust to local distortion and partial occlusion," *Pattern Analysis and Machine Intelligence, IEEE Transactions on*, vol. 27, p. 1977, 2005.
- [151] A. J. Caamano, B.-T. Rafael, J. Ramos, and J. J. Murillo-Fuentes, "Hybrid higher-order statistics learning in multiuser detection," *Systems, Man, and*

- Cybernetics, Part C: Applications and Reviews, IEEE Transactions on*, vol. 34, pp. 417-424, 2004.
- [152] L. Te-Won, M. S. Lewicki, M. Girolami, and T. J. Sejnowski, "Blind source separation of more sources than mixtures using overcomplete representations," *Signal Processing Letters, IEEE*, vol. 6, pp. 87-90, 1999.
- [153] K. Kreutz-Delgado, J. F. Murray, B. D. Rao, K. Engan, T.-W. Lee, and T. J. Sejnowski, "Dictionary Learning Algorithms for Sparse Representation," *Neural Computation*, vol. 15, pp. 349–396, 2003.
- [154] A. Hyvarinen and E. Oja, "Independent component analysis: algorithms and applications," *Neural Networks*, vol. 13, p. 411, 2000.
- [155] A. Hyvärinen, J. Karhunen, and E. Oja, *Independent component analysis*. New York: J. Wiley, 2001.
- [156] H. F. Trotter, "An elementary proof of the central limit theorem," *Archiv der Mathematik*, vol. 10, pp. 226-234, 1959.
- [157] A. Papoulis, *Probability, random variables, and stochastic processes*. London: Mcgraw-Hill Publishing Co, 1991.
- [158] M. Jones and R. Sibson, "What is projection pursuit?," *Journal of the Royal Statistical Society*, 150, pp. 1–36., vol. Series A, pp. 1-36, 1987.
- [159] A. Hyvarinen, "New approximations of differential entropy for independent component analysis and projection pursuit," in *Proceedings of the 1997 Conference on Advances in Neural Information Processing Systems 10*, Denver, Colorado, United States, 1998, pp. 273-279.
- [160] P. Dinh Tuan and P. Garat, "Blind separation of mixture of independent sources through a quasi-maximum likelihood approach," *Signal Processing, IEEE Transactions on*, vol. 45, pp. 1712-1725, 1997.

- [161] L. B. Almeida, "MISEP – Linear and Nonlinear ICA Based on Mutual Information," *Journal of Machine Learning Research* vol. 4, pp. 1297-1318, December 2003.
- [162] E. Oja and Z. Yuan, "The FastICA Algorithm Revisited: Convergence Analysis," *Neural Networks, IEEE Transactions on*, vol. 17, pp. 1370-1381, 2006.
- [163] A. Hyvarinen, "One-unit contrast functions for independent component analysis: a statistical analysis," in *Neural Networks for Signal Processing [1997] VII. Proceedings of the 1997 IEEE Workshop*, 1997, pp. 388-397.
- [164] X. Giannakopoulos, J. Karhunen, and E. Oja, "An experimental comparison of neural algorithms for independent component analysis and blind separation," *Int J Neural Syst*, vol. 9, pp. 99-114, April 1999.
- [165] A. Hyvarinen and E. Oja, "A Fast Fixed-Point Algorithm for Independent Component Analysis," *Neural Computation*, vol. 9, pp. 1483-1492, 1997.
- [166] T.-W. Lee, M. Girolami, and T. J. Sejnowski, "Independent Component Analysis Using an Extended Infomax Algorithm for Mixed Subgaussian and Supergaussian Sources," *Neural Computation*, vol. 11, pp. 417-441, 1999.
- [167] H. H. Yang and S.-i. Amari, "Adaptive Online Learning Algorithms for Blind Separation: Maximum Entropy and Minimum Mutual Information," *Neural computation.*, vol. 9, p. 1457, 1997.
- [168] J. F. Cardoso and B. H. Laheld, "Equivariant Adaptive Source Separation," *Signal Processing, IEEE Transactions on*, vol. 44, p. 3017, 1996.
- [169] A. Koutras, I. Christoyianni, E. Dermatas, and G. Kokkinakis, "Feature Extraction in Digital Mammography: An Independent Component Analysis Approach," in *Bio-Inspired Applications of Connectionism: 6th International Work-Conference on Artificial and Natural Neural Networks, IWANN 2001 Granada, Spain, June 13-15, 2001, Proceedings, Part II*, ed, 2001, p. 794.

- [170] C. Duan, X. Meng, C. Tu, and C. Yang, "How to make local image features more efficient and distinctive," *Computer Vision, IET*, vol. 2, pp. 178-189, 2008.
- [171] C. Yen-Wei, Z. Xiang-Yan, and L. Hanqing, "Edge detection and texture segmentation based on independent component analysis," in *Pattern Recognition, 2002. Proceedings. 16th International Conference on*, 2002, p. 351.
- [172] N. Tsumura, N. Ojima, K. Sato, M. Shiraishi, H. Shimizu, H. Nabeshima, S. Akazaki, K. Hori, and Y. Miyake, "Image-based skin color and texture analysis/synthesis by extracting hemoglobin and melanin information in the skin," in *International Conference on Computer Graphics and Interactive Techniques: ACM SIGGRAPH 2003*, San Diego, California, 2003, pp. 770-779.
- [173] P. Mayo, F. Rodenas, and G. Verdu, "Comparing methods to denoise mammographic images," in *Engineering in Medicine and Biology Society, 2004. IEMBS '04. 26th Annual International Conference of the IEEE*, 2004, pp. 247-250.
- [174] Y.-O. Li, T. Adah, and V. D. Calhoun., "Independent component analysis with feature selective filtering," in *Proceedings of the 2004 14th IEEE Signal Processing Society Workshop on Machine Learning for Signal Processing*, 2004, pp. 193-202.
- [175] A. Boroomand, A. Ahmadian, M. A. Oghabian, J. Alirezaie, and C. Beckman, "An Efficient Hybrid Wavelet-ICA algorithm for Analyzing Simulated fMRI Data in Noisy Environment," in *Signal Processing and Information Technology, 2007 IEEE International Symposium on*, 2007, pp. 408-413.
- [176] N. Tsumura, H. Haneishi, and Y. Miyake, "Independent-component analysis of skin color image," *J. Opt. Soc. Am. A*, vol. 16, p. 2169, 1999.

- [177] N. Tsumura, H. Haneishi, and Y. Miyake, "Independent Component Analysis of Spectral Absorbance Image in Human Skin," *Optical Review*, vol. 7, pp. 479-482, 2000/11/01/ 2000.
- [178] H. Nugroho, M. H. A. Fadzil, V. V. Yap, S. Norashikin, and H. H. Suraiya, "Determination of Skin Repigmentation Progression," in *Engineering in Medicine and Biology Society, 2007. EMBS 2007. 29th Annual International Conference of the IEEE*, 2007, p. 3442.
- [179] M. H. Ahmad Fadzil, H. A. Nugroho, H. Nugroho, and L. I. Izhar. Fundus Image Database for Non Invasive Diabetic Retinopathy Monitoring and Grading System (FINDeRS) [Online].
- [180] F. C. Delori and K. P. Pflibsen, "Spectral reflectance of the human ocular fundus," *Appl. Opt.*, vol. 28, pp. 1061-1077, 1989.
- [181] M. U. V. Department of Med. Physics, "OCT scan of a retina at 800nm with an axial resolution of 3 μ m," vol. 800 \times 250 pixel, 445 KB, Retina-OCT800, Ed., ed. Vienna, Austria, 2004.
- [182] R. A. Bone, J. T. Landrum, Y. Cao, A. N. Howard, and F. Alvarez-Calderon, "Macular pigment response to a supplement containing meso-zeaxanthin, lutein and zeaxanthin," *Nutr Metab (Lond)*, vol. 4, 2007.
- [183] S. J. Preece and E. Claridge, "Physics based medical image understanding of the colouration of the ocular fundus with application to the detection of diabetic retinopathy," in *Medical Image Understanding and Analysis 2000*, London, 2000, pp. 7-10.
- [184] A. J. Whitehead, J. A. Mares, and R. P. Danis, "Macular Pigment: A Review of Current Knowledge," *Arch Ophthalmol*, vol. 124, pp. 1038-1045, July 1, 2006 2006.
- [185] M. J. Kanis, T. T. J. M. Berendschot, and D. van Norren, "Interocular agreement in melanin and macular pigment optical density," *Experimental Eye Research*, vol. 84, pp. 934-938, 2007.

- [186] T. T. J. M. Berendschot, P. J. DeLint, and D. v. Norren, "Fundus reflectance--historical and present ideas," *Progress in Retinal and Eye Research*, vol. 22, pp. 171-200, 2003.
- [187] J. A. N. van de Kraats, T. T. J. M. Berendschot, and D. van Norren, "The Pathways of Light Measured in Fundus Reflectometry," *Vision Research*, vol. 36, pp. 2229-2247, 1996.
- [188] A. Agarwal, *Fundus fluorescein and indocyanine green angiography : a textbook and atlas*. Thorofare, NJ: SLACK, 2008.
- [189] D. Van Norren and L. F. Tiemeijer, "Spectral reflectance of the human eye," *Vision Research*, vol. 26, pp. 313-320, 1986.
- [190] F. Orihuela-Espina, E. Claridge, and I. B. Styles, "Validation of a physics based model of the reflectance of the ocular fundus," *Invest. Ophthalmol. Vis. Sci.*, vol. 45, pp. 2789-, May 1, 2004 2004.
- [191] I. B. Styles, A. Calcagni, E. Claridge, F. Orihuela-Espina, and J. M. Gibson, "Quantitative analysis of multi-spectral fundus images," *Medical Image Analysis: Special Issue on Functional Imaging and Modelling of the Heart (FIMH 2005)*, vol. 10, pp. 578-597, 2006/8 2006.
- [192] R. E. Walpole, *Probability and Statistics for Engineers and Scientists*: Pearson Prentice Hall, 2007.
- [193] W. G. Cochran, *Sampling techniques*. New York: Wiley, 1977.
- [194] J. B. Jonas, X. N. Nguyen, and G. O. Naumann, "Parapapillary retinal vessel diameter in normal and glaucoma eyes. I. Morphometric data," *Investigative ophthalmology & visual science*, vol. 30, pp. 1599-603, July 1 1989.
- [195] F. Pukelsheim, "The Three Sigma Rule," *American Statistician*, vol. 48, pp. 88-91, 1994.

- [196] M. Oren and S. Nayar, "Seeing beyond Lambert's law," in *Computer Vision — ECCV '94*. vol. 801, J.-O. Eklundh, Ed., ed: Springer Berlin / Heidelberg, 1994, pp. 269-280.
- [197] J. H. Lambert, *Photometria sive de mensura de gratibus luminis, colorum umbrae*: Eberhard Klett, 1760.
- [198] R. Jain, R. Kasturi, and B. G. Schunck, *Machine vision*. New York: McGraw-Hill, 1995.
- [199] M. H. Ahmad Fadzil, H. A. Nugroho, P. A. Venkatachalam, H. Nugroho, and L. I. Izhar, "Determination of Retinal Pigments from Fundus Images using Independent Component Analysis," in *IFMBE Proceedings: 4th Kuala Lumpur International Conference on Biomedical Engineering 2008*. vol. 21, N. A. A. Osman, F. Ibrahim, W. A. B. W. Abas, H. S. A. Rahman, and H.-N. Ting, Eds., ed Kuala Lumpur: Springer Berlin Heidelberg, 2008, pp. 555-558.
- [200] D.-C. Chang and W.-R. Wu, "Image contrast enhancement based on a histogram transformation of local standard deviation," *Medical Imaging, IEEE Transactions on*, vol. 17, pp. 518-531, 1998.
- [201] B. Moulden, F. Kingdom, and L. F. Gatley, "The standard deviation of luminance as a metric for contrast in random-dot images," *Perception*, vol. 19, pp. 79-101, 1990.
- [202] D. S. Fong, L. Aiello, T. W. Gardner, G. L. King, G. Blankenship, J. D. Cavallerano, F. L. Ferris, and R. Klein, "Diabetic Retinopathy," *Diabetes Care*, vol. 26, pp. s99-s102, January 1 2003.
- [203] P. P. Goh, "Status of Diabetic Retinopathy Among Diabetics Registered to the Diabetic Eye Registry, National Eye Database, 2007," *The Medical Journal of Malaysia*, vol. 63, pp. 24-28, September 2008.
- [204] N. Unwin and F. International Diabetes. (2009, *IDF diabetes atlas*. Available: <http://www.diabetesatlas.org/>

- [205] American Academy of Ophthalmology, "Preferred Practice Pattern," in *Diabetic Retinopathy*, ed San Francisco, California: American Academy of Ophthalmology, 2003.
- [206] G. Richard, G. I. Soubrane, L. A. Yannuzzi, and S. Courland, *Fluorescein and ICG Angiography*. New York: Thieme Medical Publisher Inc., 1998.
- [207] P. Kahai, K. R. Namuduri, and H. Thompson, "A Decision Support Framework for Automated Screening of Diabetic Retinopathy," *International Journal of Biomedical Imaging*, vol. 2006, pp. 1-7, 2006.
- [208] J. Nayak, P. Bhat, R. Acharya U, C. Lim, and M. Kagathi, "Automated Identification of Diabetic Retinopathy Stages Using Digital Fundus Images," *Journal of Medical Systems*, vol. 32, pp. 107-115, 2008.
- [209] W. L. Yun, U. Rajendra Acharya, Y. V. Venkatesh, C. Chee, L. C. Min, and E. Y. K. Ng, "Identification of different stages of diabetic retinopathy using retinal optical images," *Information Sciences*, vol. 178, pp. 106-121, 2008.
- [210] H. F. Jelinek, M. J. Cree, J. J. G. Leandro, J. V. B. Soares, R. M. Cesar, and A. Luckie, "Automated segmentation of retinal blood vessels and identification of proliferative diabetic retinopathy," *J. Opt. Soc. Am. A*, vol. 24, pp. 1448-1456, 2007.
- [211] T. Walter, J.-C. Klein, P. Massin, and A. Erginay, "A contribution of image processing to the diagnosis of diabetic retinopathy-detection of exudates in color fundus images of the human retina," *Medical Imaging, IEEE Transactions on*, vol. 21, pp. 1236-1243, 2002.
- [212] A. Sopharak, B. Uyyanonvara, S. Barman, and T. H. Williamson, "Automatic detection of diabetic retinopathy exudates from non-dilated retinal images using mathematical morphology methods," *Computerized Medical Imaging and Graphics*, vol. 32, pp. 720-727, 2008.
- [213] P. Kahai, K. R. Namuduri, and H. Thompson, "Decision support for automated screening of diabetic retinopathy," in *Signals, Systems and*

Computers, 2004. Conference Record of the Thirty-Eighth Asilomar Conference on, 2004, pp. 1630-1634 Vol.2.

- [214] G. H. Bresnick, R. Condit, S. Syrjala, M. Palta, A. Groo, and K. Korth, "Abnormalities of the foveal avascular zone in diabetic retinopathy," *Arch Ophthalmol*, vol. 102, pp. 1286-1293, September 1 1984.
- [215] J. Conrath, R. Giorgi, D. Raccach, and B. Ridings, "Foveal avascular zone in diabetic retinopathy: quantitative vs qualitative assessment," *Eye*, vol. 19, pp. 322-326, 2004.
- [216] J. Conrath, O. Valat, R. Giorgi, M. Adel, D. Raccach, F. Meyer, and B. Ridings, "Semi-automated detection of the foveal avascular zone in fluorescein angiograms in diabetes mellitus," *Clinical & Experimental Ophthalmology*, vol. 34, pp. 119-123, 2006.
- [217] V. K. Saini, P. Varma, V. Bhaisare, S. Kulkarni, P. Sodani, D. Maheshwai, and N. Pawar, "Foveal Avascular Zone Calculation and its Variation with Different Posterior Segment Diseases and Analysis of its Impact on Best Corrected Visual Acuity," in *AIOC 2006*, Bhopal, India, 2006, pp. 538-539.
- [218] B. Zeffren, R. Applegate, A. Bradley, and W. van Heuven, "Retinal fixation point location in the foveal avascular zone," *Invest. Ophthalmol. Vis. Sci.*, vol. 31, pp. 2099-2105, October 1 1990.
- [219] D. John, A. Braganza, and T. Kuriakose, "A Study of The Foveal Avascular Zone Using The Heidelberg Retina Angiogram-2 in Normal Eyes," in *34th All India Optometry Conference (AIOC 2008) Proceedings*, Amritsar, India, 2006, pp. 485-486.
- [220] M. B. Parodi, F. Visintin, P. D. Rupe, and G. Ravalico, "Foveal avascular zone in macular branch retinal vein occlusion," *International Ophthalmology*, vol. 19, pp. 25-28, 1995.
- [221] A. Bradley, R. A. Applegate, B. S. Zeffren, and W. A. J. Heuven, "Psychophysical measurement of the size and shape of the human foveal

- avascular zone," *Ophthalmic and Physiological Optics*, vol. 12, pp. 18-23, 1992.
- [222] A. M. Mansour, "Measuring fundus landmark," *Invest Ophthalmol Vis Sci*, vol. 31, pp. 41-42, 1990.
- [223] B. Sander, M. Larsen, C. Engler, and H. Lund-Andersen, "Absence of foveal avascular zone demonstrated by laser scanning fluorescein angiography," *Acta Ophthalmologica*, vol. 72, pp. 550-552, 1994.
- [224] A. K. Khurana, *Ophthalmology*. New Delhi: New Age International Publishers, 2003.
- [225] M. V. Ibanez and A. Simo, "Bayesian detection of the fovea in eye fundus angiographies," *Pattern Recognition Letters*, vol. 20, pp. 229-240, 1999.
- [226] M. Eladawy, S. M. S. Karawya, M. Elbably, and N. M. A. Salem, "Automatic detection and measurement of foveal avascular zone," in *Radio Science Conference, 2003. NRSC 2003. Proceedings of the Twentieth National*, 2003, pp. K3-1-7.
- [227] "Early photocoagulation for diabetic retinopathy. ETDRS report number 9. Early Treatment Diabetic Retinopathy Study Research Group," *Ophthalmology*, vol. 98, pp. 766-85, May 1991.
- [228] "Preliminary report on effects of photocoagulation therapy. The Diabetic Retinopathy Study Research Group.," *Am J Ophthalmol*, vol. 81, pp. 383-96, 1976.
- [229] M. H. Ahmad Fadzil and L. I. Izhar, "A Non-Invasive Method for Analysing the Retina for Ocular Manifested Diseases," Malaysia Patent patent filing no. PI20083503 September, 2008.
- [230] M. H. Ahmad Fadzil and I. Lila Iznita, "An Apparatus for Monitoring and Grading Diabetic Retinopathy. Malaysia Patent filing no. PI20091936 May, 2009. International Filing: W02010t131944, Nov 2010.," Malaysia Patent

- patent filing no. PI20091936, May 2009, International Filing No. W02010t131944, Nov 2010., 2009.
- [231] M. H. Ahmad Fadzil and I. Lila Iznita, "A Non-Invasive Method for Analysing the Retina for Ocular Manifested Diseases. Malaysia Patent filing no. PI20083503 September, 2008. PCT/MY2009/000025, 2009.," Malaysia Patent patent filing no. PCT/MY2009/000025, 2009.
- [232] N. Otsu, "A Threshold Selection Method from Gray-Level Histograms," *Systems, Man and Cybernetics, IEEE Transactions on*, vol. 9, pp. 62-66, 1979.
- [233] M. H. Ahmad Fadzil, H. A. Nugroho, and H. Nugroho, "Gaussian Bayes Classifier for Medical Diagnosis and Grading: Application to Diabetic Retinopathy," in *2010 IEEE EMBS Conference on Biomedical Engineering and Sciences (IECBES 2010)*, Kuala Lumpur, Malaysia, 2010.
- [234] R. Kohavi, "A Study of Cross-Validation and Bootstrap for Accuracy Estimation and Model Selection," in *Proceedings of the 14th International Joint Conference on Artificial Intelligence (IJCAI'95)*, Montreal, Quebec, Canada, 1995, pp. 1137-1145.
- [235] E. Micheli-Tzanakou, *Supervised and unsupervised pattern recognition: feature extraction and computational intelligence*. Boca Raton, FL: CRC Press, 2000.
- [236] W. K. Pratt, *Digital image processing*. New York: Wiley, 1978.
- [237] J. Staal, M. D. Abramoff, M. Niemeijer, M. A. Viergever, and B. van Ginneken, "Ridge-based vessel segmentation in color images of the retina," *Medical Imaging, IEEE Transactions on*, vol. 23, pp. 501-509, 2004.
- [238] M. H. Ahmad Fadzil, H. A. Nugroho, H. Nugroho, and I. Lila Iznita, "Contrast Enhancement of Retinal Vasculature in Digital Fundus Image," in *Proceeding of 2009 International Conference on Digital Image Processing (ICDIP 2009)*, Bangkok, Thailand, 2009, pp. 137-141.

- [239] M. H. Ahmad Fadzil and H. A. Nugroho, "Retinal vasculature enhancement using independent component analysis," *J. Biomedical Science and Engineering*, vol. 2, pp. 543-549 2009.
- [240] A. Colin Cameron and F. A. G. Windmeijer, "An R-squared measure of goodness of fit for some common nonlinear regression models," *Journal of Econometrics*, vol. 77, pp. 329-342, 1997.
- [241] C. E. Rasmussen and C. K. I. Williams, *Gaussian processes for machine learning*. Cambridge, Mass.: MIT Press, 2006.
- [242] R. O. Duda, P. E. Hart, and D. G. Stork, *Pattern classification*. New York: Wiley, 2001.
- [243] T. M. Mitchell, *Machine Learning*. New York: McGraw-Hill, 1997.
- [244] S. Theodoridis and K. Koutroumbas, *Pattern recognition*. London,UK: Elsevier Inc. , 2009.
- [245] M. Stone, "Cross-Validatory Choice and Assessment of Statistical Predictions," *Journal of the Royal Statistical Society. Series B (Methodological)*, vol. 36, pp. 111-147, 1974.
- [246] A. J. Izenman, *Modern Multivariate Statistical Techniques : Regression, Classification, and Manifold Learning*. Berlin: Springer New York, 2008.
- [247] E. Hart, M. Goldbaum, B. Côté, P. Kube, and M. R. Nelson, "Automated measurement of retinal vascular tortuosity," in *Proc AMIA Annu Fall Symp*, 1997, pp. 459-463.
- [248] S. L. Wood, Q. Gongyuan, and L. W. Roloff, "Detection and labeling of retinal vessels for longitudinal studies," in *Image Processing, 1995. Proceedings., International Conference on*, 1995, pp. 164-167 vol.3.
- [249] F. Zana and J.-C. Klein, "Robust segmentation of vessels from retinal angiography," in *Digital Signal Processing Proceedings, 1997. DSP 97., 1997 13th International Conference on*, 1997, pp. 1087-1090 vol.2.

- [250] W. E. Higgins, W. J. T. Spyra, R. A. Karwoski, and E. L. Ritman, "System for analyzing high-resolution three-dimensional coronary angiograms," *Medical Imaging, IEEE Transactions on*, vol. 15, pp. 377-385, 1996.
- [251] M. Niemeijer, J. Staal, B. v. Ginneken, M. Loog, and M. D. Abramoff, "Comparative study of retinal vessel segmentation methods on a new publicly available database," in *Medical Imaging 2004: Image Processing*, Milan, 2004, pp. pp. 648-656.
- [252] F. Zana and J.-C. Klein, "Segmentation of vessel-like patterns using mathematical morphology and curvature evaluation," *Image Processing, IEEE Transactions on*, vol. 10, pp. 1010-1019, 2001.
- [253] J. Carletta, "Assessing Agreement on Classification Tasks: The Kappa Statistic," *Computational Linguistics*, vol. 22, pp. 249--254, 1996.
- [254] M. H. Zweig and G. Campbell, "Receiver-operating characteristic (ROC) plots: a fundamental evaluation tool in clinical medicine," *Clin Chem*, vol. 39, pp. 561-577, April 1, 1993 1993.
- [255] O. Arend, S. Wolf, F. Jung, B. Bertram, H. Pöstgens, H. Toonen, and M. Reim, "Retinal microcirculation in patients with diabetes mellitus: dynamic and morphological analysis of perifoveal capillary network," *British Journal of Ophthalmology*, vol. 75, pp. 514-518, September 1 1991.
- [256] C. Metz, "ROC analysis in medical imaging: a tutorial review of the literature," *Radiological Physics and Technology*, vol. 1, pp. 2-12, 2008.
- [257] J. A. Hanley and B. J. McNeil, "The meaning and use of the area under a receiver operating characteristic (ROC) curve," *Radiology*, vol. 143, pp. 29-36, 1982.
- [258] J. L. Myers and A. D. Well, *Research design and statistical analysis*. Mahwah, N.J.: Lawrence Erlbaum Associates, 2003.

- [259] L. Ballerini, "Detection and Quantification of Foveal Avascular Zone Alterations in Diabetic Retinopathy (DR)," presented at the 5th Internet World Congress for Biomedical Sciences – INABIS 1998, McMaster University, Hamilton, Ontario, Canada, 1998.
- [260] Y. Zheng, J. S. Gandhi, A. N. Stangos, C. Campa, D. M. Broadbent, and S. P. Harding, "Automated Segmentation of Foveal Avascular Zone in Fundus Fluorescein Angiography," *Invest. Ophthalmol. Vis. Sci.*, February 3 2010.
- [261] A. Haddouche, M. Adel, M. Rasigni, J. Conrath, and S. Bourennane, "Detection of the foveal avascular zone on retinal angiograms using Markov random fields," *Digital Signal Processing*, vol. 20, pp. 149-154, 2010.
- [262] M. H. Ahmad Fadzil, I. Lila Iznita, and H. A. Nugroho, "Analysis of Foveal Avascular Zone in Color Fundus Image for Grading of Diabetic Retinopathy," *International Journal of Recent Trends in Engineering*, vol. 2, pp. 101-104, November 2009.
- [263] M. H. A. Fadzil, I. Lila Iznita, and N. Hanung Adi, "Determination of foveal avascular zone in diabetic retinopathy digital fundus images," *Computers in Biology and Medicine*, vol. 40, pp. 657-664, July 2010.
- [264] M. Ahmad Fadzil, L. Izhar, H. Nugroho, and H. A. Nugroho, "Analysis of retinal fundus images for grading of diabetic retinopathy severity," *Medical and Biological Engineering and Computing*, vol. 49 pp. 1-8, January 2011.
- [265] M. H. Ahmad Fadzil, L. I. Izhar, and H. A. Nugroho, "Area Analysis of Foveal Avascular Zone in Diabetic Retinopathy Color Fundus Images," *International Journal of Medical Engineering and Informatics*, vol. 3, pp. 84-98, 2011.
- [266] J. W. Tukey, *Exploratory Data Analysis*: Addison-Wesley, 1977.
- [267] J. A. Olson, F. M. Strachan, J. H. Hipwell, K. A. Goatman, K. C. McHardy, J. V. Forrester, and P. F. Sharp, "A comparative evaluation of digital imaging,

- retinal photography and optometrist examination in screening for diabetic retinopathy," *Diabetic Medicine*, vol. 20, pp. 528-534, 2003.
- [268] A. Singalavanija, J. Supokavej, P. Bamroongsuk, C. Sinthanayothin, S. Phoojaruenchanachai, and V. Kongbunkiat, "Feasibility Study on Computer-Aided Screening for Diabetic Retinopathy," *Japanese Journal of Ophthalmology*, vol. 50, pp. 361-366, 2006.
- [269] J. Ahmed, T. P. Ward, S.-E. Bursell, L. M. Aiello, J. D. Cavallerano, and R. A. Vigersky, "The Sensitivity and Specificity of Nonmydriatic Digital Stereoscopic Retinal Imaging in Detecting Diabetic Retinopathy," *Diabetes Care*, vol. 29, pp. 2205-2209, October 2006.
- [270] "Grading diabetic retinopathy from stereoscopic color fundus photographs--an extension of the modified Airlie House classification. ETDRS report number 10. Early Treatment Diabetic Retinopathy Study Research Group," *Ophthalmology*, vol. 98, pp. 786-806, May 1991.

LIST OF PUBLICATIONS

Conferences:

1. H. A. Nugroho, M. H. Ahmad Fadzil, and P. A. Venkatachalam, "Contrast Enhancement of Retinal Blood Vessels using Independent Component Analysis," in *National Postgraduate Conference on Engineering, Science and Technology (NPC 2008)*, Bandar Seri Iskandar, Tronoh, Perak, Malaysia, 2008.
2. M. H. Ahmad Fadzil, H. A. Nugroho, H. Nugroho, and I. Lila Iznita, "Contrast Enhancement of Retinal Vasculature in Digital Fundus Image," in *Proceeding of 2009 International Conference on Digital Image Processing (ICDIP 2009)*, Bangkok, Thailand, 2009, pp. 137-141.
3. P. Kee Yong, I. L. Iznita, M. H. A. Fadzil, H. A. Nugroho, N. Hermawan, and S. A. Vijanth, "Segmentation of retinal vasculature in colour fundus images," in *Innovative Technologies in Intelligent Systems and Industrial Applications, 2009. CITISIA 2009*, Kuala Lumpur, 2009, pp. 398-401.
4. M. H. Ahmad Fadzil and H. A. Nugroho, "Model-based retinal vasculature enhancement in digital fundus image using independent component analysis," in *Proc. 2009 IEEE Symposium on Industrial Electronics & Applications (ISIEA2009)*, Kuala Lumpur, Malaysia, 2009, pp. 137-141.
5. M. H. Ahmad Fadzil, N. F. Ngah, T. M. George, H. A. Nugroho, and H. Nugroho, "Grading of diabetic retinopathy severity by analysing foveal avascular zone in colour fundus images," presented at the 4th National Conference for Clinical Research 2010, Kuala Lumpur, Malaysia, 2010.
6. A. F. M. Hani, N. F. Ngah, T. M. George, L. I. Izhar, H. Nugroho, and H. A. Nugroho, "Analysis of foveal avascular zone in colour fundus images for grading of diabetic retinopathy severity," in *Engineering in Medicine and*

Biology Society (EMBC), 2010 Annual International Conference of the IEEE, Buenos Aires 2010, pp. 5632-5635.

7. A. F. M. Hani, H. A. Nugroho, and H. Nugroho, "Gaussian Bayes classifier for medical diagnosis and grading: Application to diabetic retinopathy," in *Biomedical Engineering and Sciences (IECBES), 2010 IEEE EMBS Conference on, 2010, pp. 52-56.*

Book Chapters:

1. M. H. Ahmad Fadzil, H. A. Nugroho, P. A. Venkatachalam, H. Nugroho, and L. I. Izhar, "Determination of Retinal Pigments from Fundus Images using Independent Component Analysis," in *IFMBE Proceedings: 4th Kuala Lumpur International Conference on Biomedical Engineering 2008*. vol. 21, N. A. A. Osman, F. Ibrahim, W. A. B. W. Abas, H. S. A. Rahman, and H.-N. Ting, Eds., ed Kuala Lumpur: Springer Berlin Heidelberg, 2008, pp. 555-558.
2. A. F. M. Hani, H. Nugroho, H. A. Nugroho, L. I. Izhar, N. F. Ngah, T. M. George, M. Ismail, E. Hussein, and G. P. Pin, "Toward a Fully Automated DR Grading System," in *5th European Conference of the International Federation for Medical and Biological Engineering IFMBE Proceedings*. vol. 37, Á. Jobbágy and R. Magjarevic, Eds., ed Budapest, Hungary: Springer Berlin Heidelberg, 2012, pp. 663-666.

Journals:

1. M. H. Ahmad Fadzil and H. A. Nugroho, "Retinal vasculature enhancement using independent component analysis," *J. Biomedical Science and Engineering*, vol. 2, pp. 543-549 2009.
2. M. H. A. Fadzil, I. Lila Iznita, and N. Hanung Adi, "Determination of foveal avascular zone in diabetic retinopathy digital fundus images," *Computers in Biology and Medicine*, vol. 40, pp. 657-664, July 2010.
3. M. H. Ahmad Fadzil, I. Lila Iznita, and H. A. Nugroho, "Analysis of Foveal Avascular Zone in Color Fundus Image for Grading of Diabetic Retinopathy,"

International Journal of Recent Trends in Engineering, vol. 2, pp. 101-104, November 2009.

4. M. Ahmad Fadzil, L. Izhar, H. Nugroho, and H. A. Nugroho, "Analysis of retinal fundus images for grading of diabetic retinopathy severity," *Medical and Biological Engineering and Computing*, vol. 49 pp. 1-8, January 2011.
5. M. H. Ahmad Fadzil, L. I. Izhar, and H. A. Nugroho, "Area Analysis of Foveal Avascular Zone in Diabetic Retinopathy Color Fundus Images," *International Journal of Medical Engineering and Informatics*, vol. 3, pp. 84-98, 2011.
6. M. H. Ahmad Fadzil, L. I. Izhar, and H. A. Nugroho, "Analysis of Foveal Avascular Zone for Grading of Diabetic Retinopathy," *International Journal Biomedical Engineering and Technology*, vol. 6, pp. 232-50, 2011.

Exhibition(s) and Competition(s):

1. RETINO: Computerised Diabetic Retinopathy Monitoring & Grading System in 20th International Invention Innovation and Technology Exhibition (ITEX) 2009, 15-17 May 2009, Kuala Lumpur Convention Centre, Malaysia. Gold medal achieved (Appendix E).
2. RETINO: Computerised Diabetic Retinopathy Monitoring & Grading System in iENA 2009, 5-8 November 2009, Exhibition Centre Nürnberg, Nürnberg, Germany. Gold medal achieved (Appendix F).
3. RETINO - A Computerized Diabetic Retinopathy Grading and Monitoring System. Finalist for Wyss Institute - IEEE EMBS Award for Translational Research. EMBC 2012 Conference in San Diego, California on August 29, 2012.

APPENDIX A: APPROVAL OF INTERVENTIONAL CLINICAL STUDY

(MOH/CRC/CTA004/100209-RVD130309)

15/05 2009 16:22 FAX

NIK SECRETARIAT

001



PEJABAT TIMBALAN KETUA PENGARAH KESIHATAN
OFFICE OF THE DEPUTY DIRECTOR-GENERAL OF HEALTH
(PENYELIDIKAN & BOKONGAN TEKNIKAL)
(RESEARCH & TECHNICAL SUPPORT)
KEMENTERIAN KESIHATAN MALAYSIA
MINISTRY OF HEALTH MALAYSIA
Ara 12, Blok E7, Parcel E, Precinct 1
Level 12, Block E7, Parcel E, Precinct 1
Pusat Pentadbiran Kerajaan Persekutuan
Federal Government Administrative Centre
62590 PUTRAJAYA

Tel : 03 88832543
Faks : 03 88896184

MEDICAL RESEARCH & ETHICS COMMITTEE
MINISTRY OF HEALTH MALAYSIA
National Institutes of Health
Institute Health Management
Jalan Rumah Sakit, Bangsar
59000 Kuala Lumpur

(5)dim.KKM/NIHSEC/08/0804/P09-46
07 May 2009

Attn: Bao Wen
Faka: 03-4043 9446

Dr Nor Fariza Ngah
Jabatan Oftalmologi
Hospital Selayang

Protocol Title :

Accuracy analysis of computerized diabetic retinopathy (DR) monitoring and grading algorithm

Principal Investigator : Dr Nor Fariza Ngah

Hospital Selayang

Documents received and reviewed with reference to the above study:

1. Study Proposal, Dated 18 March 2009.
2. Amended Inform Consent Form, Version 2, (English, Malay, Mandarin and Tamil), Dated 20 March 2009.
3. Clinical Trial Agreement : MOH/CRC/CTA004/100209-rvd130309-amd060409.

The Medical Research & Ethics Committee, Ministry of Health Malaysia operates in accordance to the International Conference of Harmonization Good Clinical Practice Guidelines.

Project Sites: Hospital Selayang

Decision by Medical Research & Ethics Committee:

- Approved
 Conditionally Approved
 Disapproved

Date of Approval: 07 May 2009

DATO' DR. CHANG KIAN MENG
Chairman
Medical Research & Ethics Committee
Ministry of Health Malaysia

APPENDIX B: APPROVAL OF OBSERVATIONAL CLINICAL STUDY

(NMRR-08-842-1997)

NATIONAL INSTITUTE OF HEALTH'S APPROVAL FOR CONDUCTING RESEARCH IN THE MINISTRY OF HEALTH MALAYSIA

PENGESAHAN INSTITUSI PENYELIDIKAN NEGARA UNTUK MENJALANKAN PENYELIDIKAN DI KEMENTERIAN KESIHATAN

This is an auto computer - generated document. It is issued by one of the research institute under the National Institutes of Health (NIH). These are the Institute for Medical Research (IMR), Clinical Research Centre (CRC), Institute of Public Health (IPH), Institute for Health Management (IHM), Institute for Health Systems Research (IHSR), and Institute for Health Behavioural Research (IHBR)

Dokumen ini adalah cetakan berkomputer. Borang ini dikeluarkan oleh salah satu institusi dibawah National Institutes of Health (NIH) iaitu Institut Penyelidikan Perubatan (IMR), Pusat Penyelidikan Klinikal (CRC), Institut Kesihatan Umum (IKU), Institut Pengurusan Kesihatan (IPK), Institut Pengurusan Sistem Kesihatan (IPSK), Institut Penyelidikan Tingkahlaku Kesihatan (IPTK)

Unique NMRR Registration ID : [Nombor Pendaftaran]	NMRR-08-842-1997
Research Title : [Tajuk]	Computerized Diabetic Retinopathy (DR) Grading and Monitoring System
Protocol Number if available : [Nombor Protokol jika ada]	

#	Investigator Name [Name Penyelidik]	Institution Name [Nama Institusi]
1	Hermawan Nugroho	
2	Ahmad Fadzil M Hani	
3	Lila Iznita Bt Izhar	
4	Nor Fariza Ngah	Selayang Hospital
5	Tara Mary George	Selayang Hospital

I have reviewed the above titled research, and approve of its design and conduct.

Saya telah menyemak kajian yang bertajuk seperti di atas dan meluluskan rekabentuk dan perlaksanaannya.

Name of Director : [Nama Pengarah]	Dr. Lim Teck Onn
NIH Institute (IMR, CRC, IPH, IHM, IHSR and IHBR) [Nama Institusi di bawah NIH]	Clinical Research Centre (for submission to CRC Hospital Selayang)
Signature & Official stamp : [Tandatangan dan Cop Rasmi]	This is a computer generated document, therefore no signature is required.
Date : [Tarikh]	21-04-2008

(Note: This is a computer generated document. It may not carry any signature)

APPENDIX C: RETICA ALGORITHM (MATLAB CODE)

```
% RETICA
% Input image is RGB and is processed to Retinex and followed by ICA to get
% the results in which one of them is the haemoglobin-related component image.

% LOAD IMAGE
[FileName,PathName] = uigetfile('*.','Select any RGB image');
y = [PathName,FileName];
I = imread(y);

imgr = I(:,:,1);
imgg = I(:,:,2);
imgb = I(:,:,3);
[M2 N2] = size(imgg);
ratio = 0.4;

% Automatic cropping by selecting centre of the macular region
rectOri=[(x-0.5*ratio*M2) (y-0.5*ratio*M2) (round(ratio*M2)) (round(ratio*M2))];
Icr = imcrop(I,rectOri);
[xx yy] = size(Icr(:,:,2));
Icr = Icr(1:xx-mod(xx,2),1:yy-mod(yy,2),:);
figure(10), imshow(Icr)

% to substitute variable Icr dengan I and transform into log
Ircr = log(double(Icr(:,:,1)+1))/log(255);
Igrcr = log(double(Icr(:,:,2)+1))/log(255);
Ibcrcr = log(double(Icr(:,:,3)+1))/log(255);

maximuter = 10;
dd = 2;
```

```
for muter =1:maximuter
```

```
    IrcrR2 = my3retinex_mccann99(Ircr, muter);  
    IgcrR2 = my3retinex_mccann99(Igcr, muter);  
    IbcrR2 = my3retinex_mccann99(Ibcr, muter);
```

```
    % Kurtosis Cropped Area
```

```
    kur_IrcrR2 = kurtosis(nonzeros(IrcrR2(:)));  
    kur_IgcrR2 = kurtosis(nonzeros(IgcrR2(:)));  
    kur_IbcrR2 = kurtosis(nonzeros(IbcrR2(:)));
```

```
    kur_IcrR2(dd,1) = kur_IrcrR2;  
    kur_IcrR2(dd,2) = kur_IgcrR2;  
    kur_IcrR2(dd,3) = kur_IbcrR2;
```

```
    dd = dd+1
```

```
end
```

```
% Select Component
```

```
    kur_IcrR2_r = kur_IcrR2(:,1);  
    kur_IcrR2_g = kur_IcrR2(:,2);  
    kur_IcrR2_b = kur_IcrR2(:,3);  
    kur_IcrR2_max_r = find(kur_IcrR2_r==max(kur_IcrR2_r));  
    kur_IcrR2_max_g = find(kur_IcrR2_g==max(kur_IcrR2_g));  
    kur_IcrR2_max_b = find(kur_IcrR2_b==max(kur_IcrR2_b));
```

```
    IrRkma = exp(my3retinex_mccann99(Ircr, kur_IcrR2_max_r)*log(255));  
    IgRkma = exp(my3retinex_mccann99(Igcr, kur_IcrR2_max_g)*log(255));  
    IbRkma = exp(my3retinex_mccann99(Ibcr, kur_IcrR2_max_b)*log(255));
```

```
% Output of Part 1 RETICA
```

```

imVCr = uint8(IrRkma);
imVCg = uint8(IgRkma);

imVCb = uint8(IbRkma);

imgrl2 = im2double(imVCr);
imggl2 = im2double(imVCg);
imgbl2 = im2double(imVCb);

% Input for PCA ICA
img_in2 = [imgrl2(:) imggl2(:) imgbl2(:)];

% the next process is using the FastICA
[img_est2, A_est2, W2]=fastica(img_in2, 'approach', 'symm', 'g',
'tanh','stabilization','on');

Rout2 = img_est2(1,:);Gout2 = img_est2(2,:);Bout2 = img_est2(3,:);

% Rescale the image intensity value from min and max log into 0 to 255
Romax2 = max(Rout2);
Romin2 = min(Rout2);
Ro2 = round((255*(Rout2 - Romin2)/(Romax2-Romin2))); % With log
Gomax2 = max(Gout2);
Gomin2 = min(Gout2);
Go2 = round((255*(Gout2 - Gomin2)/(Gomax2-Gomin2))); % With log
Bomax2 = max(Bout2);
Bomin2 = min(Bout2);
Bo2 = round((255*(Bout2 - Bomin2)/(Bomax2-Bomin2))); % With log

ROim2 = uint8(reshape(Ro2,M2,N2));GOim2 = uint8(reshape(Go2,M2,N2));BOim2
= uint8(reshape(Bo2,M2,N2));

```

```

% Find kurtosis for each of the components
kur(1)=kurtosis(double(ROim2(:)));
kur(2)=kurtosis(double(GOim2(:)));

kur(3)=kurtosis(double(BOim2(:)));

%% Find haemoglobin-related image component
[mkur pkur]=min(kur);

if pkur==1
    A20=ROim2;
end
if pkur==2
    A20=GOim2;
end
if pkur==3
    A20=BOim2;
end

A21=imcomplement(uint8(A20));

if mean2(A20)>mean2(A21)
    A1=A20;
else
    A1=A21;
end

imgica = A1;

figure(20), imshow(imgica)

```

APPENDIX D: RETINO ALGORITHM (MATLAB CODE)

```
% RETINO Fully-Automated
% Input image is RGB, image is automatically cropped and is processed to RETICA
% (Retinex and followed by ICA to get the results which one of them is the
% haemoglobin related component image)
% The haemoglobin related component image is inputted to segmentation
% process by automated region growing developed based on combination of
% Chauduri filters followed by Higgins technique.
% The segmented vessels are inputted for FAZ determination.
% The FAZ area is measured and inputted for DR stage classification.
tic
close all;
clear all;
clc;

% Load Image
[FileName,PathName] = uigetfile('*.png','Select any RGB image');
y = [PathName,FileName];
I = imread(y);

figure(1),imshow(I);
[x,y] = ginput(1);
x = round(x);
y = round(y);
c(1).input=I;
c(1).titik=[x,y];
c(1).filename=FileName;

imgr = I(:,:,1);
imgg = I(:,:,2);
```

```

imgb = I(:,:,3);

[m n] = size(imgg);
ratio = 0.4;

% automatic cropping by selecting centre of the macular region
rectOri=[(x-0.5*ratio*m) (y-0.5*ratio*m) (round(ratio*m)) (round(ratio*m))];
Icr = imcrop(I,rectOri);
[xx yy] = size(Icr(:,:,2));
Icr = Icr(1:xx-mod(xx,2),1:yy-mod(yy,2),:);
figure(10), imshow(Icr)

% substitute variable Icr with I and transform into log
Icr = log(double(Icr(:,:,1)+1))/log(255);
Igr = log(double(Icr(:,:,2)+1))/log(255);
Ibr = log(double(Icr(:,:,3)+1))/log(255);

[M2 N2] = size(Igr); % Size of cropped image
maximuter = 40;
dd = 2;
for muter =1:maximuter
    IcrR2 = my3retinex_mccann99(Icr, muter);
    IgrR2 = my3retinex_mccann99(Igr, muter);
    IbrR2 = my3retinex_mccann99(Ibr, muter);

% Kurtosis Cropped Area
kur_IcrR2 = kurtosis(nonzeros(IcrR2(:)));
kur_IgrR2 = kurtosis(nonzeros(IgrR2(:)));
kur_IbrR2 = kurtosis(nonzeros(IbrR2(:)));

kur_IcrR2(dd,1) = kur_IcrR2;
kur_IcrR2(dd,2) = kur_IgrR2;

```

```

kur_IcrR2(dd,3) = kur_IbcrR2;

    dd = dd+1;
end

% Select Component
kur_IcrR2_r = kur_IcrR2(:,1);
kur_IcrR2_g = kur_IcrR2(:,2);
kur_IcrR2_b = kur_IcrR2(:,3);
kur_IcrR2_max_r = find(kur_IcrR2_r==max(kur_IcrR2_r));
kur_IcrR2_max_g = find(kur_IcrR2_g==max(kur_IcrR2_g));
kur_IcrR2_max_b = find(kur_IcrR2_b==max(kur_IcrR2_b));

IrRkma = exp(my3retinex_mccann99(Ircr, kur_IcrR2_max_r)*log(255));
IgRkma = exp(my3retinex_mccann99(Igcr, kur_IcrR2_max_g)*log(255));
IbRkma = exp(my3retinex_mccann99(Ibcr, kur_IcrR2_max_b)*log(255));

% Output of Part 1 RETICA
imVCr = uint8(IrRkma);
imVCg = uint8(IgRkma);
imVCb = uint8(IbRkma);

imgrl2 = im2double(imVCr);
imggl2 = im2double(imVCg);
imgbl2 = im2double(imVCb);

% Input for PCA ICA
img_in2 = [imgrl2(:) imggl2(:) imgbl2(:)]';

[img_est2, A_est2, W2]=fastica(img_in2, 'approach', 'symm', 'g',
'tanh','stabilization','on');

```

```

Rout2 = img_est2(1,:);Gout2 = img_est2(2,:);Bout2 = img_est2(3,:);

% Rescale the image intensity value from min and max log into 0 to 255
Romax2 = max(Rout2);
Romin2 = min(Rout2);
Ro2 = round((255*(Rout2 - Romin2)/(Romax2-Romin2))); % With log

Gomax2 = max(Gout2);
Gomin2 = min(Gout2);
Go2 = round((255*(Gout2 - Gomin2)/(Gomax2-Gomin2))); % With log

Bomax2 = max(Bout2);
Bomin2 = min(Bout2);
Bo2 = round((255*(Bout2 - Bomin2)/(Bomax2-Bomin2))); % With log
% Bo2 = Bout2; % No log

ROim2 = uint8(reshape(Ro2,M2,N2));GOim2 = uint8(reshape(Go2,M2,N2));BOim2
= uint8(reshape(Bo2,M2,N2));

% Find kurtosis for each of the components
kur(1) = kurtosis(double(ROim2(:)));
kur(2) = kurtosis(double(GOim2(:)));
kur(3) = kurtosis(double(BOim2(:)));

%% Find hemoglobin image
[mkur pkur] = max(kur);
if pkur==1
    A20 = ROim2;
end
if pkur==2

```

```

    A20 = GOim2;
end
if pkur==3
    A20 = BOim2;

end
A21=imcomplement(uint8(A20));

if mean2(A20)>mean2(A21)
    A1 = A20;
else
    A1 = A21;
end

imgica = A1;

figure(19),
subplot(231),imshow(imVCr),title('RETICA p1 RB');
subplot(232),imshow(imVCg),title('RETICA p1 GB');
subplot(233),imshow(imVCb),title('RETICA p1 BB');
subplot(234),imshow(ROim2),title('IC 1');
subplot(235),imshow(GOim2),title('IC 2');
subplot(236),imshow(BOim2),title('IC 3');

figure(20),
subplot(131),imshow(ROim2),title('IC 1');
subplot(132),imshow(GOim2),title('IC 2');
subplot(133),imshow(BOim2),title('IC 3');

figure(30), imshow(imgica), title('Haemoglobin-related component image');

figure(35),

```

```

subplot(331), imshow(Ircr), title('Red band');
subplot(334), imshow(Igcr), title('Green band');
subplot(337), imshow(Ibcr), title('Blue band');
subplot(132), imshow(imVCg), title('RETICA p1 GB');
subplot(133), imshow(imgica), title('RETICA p2 Haemo');

```

```

figure(37),
subplot(131), imshow(Igcr), title('Green band');
subplot(132), imshow(imVCg), title('RETICA p1 GB');
subplot(133), imshow(imgica), title('RETICA p2 Haemo');

```

```

%% Segmentation of retinal blood vessels

```

```

buf1=[];

```

```

buf2=[];

```

```

buf3=[];

```

```

% 12 matched filters analysis

```

```

load('12cha04.mat')

```

```

% Procedure to find blood vessel

```

```

for i=1:12

```

```

    buf1(i).image = conv2(im2double(A1),fil(i).image,'same');

```

```

    buf2 = reshape(buf1(i).image,1,[]);

```

```

    buf3 = [buf3;buf2];

```

```

end

```

```

% Find max response from 12 filtered images

```

```

buf4 = max(buf3);

```

```

buf4 = reshape(buf4,M2,N2);

```

```

mn = min(min(buf4));

```

```

buf5 = buf4-mn;

```

```

mx = max(max(buf5));
buf6 = round(buf5/mx*255);
buf7 = uint8(buf6);

% Generate seeds
thh = mean2(buf7);

buf8 = im2bw(buf7,(thh)/255);

figure(40),
subplot(121),imshow(imgica),title('Haemoglobin-related component image');
subplot(122),imshow(buf4,[]),title('Output from Chauduri filter');

buf4_img = imagestretchminmax(buf4);

buf9 = 400*buf8;
buf9 = double(buf9);
out2 = imadd(buf9,double(buf7));

[xlist,ylist,BW] = HigginsPoints1107(buf8,double(buf7));

% Region growing
A2 = imcomplement(A1);
[output2,outPlus,outMinus,intPoint] = ngalusin2(buf7,ylist,xlist);
output4 = imadd(double(A2),100*output2);

% figure(1236),subplot(121),imshow(output2,[]),title('Output ');
% figure(1236),subplot(122),imshow(output4,[]);
% toc
%
mn1 = min(min(output2));
output2_buf = output2-mn1;

```

```

mx1 = max(max(output2_buf));
output3 = round(output2_buf/mx1*255);
output3 = uint8(output3);

%% Procedure to find end points of blood vessels
[labTitik posTitik] = fitur_1107(output2);
[endObjects imgEndPoints] = fltr_1107(labTitik,posTitik);

pTitik = 60;
[areaNonLingkaran imgConnect BW2
listEndPoints]=akhiro_1107(buf7,imgEndPoints,pTitik);

out3 = imadd(output4,double(imgConnect));

figure(60),
subplot(131),imshow(imgEndPoints,[]),title('End-points detection');
subplot(132),imshow(imgConnect,[]),title('End-points connection');
subplot(133),imshow(out3,[]),title('FAZ area obtained');

imgEndPoints_img = imagestretchminmax(imgEndPoints);
imgConnects_img = imagestretchminmax(imgConnect);
out3_img = imagestretchminmax(out3);

xk = listEndPoints(:,1);
yk = listEndPoints(:,2);

[t top tlow thigh radius] = ttbaru1107(out3,xk,yk,rectOri);
[u1 u2] = size(out3);
Z2 = zeros(u1,u2);

%% The FAZ area
Z2 = func_Drawline(Z2,tlow(1),tlow(2),thigh(1),thigh(2),160);

```

```
Z3 = imadd(Z2,out3);
```

```
radiusFAZ=radius;
```

```
areaFAZ=areaNonLingkaran;
```

```
kurt_r = kur_IcrR2_max_r-1;
```

```
kurt_g = kur_IcrR2_max_g-1;
```

```
kurt_b = kur_IcrR2_max_b-1;
```

```
figure(70),
```

```
imshow(Z3,[]),title(['FAZ with radius is ',num2str(radius),' pixels and area is ',num2str(areaNonLingkaran),' pixels'])
```

```
Z3_img = imagestretchminmax(Z3);
```

```
kurr = kur_IcrR2_max_r-1;
```

```
kurg = kur_IcrR2_max_g-1;
```

```
kurb = kur_IcrR2_max_b-1;
```

```
radiusFAZ;
```

```
areaFAZ;
```

```
x;
```

```
y;
```

```
d(1)=radiusFAZ;
```

```
d(2)=areaFAZ;
```

```
d(3)=x;
```

```
d(4)=y;
```

```
d(5)=kurt_r;
```

```
d(6)=kurt_g;
```

```
d(7)=kurt_b;
```

```
e(i,1).output=imgica;
```

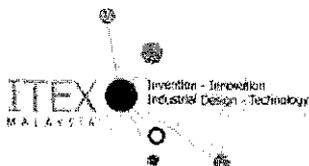
```
e(i,2).output=output4;
```

```
e(i,3).output=out3;
```

```
e(i,4).output=Z3;
```

```
toc
```

APPENDIX E: CERTIFICATE OF AWARD (ITEX 2009)



Certificate of Award

This is to certify that

**PROF IR DR AHMAD FADZIL M HANI, LILA IZNITA IZHAR,
HERMAWAN NUGROHO, HANUNG ADI NUGROHO**

has been awarded the

ITEX GOLD MEDAL

for the invention

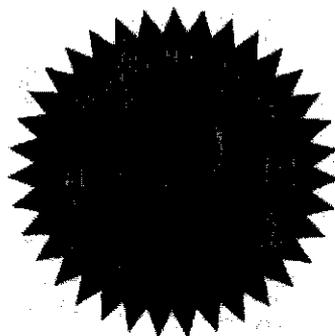
**COMPUTERISED DIABETIC RETINOPATHY MONITORING AND
GRADING SYSTEM**

at the

**20th International Invention, Innovation & Technology Exhibition
ITEX 2009, Kuala Lumpur, Malaysia**

held from

15th – 17th May 2009




Academician Tan Sri Emeritus Professor
Datuk Dr Augustine S. H. Ong
President
Malaysian Invention and Design Society

APPENDIX F: CERTIFICATE OF AWARD (iENA 2009)

URKUNDE/CERTIFICATE



INTERNATIONALE FACHMESSE
» IDEEN - ERFINDUNGEN - NEUHEITEN «
INTERNATIONAL TRADE FAIR
» IDEAS - INVENTIONS - NEW PRODUCTS «
NUREMBERG

Erfindung Universität / Hochschule

Prof. Ir. Dr. Ahmad Fadzil M. Haniffa, Lila Izmita bt. Izhar, Hermawan Nugroho,
Hanung Adi Nugroho
Universiti Teknologi Petronas

MALAYSIA

Aurde für hervorragende Leistungen eine
Goldmedaille
verliehen.

Erfindung/ Neuhheit
Diabetische Retinopathie
Diabetic retinopathy

International Fair of iENA 2009

Kenn. für Verleih in Höhe von
Ausweis über den Antrag (Antrag) 07/100-000

7. November 2009

APPENDIX G:

A KERNEL USED IN THE SEGMENTATION OF RETINAL BLOOD VESSELS
(SECTION 5.3.2)

